

Isotopic Variability as an Indicator for Earth and Solar System Processes

by  
Shelby Nicole Johnston

A dissertation submitted to the Department of Earth and Atmospheric Sciences,  
College of Natural Sciences and Mathematics  
in partial fulfillment of the requirements for the degree of

Doctor of Philosophy

in Geology

Chair of Committee: Peter Copeland

Committee Member: Alan Brandon

Committee Member: Jonny Wu

Committee Member: Barbara Carrapa

University of Houston  
May 2021

## **DEDICATION**

To my cat, Miel, who insisted on contributing numerous typos to the original draft of this manuscript.

## ABSTRACT

Isotope analyses of natural materials are used by geochemists and cosmochemists to investigate Earth and solar system processes. Resolvable differences in the measured isotopic compositions for natural materials are caused by numerous natural and laboratory-induced processes, including mass-dependent fractionation, radioactive decay, nucleosynthetic anomalies, and mass-independent fractionation.

Earth-surface processes were investigated using variations in  $^{40}\text{Ar}/^{39}\text{Ar}$  ages in muscovites in the Central Nepalese Himalayas. Age variations in these samples are due to the radioactive decay of  $^{40}\text{K}$  to  $^{40}\text{Ar}$ , coupled with temperature-dependent diffusion of Ar. The isotopic variability in these samples, coupled with geomorphologic and structural data, provided information about uplift and erosion. We used this variability to interpret a zone of increased erosion that is centered above recently proposed locations of mid-crustal ramps in the Main Himalayan Thrust. This zone of increased erosion was consistent with a duplex growing along the ramp back-tilting and uplifting older duplex faults. This zone also coincides with a dynamically supported bulge in the High Himalaya where a reservoir of elastic strain appears to be maintained over numerous seismic cycles.

Solar system processes, including accretion in the protoplanetary disk, were investigated using nucleosynthetic Nd isotope variations and mass-independent fractionation in enstatite and carbonaceous chondrite samples. Our Nd isotopic analyses show that Earth and enstatite chondrites have resolvable differences in their  $^{142}\text{Nd}/^{144}\text{Nd}$  ratios, even after correcting for radiogenic  $^{142}\text{Nd}$ . This likely indicates that

the materials in the solar nebula that accreted to form Earth and enstatite chondrites had different starting Sm/Nd ratios. This resolvable difference can be explained by mineral sorting in the solar nebula, via mineral evaporation fronts in the protoplanetary disk that could preferentially enrich Earth with material that has a higher Sm/Nd ratio. The Nd isotopic compositions of CK (Karoonda-like) chondrites are not resolvable from CV (Vigarano-like) chondrites. Numerous chondrite samples analyzed for their Nd isotopic compositions have  $^{150}\text{Nd}/^{144}\text{Nd}$  anomalies that are inconsistent with nucleosynthetic models. The Nd isotopic compositions of these samples are not consistent with laboratory-induced mass-independent fractionation. Rather, we propose that they are consistent with a combination of nucleosynthetic anomalies and nuclear field shift effects produced by natural processes.



# TABLE OF CONTENTS

<b>DEDICATION.....</b>	<b>ii</b>
<b>ABSTRACT .....</b>	<b>iii</b>
<b>LIST OF TABLES.....</b>	<b>viii</b>
<b>LIST OF FIGURES .....</b>	<b>x</b>
<b>I. POST-MIOCENE EROSION IN CENTRAL NEPAL CONTROLLED BY MID-CRUSTAL RAMP POSITION, DUPLEX GROWTH, AND DYNAMICALLY MAINTAINED ELASTIC STRAIN .....</b>	<b>1</b>
1.1 Introduction.....	1
1.2 Geologic Setting.....	3
1.3 Previous Work.....	6
1.4 Muscovite $^{40}\text{Ar}/^{39}\text{Ar}$ Enrichment Factor Model.....	8
1.4.1 Bedrock and Detrital Muscovite $^{40}\text{Ar}/^{39}\text{Ar}$ Compilation.....	8
1.4.2 Calculating Enrichment Factors.....	10
1.5 Comparisons of Erosional, Structural, Geomorphological, and Climatic Data.....	16
1.5.1 Comparisons of Erosion Profiles .....	16
1.5.2 Comparison of Erosion Profiles with Climate and River Channel Steepness.....	18
1.5.3 Comparison of Erosion Profiles with Local Structure.....	20
1.6 Discussion.....	22
1.7 Conclusion.....	26
<b>II. ND NUCLEOSYNTHETIC ANOMALIES IN ENSTATITE CHONDRITES AND THEIR IMPLICATIONS FOR AN ENSTATITE CHONDRITE – EARTH CONNECTION.....</b>	<b>27</b>
2.1 Introduction.....	27
2.2 Neodymium s- and r- process Nucleosynthesis.....	28
2.3 Classes of Meteorites.....	30
2.3.1 Enstatite Chondrites.....	31
2.4 Components of Chondrites.....	32
2.4.1 Chondrules.....	33
2.4.2 Calcium-aluminum-rich Inclusions.....	33

2.4.3 Presolar Grains.....	34
2.5 Samples and Standards.....	35
2.6 Methods.....	37
2.6.1 Chemistry.....	37
2.6.2 Thermal Ionization Mass Spectrometry.....	39
2.6.3 Correction of $\mu^{142}\text{Nd}$ Using $^{143}\text{Nd}/^{144}\text{Nd}$ Ratios.....	41
2.7 Results.....	43
2.8 Discussion.....	55
2.8.1 Laboratory Averages.....	55
2.8.2 Weathering of Sm/Nd – Host Phases.....	60
2.8.3 Variability in the $^{142}\text{Nd}$ Compositions of Earth and Enstatite Chondrites.....	61
2.8.3.1 Hidden Reservoir .....	63
2.8.3.2 Collisional Erosion .....	64
2.8.3.3 Mineral Sorting.....	65
2.9 Conclusion.....	67

### **III. ND ISOTOPIC ANALYSES OF CV-CK CHONDRITES AND EVALUATION OF EXCESS $^{150}\text{Nd}$ IN THE SOLAR SYSTEM.....69**

3.1 Introduction.....	69
3.2 CK and CV Chondrites .....	71
3.3 Samples.....	73
3.4 Results.....	74
3.4.1 Group Averages .....	77
3.5 Discussion .....	78
3.5.1 CK Nd Isotope Compositions .....	78
3.5.2 CC Group Variations .....	79
3.5.3 The Role of CAIs in CK and CV Chondrites .....	84
3.5.4 The Heterogeneity of Nd Isotopes in Allende .....	86
3.5.5 Excess $^{150}\text{Nd}$ in Solar System Materials.....	87
3.5.5.1 150-x Sample Summary.....	88

3.5.5.2 Data Evaluation.....	90
3.5.5.3 Assessing Potential Nuclear Field Shift Effects.....	93
3.5.5.4 Excess $^{150}\text{Nd}$ not from Spike Contamination.....	100
3.5.5.5 Nuclear Field Shift Effects and Nucleosynthesis.....	104
3.5.6 The Effect of Excess $^{150}\text{Nd}$ on CK and CV Chondrites.....	106
3.6 Conclusion.....	106
<b>IV. NON-ARRHENIUS <math>^4\text{He}</math> DIFFUSION KINETICS IN TREATED ZIRCONS.....</b>	<b>110</b>
4.1 Introduction.....	110
4.2 Experimental Procedure .....	110
4.2.1 Sample Preparation.....	110
4.2.2 $^4\text{He}$ Step-Heating Analyses .....	111
4.2.3 Mass, Volume, and Surface Area.....	112
4.3 Results.....	112
4.3.1 $^4\text{He}$ Step-heating .....	112
4.3.2 Mass, Volume, and Surface Area.....	116
4.4 Discussion .....	117
4.4.1 $^4\text{He}$ Step-heating .....	117
4.4.2 $^4\text{He}$ Concentration vs. Surface Area and Volume.....	118
4.5 Conclusion.....	119
<b>APPENDICES</b>	
<b>A. MUSCOVITE <math>^{40}\text{Ar}/^{39}\text{Ar}</math> AGES AND ENRICHMENT FACTOR CALCULATIONS IN THE NARAYANI CATCHMENT .....</b>	<b>120</b>
<b>B. THE ND RATIOS AND <math>\mu^i\text{Nd}</math> VALUES FOR ENSTATITE AND ORDINARY CHONDRITES AND MANTLE-DERIVED MELTS .....</b>	<b>127</b>
<b>C. ALL <math>\mu^i\text{Nd}</math> VALUES FOR SOLAR SYSTEM MATERIALS .....</b>	<b>135</b>
<b>BIBLIOGRAPHY .....</b>	<b>146</b>

## LIST OF TABLES

2.1	Nucleosynthetic Production of Nd Isotopes.....	29
2.2	Enstatite Chondrite Sample List. ....	36
2.3	TIMS Multistatic Nd Configuration.....	40
2.4	Workflow of Initial TIMS Steps to Prevent Reverse Fractionation. ....	41
2.5	JNdi Standard Nd Isotope Compositions.....	44
2.6	Enstatite Chondrite Nd Isotope Compositions.....	44
2.7	The Nd Isotope Compositions of Mantle-Derived Samples. ....	45
2.8	Average Nd Isotope Compositions for Enstatite Chondrite Groups.....	48
2.9	Same-Sample Composition Comparisons for Different Laboratories.....	51
2.10	Average Enstatite-Chondrite Nd Isotope Compositions for various Laboratories. ....	56
2.11	Average Nd Isotope Compositions for All ECs versus Falls. ....	57
2.12	Average Enstatite-Chondrite Nd Isotope Compositions for various Laboratories. ....	61
3.1	Sample List of CV-CK Chondrites. ....	74
3.2	CV-CK Nd Isotope Ratios .....	75
3.3	CV-CK Nd Isotope Compositions .....	76
3.4	Nd Isotope Averages for CC groups .....	76
3.5	Samples Used to Evaluate $^{150}\text{Nd}$ Anomalies in Solar System Materials .....	89
3.6	Full List of Samples with Anomalous, Non-Stellar $^{150}\text{Nd}$ .....	104
4.1	$^4\text{He}$ Step-heating Results for Zircon Fragments from This Study .....	113
4.2	$^4\text{He}$ concentrations, Volume, and Surface Area for Zircon Fragments from This Study .....	116
A.1	Full List of Samples used to Create Age Contours in the Narayani Catchment.....	120
A.2	Calculated EF and log(EF) Values for the Narayani and Subcatchments Within .....	125
B.1	Nd Ratios for Enstatite Chondrites from This Study .....	127
B.2	Nd Ratios for Mantle-derived Melts from This Study .....	128

B.3	Nd Isotope Compositions for Enstatite Chondrites from This Study and Literature .....	129
B.4	Nd Isotope Compositions for Mantle-derived melts from This Study and Literature .....	131
B.5	Nd Isotope Compositions for Ordinary Chondrites from Literature .....	132
C.1	Nd Isotope Compositions for Carbonaceous Chondrites from This Study and Literature .....	135
C.2	Nd Isotope Compositions for Solar System Materials .....	137

## LIST OF FIGURES

1.1	Geologic Map of Central Nepal ..	3
1.2	Map of $k_{sn}$ Values in the Narayani Catchment.....	5
1.3	$^{40}\text{Ar}/^{39}\text{Ar}$ Probability Density Plots and Their Locations.....	7
1.4	Muscovite $^{40}\text{Ar}/^{39}\text{Ar}$ Age Contour Map.....	9
1.5	Illustration of EF Calculation.....	11
1.6	$\log(\text{EF})$ Map of the Narayani, Marsyangdi, and Trishuli Catchments .....	13
1.7	$\log(\text{EF})$ Maps of the Marsyangdi and Trishuli Catchments.....	14
1.8	Locations of Profiles Used in This Study .....	15
1.9	Comparison of Erosion Profiles with Local Structure, $k_{sn}$ Profiles, $\log(\text{EF})$ Profiles, and rainfall Profile .....	17
2.1	$\mu^{148}\text{Nd}$ vs. $\mu^{145}\text{Nd}$ for Berlin Samples vs. All Other Samples .....	46
2.2	Nd Isotope Compositions of the Different Enstatite Chondrite Groups.....	49
2.3	Nd Isotope Compositions of the Enstatite Chondrite Class .....	50
2.4	$\mu^{148}\text{Nd}$ vs. $\mu^{145}\text{Nd}$ and $\mu^{150}\text{Nd}$ vs. $\mu^{148}\text{Nd}$ Averages for Enstatite and Ordinary Chondrites .....	52
2.5	$\mu^{145}\text{Nd}$ vs. $\mu^{142}\text{Nd}_{\text{corr}}$ . Averages for Enstatite Chondrite Groups and Total Enstatite and Ordinary Chondrites.....	53
2.6	$\mu^{148}\text{Nd}$ vs. $\mu^{142}\text{Nd}_{\text{corr}}$ . Averages for Enstatite Chondrite Groups and Total Enstatite and Ordinary Chondrites.....	54
2.7	$\mu^{145}\text{Nd}$ vs. $\mu^{142}\text{Nd}_{\text{corr}}$ . Averages for Enstatite and Ordinary Chondrites .....	55
2.8	$\mu^{145}\text{Nd}$ vs. $\mu^{142}\text{Nd}_{\text{corr}}$ . Data and Averages for Various Laboratories.....	58
2.9	$\mu^{148}\text{Nd}$ vs. $\mu^{142}\text{Nd}_{\text{corr}}$ . Data and Averages for Various Laboratories.....	59
2.10	$\mu^{150}\text{Nd}$ vs. $\mu^{142}\text{Nd}_{\text{corr}}$ . Data and Averages for Various Laboratories.....	60
2.11	$\mu^{145}\text{Nd}$ vs. $\mu^{142}\text{Nd}_{\text{corr}}$ . and $\mu^{148}\text{Nd}$ vs. $\mu^{142}\text{Nd}_{\text{corr}}$ . Averages for Enstatite and Ordinary Chondrites.....	63
3.1	Nd Isotope Compositions of the Different Carbonaceous Chondrite Groups .....	77
3.2	CK Nd-Isotope Spider Diagram.....	79

3.3	$\mu^{145}\text{Nd}$ vs. $\mu^{142}\text{Nd}_{\text{corr.}}$ for the Different Carbonaceous Chondrite Groups, the EC Class, and the OC class .....	80
3.4	$\mu^{150}\text{Nd}$ vs. $\mu^{148}\text{Nd}$ for the Different Carbonaceous Chondrite Groups, the EC Class, and the OC class .....	81
3.5	$\mu^{145}\text{Nd}$ vs. $\mu^{145}\text{Nd}$ for the Different Carbonaceous Chondrite Groups, the EC Class, and the OC class .....	82
3.6	$\varepsilon^{54}\text{Cr}$ vs. $\mu^{142}\text{Nd}_{\text{corr.}}$ for the Different Carbonaceous Chondrite Groups, the EC and OC classes, and Earth .....	83
3.7	CAI Nd-Isotope Spider Diagram .....	85
3.8	Allende Nd Isotope Spider Diagram .....	86
3.9	$\mu^{150}\text{Nd}$ vs. $\mu^{148}\text{Nd}$ for Solar System Materials .....	87
3.10	$\mu^{150}\text{Nd}$ vs. $\mu^{148}\text{Nd}$ for Materials with Anomalous $\mu^{150}\text{Nd}$ .....	90
3.11	$\mu^{150}\text{Nd}$ vs. $\mu^{148}\text{Nd}$ vs. $\mu^{145}\text{Nd}$ for Solar System Materials .....	92
3.12	Measured Nd Isotope vs. Nuclear Field Shift Spider Diagrams for Representative Samples .....	96
3.13	$\mu^{148}\text{Nd}$ vs. $\mu^{145}\text{Nd}$ for Materials with Anomalous $\mu^{150}\text{Nd}$ .....	97
3.14	$\mu^{150}\text{Nd}$ vs. $\mu^{145}\text{Nd}$ for Materials with Anomalous $\mu^{150}\text{Nd}$ .....	98
3.15	$\mu^{145}\text{Nd}$ vs. $\mu^{142}\text{Nd}$ for Materials with Anomalous $\mu^{150}\text{Nd}$ .....	99
3.16	Hypothetical $\mu^{150}\text{Nd}$ Spike Contamination of Measured Solar System Materials .....	101
3.17	$\mu^{150}\text{Nd}_{\text{excess}}$ vs. $\mu^{148}\text{Nd}$ for Materials with Anomalous $\mu^{150}\text{Nd}$ .....	103
3.18	$\mu^{150}\text{Nd}_{\text{excess}}$ vs. $\mu^{145}\text{Nd}$ for Materials with Anomalous $\mu^{150}\text{Nd}$ .....	103
3.19	Corrected $\mu^{150}\text{Nd}$ vs. $\mu^{148}\text{Nd}$ for the Different Carbonaceous Chondrite Groups, the EC Class, and the OC class .....	107
4.1	Heating Schedule for Zircon Fragments from This Study .....	112
4.2	Arrhenius Plots for Zircon Fragments from This Study .....	115
4.3	Arrhenius Plots for Zircon Fragments from This Study and Literature .....	118
4.4	Plot of $^4\text{He/g}$ vs. Surface Area/Volume for Zircon Fragments from This Study .....	119

# **Chapter I: Post-Miocene Erosion in central Nepal controlled by mid-crustal ramp position, duplex growth, and dynamically maintained elastic strain**

\*A previous version of this paper has appeared: Johnston, S. N., Cannon, J. M., and Copeland, P. (2020) Post-Miocene erosion in Central Nepal controlled by midcrustal ramp position, duplex growth, and dynamically maintained elastic strain. *Tectonics*, 39 (12), 1-15.

## **1.1 Introduction**

The primary influence on location of erosion in the Himalayas has long been debated (Burbank et al., 2003; Wobus et al., 2003; Godard et al., 2014). Some studies have argued climate and precipitation are the primary drivers of where erosion occurs (Hodges et al., 2004; Thiede et al., 2004; Wobus et al., 2005; Huntington et al., 2006; Clift et al., 2008; Whipple et al., 2009). Other studies have argued that location of erosion is primarily driven by tectonic forces, with precipitation playing a secondary role (Burbank et al., 2003; Godard et al., 2014; Scherler et al., 2014; Landry et al., 2016; van der Beek et al., 2016; Stübner et al., 2018). Multiple methods have been used to understand erosion and exhumation patterns in central Nepal including  $^{10}\text{Be}$  dating (Godard et al., 2014; Olen et al., 2016), fluvial incision rates (Lavé and Avouac, 2001),  $^{40}\text{Ar}/^{39}\text{Ar}$  dating of both bedrock and modern river sediment (Catlos et al., 2001; Godin et al., 2001; Brewer et al., 2006; Ruhl and Hodges, 2005, Huntington and Hodges, 2006; Herman et al., 2010; Copeland et al., 2015a, Martin et al., 2015), apatite fission-track dating (Robert et al., 2009; Thiede and Ehlers, 2013; van der Beek et al., 2016), suspended-sediment flux analysis (Gabet et al., 2008), and modern-sediment compositional analyses (Garzanti et al., 2007). These erosion and exhumation patterns have been compared to multiple climatic, tectonic, and geomorphic variables, such as



mean annual rainfall, normalized river-channel steepness ( $k_{sn}$ ), local relief, hillslope gradients, stream power, coupling with major faults, and local fault geometry (Burbank et al., 2003; Blythe et al., 2007; Whipp et al., 2007; Garzanti et al., 2007; Gabet et al., 2008; Robert et al., 2009; Herman et al., 2010; Thiede and Ehlers, 2013; Godard et al., 2014; Olen et al., 2016; van der Beek et al., 2016) over the past few decades.

Of studies proposing tectonically driven erosion across the Himalayas, some have argued that erosion and exhumation patterns are driven by out-of-sequence thrusting of the MCT (Mukul, 2000; Catlos et al., 2001; Hodges et al., 2004; Wobus et al., 2005), while newer studies argue primarily for erosion driven by local MHT ramp geometries (Robert et al., 2009; Coutand et al., 2014; Godard et al., 2014; Scherler et al., 2014; Landry et al., 2016; van der Beek, 2016) with others also invoking growth and geometry of the Lesser Himalayan Duplex in conjunction with the MHT ramp (Bollinger et al., 2004, 2006; C  lerier et al., 2009; Thiede et al., 2009; Herman et al., 2010; Robinson and Martin, 2014; McQuarrie and Ehlers, 2015; Landry et al., 2016). With the 2015  $M_w$  7.8 Gorkha earthquake spurring new MHT geometry models in central Nepal (Elliot et al., 2016; Hubbard et al., 2016; Whipple et al., 2016; Mendoza et al., 2019), it is important to compare previous erosion and exhumation patterns to these new tectonic models. In this paper, we have used a new method that combines muscovite  $^{40}\text{Ar}/^{39}\text{Ar}$  bedrock and detrital data to analyze the erosion patterns in central Nepal. Unlike many previous studies in the region, our use of widespread, high closure-temperature  $^{40}\text{Ar}/^{39}\text{Ar}$  data gives insight into the deep-seated exhumation patterns across central Nepal. We have compared our model to the previous erosion patterns from this area, along with  $k_{sn}$ , mean annual rainfall, and post-Gorkha MHT geometries in order to investigate if newer structural interpretations and MHT geometries in this region

support the interpretation of tectonically driven erosion, and if so, which features are likely to be primary drivers.

## 1.2 Geologic Setting

Central Nepal is composed of four main tectonostratigraphic units separated by Cenozoic orogen-parallel north-dipping faults (Figure 1.1; Murphy and Yin, 2003). From south to north, the geology can be described as follows: The Main Frontal Thrust (MFT), a series of blind-thrust anticlines and surface-breaking faults that mark the intersection of the India-Asia intracontinental subduction zone, the Main Himalayan Thrust (MHT),

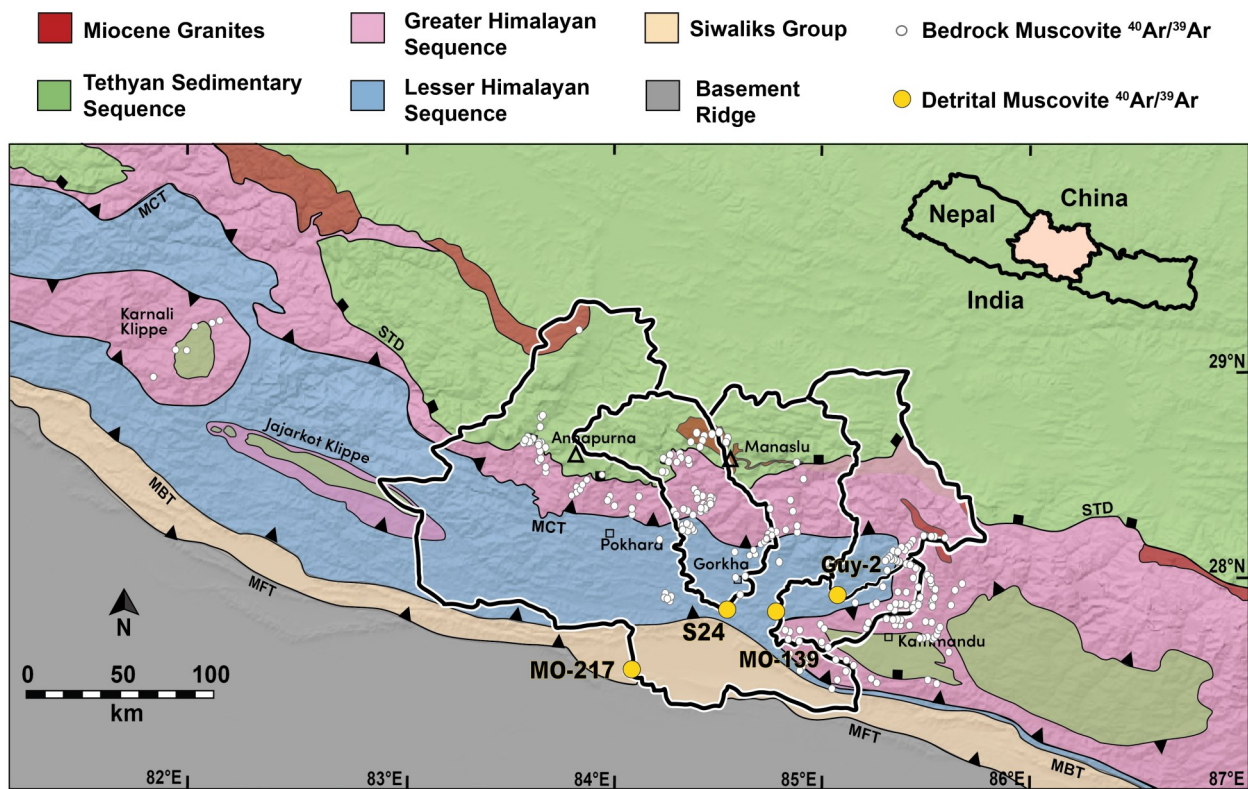


**Figure 1.1** Geologic map of central Nepal and surround area with the Narayani catchment and two subcatchments outlined in black, modified from Copeland et al. (2015), Parsons et al. (2016), and Cannon et al. (2018). Bedrock muscovite  $^{40}\text{Ar}/^{39}\text{Ar}$  samples are shown in white and detrital muscovite  $^{40}\text{Ar}/^{39}\text{Ar}$  samples are shown in yellow (references in text).

with the Earth's surface. The MFT marks the most-recent foreland propagation of the Himalaya thrust system and is uplifting the foreland basin and incorporating it into the thrust wedge. The MFT lies south of the Siwalik Group, a sequence of Miocene-Recent conglomerates, arkosic sandstones, and mudstones. Structurally above the MFT is the Main Boundary Thrust (MBT). The MBT separates the Siwaliks from the Lesser Himalayan Sequence (LHS), which is composed of Precambrian to Mesozoic metasedimentary rocks, increasing in metamorphic grade from southwest to northeast, and encompasses the hinterland-dipping Lesser Himalayan duplex. Moving up through the thrust wedge the next major fault is The Main Central Thrust (MCT), which separates the LHS from the Greater Himalayan Sequence (GHS), a series of kyanite to sillimanite grade gneisses intruded by Miocene leucogranites. Finally, the structurally highest major fault system is the South Tibetan Detachment (STD), a down-to-the-north system of normal faults separating the GHS from the Tethyan Sedimentary Sequence (TSS), a low-grade to unmetamorphosed Paleozoic to Paleogene shallow marine sedimentary sequence of marbles, calc-schists, limestones, and marls (Hodges et al., 1996; DeCelles et al., 2001; Bollinger et al., 2004). The LHS, GHS, TSS, and Siwalik Group are all muscovite-rich (Copeland et al., 2015a).

Although the four-fault architecture of the Himalayan thrust wedge has been known since the discovery of the STD in the early 1980s, the geometry of the basal-thrust (MHT), separating India and Asia, has been more difficult to elucidate. The 2015  $M_w$  7.8 Gorkha earthquake was the most well-instrumented earthquake in the region thus far and the outpouring of data from this event has prompted numerous new models of the MHT ramp geometry in central Nepal (Elliot et al., 2016; Hubbard et al., 2016; Whipple et al., 2016; Mendoza et al., 2019). Hubbard et al., (2016) proposed a

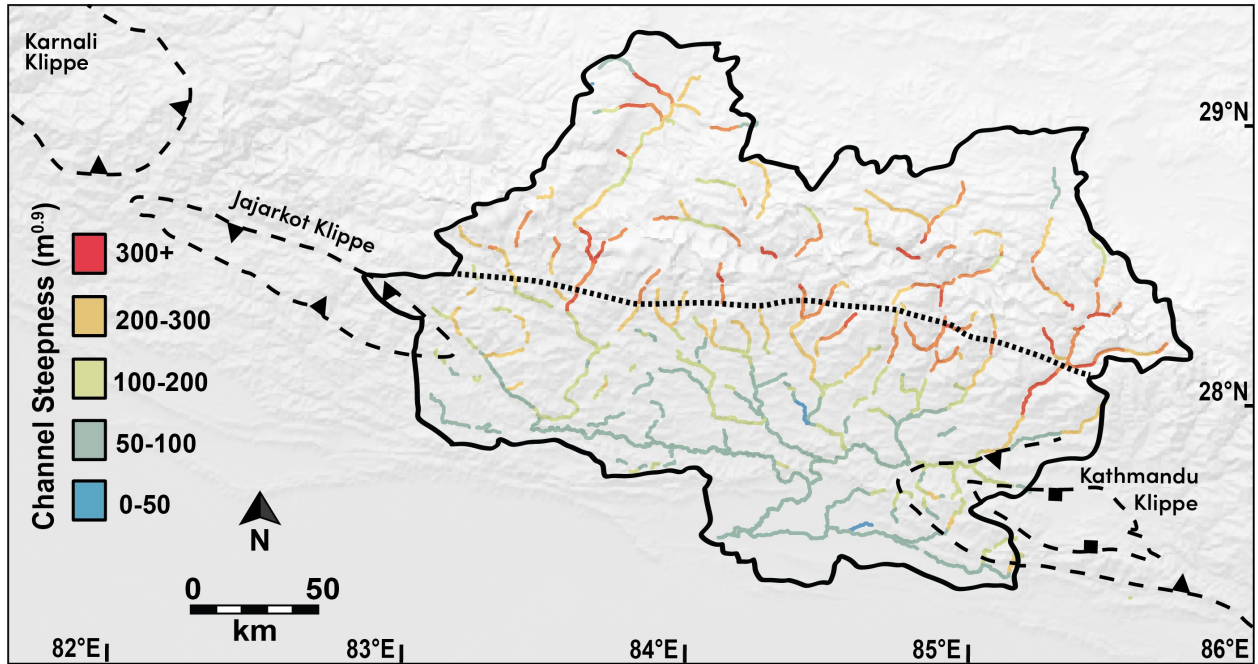


**Figure 1.2** Map of  $k_{sn}$  (channel steepness) values for rivers throughout the catchment. The outline of the catchment is shown as a solid black line. Local klippen are shown by black dashed lines. The MHT locking line is shown by a black dotted line. North of this line, the MHT is more-weakly coupled. South of this line, the MHT is strongly coupled. Local klippen are shown by black dashed lines.

geometry for the MHT that includes both a middle ramp located 50 km north of the MFT, and a deep ramp located ~90 km north of the MFT. Elliott et al., (2016) proposed a ramp ~90 km north of the MFT. Whipple et al., (2016) proposed a ramp ~110 km north of the MFT. Mendoza et al. (2019) suggest the presence of a major duplex system 50 to 70 km north of the surface trace of the MBT. Although a best-fit geometry is still debated, the mid-crustal ramps and duplex structures of these newer geometries are consistently further north than pre-Gorkha models (Pearson, 2002; Herman et al., 2010; Khanal and Robinson, 2013; Robinson and Martin, 2014) and are more in line with the northern mid-crustal ramp proposed in Western Nepal (DeCelles et al., 1998; Cannon and Murphy, 2014; Harvey, et al., 2015).

### 1.3 Previous Work

Due to the relative ease of access and the heightened human and socioeconomic interest in the densely populated Kathmandu region, the Marsyangdi river catchment, and the Annapurna region, there are a wealth of climatic, topographic, and thermochronologic data in central Nepal available to understand the forces driving erosion in this area. Cannon and Murphy (2018) mapped normalized river-channel steepness ( $k_{sn}$ ), a proxy for rock uplift rate, when uplift is sustained over long time periods, (Whipple and Tucker, 1999; Kirby and Whipple, 2001; Wobus et al., 2006; Kirby and Whipple, 2012) throughout the central Himalaya (Figure 1.2) They conducted a statistical analysis comparing the correlation between  $k_{sn}$  and precipitation rate, MHT coupling (Stevens and Avouac, 2015), lithology, and MHT geometry. Their  $k_{sn}$  analysis used ASTER 30 m DEMs. In areas with good DEM data a 250 m smoothing was used. In areas with steep, narrow canyons, the DEM data was poorer, and a 500 m smoothing window was used. Their study also used a 0.45 reference concavity (the standard choice for active mountain ranges). Their results found that the location of high- $k_{sn}$  rivers lies above predicted MHT mid-crustal ramps and the reservoir of elastic strain located in the High Himalaya (Bilham et al., 1997; Bilham et al., 2001; Cattin and Avouac, 2000; Meade, 2010; Ader et al., 2012; Grandin et al., 2012; Stevens and Avouac, 2015). The high- $k_{sn}$  values found in the northern half of the Narayani catchment occur in areas where the material along the MHT is undergoing a rheologic transition from plastic-to-brittle deformation (Ader et al., 2012; Stevens and Avouac, 2015). This north-to-south plastic-to-brittle transition manifests geodetically as a rapid reduction in south-directed interseismic motion beneath the High Himalaya. Southern

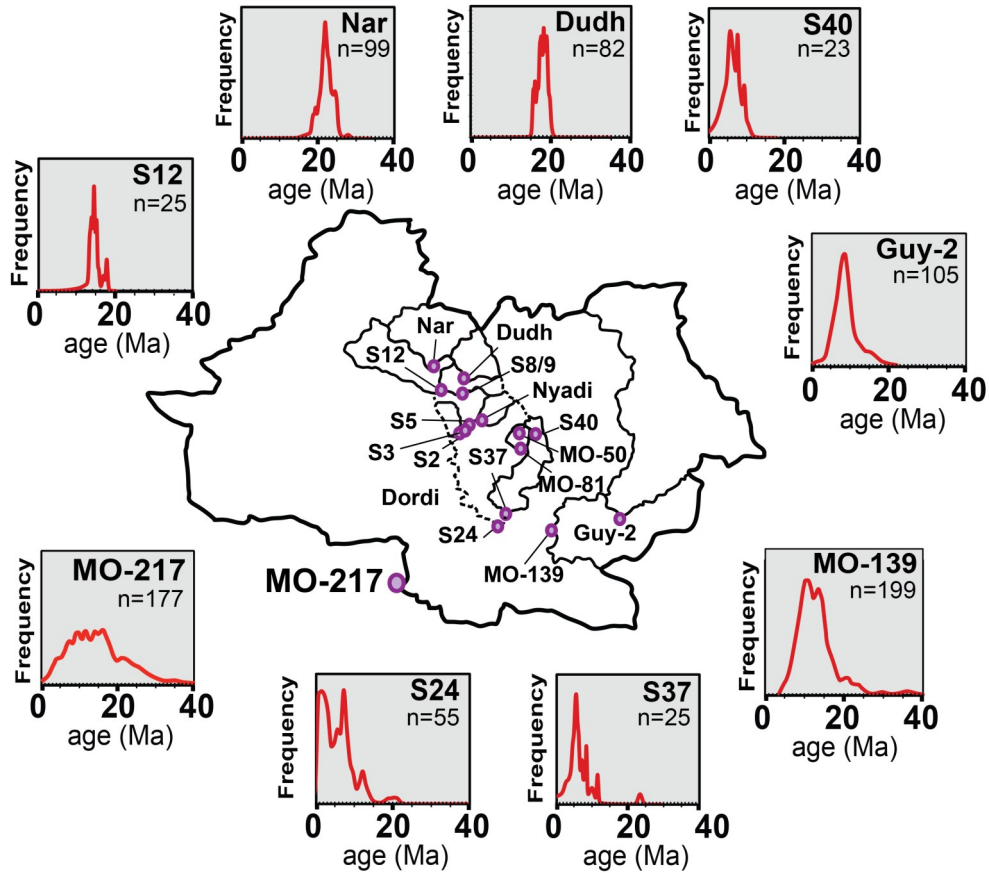


**Figure 1.3** Locations and probability density plots of detrital muscovite  $^{40}\text{Ar}/^{39}\text{Ar}$  samples. Outline of catchments shown in black. The outline of the S24 subcatchment is shown as a dashed line as it is downstream from the Nar, Dudh, S5, S40 and S37 samples (Brewer et al., 2003; Ruhl & Hodges, 2005; Copeland et al., 2015).

Tibet is converging with northern India at  $\sim 20\text{mm-A}$ . South of the geodetically determined locking line (boundary between the strongly and weakly coupled portions of the MHT; Jouanne et al. 2004), there is little to no interseismic rock uplift or horizontal convergence, whereas to the north, interseismic uplift rates reach  $6\text{--}7\text{ mmyr}^{-1}$  (Ader et al., 2012; Stevens and Avouac, 2015). However, much of this uplift is lost as elastic strain is transferred from the High Himalaya to the Lesser Himalaya during plate boundary earthquakes, as highlighted in the 2015 Gorkha earthquake. InSAR analysis after the Gorkha earthquake showed that the High Himalaya immediately north of the

rupture patch lost 0.5 m of elevation, while the rupture patch itself gained 1.0 m of elevation (Elliot et al., 2016). This supports a model of Himalayan seismotectonics in which the High Himalaya “inflate” like a blacksmith’s bellows by bending in response to interseismic India-Asia convergence, storing seismic potential energy and then transferring that energy to the hypocenter of the next great Himalayan earthquake.

Several muscovite  $^{40}\text{Ar}/^{39}\text{Ar}$  studies have been conducted in this area, from both bedrock samples (Table A.1; Copeland et al., 1990; Copeland et al., 1991; Vannay and Hodges., 1996; Arita et al., 1997; Catlos et al., 2001; Godin et al., 2001; Brewer et al., 2003, 2006; Bollinger, et al., 2004; Hodges et al., 2004; Ruhl and Hodges, 2005; Huntington et al., 2006; Herman et al., 2010; Martin et al., 2015) and modern sands from the Narayani River and its tributaries the Trishuli and Marsyangdi (Figure 1.3; Brewer et al., 2003, 2006; Ruhl and Hodges, 2005; Copeland et al., 2015a). Sample MO-217 of Copeland et al. (2015a) comes from below the point where the Trishuli, Burhi Gandaki, Marsyangdi, and Kali Gandaki rivers all come together to form the Narayani; all other samples from modern rivers discussed here are upstream from this point on the Trishuli and the Marsyangdi.

## **1.4 Muscovite $^{40}\text{Ar}/^{39}\text{Ar}$ Enrichment Factor Model**

### **1.4.1 Bedrock and Detrital Muscovite $^{40}\text{Ar}/^{39}\text{Ar}$ Data Compilation**

We compiled 168 bedrock muscovite  $^{40}\text{Ar}/^{39}\text{Ar}$  ages from within the Narayani catchment (Figure 1.1, 1.4) and 47 bedrock muscovite  $^{40}\text{Ar}/^{39}\text{Ar}$  ages from outside the



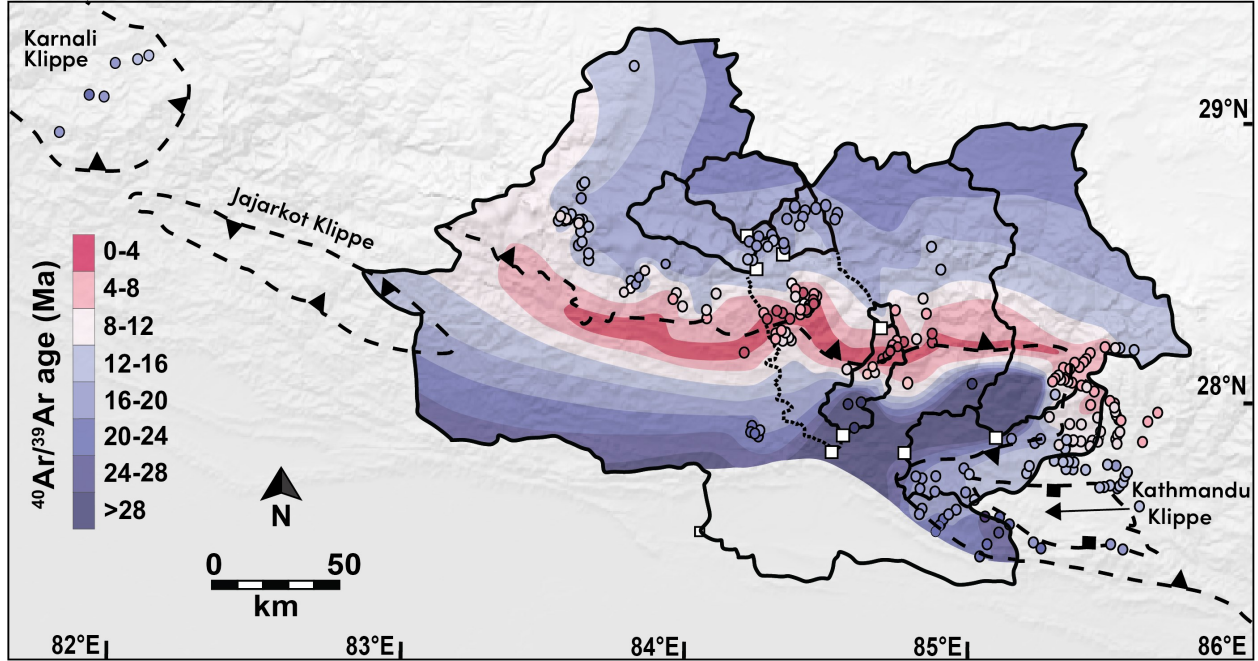


**Figure 1.4** Muscovite  $^{40}\text{Ar}/^{39}\text{Ar}$  age contours for the Narayani catchment. Bedrock muscovite  $^{40}\text{Ar}/^{39}\text{Ar}$  ages, shown as colored circles, are from Copeland et al., 1990; Copeland et al., 1991; Vannay et al., 1996; Arita et al., 1997; Catlos et al., 2001; Godin et al., 2001; Bollinger et al., 2004; Huntington et al., 2006; Herman et al., 2010; Martin et al., 2015; and Soucy La Roche et al., 2018. Catchment and subcatchments are shown by solid black lines. Local klippen and the MCT are shown by dashed lines. The locations of detrital samples from Brewer et al., 2003, 2006; Ruhl & Hodges, 2005; Copeland et al., 2015 are shown as white squares. Age contours were created using a combination of bedrock data and downstream subcatchment detrital data for where bedrock data is sparse. Contours were broken into 4 m.y. intervals.

catchment, to create a contour model of bedrock ages across the catchment. These sample locations are mostly concentrated near the Marsyangdi River, the Kathmandu Complex, and Annapurna with a scarcity of data in the southwest portion of the catchment. To guide the southwestern edge of our model of bedrock muscovite  $^{40}\text{Ar}/^{39}\text{Ar}$  ages in the Narayani catchment, we included sample locations from the Karnali catchment to the west (Soucy La Roche et al., 2018) and correlated the data from the Karnali catchment (west Nepal) to the corresponding geology in the Narayani catchment. We also considered the distribution of ages from detrital muscovites from



subcatchments within the Marsyangdi and Trishuli catchments (Figure 1.3; Brewer et al., 2003, 2006; Ruhl and Hodges, 2005; Copeland et al., 2015a) while determining the position of contours within the subcatchments, particularly where bedrock coverage was sparse or absent. Many of these detrital samples had very small sample sizes, so it is possible for these samples to not represent all of the  $^{40}\text{Ar}/^{39}\text{Ar}$  age ranges that exist upstream. However, if there are age ranges present in the detrital samples, we know the bedrock upstream, within that subcatchment, must contain at least those age ranges; this helped guide the placement of some age contours in the absence of bedrock data. We did not use the  $^{40}\text{Ar}/^{39}\text{Ar}$  detrital muscovite data of Wobus et al. (2003) even though these samples were collected from within our larger Narayani catchment. These analyses were on muscovite aliquots of 20-80 grains rather than the single crystal analyses from Brewer et al. (2003, 2006), Ruhl and Hodges (2005), and Copeland et al. (2015a). Figure 1.4 shows our contour model of the distribution of muscovite  $^{40}\text{Ar}/^{39}\text{Ar}$  ages of bedrock in the Narayani catchment upstream from sample MO-217 of Copeland et al. (2015a). Our age contours are broken up into 4 m.y. intervals, from 0 Ma to >30 Ma.

#### **1.4.2 Calculating Enrichment Factors**

We now have two representations of muscovite  $^{40}\text{Ar}/^{39}\text{Ar}$  age data for the Narayani catchment upstream from sample MO-217: our compilation of bedrock data (Figure 1.4) and the distribution of ages from muscovites in the modern rivers for the catchment overall (sample MO-217 of Copeland et al., 2015a) as well as several smaller subcatchments of the Marsyangdi (Nar, Dudh, S12, S37, and S40; Brewer et al., 2003, 2006; Ruhl and Hodges, 2005) and the Trishuli (samples MO139 and Guy-2,

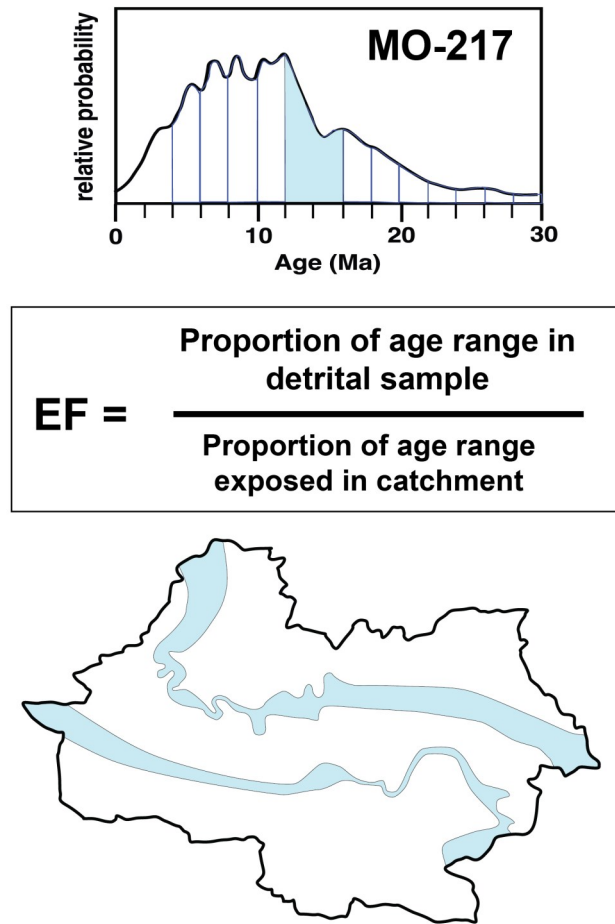


**Figure 1.5** An illustration of the method used for calculating enrichment factor (EF) for erosion in the Narayani basin.

Copeland et al., 2015a). Figure 1.5 shows how we compared these two approaches. First, we calculated the surface area of each catchment. We ignored any variation in elevation and approached the surface area estimates as a simple 2D problem. We then calculated the proportion of the surface area of each age contour within the catchments relative to the total area of the catchment. Next, we calculated the proportion of each age fraction in the detrital sample by calculating the proportion of area under the detrital probability density plot curve for each age range relative to the entire curve. We then obtained the ratio of the proportion of  $^{40}\text{Ar}/^{39}\text{Ar}$  muscovite ages in the detrital sample to

the proportion of the area of the catchment with bedrock muscovites in the same age fraction (Table A.2); we refer to this quantity as the enrichment factor (EF). This measures relative erosion in the catchment area, rather than erosion rates. If all areas within the catchment are eroding at the same rate, the proportion of each age fraction in the detrital sample would mirror the proportion of exposed bedrock for that age fraction (i.e., all EF values would be close to 1). Instead what we see is a range of EF values from 0 to 4.6, indicating variable erosion throughout the catchment. When an age range is underrepresented in the detrital sample relative to our bedrock model, EF will be less than 1 but cannot be less than 0. Conversely, when the age range is overrepresented in the detrital sample relative to our bedrock model, EF will be greater than 1 but its maximum value is unconstrained. To account for this asymmetry, we use  $\log(\text{EF})$  in our figures below and we map values of less than or equal to -0.5 to greater than or equal to 0.5. Some sub-catchments (most notably Guy-2) contain no grains in the detrital sample from the oldest age range in the bedrock model; this results in an EF value of zero for that portion of the bedrock but because log of zero is undefined, we include this in the bin for  $\log(\text{EF}) < -0.5$ . This model operates under the major assumption that all exposed bedrock has a similar muscovite fertility. This homogenous fertility is, however, unlikely, as the THS is composed of low-grade metamorphic and sedimentary units. While it is still muscovite rich (Copeland et al., 2015a) it likely contributes fewer detrital muscovites per unit area than the GHS and LHS, potentially causing EF values for primarily the 16-24 Ma age interval to be lower than expected. This could cause the THS to appear as though it is eroding somewhat more slowly than it is, relative to the GHS.

This method is a simplification of a complex, multi-faceted erosional system that isn't yet fully understood. This simplified approach does not take into account

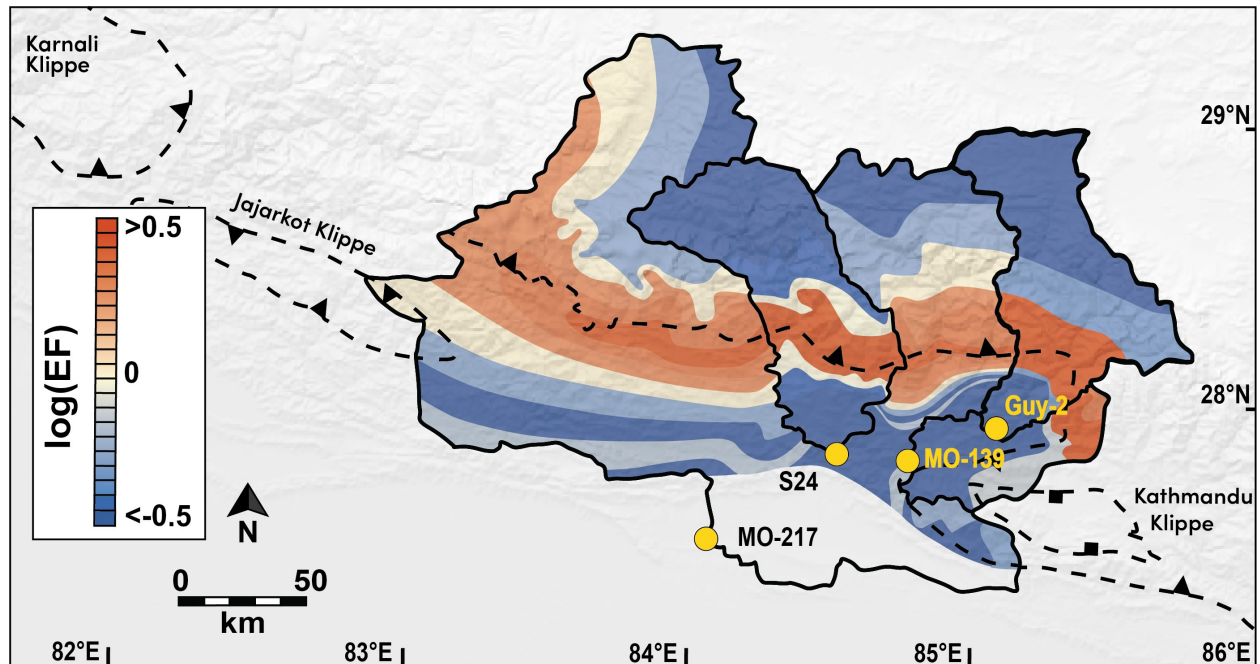


**Figure 1.6**  $\log(EF)$  values for the Narayani catchment (MO-217 detrital sample), the Marsyangdi subcatchment (S24 detrital sample), and the Trishuli subcatchment (MO-139 detrital sample). The two subcatchments are outlined in black. Locations of the detrital samples are shown as yellow circles. Klippen and the MCT are shown as dashed lines.

topography, varying hillslopes, or varying erodibility of different units. Due to the large area encompassed by central Nepal and the heterogeneous distribution of data, this is an adequate model on which to build future evaluations. This model was applied to the Narayani catchment as a whole (sample MO-217, Copeland et al., 2015a). We also used the detrital samples at the mouth of Marsyangdi subcatchment (sample S24; Brewer et al., 2006) and the Trishuli subcatchment (samples Guy-2, MO-139, Copeland et al., 2015a) to calculate their EF, separate from the Narayani calculation. The bedrock contours in the Marsyangdi and Trishuli subcatchments are based on a denser population of bedrock data than the Narayani data. We mapped the  $\log(EF)$  values for the Marsyangdi and Trishuli subcatchments and overlaid them onto the  $\log(EF)$  map for

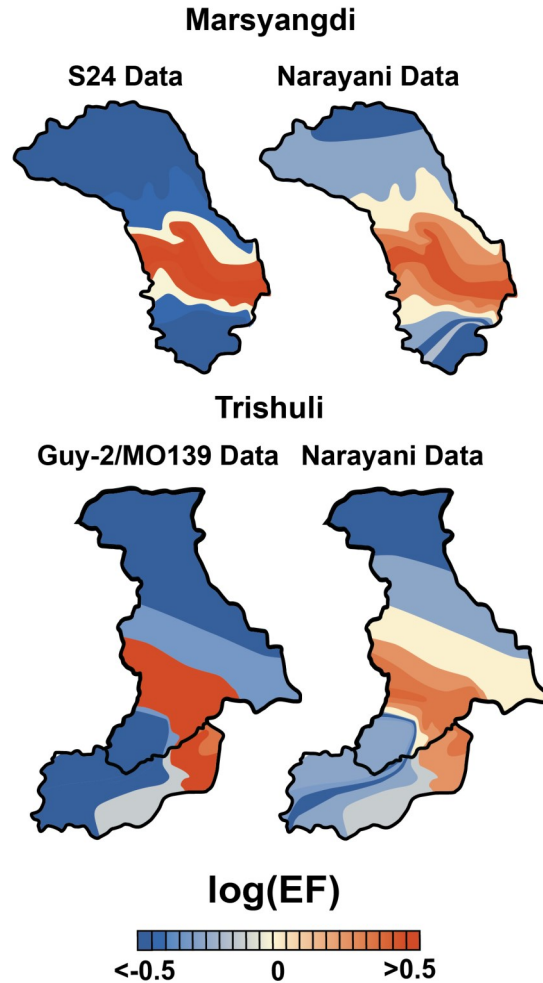


**Figure 1.7** A comparison of  $\log(EF)$  values for the Marsyangdi (top) and Trishuli (bottom) subcatchments with  $\log(EF)$  values being based on their subcatchment detrital samples (left) and with Narayani catchment  $\log(EF)$  values (right).

the Narayani catchment (Figure 1.6). Despite the Narayani catchment having some regions with low concentrations of bedrock data, it has a similar  $\log(EF)$  pattern to both subcatchments, which have denser bedrock data. To show this similarity, we mapped both subcatchments with the  $\log(EF)$  values from their individual subcatchment calculations next to the  $\log(EF)$  values from the Narayani calculations (Figure 1.7). Both  $\log(EF)$  patterns show strong preferential erosion in a central band where the youngest  $^{40}\text{Ar}/^{39}\text{Ar}$  ages are located. Both patterns also show a progressive decrease in  $\log(EF)$

values towards the north and south, where older  $^{40}\text{Ar}/^{39}\text{Ar}$  ages are located. The similarity in the two patterns produced by different detrital samples and bedrock data concentration gives us confidence that our Narayani log(EF) pattern is appropriate despite the lack of data in the southwest quadrant. Additionally, if there was significant recycling of muscovite grains from the Siwalik Group, this would only affect our MO-217 sample, and we would not expect to see the agreement between the log(EF) values for the larger Narayani catchment and the log(EF) values for the two subcatchments that contain no Siwalik sediments.

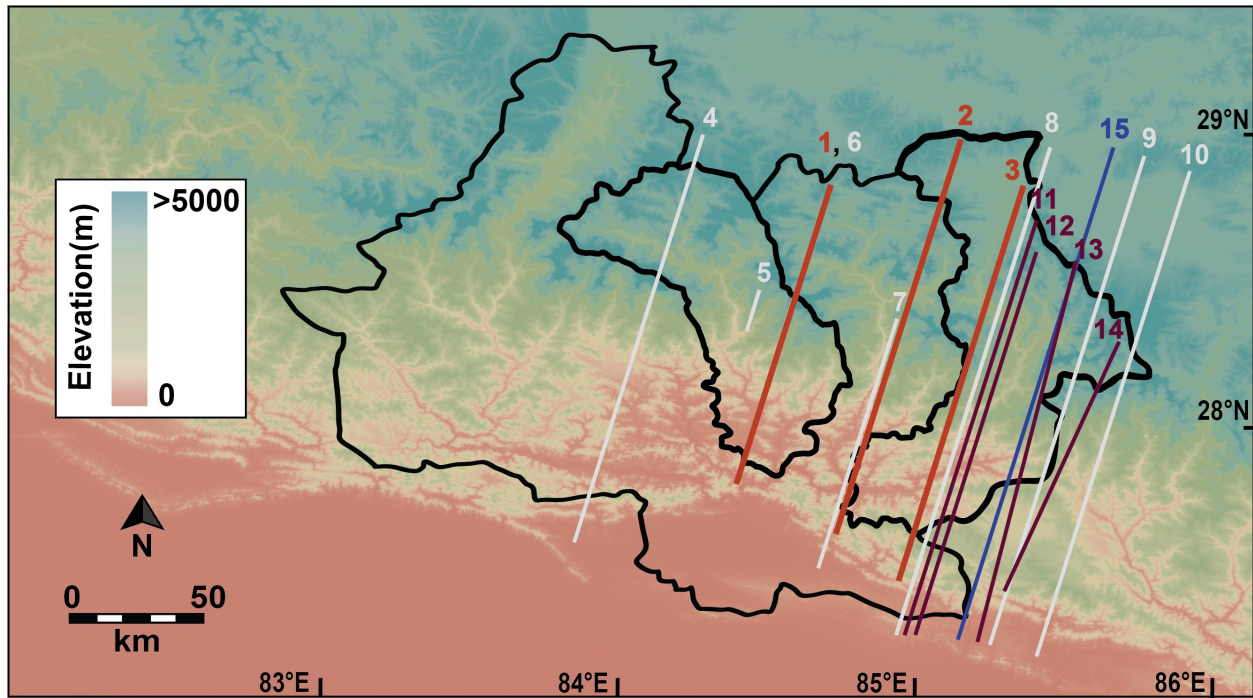


**Figure 1.8** Locations of erosion,  $k_{sn}$ , rainfall, and MHT geometry profiles compared in this study. Red lines are our log(EF) profiles. White lines are the erosion profiles from previous studies as numbered: **4.** Garzanti et al., 2007; **5.** Whipp et al., 2007; **6.** Burbank et al., 2003; **7.** Godard et al., 2014; **8.** Herman et al., 2010 and Robert et al., 2009; **9.** Lave & Avouac, 2001; **10.** Godard et al., 2004. Pink lines are MHT geometry studies as numbered: **11.** Hubbard et al., 2016; **12.** Whipple et al., 2016; **13.** Elliott et al., 2016; **14.** Mendoza et al., 2019. The purple line, **15**, is the mean annual rainfall profile from Andermann et al., 2011. The teal lines are the  $k_{sn}$  profiles from Cannon and Murphy (2018) used in this study.

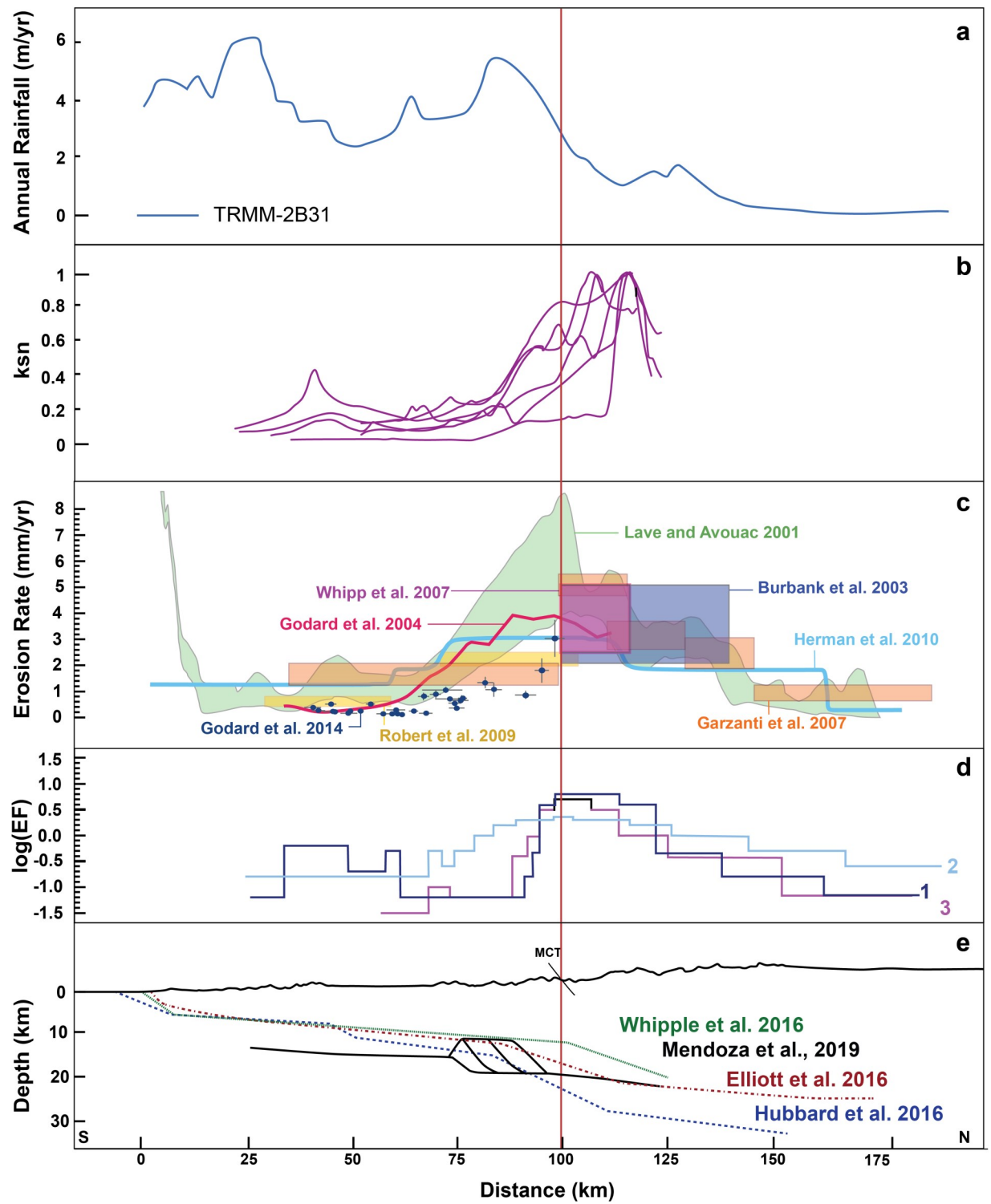
## 1.5 Comparisons of Erosional, Structural, Geomorphological, and Climatic Data

### 1.5.1 Comparisons of Erosion Profiles

We compared our  $\log(EF)$  values, along a series of profiles between the Marsyangdi subcatchment and the Trishuli subcatchment, to various published erosion profiles,  $k_{sn}$  profiles, precipitation profiles, and predicted MHT geometries from previous studies in this area. The locations of each of these profiles are shown in Figure 1.8. Although many previous studies compare profiles relative to distance from the MFT, the distance between the MFT and predicted MHT ramps vary laterally across central Nepal (Roberts et al., 2009). Instead, we used the location of exposure of the MCT as a datum to align the profiles from each study, as it is a well-established feature common to all of the studies used in our comparisons, and is the nearest surface feature to the zone of peak erosion and MHT ramp. The results of this compilation can be seen in Figure 1.9. Our  $\log(EF)$  patterns show preferential erosion directly above the MHT ramps modelled using Gorkha earthquake data, in an area from ~5 km south of the MCT to ~20 km north of the MCT, with peak erosion occurring in a 5-km zone immediately north of the MCT. This is consistent with erosion and exhumation patterns from previous studies (Figure 1.9; Lave and Avouac, 2001; Burbank et al., 2003; Garzanti et al., 2007; Whipp et al., 2007; Robert et al., 2009).

**Figure 1.9 (on following page)** Comparison of erosion profiles and  $k_{sn}$  profiles with the location of the MHT midcrustal ramp with respect to distance from the MCT. **(a)** Mean annual rainfall profiles for the Kathmandu region. Modified from Andermann et al., 2011. **(b)**  $k_{sn}$  profiles along N18E transects between the Marsyangdi river and Kathmandu klippe (Cannon & Murphy, 2018). **(c)** A compilation of erosion profiles along N18E transects throughout the catchment. The corresponding studies are shown alongside the profiles. **(d)**  $\log(EF)$  values along three profiles between the Marsyangdi river and Kathmandu klippe. **(e)** Cross sections of four previously predicted MHT geometries.







### 1.5.2 Comparison of Erosion Profiles with Climate and River Channel Steepness

We compared these erosion profiles to a profile of mean annual rainfall from the Kathmandu region (Figure 1.9a). The profile was collected from the TRMM 23B1 (Tropical Rainfall Measuring Mission) calibrated 12-year data (Bookhagen and Burbank, 2006; Andermann et al., 2011). This profile shows highest rainfall 15 km in front (i.e., to the south) of the peak-erosion zone. This rainfall peak falls within the LHS. Because the location of peak erosion does not coincide with that of peak rainfall, we assume that rainfall is either subordinate to other erosion drivers, such as deformation, or that rainfall patterns in the past differed significantly from the pattern shown by TRMM 23B1. We then compared the erosion profiles to  $k_{sn}$  values (Figure 1.2, 1.9b). High  $k_{sn}$  values persist north of the zone of rapid erosion in some places. Rivers increase in steepness where rock uplift rate outpaces the river's incision rate or where rivers flow from a region with a less-resistant substrate to one with a more-resistant substrate (Whipple et al., 2001; Wobus et al., 2006; Kirby and Whipple, 2012). In our study area the first condition is influenced by two factors. First, beneath the High Himalaya, the material the MHT is located within undergoes a rheologic change from crystal-plastic deformation to brittle deformation and an accompanying seismotectonic change from stable-sliding to seismic stick-slip behavior (seen geodetically as uncoupled-coupled). This change in kinematic behavior leads to an increase in elastic-strain accumulation, where the material between stably sliding southern Tibet and the seismically locked Lesser Himalaya bends to accommodate plate convergence (Bilham et al. 2001; Feldl and Bilham, 2006; Meade, 2010). If all the accumulated strain were routinely released during plate-boundary earthquakes, we would not expect this accumulation of elastic strain to contribute much to the rock uplift record. However, many studies have concluded that

much of this elastic strain is maintained over numerous seismic cycles, seemingly creating a long-term “elastic bulge” located in the High Himalaya (Bilham and Ambraseys, 2005; Meade 2010; Stevens and Avouac, 2016). Second, the amount of rainfall diminishes rapidly within the rain shadow near the base of the High Himalaya. Although we do not find a strong correlation between precipitation rate and erosion rate, diminishing rainfall decreases the stream power available for plucking rocks from the channel and transporting loose material downstream. This suggests that a lower rate of rock uplift within the rain shadow should produce river segments with a higher  $k_{sn}$  when compared to segments further south where the precipitation rate is higher. In addition to these drivers of river steepening, the STD is also located within this region. As these rivers flow across the STD, the substrate changes—from the low-grade metamorphic rocks and unmetamorphosed sedimentary rocks of the TSS to the igneous and high-grade metamorphic rocks of the GHS. Assuming that the rock strength of the TSS or GHS has not been substantially altered by fracturing and secondary weathering, rivers flowing across the STD would respond to the change in substrate erodibility, by steepening their channels. These factors (seismotectonic, climatic, and lithologic) produce a broad region of high  $k_{sn}$  rivers that coincides with and continues north of the high-erosion zone documented here. Our  $\log(EF)$  values are moderately to strongly correlated to  $k_{sn}$  values throughout the catchment ( $r^2=0.65-0.92$ ), indicating a strong relationship in this area between erosion and rapid rock uplift. This agrees with previous interpretations of  $k_{sn}$ -uplift relationships in the Himalayas. Nennewitz et al., (2018) argued that  $k_{sn}$  could be used as a proxy for differential uplift in the western Himalayas. Kirby and Whipple, (2012) advanced a similar argument for central and eastern Nepal and Sherler et al., (2014) found a similar relationship in the Garhwal Himalaya.

### 1.5.3 Comparison of Erosion Profiles with Local Structure

We plotted the geometry of the MHT as predicted by four post-Gorkha models from Whipple et al., (2016), Elliott et al., (2016), Hubbard et al., (2016) and Mendoza et al., (2019) (Figure 1.9e). The zone of peak erosion shown here is located above the proposed position of MHT mid-crustal ramps determined using data obtained during the Gorkha earthquake (Elliott et al., 2016; Hubbard et al., 2016; Whipple et al., 2016). Peak erosion, revealed using the EF method (Figure 1.9d), lies north of the duplex structure of Mendoza et al., (2019). The zone of peak erosion is shown using methods that represent processes that operate on a variety of timescales, from the 100-1000 yr process represented by  $^{10}\text{Be}$  data (Godard et al., 2014) to the 1-10 kyr process represented by fluvial incision (Lavé and Avouac, 2001), to the 100 kyr process shown by the thermokinematic model of Godard et al. (2004) and river channel steepness, to the million-year-scale processes represented by models based on bedrock thermochronology (Burbank et al., 2003; Whipp et al., 2007; Robert et al., 2009; Herman et al., 2010). The erosion and exhumation patterns of these studies are consistent, regardless of the relevant time scale (hundreds to millions of years).

The zone of peak erosion coincides with the location of our central band of youngest  $^{40}\text{Ar}/^{39}\text{Ar}$  ages, suggesting that erosion in central Nepal has remained focused in a central, orogen-parallel band for two-four million years. We can assume that all muscovite ages in this study (from either bedrock or river samples) represent the last time the material was at  $\sim 400^\circ\text{C}$  (Harrison et al., 2009). However, interpretations of exhumation ages can be complicated by variable geothermal gradients. Copeland et al. (1991) proposed a perturbation of the thermal structure in the Narayani catchment calling for hydrothermal fluids of  $\sim 500^\circ\text{C}$  passing through a zone approximately 1 km

wide, centered on the MCT, for around 200,000 years at approximately 4 Ma after the samples had been brought close enough to the surface to allow heating along this narrow zone via hot fluids to be much greater than the surrounding rocks. However, a later study, combining garnet-biotite thermobarometry and U-Pb dating of monazite inclusion in garnet, showed these young samples near the MCT were at ~700 MPa when they cooled below the closure temperature of Ar in muscovite, inconsistent with the shallow depths associated with the hydrothermal-resetting hypothesis (Harrison et al., 1998). Additional garnet-biotite thermobarometry, Th-Pb dating of monazites, and muscovite  $^{40}\text{Ar}/^{39}\text{Ar}$  analyses by Catlos et al. (2001) found no evidence for hydrothermal alteration in their young samples. However later analyses of GHS rocks from these same regions by Martin et al. (2007) showed evidence of metasomatism and they found that microcracks in monazite-hosting garnets affected monazite U-Pb and Th-Pb ages by facilitating Pb loss. Derry et al. (2009) showed numerous hot springs along the MCT in central Nepal that produced hydrothermal gradients of  $75^\circ \text{C km}^{-1}$ . These steep hydrothermal gradients were highly localized and not found to represent the overall geothermal gradient of the area (Robert et al., 2011). Although these increased hydrothermal gradients were found to be sufficient to alter low-temperature thermochronometers, such as the apatite-helium system, they were not sufficient to reset the much higher closure-temperature system of muscovite  $^{40}\text{Ar}/^{39}\text{Ar}$  (Derry et al., 2009). Based on this, we carry forward assuming that all  $^{40}\text{Ar}/^{39}\text{Ar}$  ages used in this study represent the time it each sample to be exhumed from a common depth. The data from Derry et al. (2009) suggests that a similar assumption may not be appropriate if this exercise were to be repeated with a thermochronometer with a much lower closure temperature, such as He in apatite.

## 1.6 Discussion

The location of our highest EF zone, relative to major structural features, suggests four potential tectonic drivers. First, the location of our high EF zone overlaps the positions of major ramps in the MHT proposed by three studies using data derived from the Gorkha earthquake (Elliott et al., 2016; Hubbard et al., 2016; Whipple et al., 2016). Passive fluxing of the MHT hanging wall over a mid-crustal ramp will produce a zone of rapid erosion at the surface (Coutand et al., 2014; Robert et al., 2009, 2011). However, if the dimensions and location of any these ramps accurately represent the geometry of the MHT they cannot, by themselves, account for the exhumation recorded in our high EF zone. The closure temperature of  $^{40}\text{Ar}/^{39}\text{Ar}$  in muscovite is 400 °C (Harrison et al., 2009), and if we assume a geothermal gradient of 25 °Ckm<sup>-1</sup> this requires a 16 km high ramp. The ramp proposed by Whipple et al. (2016) is not tall enough, whereas the ramps proposed by Elliott et al. (2016) and Hubbard et al. (2016) are sufficiently high, but the portion of those ramps north of the MCT is not. In addition, relying upon passive fluxing of material over a ramp to accommodate mid-crustal deformation ignores the recently documented internal shortening and structural complexity of the GHS (Carosi et al., 2010; Corrie and Kohn, 2011; Montomoli et al., 2013; Larson et al., 2013; Ambrose et al., 2015; Cottle et al., 2015; Walters and Kohn, 2017). The discovery of multiple mid-crustal tectonometamorphic discontinuities within the core of the orogen shows that duplexing has been pervasive in the middle and lower crust, from the Oligocene to at least the mid Miocene (Larson et al., 2015; He et al., 2015). While it is possible that the style of mid-crustal deformation has changed significantly since then, none of the recently proposed MHT ramp dimensions and locations can explain our high EF zones by themselves. Even in the absence of the

thermochronologic constraints, the locations and dimensions of the ramps require some additional driver of rock uplift. The southern limit of our swath of high EF coincides with the updip (southern) limit of the ramps proposed by Elliott et al. (2016) and Hubbard et al. (2016), but the high EF region extends 10-15 km north of their ramps downdip (northern) limits. While the downdip (northern) limit of the ramp proposed by Whipple et al. (2016) coincides with the northern limit of our high EF zone, the ramps updip limit is 15-20 km north of the southern boundary of the high EF zone. It should be noted that these studies do not explicitly quantify the uncertainties in their modelled ramp positions, and we acknowledge that if the ramp's position or dimensions are significantly different from published models, it could affect our interpretation of driving mechanism.

Second, recent studies have shown that duplexing is currently the dominant internal shortening mechanism in the Himalaya (Bollinger et al., 2004, 2006; C  lerier et al., 2009; Herman et al., 2010; He et al., 2015; McQuarrie and Ehlers, 2015; Landry et al., 2016), and there is every reason to think that the more northerly ramp positions predicted using Gorkha earthquake data are sites of active duplexing as suggested by Elliott et al. (2016) and Hubbard et al. (2016). In a foreland-propagating, hinterland-dipping duplex or antiformal stack, the addition of new horses to the hanging wall of the basal thrust (underplating) drives back-tilting of older duplex faults and rock uplift along a broad swath of the hanging wall of the roof thrust (Boyer and Elliott, 1982). An active duplex on a mid-crustal ramp, 80-100 km from the MFT, can explain the dimensions of our high EF zone, as it provides a mechanism for extending the area experiencing rock uplift north of the ramps proposed by Elliott et al. (2016) and Hubbard et al. (2016).

Third, the zone of increased erosion documented here could be explained by an active surface-breaking fault located at or near the mapped surface expression of the MCT or the High Himalayan Discontinuity (HHD) of Montomoli et al. (2013). However, this requires invoking an undiscovered, active, out-of-sequence thrust accommodating at least 10% of Himalayan convergence in one of the most-well-studied segments of the Himalaya. Although there is evidence for some degree of post-Miocene activity on the MCT (Seeber and Gornitz, 1983; Copeland et al., 1991; Harrison et al. 1997; Hodges et al., 2001; Catlos et al., 2001; Wobus et al., 2005; Mukhopadhyay, 2011; Catlos et al. 2018;) the magnitude of shortening required to explain our high EF zone with a surface breaking fault is difficult to reconcile with the bedrock geology of the region and with the historical record of great earthquakes. Over the past 1000 years, great Himalayan earthquakes have been blind thrusts or surface breaking ruptures associated with the MBT or MFT well to the south of our high EF zone (Wesnousky et al., 1999; Bilham et al., 2001; Kumar et al., 2006; Kumar et al., 2010; Sapkota et al., 2013; Hetényi et al., 2016; Bilham, 2019). Since our highest EF zone contains muscovite  $^{40}\text{Ar}/^{39}\text{Ar}$  ages of less than a million years, whatever process drives uplift must be active today. No geomorphic evidence has been shown to suggest that a major surface breaking out-of-sequence fault accommodates a significant portion of modern Himalayan deformation in our study area.

Finally, our high EF zone is collocated with the High Himalaya elastic-strain reservoir predicted by GPS-derived fault-coupling studies and geomorphic evidence (Bilham et al., 2001; Stevens and Avouac, 2015; Cannon and Murphy, 2018). This reservoir grows as elastic strain accumulates and is partially drained during plate-

boundary earthquakes, but does not seem to be fully depleted during even large Himalayan earthquakes (Bilham et al. 2001; Bilham and Ambraseys, 2005; Feldl and Bilham, 2006; Jouanne et al., 2004; Meade, 2010; Ader et al. 2012; Stevens and Avouac, 2015; Stevens and Avouac, 2016). This driver of persistent rock uplift, although occasionally interrupted by rapid subsidence as elastic strain is transferred from the High Himalaya to brittle deformation beneath the Lesser Himalaya, appears to be a driver of erosion in central Nepal.

The zone of rapid erosion shown here does not, by itself, allow us to distinguish between these potential drivers of rock uplift. However, when thrust wedge architecture and seismotectonics are considered, it suggests that the high EF zone is the product of a duplex growing along a mid-crustal ramp 80-100 km from the MFT, enhanced by dynamically maintained elastic bending. To explain the portion of the peak-erosion zone north of the downdip limit of the proposed ramps without invoking a duplex requires that either the ramp's proposed location and dimensions are incorrect or that dynamically maintained elastic bending account for a more significant proportion of hinterland rock uplift. As evidence for an internally deformed GHS has grown over past decade (Carosi et al., 2010; Corrie and Kohn, 2011; Montomoli et al., 2013; Larson et al., 2013; Ambrose et al., 2015; Cottle et al., 2015; Walters and Kohn, 2017) it has become difficult to envision mid-crustal Himalayan deformation occurring by means of emplacement of a single monolithic sheet, as is implied by passive fluxing of material over amid-crustal ramp. Although dynamically maintained elastic bending appears to contribute to rock uplift rates in the Himalayan hinterland, its magnitude is poorly constrained. However, its role seems certain to be subordinate to that of the crustal architecture of the thrust wedge.



## 1.7 Conclusions

Using our method of comparing muscovite  $^{40}\text{Ar}/^{39}\text{Ar}$  ages in a detrital sample to similar ages in bedrock we produced a map of erosion rates in central Nepal that is consistent with the patterns found in previous studies. Our method of comparing the proportion of a given age range for muscovites in a detrital sample to the proportion of the area of the bedrock in the Narayani catchment contributing those ages shows a ~25 km-wide zone of increased erosion relative to the rest of the catchment. This zone of increased erosion is centered above recently proposed locations of mid-crustal ramps in the MHT where duplexing has been predicted by Elliot et al. (2016) and Hubbard et al. (2016). We propose that erosion in central Nepal is primarily a function of a duplex growing along a mid-crustal ramp in the MHT 80-100 km from the MFT, accompanied by dynamically maintained elastic bending of the High Himalaya.

## **Chapter II: Nd nucleosynthetic anomalies in Enstatite Chondrites and their implications for an Enstatite Chondrite-Earth connection**

### **2.1 Introduction**

To understand the formation and evolution of our solar system, it is critical to be able to reconstruct the building blocks present during the accretion of terrestrial bodies in the protoplanetary disk. Of particular interest is identifying the potential building blocks of Earth. Although chondrites are considered a promising candidate, no single chondrite group has both the same chemical and isotope compositions as the Bulk Silicate Earth (Javoy, 1995; Miyazaki and Korenaga, 2021). For many years, models assumed that the bulk silicate Earth and chondrites had the same isotope compositions for many elements (Jacobsen and Wasserburg, 1980; Bouvier et al., 2008; Campbell and O'Neill, 2012). However, advances in measurement capability, have made it possible to observe nucleosynthetic anomalies for many isotopes. Nucleosynthetic anomalies act as fingerprints for the nebular feeding zones of different rocky bodies and as such can provide clues as to the potential building blocks of Earth.

Enstatite chondrites have been considered a potential building block for Earth (Javoy, 1995; Javoy, et al., 2010; Dauphas and Schauble, 2016; Boyet et al., 2018) due to their isotopic similarity. Earth and enstatite chondrites have nearly indistinguishable compositions for numerous isotopic systems, including O, Ca, Ti, Cr, Ni, and Mo (Burkhardt et al., 2011; Warren, 2011; Dauphaus 2017; Fischer-Gödde and Kleine, 2017). There is currently a small resolvable discrepancy for Ru compositions (Fischer-Gödde and Kleine, 2017) between Earth and enstatite chondrites. However, bulk Earth and

enstatite chondrites have differing major-element abundances, with discrepancies in their Mg, Al, Si, Ca, and Fe abundances (Jagoutz et al., 1979; Mezger et al., 2020). This observation has led to the question: did the Earth and enstatite chondrites share a nebular feeding zone?

The Nd isotope makeup of enstatite chondrites is still poorly understood, due to a small sample population ( $n = 35$ ), with multiple subgroups (i.e. EH4/5; EL4) having never been analyzed for their Nd isotope compositions. Because enstatite chondrites may represent up to eight different parent bodies (Weyrauch et al., 2018), understanding the Nd isotope composition of each subgroup is important for evaluating a connection between enstatite chondrites and Earth. In order to assess potential similarities between the Nd isotope ratios of enstatite chondrites and Earth, we measured the Nd isotope compositions of enstatite chondrites from the EH and EL groups. Samples from the EH4/5 and EL4 groups were analyzed for the first time, to evaluate if their Nd isotope compositions were consistent with other enstatite chondrite groups. The Nd isotope makeup of these chondrites was also compared with newly measured Nd isotope compositions from samples of mantle-derived melts from Earth.

## **2.2 Neodymium s- and r- process Nucleosynthesis**

Neodymium is a refractory, lithophile element, that is abundant in the silicate fractions of meteorites and differentiated planetary bodies. Enstatite chondrites are unique amongst chondrites in that they preferentially host Nd in sulfides. Neodymium has seven naturally occurring isotopes ( $^{142}\text{Nd}$ ,  $^{143}\text{Nd}$ ,  $^{144}\text{Nd}$ ,  $^{145}\text{Nd}$ ,  $^{146}\text{Nd}$ ,  $^{148}\text{Nd}$ , and  $^{150}\text{Nd}$ ). Each of these is made with various proportions of p-, s-, and r-process nucleosynthesis

(Table 2.1), and  $^{142}\text{Nd}$  and  $^{143}\text{Nd}$  also have radiogenic contributions from the decay of  $^{146}\text{Sm}$  with a half-life of 103 Myr, and  $^{147}\text{Sm}$  with a half-life of 106 Gyr, respectively (Render and Brennecke, 2021).

**Table 2.1.** The p-, s-, and r-process relative abundances of Nd isotopes (Arlandini et al., 1999).

Nd:	$^{142}\text{Nd}$	$^{143}\text{Nd}$	$^{144}\text{Nd}$	$^{145}\text{Nd}$	$^{146}\text{Nd}$	$^{148}\text{Nd}$	$^{150}\text{Nd}$
p	4						
s	96	35	53	29	63	19	
r		65	47	71	37	81	100

The slow neutron-capture process (s-process) occurs when neutron captures are slow compared to  $\beta$  decays due to low neutron densities. In contrast, the rapid neutron-capture process (r-process) occurs when neutron captures are rapid compared to  $\beta$  decays due to high neutron densities. For elements such as Nd ( $Z=60$ ), between Sr ( $Z=38$ ) and Pb ( $Z=82$ ), s-process nucleosynthesis is thought to occur in low-metallicity, low-mass, asymptotic branch stars (Arlandini et al., 1999; Karakas and Lattanzio, 2014). Neutron star mergers are currently favored as the dominant source for r-process nucleosynthesis (Thielemann et al., 2017; Côté et al., 2018), although other potential sites, such as collapsars (Siegel et al., 2019), compact binary-mergers (Hotokezaka et al., 2015; Bonetti et al., 2019), magnetohydrodynamic-jet supernovae (Nishimura et al., 2006; Siegel et al., 2017), and core-collapse supernovae (Hoyle and Fowler, 1960; Matthews and Cowan, 1990) have been proposed. Core-collapse supernovae, also referred to as Type II, Ib, or Ic supernovae were once favored as the dominant source for r-process nuclei, but multiple studies have shown the need for an r-process production site with a lower event rate than core-collapse supernovae (Thielemann et al., 2017).

Proton-capture process nucleosynthesis (p-process) occurs when s- and r-process isotopes are shock-heated, stripping them of neutrons, protons, and  $\alpha$  particles. The p-process is only present in one isotope of Nd,  $^{142}\text{Nd}$ , and contributes only 4% of the nuclei for that isotope. Comparing Nd isotopes that have different nucleosynthetic origins gives us insight into the mixing processes that occurred in the early solar nebula (Trinquier et al., 2009). The variety of rocky-body compositions that resulted from these mixing processes, along with the heterogeneous incorporation of material enriched in either s- or r-process Nd is discussed in the following sections.

### **2.3 Classes of Meteorites**

The original reservoir compositions for all planetary and meteorite parent bodies, including the building blocks of Earth, was the solar nebula. Because the Sun makes up >99% of the mass of the solar system, the averaged measured composition of the Sun's photosphere is considered to be representative of the bulk nebular composition for elements heavier than He (Anders and Ebihara, 1982). The material in each reservoir underwent numerous processes that changed its chemical and isotope compositions. These processes included condensation and evaporation of solids, thermal processing of presolar grains, and planetary accretion. Meteorites are divided into two major categories based on their bulk composition and textures: chondrites which have a solar-like composition and typically contain chondrules, and achondrites which are the melts, partial melts, or igneous breccias from differentiated asteroids and planetary bodies (Mezger et al., 2020). Chondrites are divided into two major classes, carbonaceous chondrites (CC) and non-carbonaceous chondrites (NC). Carbonaceous chondrites are thought to have

formed in the outer regions of the solar system, while non-carbonaceous chondrites are thought to have formed in the inner region of the solar system (Kruijer et al., 2017; Nann et al., 2019; Kleine et al., 2020). A dichotomy between the isotope compositions of numerous elements, including Ti, Mo, Ni, and Cr suggest that CCs preserve the signature of the early protoplanetary disk, whereas NCs reflect later-infalling material that collected in the inner region of the solar system (Nanne et al., 2019). The inner region (non-carbonaceous) and outer region (carbonaceous) may have been unable to homogenize due to the rapid accretion of Jupiter (Kruijer et al., 2017). These two different accretion regimes in the nebula may have preserved distinct Nd isotope compositions (Burkhardt et al., 2016; Fukai and Yokoyama, 2019; Render and Brennecka, 2021).

The NCs include the ordinary, enstatite, rumuruti-like, and kakangari-like chondrite classes (Kallemeyn, et al., 1996; Weisburg et al., 2006; Warren et al., 2011; Krot et al., 2014). Each of these classes of chondrites is further divided into subgroups. Each subgroup shares similar O-isotope, bulk-rock geochemistry, textural, and mineralogical features (Weisburg et al., 2006). These subgroups are thought to have single parent bodies or related parent bodies amongst their members, unlike the larger classes which may have simply formed in similar nebular feeding zones.

### **2.3.1 Enstatite Chondrites**

Enstatite chondrites are composed of Fe-free enstatite, plagioclase, kamacite, troilite (FeS), and numerous rare sulfides (Keil, 1968; Keil, 1989; Lodders, 1993; Hopp et al., 2016). Because sulfides don't condense from nebular gasses with initial solar system compositions, enstatite chondrites are thought to have condensed from a gas with a high

C/O ratio (Larimer and Bartholomay, 1979; Grossman et al., 2008). However, models of enstatite chondrite condensation from a nebular gas with a higher C/O ratio than the solar average predict abundant graphite, rather than the accessory amounts found in current samples, prompting alternative explanations of sulfide formation, such as a reaction between oxides and a S-rich gas (Lehner et al., 2013).

Enstatite chondrites are divided into the EL and EH subgroups, based on their Fe/Si bulk ratios and mineralogy. The EL chondrites are defined as having low Fe/Si bulk ratios while EH chondrites have high Fe/Si bulk ratios (Sears et al., 1982; Hertogen et al., 1983; Weeks and Sears, 1985; Kallemeyn and Wasson, 1986). Each subgroup contains unequilibrated and highly equilibrated samples, depending on their degree of thermal metamorphism. Sulfide mineralogy also differs between these two subgroups. Although there are numerous sulfides such as oldhamite (CaS) and troilite (FeS), found in both subgroups, alabandite (MnS) is a sulfide found only in the EL subgroup while niningerite (MgS) is a sulfide found only in the EH subgroup. Bulk compositional differences in non-volatile elements suggest that EL and EH chondrites represent different parent bodies (Sears et al., 1982; Keil 1989). Variations in sulfide Cr and Fe compositions have been used to suggest up to eight different parent bodies for the enstatite chondrite subgroups (Weyrauch et al., 2018).

## **2.4 Components of Chondrites**

Each chondritic group has a unique isotope composition due to the mixing of various components. Varying concentrations of these components change not only the major element chemistry but the isotope composition of chondrite groups. Understanding

the composition of each individual component of chondrites may lead to a better understanding of the material that accreted to form the early Earth. These chondritic components are all potential Nd isotope reservoirs. Their formation and variability in the different chondrite groups are presented in the following sections.

#### **2.4.1 Chondrules**

Chondrules are igneous inclusions, composed of mostly olivine and pyroxene, that were flash-melted and then rapidly cooled in minutes to hours. The Al-Mg data from various studies has suggested that chondrules formed 1.8-2.5 Myrs after the first matter condensed in the solar system (Bizzaro et al., 2004; Pape et al., 2019). Chondrules are a main component in most chondrites with varying proportions from 15-80% (Scott and Krot, 2014). Only CI chondrites have a marked deficiency in chondrules, containing <5% chondrule fragments (Leshin et al., 1997).

#### **2.4.2 Calcium-aluminum-rich Inclusions**

Calcium-Aluminum-rich Inclusions (CAIs) were the first matter to condense in our Solar System (MacPherson et al., 2005). These refractory inclusions are composed primarily of the minerals hibonite ( $\text{CaAl}_{12}\text{O}_{19}$ ), melilite ( $\text{Ca}_2(\text{Al}_2\text{MgSi})\text{SiO}_7$ ), spinel ( $\text{MgAl}_2\text{O}_4$ ), perovskite ( $\text{CaTiO}_3$ ), anorthite ( $\text{CaAl}_2\text{Si}_2\text{O}_8$ ), forsterite ( $\text{Mg}_2\text{SiO}_4$ ), and less commonly grossite ( $\text{CaAl}_4\text{O}_7$ ) and corundum ( $\text{Al}_2\text{O}_3$ ) (MacPherson et al., 2005; Russell et al., 2005). In chondrites, calcium-aluminum-rich inclusions are enriched in Nd (Burkhardt et al., 2016; Jacquet et al., 2018). They are distributed amongst all chondrite groups except CI's in which only one CAI has ever been found (Frank et al., 2011). Although CAIs are widespread, their populations in different chondritic groups are distinct in size,



texture, mineralogy, and isotope compositions (Larsen et al., 2020). The CAIs are primarily concentrated in CCs. Their formation has been suggested to be episodic and recurrent, spanning an 8,000 yr time period during earliest cooling and condensation in the solar nebula (Larsen et al., 2020).

### **2.4.3 Presolar Grains**

A small fraction of the dust that made up the interstellar molecular cloud that eventually became our Solar System, escaped the thermal processes that occurred during gravitational collapse and accretion. These remained as intact, presolar grains (Lodders and Amari, 2005). Presolar grains offer a glimpse into the stellar environments in which they formed. Their isotope compositions provide fingerprints of the stellar environments in which they formed (Trinquier et al., 2009). Their heterogeneous incorporation into nebular feeding zones could impart distinct isotopic fingerprints to trace source reservoirs for planetary and chondritic material. Due to their exceptionally small size (0.001-20  $\mu\text{m}$ ; Huss and Lewis, 1983; Zinner, 1998; Hoppe and Zinner, 2000; Lodders and Amari, 2005) and the current capabilities of isotopic analytical methods, only a handful of presolar grain types have been analyzed for certain isotopes (Zinner, 2014; Floss and Haenecour, 2016; Stephan et al., 2018). Numerous additional studies will be required to understand the nucleosynthetic anomalies contained in different types of presolar grains.

Although bulk presolar SiC grain samples have been analyzed for their Nd isotope composition in one study (Hoppe and Ott, 1997), these SiC grains may have formed in multiple stellar environments (Amari and Zinner, 1997; Amari et al., 1999; Nittler, 2003;

Lodders and Amari, 2005; Zinner, 2014) and thus may have unique single-grain Nd isotope compositions. No single presolar grains have been analyzed for Nd isotopes due to low Nd concentrations in presolar grains (Liu, 2014). Because presolar grains potentially provide strong leverage on the isotope compositions observed in the different meteorite classes, understanding their individual Nd isotope compositions may provide key information insight into mixing processes in the solar nebula.

In summary, each of these components contributes to the isotope diversity observed in bulk measurements of chondrites and materials from rocky bodies such as Earth. Differences between p-, s-, and r-process isotope compositions are directly related to inhomogeneity in these different components between the parent bodies. As shown above, breaking out the Nd isotope compositions of these different components is in its infancy and will be future goals in understanding nucleosynthesis. At present, with the exception of sparse data discussed above, to get enough Nd to accurately measure the Nd isotope compositions of materials for nucleosynthetic differences, bulk fractions are measured. In section 2.5, a description of the bulk samples measured in this study is presented in order to distinguish nucleosynthetic differences in the parent bodies represented.

## **2.5 Samples and Standards**

Thirty enstatite chondrite samples were analyzed for their Nd isotope compositions (Table 2.2). Two grams of each sample were dissolved. High-precision Nd measurements in chondrites have increasingly been standardized to the synthetically processed JNdi standard (Burkhardt et al., 2016; Gautam et al., 2017; Boyet et al., 2018). Two other

**Table 2.2** Enstatite Chondrites Analyzed for Nd Isotope Compositions

<b>UH</b>	<b>class.</b>	<b>Campaign</b>
GRO 95517	EH3	2
GRO 95517	EH3	2
LAR 06252	EH3	2
MET 01018	EH3	2
MIL 07028	EH3	2
EET 88746	EH4	2
EET 96341	EH4/5	2
EET 96135	EH4/5	2
EET 96299	EH4/5	2
LEW 88180	EH5	2
LEW 87223	EL3	2
MAC 02839	EL3	2
MAC 02747	EL4	2
ALHA 81021	EL6	2
GRO 95626	EL6	2
PCA91238	EH3	3
PCA91020	EL3	3
QUE 94204	AUB	3

<b>Berlin</b>	<b>class.</b>	<b>Campaign</b>
PCA 91461	EH3	1
KLE 98300	EH3	1
ALH 84170	EH3	1
EET 96341	EH4/5	1
MAC 88136	EL3	1
MAC 88136 dup	EL3	1
MAC 02747	EL4	1
Blithfield	EL6	1
Blithfield dup	EL6	1
Blithfield dup 2	EL6	1
LON 94100	EL6	1
ALH 81021	EL6	1

commonly used standards include the synthetically-processed La Jolla and Ames standards. These two standards have shown results consistent with equilibrium mass-dependent fractionation due to the purification process (Saji et al., 2016) and have

resolvable  $\mu^{148}\text{Nd}$  and  $\mu^{150}\text{Nd}$  values in comparison to JNdi. Samples in this study were thus normalized to the JNdi standard for consistency with the literature data and because it is generally accepted to represent bulk Earth for nonradiogenic Nd isotope abundances.

## **2.6 Methods**

### **2.6.1 Chemistry**

Samples were processed and measured at two different labs, the University of Houston (UH), and Freie University of Berlin. Samples analyzed at the UH laboratory were crushed into a fine powder with a ceramic mortar and pestle that is dedicated to chondritic meteorites. The mortar and pestle were thoroughly cleaned with silica sand and ethanol between each use, then rinsed in ultrapure water. Samples were combined with 2.5 mL 2x-distilled conc.  $\text{HNO}_3$  and 7.5 mL of Optima conc. HF in PTFE inserts. These were placed into stainless-steel jackets (Parr bombs) and heated at  $170^\circ\text{C}$ , under pressure, for one week. Following this initial digestion, each sample was taken to dryness. Samples were further digested in Teflon beakers on a hot plate. Each sample was combined with 2 mL 2x-distilled conc.  $\text{HNO}_3$  at  $120^\circ\text{C}$  for 12 hours, then taken to dryness. These samples were then combined with 1 mL conc. HCl at  $80^\circ\text{C}$  for 12 hours, then taken to dryness. This step was repeated an additional time. For each sample, this resulted in a small final residue.

The Rare-Earth Elements (REEs), including Nd and Sm, were purified through cation exchange chromatography using Biorad AG50W-X8 resin and distilled HCl. The REE cuts were purified of Ce as  $^{142}\text{Ce}$  is a major mass interference with  $^{142}\text{Nd}$ . Cerium in the REE cuts were oxidized from +3 to +4 in 1 mL of 5 mM  $\text{NaBrO}_3$  +10M  $\text{HNO}_3$  solution

for one hour. These solutions were eluted through Ln-Spec resin using additional  $\text{NaBrO}_3$  +  $\text{HNO}_3$  solution while oxidized  $\text{Ce}^{+4}$  remained complexed with the Ln-Spec resin. (Tazoe et al., 2007; Li et al., 2015). Sodium introduced from the  $\text{NaBrO}_3$  was removed by eluting the samples through small, 1 mL Biorad AG50W-X8 resin columns with distilled HCl. Neodymium and Sm were purified through an additional LN-Spec column using 0.25N and 0.4N distilled HCl, respectively. This step was repeated to purify Sm. Purified Nd cuts were loaded onto outgassed Re filaments in 1.5  $\mu\text{L}$  of  $\text{H}_3\text{PO}_4$ . These loaded filaments were placed in a double-filament configuration as the evaporation filament, using an additional outgassed rhenium filament as the ionization filament.

Samples analyzed at the Berlin laboratory were digested, purified, and measured for their Nd isotope composition by Dr. Kai Rankenburg. Samples were first crushed into a fine powder. The method used a  $\text{NaOH}\cdot\text{H}_2\text{O}$  solution that was molten at  $400^\circ\text{C}$  and contained in a graphite crucible. This molten solution was poured over a sample/ $\text{Na}_2\text{O}_2$  mixture in a separate graphite crucible with a sample to  $\text{Na}_2\text{O}_2$  to NaOH ratio of 1:6:3. This mixture was then molten at  $650^\circ\text{C}$  for 15 minutes and then swirled to ensure complete sample dissolution. This step was repeated twice. After the crucible cooled down, ultrapure water was added in small quantities to decompose the melt cake. The resulting hydroxide precipitates were then centrifuged and washed with ultrapure water five times. They were then dissolved in 6 M HCl. At this stage, a clear solution was obtained. Occasionally, small nuggets of metal remained. These were attacked separately with conc.  $\text{HNO}_3$ , and the resulting solutions were combined with the main cuts.

At Berlin, the REEs were purified through 10 mL columns using Biorad AG50W-X8 resin and distilled HCl. Neodymium, Sm, and Gd were initially separated on LN-spec columns. The Nd and Sm fractions were then cleaned on custom-made quartz glass columns using 0.21 M  $\alpha$ -HIBA at pH 4.60. The samples were subsequently loaded onto small 2 mL cation columns to wash off residual organics. Finally, all Nd and Sm cuts were again loaded onto the LN-spec columns to obtain pure final separates. Purified Nd cuts were loaded onto outgassed Re filaments and placed in a double-filament configuration as the evaporation filament, using an additional outgassed rhenium filament as the ionization filament.

### **2.6.2 Thermal Ionization Mass Spectrometry**

The Nd isotopes of samples and standards analyzed at the UH laboratory were measured on a ThermoScientific Triton-Plus Thermal Ionization Mass Spectrometer (TIMS) using the three-line multistatic cup configuration shown in Table 2.3. This configuration allows for  $^{148}\text{Nd}$  to be measured across three Faraday cups and  $^{150}\text{Nd}$  to be measured across two cups. Measuring across multiple cups cancels out potential analytical biases introduced by small differences in the cups and the connected amplifiers. The Nd isotopes of samples analyzed at the Berlin laboratory were measured on a ThermoScientific Triton TIMS using the three-line multistatic technique outlined in Caro et al. (2006). All Nd isotope data from both laboratories were internally normalized to a  $^{146}\text{Nd}/^{144}\text{Nd}$  ratio of 0.7129 and corrected for mass bias using the exponential law (Russell et al., 1978; Hart and Zindler, 1989). All Nd isotope data, excluding  $^{143}\text{Nd}/^{144}\text{Nd}$ , are given in  $\mu\text{iNd}$ -notation, as parts per million deviations from the average Nd isotope

composition of the measured JNdi standard, and are calculated using the following equation:

$$\mu^i Nd = \left( \frac{(^iNd/^{144}Nd)_{sample}}{(^iNd/^{144}Nd)_{JNdi}} \right) \times 10^6$$

All  $^{143}\text{Nd}/^{144}\text{Nd}$  data are given in  $\varepsilon^{143}\text{Nd}$ -notation, as parts per ten-thousand deviations from the  $^{143}\text{Nd}/^{144}\text{Nd}$  ratio of the chondritic uniform reservoir (CHUR), and are calculated using the following equation:

$$\varepsilon^{143}\text{Nd} = \left[ \left( \frac{(^{143}\text{Nd}/^{144}\text{Nd})_{sample}}{(^{143}\text{Nd}/^{144}\text{Nd})_{CHUR}} \right) - 1 \right] \times 10^4$$

in which the  $^{143}\text{Nd}/^{144}\text{Nd}$  ratio of CHUR is 0.512630 (Bouvier et al., 2008).

**Table 2.3** The UH TIMS Multistatic Nd Configuration

	Clip	M		M		M		M	Clip
Mass Diff	2	1	1	1	1	1	1	1	2
Cup	L4	L3	L2	L1	Axial	H1	H2	H3	H4
<b>Line 1</b>	142Nd	144Nd	145Nd	146Nd	147Sm	148Nd		150Nd	
<b>Line 2</b>	140Ce	142Nd	143Nd	144Nd	145Nd	146Nd	147Sm	148Nd	150Nd
<b>Line 3</b>		140Ce		142Nd	143Nd	144Nd	145Nd	146Nd	148Nd

Reverse fractionation during TIMS measurements can produce erroneous results (Upadhyay et al., 2008; Andreasen and Sharma, 2009). Preventing evaporation (with the EVAP filament near 1700 mA) until the Ionization filament reached 1600°C was necessary to prevent reverse fractionation of the samples. The filament current turn-up procedure to prevent reverse fractionation is presented in Table 2.4. As each sample is different in how it ionizes, these conditions are generalizations, and the Nd yield, potential

interferences, and overall beam growth determined the rate of increase after the initial two steps.

**Table 2.4** Parameters for evaporation and ionization filament turnup to prevent reverse fractionation of Nd.

Speed mA/m		Final mA	
IONI	EVAP	IONI	EVAP
24	12	3000	1500
30	1	4500	2200
↓	↓		↓
0	5-8		2200+

### 2.6.3 Correction of $\mu^{142}\text{Nd}$ Using $^{143}\text{Nd}/^{144}\text{Nd}$ Ratios

A sample's measured  $^{142}\text{Nd}$  has two distinct sources: nucleosynthetic, s-process  $^{142}\text{Nd}$ , and radiogenic  $^{142}\text{Nd}$ . The  $^{142}\text{Nd}/^{144}\text{Nd}$  ratios are affected by early fractionation of Sm/Nd because of the  $^{146}\text{Sm}$ - $^{142}\text{Nd}$  decay scheme ( $t_{1/2} = 103$  My; Friedman et al., 1966; Meissner et al., 1987). The short-lived  $^{146}\text{Sm}$  is thus effectively decayed away by 500 Myr after solar system formation, such that no change to  $^{142}\text{Nd}/^{144}\text{Nd}$  ratios in a sample will occur after this time. To compare the starting  $^{142}\text{Nd}/^{144}\text{Nd}$  ratios of chondritic materials at a 4.568 Ga formation time, ingrowth of radiogenic  $^{142}\text{Nd}$  from radioactive  $^{146}\text{Sm}$  must be corrected for. The amount of decayed  $^{146}\text{Sm}$  can be calculated in two ways: by using the samples measured  $^{147}\text{Sm}/^{144}\text{Nd}$  ratios, or by using integrated  $^{147}\text{Sm}/^{144}\text{Nd}$  ratios calculated from measured  $^{143}\text{Nd}/^{144}\text{Nd}$  ratios. Measured  $^{147}\text{Sm}/^{144}\text{Nd}$  ratios are more susceptible to changes from terrestrial weathering, and recent changes in Sm/Nd ratios will not be recorded in the integrated  $^{147}\text{Sm}/^{144}\text{Nd}$ .



When correcting the  $\mu^{142}\text{Nd}$  values of enstatite chondrites for radiogenic ingrowth of  $^{142}\text{Nd}$ , Boyet et al. (2018) did not find that using the integrated  $^{147}\text{Sm}/^{144}\text{Nd}$ , as opposed to the measured  $^{147}\text{Sm}/^{144}\text{Nd}$ , changed the sample  $\mu^{142}\text{Nd}$  values. However, Render and Brennecka (2021) found that the integrated  $^{147}\text{Sm}/^{144}\text{Nd}$  method used in other chondrite groups produced more consistent results. Because of this, all samples were corrected using the integrated  $^{147}\text{Sm}/^{144}\text{Nd}$  method. This correction method assumes the initial  $^{143}\text{Nd}/^{144}\text{Nd}$  values for all samples is 0.506686 (the value of CHUR at 4.568 Ga), an initial Solar System  $^{146}\text{Sm}/^{144}\text{Sm}$  value of 0.0085, and a chondritic  $^{147}\text{Sm}/^{144}\text{Nd}$  value of 0.1960 (Bouvier et al., 2008). Assuming these values, the following equations were used to correct for radiogenic  $^{142}\text{Nd}$ :

$$\left(\frac{^{143}\text{Nd}}{^{144}\text{Nd}}\right)_{\text{today}}^{\text{CHUR}} = \left(\frac{^{143}\text{Nd}}{^{144}\text{Nd}}\right)_{4.568 \text{ Ga}} + \left(\frac{^{147}\text{Sm}}{^{144}\text{Nd}}\right)(e^{\lambda t} - 1)$$

$$\left(\frac{^{143}\text{Nd}}{^{144}\text{Nd}}\right)_{4.568 \text{ Ga}} = 0.512630 - 0.196(e^{6.54 \times 10^{-12} \text{ yr} \times 4.568 \times 10^9 \text{ yr}} - 1) = 0.506686212$$

$$\left(\frac{^{143}\text{Nd}}{^{144}\text{Nd}}\right)_{\text{measured}}^{\text{sample}} = \left(\frac{^{143}\text{Nd}}{^{144}\text{Nd}}\right)_{4.568 \text{ Ga}} + \left(\frac{^{147}\text{Sm}}{^{144}\text{Nd}}\right)_{\text{calc}}^{\text{sample}}(e^{\lambda t} - 1)$$

$$\left(\frac{^{147}\text{Sm}}{^{144}\text{Nd}}\right)_{\text{calc}}^{\text{sample}} = \frac{\left(\frac{^{143}\text{Nd}}{^{144}\text{Nd}}\right)_{\text{measured}}^{\text{sample}} - 0.506686212}{(e^{6.54 \times 10^{-12} \text{ yr} \times 4.568 \times 10^9 \text{ yr}} - 1)}$$

$$\left(\frac{^{146}\text{Sm}}{^{144}\text{Nd}}\right)_{\text{calc}}^{\text{sample}} = \frac{\left(\frac{^{146}\text{Sm}}{^{144}\text{Nd}}\right)_{\text{CHUR}}^{4.568 \text{ Ga}}}{\left(\frac{^{147}\text{Sm}}{^{144}\text{Nd}}\right)_{\text{avg}}^{\text{samples}}} \times \left(\frac{^{147}\text{Sm}}{^{144}\text{Nd}}\right)_{\text{calc}}^{\text{sample}}$$

$$\Delta\left(\frac{^{146}\text{Nd}}{^{144}\text{Nd}}\right)_{\text{sample}} = \left(\frac{^{146}\text{Sm}}{^{144}\text{Nd}}\right)_{\text{calc}}^{\text{sample}} - \left(\frac{\left(\frac{^{146}\text{Sm}}{^{144}\text{Nd}}\right)_{\text{CHUR}}^{4.568 \text{ Ga}}}{\left(\frac{^{147}\text{Sm}}{^{144}\text{Nd}}\right)_{\text{avg}}^{\text{samples}}} \times \left(\frac{^{147}\text{Sm}}{^{144}\text{Nd}}\right)_{\text{CHUR}}^{4.568 \text{ Ga}}\right)$$

$$\left(\frac{^{142}\text{Nd}}{^{144}\text{Nd}}\right)_{\text{correction}}^{\text{sample}} = \Delta\left(\frac{^{146}\text{Nd}}{^{144}\text{Nd}}\right)_{\text{sample}} (e^{6.73 \times 10^{-9} \text{ yr} \times 4.568 \times 10^9 \text{ yr}} - 1)$$

$$\left(\frac{^{142}\text{Nd}}{^{144}\text{Nd}}\right)_{\text{corrected}} = \left(\frac{^{142}\text{Nd}}{^{144}\text{Nd}}\right)_{\text{measured}} + \left(\frac{^{142}\text{Nd}}{^{144}\text{Nd}}\right)_{\text{correction}}^{\text{sample}}$$

## 2.7 Results

The Nd isotope compositions for all JNdi standard runs, measured on separate filaments, used in this study are given in Table 2.5. The  $\pm 2\text{SE}$  errors are listed in parentheses after each ratio for each measured run are for the last 2 decimal places in the listed ratios. The errors for the averages of the JNdi ratios are  $\pm 2\text{SD}$ . The measured Nd ratios for all enstatite chondrites analyzed are given in Table B.1. and  $\mu^{\text{iNd}}$  values for enstatite chondrites are given in Table 2.6. The measured Nd ratios of all mantle-derived melt samples analyzed in this study are given in Table B.2 and  $\mu^{\text{iNd}}$  and  $\epsilon^{143}\text{Nd}$  values are given in Table 2.7.

**Table 2.5** Measured  $^{142}\text{Nd}/^{144}\text{Nd}$  ratios of the JNdi standard. The  $\pm 2\text{SE}$  errors are listed in parentheses as the last two decimal places for each ratio. The average error is  $\pm 2\text{SD}$ .

Sample	Cycles	$^{142}\text{Nd}/^{144}\text{Nd}$	$^{143}\text{Nd}/^{144}\text{Nd}$	$^{145}\text{Nd}/^{144}\text{Nd}$	$^{148}\text{Nd}/^{144}\text{Nd}$	$^{150}\text{Nd}/^{144}\text{Nd}$
JNdi - 3238	540	1.1418287 (14)	0.5120967 (8)	0.3484025 (1)	0.2415810 (4)	0.2364525 (7)
JNdi - 3249	360	1.1418310 (22)	0.5120979 (11)	0.3484026 (5)	0.2415814 (5)	0.2364537 (9)
JNdi - 3251	270	1.1418344 (26)	0.5120983 (13)	0.3484026 (6)	0.2415819 (7)	0.2364544 (11)
JNdi - 3332	360	1.1418341 (30)	0.5120976 (16)	0.3484026 (9)	0.2415818 (8)	0.2364535 (14)
JNdi - 3411a	270	1.1418321 (29)	0.5120989 (14)	0.3484029 (6)	0.2415806 (9)	0.2364537 (13)
JNdi - 3411b	270	1.1418302 (24)	0.5120968 (11)	0.3484027 (7)	0.2415806 (7)	0.2364509 (13)
JNdi - 3419	540	1.1418364 (20)	0.5120984 (9)	0.3484030 (5)	0.2415814 (5)	0.2364550 (9)
JNdi - 3496	450	1.1418303 (26)	0.5120975 (13)	0.3484031 (6)	0.2415812 (7)	0.2364525 (13)
JNdi - 3505	270	1.1418354 (26)	0.5120999 (13)	0.3484048 (7)	0.2415802 (1)	0.2364530 (13)
Average		1.1418325 (24)	0.5120980 (12)	0.3484030 (6)	0.2415811 (6)	0.2364532 (11)

**Table 2.6** The Nd isotope compositions of all enstatite chondrite samples analyzed at the UH and Berlin laboratories. Errors for each sample are given as  $\pm 2\text{SE}$  ( $\text{SE} = \text{standard error} = \text{standard deviation}/\sqrt{n}$  in which  $n$  is the number of cycles per sample measurement).

	$\mu^{142}\text{Nd}$	$\mu^{142}\text{Nd}_{\text{corr}}$	$\pm 2\text{SE}$	$\mu^{145}\text{Nd}$	$\pm 2\text{SE}$	$\mu^{148}\text{Nd}$	$\pm 2\text{SE}$	$\mu^{150}\text{Nd}$	$\pm 2\text{SE}$
<b>UH</b>									
GRO 95517 EH3	-7.83	-11.36	3.6	-0.81	3.2	7.77	7.0	<u>783.87</u>	<u>32.5</u>
GRO 95517 dup	-11.49	-10.74	3.0	2.49	2.2	5.00	4.6	<u>349.75</u>	<u>9.3</u>
LAR 06252 EH3	-9.69	-8.51	4.6	-1.70	3.4	13.28	7.0	<u>372.92</u>	<u>13.1</u>
MET 01018 EH3	-12.36	-10.18	3.6	3.15	2.6	14.97	5.4	34.42	10.6
MIL 07028 EH3	-7.75	-3.87	3.2	-3.19	2.5	0.53	6.2	15.22	11.0
PCA91238 EH3	-0.68	-0.68	9.7	-3.70	8.4	8.52	12.0	32.08	21.4
EET 88746 EH4	-11.47	-10.27	5.7	-1.44	5.1	2.84	8.7	65.76	16.9
EET 96341 EH4/5	-12.63	-11.23	4.6	-3.08	3.7	18.62	7.5	37.97	17.3
EET 96135 EH4/5	-4.26	-2.88	5.1	2.83	3.7	-7.13	8.7	40.30	17.8
EET 96299 EH4/5	-7.33	-5.97	5.2	2.14	3.6	1.23	9.5	6.08	15.9
LEW 88180 EH5	-7.78	-6.30	4.9	0.91	3.4	7.48	7.9	35.65	15.2
LEW 87223 EL3	-2.65	2.49	7.8	2.00	5.7	-15.53	12.0	17.21	25.0
MAC 02839 EL3	-8.57	-10.37	12.2	2.14	6.3	8.18	17.0	47.74	25.8
PCA91020 EL3	-17.35	-18.42	13.0	2.67	11.8	6.08	17.8	77.12	26.9

MAC 02747 EL4	-9.60	-9.58	5.3	0.68	3.2	5.78	8.7	17.46	17.3
ALHA 81021 EL6	-11.13	-9.22	4.0	-2.30	3.2	36.83	7.5	110.67	12.7
GRO 95626 EL6	-9.27	-9.41	7.0	0.91	5.5	22.38	10.8	23.93	19.5
QUE94204 AUB	47.17	-7.10	4.4	6.08	3.6	-5.80	5.2	9.29	9.1
<b>Berlin</b>									
PCA 91461 EH3	-10.95	-10.22	3.6	1.46	2.7	32.43	5.7	21.82	11.9
KLE 98300 EH3	-11.29	-7.66	2.7	2.00	2.4	34.00	4.6	14.38	9.6
ALH 84170 EH3	-12.12	-12.07	6.1	1.06	3.7	28.87	8.2	16.70	18.7
EET 96341 EH4/5	-7.26	-7.21	2.7	2.06	2.0	69.64	4.6	28.63	8.5
MAC 88136 EL3	-6.57	-7.70	3.2	2.75	2.7	49.23	5.2	16.83	10.5
MAC 88136 dup	-10.01	-11.08	2.8	1.34	2.0	51.47	4.6	21.65	8.3
MAC 02747 EL4	-7.76	-7.86	2.4	2.49	1.6	43.23	3.7	4.06	7.1
Blithfield EL6	-4.94	-77.94	3.9	2.55	3.1	26.84	7.3	3.25	12.3
Blithfield dup	-5.17	-78.13	2.8	-1.07	1.8	79.33	5.1	71.17	8.9
Blithfield dup 2	-2.83	-75.84	2.5	1.83	2.0	20.17	3.8	-2.12	8.0
LON 94100 EL6	-6.70	-9.85	2.4	1.69	1.7	22.66	3.5	23.77	7.9
ALH 81021 EL6	-6.11	-12.10	2.5	1.03	1.8	45.47	3.9	-21.02	7.9

**Table 2.7** The Nd isotope compositions of all mantle-derived melt samples analyzed at the UH and Berlin laboratories. Errors for each sample are given as 2SE.

	$\mu^{142}\text{Nd}$	$\pm 2\text{SE}$	$\epsilon^{143}\text{Nd}$	$\pm 2\text{SE}$	$\mu^{145}\text{Nd}$	$\pm 2\text{SE}$	$\mu^{148}\text{Nd}$	$\pm 2\text{SE}$	$\mu^{150}\text{Nd}$	$\pm 2\text{SE}$
<b>UH</b>										
ICE9a-3249	2.87	4.2	7.78	0.02	-5.80	3.1	6.16	5.6	-0.10	8.8
ICE9a-3296	4.41	1.3	7.85	0.04	-2.01	1.2	-3.73	1.6	-0.19	3.6
ICE9a-3497	3.35	2.3	7.89	0.02	4.25	1.7	-12.26	2.9	9.20	4.9
ICE9a-3502	10.36	2.5	7.93	0.02	0.82	2.0	-8.44	3.3	9.01	6.3
ICE9a-3503	10.08	4.4	7.83	0.02	-2.19	3.6	-14.90	5.8	-1.09	10.2
ICE9a-3504	13.45	2.5	7.87	0.02	0.90	1.7	-6.42	3.1	2.56	5.6
<b>Berlin</b>										
Biu8 Basalt	-4.88	2.2	5.47	0.02	0.28	1.8	9.33	3.5	0.42	7.1
Miringa Basalt	0.73	3.9	6.23	0.03	-1.64	2.9	15.95	6.5	-21.91	10.4
Komatiit	0.18	3.1	7.27	0.03	-0.84	2.4	126.9	5.6	10.78	10.3

Three samples processed at the UH laboratory (GRO 95517, GRO 95517 dup, and LAR 06252) showed anomalously high  $\mu^{150}\text{Nd}$  values (Table 2.6), which may be the result of sample contamination. These  $\mu^{150}\text{Nd}$  values are disregarded in all subsequent averages and plots. Additionally,  $\mu^{148}\text{Nd}$  values for samples measured at the Berlin laboratory show erroneously high values as shown in Figure 2.1. The  $\mu^{148}\text{Nd}$  measurements for these samples were always higher than  $\mu^{150}\text{Nd}$ , despite no proportional increase in other s-process isotopes to explain that ratio. They do not follow the  $^{148}\text{Nd}$  to  $^{145}\text{Nd}$  trends of other enstatite chondrite samples. These values are also disregarded in all subsequent averages and plots.

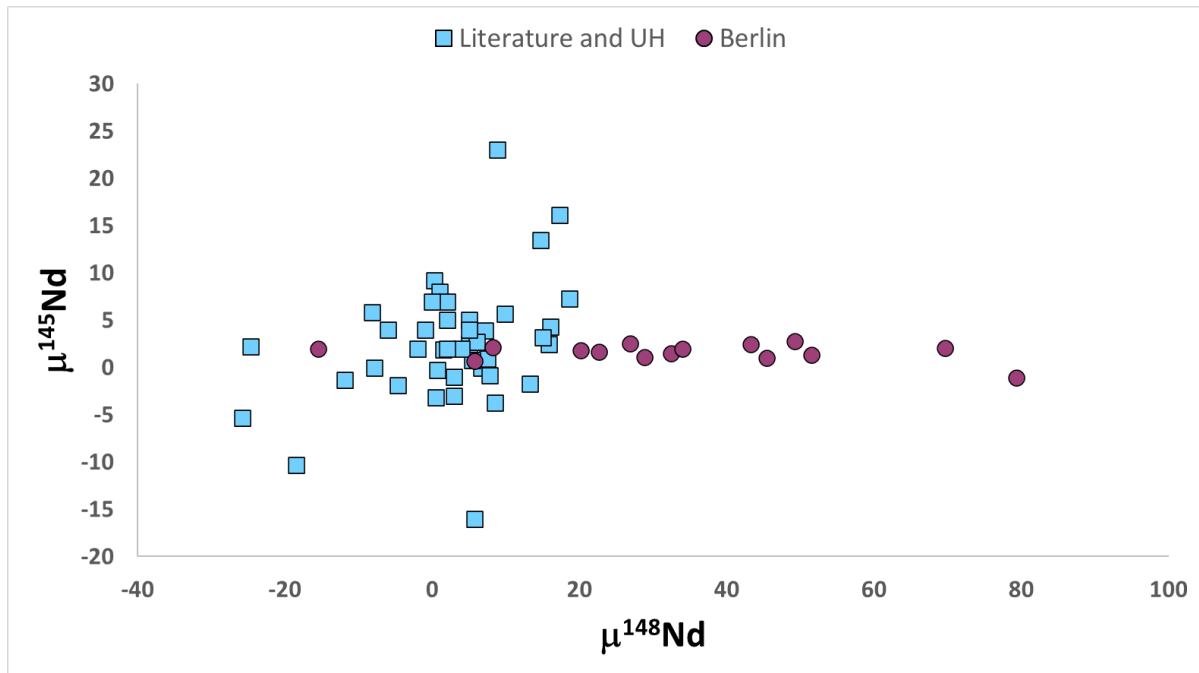


**Figure 2.1** The  $\mu^{148}\text{Nd}$  vs  $\mu^{145}\text{Nd}$  values for enstatite chondrites analyzed at the Berlin laboratory vs. values from all other laboratories (UH – This study; Carlson et al., 2007; Gannoun et al., 2011b; Bouvier and Boyet, 2016; Burkhardt et al., 2016; Boyet et al., 2018; Fukai and Yokoyama, 2019). Samples analyzed at the Berlin laboratory show a different  $\mu^{148}\text{Nd}$  vs.  $\mu^{145}\text{Nd}$  trend than samples from other laboratories.

Samples from this study are compared with all high-precision Nd enstatite chondrite analyses to date (Table B.3), with notable exceptions. The sample Abee from Boyet and Carlson (2005) was removed due to extremely large error bars thought to be due to the small sample size and consequent low amounts of Nd processed that resulted in low beam intensities and higher uncertainties in the measurement. The samples Blithfield and Atlanta from Burkhardt et al. (2016) and Kota Kota from Gannoun et al. (2011b) plot away from the Sm/Nd isochron, interpreted to reflect disturbances in their Sm/Nd systematics by late-stage impacts. The analyses of the impact melt Blithfield, at Berlin by Rankenburg found superchondritic  $^{143}\text{Nd}/^{144}\text{Nd}$  ratios ( $\epsilon^{143}\text{Nd} = 27.8$ ), indicating a later  $^{147}\text{Sm}/^{144}\text{Nd}$  fractionation event relative to the initial parent body processing. These samples were removed from further consideration in the discussion to follow. Sample NWA 8522 from Saji et al. (2020) was removed due to superchondritic  $^{143}\text{Nd}/^{144}\text{Nd}$  ( $\epsilon^{143}\text{Nd} = 8.2$ ) which they interpreted to be a result of weathering of an accessory mineral phase that was depleted in Sm.

Compositional weighted averages were calculated for each enstatite chondrite group with 3 or more samples from all studies, and for all enstatite chondrites as a whole (Table 2.8). A 95% confidence interval was calculated for each group average, following the approach of previous Nd isotope studies of chondrites (Bouvier et al., 2016; Burkhardt et al., 2016; Fukai and Yokoyama, 2017; 2019; Boyet et al., 2018) Confidence intervals were calculated using the following equation:

$$CI = \bar{X} \pm t_{95} \left( \frac{s_{\bar{X}}}{\sqrt{n}} \right)$$

in which CI is the 95% confidence interval,  $\bar{X}$  is the group average,  $t_{95}$  is the t value for a two-tailed test with an alpha value of .05, and  $s_{\bar{X}}$  is the standard deviation of the group population, and n is the population number. The confidence interval gives the range that contains a population's average with a 95% level of confidence. Populations with larger sample numbers or smaller standard deviations will have smaller confidence intervals. Although standard deviations factor in analytical biases, measurement uncertainties, and the variability of inter-group sample isotope compositions (i.e. a single sample is not representative of the bulk parent body), confidence intervals determine the variance of the isotope compositional average of the group, which we assume to represent the bulk parent body.

**Table 2.8** Average Nd isotope compositions for enstatite chondrite groups. Errors are given as the 95% confidence interval.

Group	n	$\mu^{142}\text{Nd}_{\text{corr.}}$	$\pm\text{CI}$	$\epsilon^{143}\text{Nd}$	$\pm\text{CI}$	$\mu^{145}\text{Nd}$	$\pm\text{CI}$	$\mu^{148}\text{Nd}$	$\pm\text{CI}$	$\mu^{150}\text{Nd}$	$\pm\text{CI}$
EH3	17	-9.49	1.2	-0.98	0.4	1.51	1.1	7.55	2.2	19.42	7.9
EH4	7	-11.13	3.8	-1.02	1.3	0.81	2.6	0.93	3.0	12.81	19.5
EH4/5	4	-6.98	2.1	-0.63	0.1	1.19	1.4	5.10	24.5	27.88	15.3
EL3	11	-6.25	1.8	0.02	0.0	2.12	1.2	-1.75	8.4	33.59	23.4
EL6	10	-11.21	1.0	0.98	0.0	1.36	2.3	7.59	11.8	15.23	22.7
EC	55	-9.19	0.8	-0.25	0.3	1.56	0.7	5.67	2.5	21.93	10.4

Prior to this study, the EL3 group was considered to have a Nd isotope composition indistinguishable from the Bulk Silicate Earth (Boyett et al., 2018). However, the addition of new analyses has moved the EL3-group  $\mu^{142}\text{Nd}_{\text{corr.}}$  weighted average to  $-6.3 \pm 1.8$  (CI) (n = 11). This is closer to the new bulk enstatite weighted average of  $-9.2 \pm 0.8$  (CI). Prior to this study, the EL3  $\mu^{142}\text{Nd}_{\text{corr.}}$  weighted average was  $-0.8 \pm 4.4$  (CI) (n = 6).

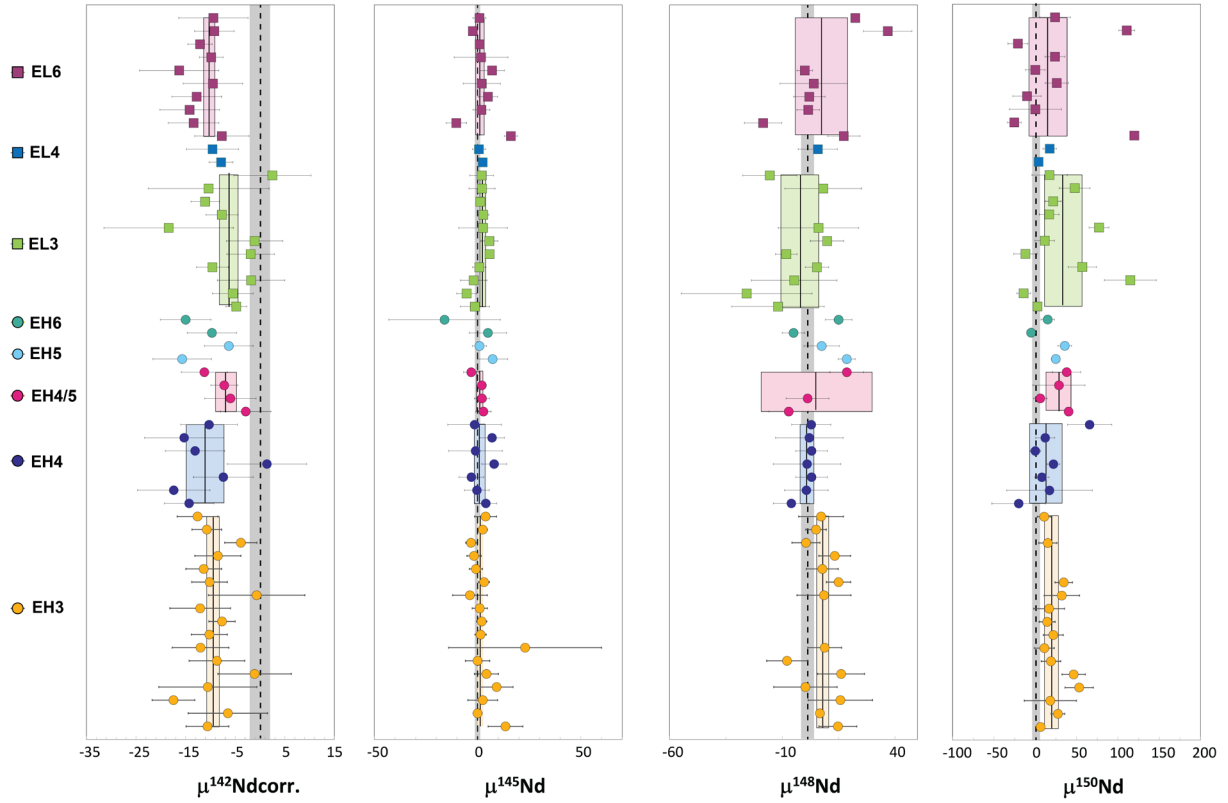


**Figure 2.2** The Nd isotope compositions of enstatite chondrite groups. All  $\mu^{142}\text{Nd}$  values have been corrected for radiogenic ingrowth. For chondrite groups with 3 or more samples, weighted averages of the group have been calculated and are shown as black lines. Error bars for each sample are given as 2SE. The 95% confidence interval of the weighted average of each enstatite chondrite group measurement is shown as a box in the corresponding group color. The average Bulk Silicate Earth (BSE) is shown as a dashed black line with a 95% confidence interval shown as a dark gray box. The BSE compositions and errors were calculated using data from Murphy et al. (2010) and This Study (Table B.4).



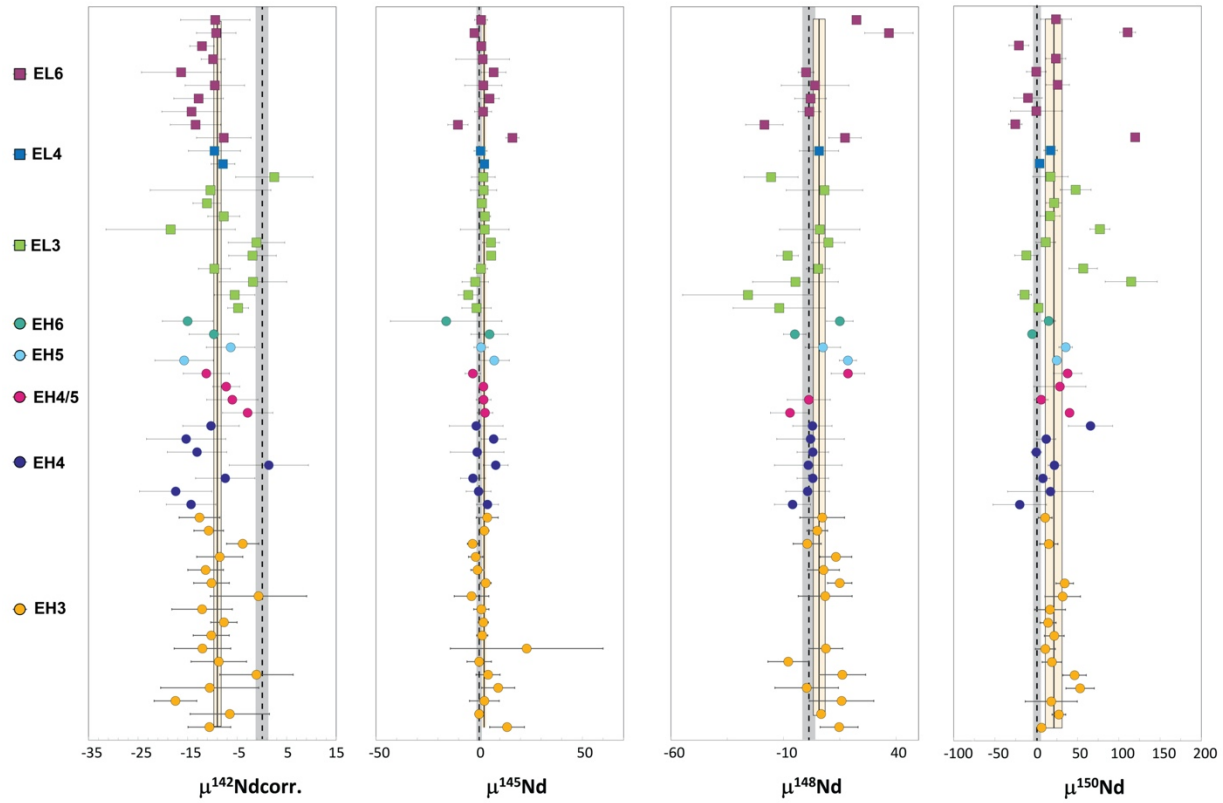


**Figure 2.3** The Nd Isotope compositions of enstatite chondrite groups. Error bars for each sample are given as 2SE. The 95% confidence interval of the weighted average for all enstatite chondrites for each isotope is shown as a manilla-colored box. All  $\mu^{142}\text{Nd}$  have been corrected for radiogenic ingrowth. For chondrite groups with 3 or more samples, weighted averages of the group have been calculated and are shown as black lines. The average Bulk Silicate Earth is shown as a dashed black line with a 95% confidence interval shown as a dark gray box. BSE compositions and errors were calculated using data from Murphy et al. (2010) and This Study (Table B.4).

Thirty three percent of enstatite chondrites analyzed to date, from all labs, show anomalous  $\mu^{150}\text{Nd}$  excesses that are inconsistent with any current nucleosynthetic models. These data are discussed in further detail in section 3.5.5 of this study. The  $\mu^{148}\text{Nd}:\mu^{150}\text{Nd}$  ratios in these samples may be consistent with nuclear field shift effects, but additional work is needed to examine this relationship. These  $\mu^{150}\text{Nd}$  data cannot be used to approximate nucleosynthetic  $\mu^{142}\text{Nd}$  until the cause of this excess is established.

When these anomalous data are removed from the total average, enstatite chondrite  $\mu^{150}\text{Nd}$  becomes  $9.5 \pm 6.3$  (CI), indistinguishable from the BSE  $\mu^{150}\text{Nd}$  of  $0.7 \pm 3.9$  (CI), within error. Removing these anomalously fractionated samples has a negligible (0.09 – 0.29 ppm) effect on the averages for the other Nd isotopes (Table 2.9).

**Table 2.9** Weighted average Nd isotope composition for enstatite chondrites vs. enstatite chondrites in which samples with  $\mu^{150}\text{Nd}$  have been removed. Errors are given as the 95% confidence interval.

	n	$\mu^{142}\text{Nd}$	$\pm\text{CI}$	$\mu^{142}\text{Nd}_{\text{corr.}}$	$\pm\text{CI}$	$\mu^{145}\text{Nd}$	$\pm\text{CI}$	$\mu^{148}\text{Nd}$	$\pm\text{CI}$	$\mu^{150}\text{Nd}$	$\pm\text{CI}$
ECs	55	-9.80	0.9	-9.19	0.8	1.56	0.7	5.67	2.5	21.93	10.4
ECs minus anomalous $\mu^{150}\text{Nd}$	34	-9.91	1.2	-9.48	0.9	1.43	0.8	5.75	4.4	9.55	6.3

The weighted-average Nd isotope relationships of the enstatite chondrite groups are compared to those of ordinary chondrites (Table B.5; Boyet and Carlson, 2005; Andreasen and Sharma, 2006; Carlson et al., 2007; Gannoun et al., 2011b; Bouvier and Boyet, 2016; Burkhardt et al., 2016; Fukai and Yokoyama, 2017; 2019; Saji et al., 2020). Enstatite and ordinary chondrite weighted-averages for Nd isotopes with no radiogenic component ( $\mu^{145}\text{Nd}$ ,  $\mu^{148}\text{Nd}$ ,  $\mu^{150}\text{Nd}$ ) plot near stellar-predicted s-deficit lines (Figure 2.4). When these isotopes are compared with  $\mu^{142}\text{Nd}_{\text{corr.}}$ , both enstatite and ordinary chondrite weighted averages plot away from the stellar-predicted s-deficit lines, showing additional deficits in  $\mu^{142}\text{Nd}$  than predicted by both the radiogenic correction and a nucleosynthetic component (Figure 2.5-2.7). The EH and EL groups show no systematic trend in  $\mu^{145}\text{Nd}$  vs.  $\mu^{142}\text{Nd}_{\text{corr.}}$  or  $\mu^{148}\text{Nd}$  vs.  $\mu^{142}\text{Nd}_{\text{corr.}}$  with petrologic grade (Figure 2.5-2.6), and the group averages are not resolvable from each other.

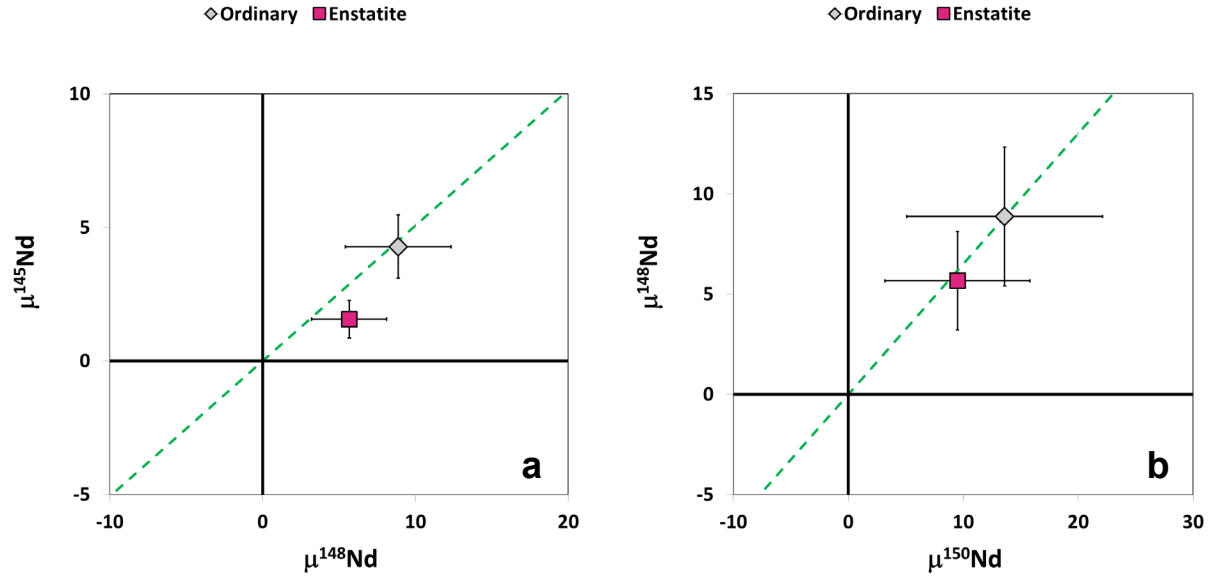


**Figure 2.4** (a) Weighted average  $\mu^{148}\text{Nd}$  vs  $\mu^{145}\text{Nd}$  values for the enstatite and ordinary chondrite classes. (b)  $\mu^{150}\text{Nd}$  vs  $\mu^{148}\text{Nd}$  values for the weighted averages of enstatite and ordinary chondrite classes. Error bars in both panes show the 95% confidence interval. The s-deficit relationships predicted by the stellar model are shown as dashed green lines. Weighted average  $\mu^{150}\text{Nd}$  values were calculated after removing samples that show anomalous, mass-independent fractionation of  $^{150}\text{Nd}$ .

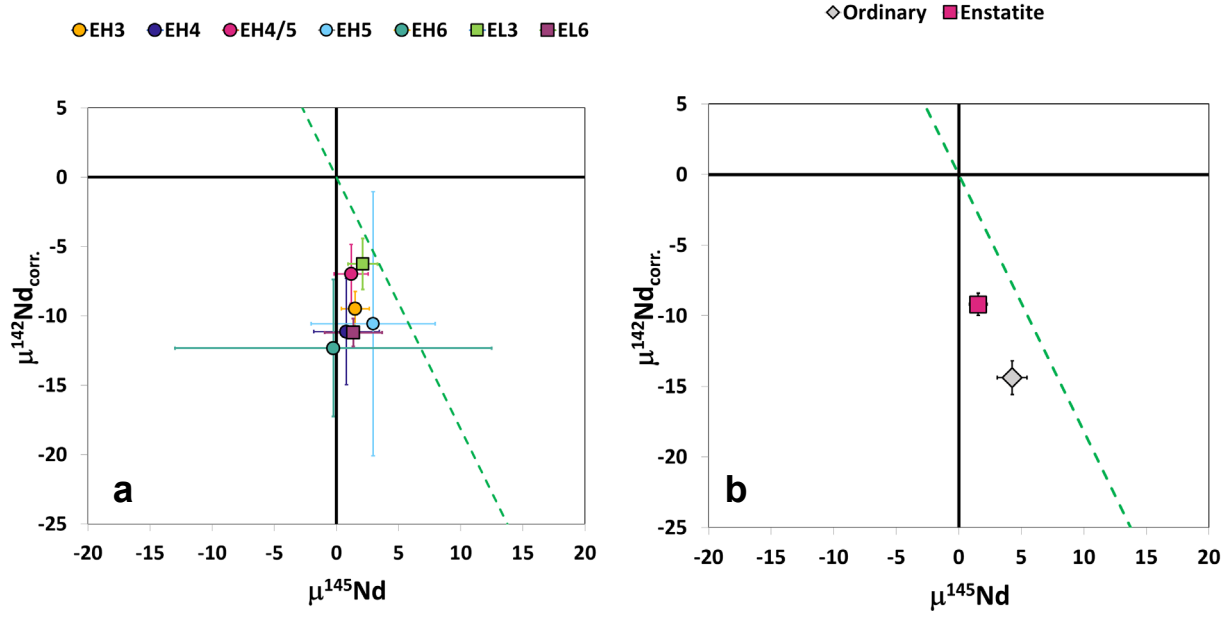


**Figure 2.5 (a)** Weighted average  $\mu^{145}\text{Nd}$  vs  $\mu^{142}\text{Nd}_{\text{corr.}}$  values for enstatite chondrite groups. Error bars for each sample are given as 2SE. **(b)** Weighted average  $\mu^{148}\text{Nd}$  vs  $\mu^{142}\text{Nd}_{\text{corr.}}$  values for the enstatite and ordinary chondrite classes. Error bars show the 95% confidence interval. The s-deficit relationship predicted by the stellar model is shown as a dashed green line.

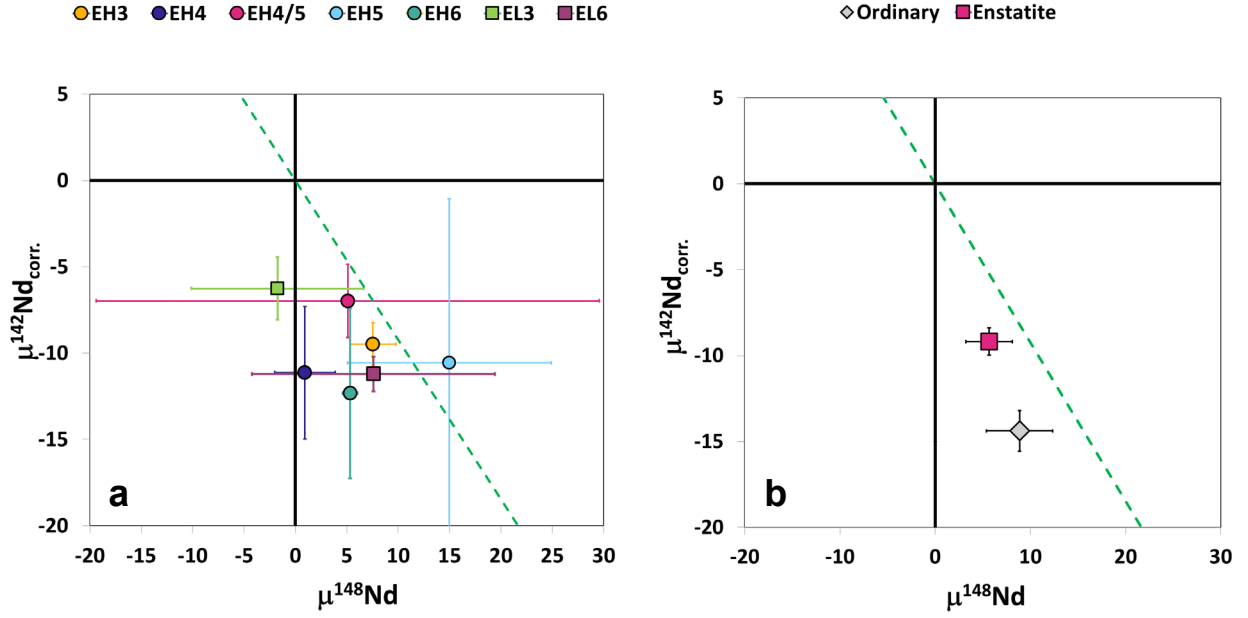


**Figure 2.6 (a)** Weighted average  $\mu^{148}\text{Nd}$  vs  $\mu^{142}\text{Nd}_{\text{corr.}}$  values for enstatite chondrite groups. Error bars for each sample are given as 2SE. **(b)** Weighted average  $\mu^{148}\text{Nd}$  vs  $\mu^{142}\text{Nd}_{\text{corr.}}$  values for the enstatite and ordinary chondrite classes. Error bars show the 95% confidence interval. The s-deficit relationship predicted by the stellar model is shown as a dashed green line.

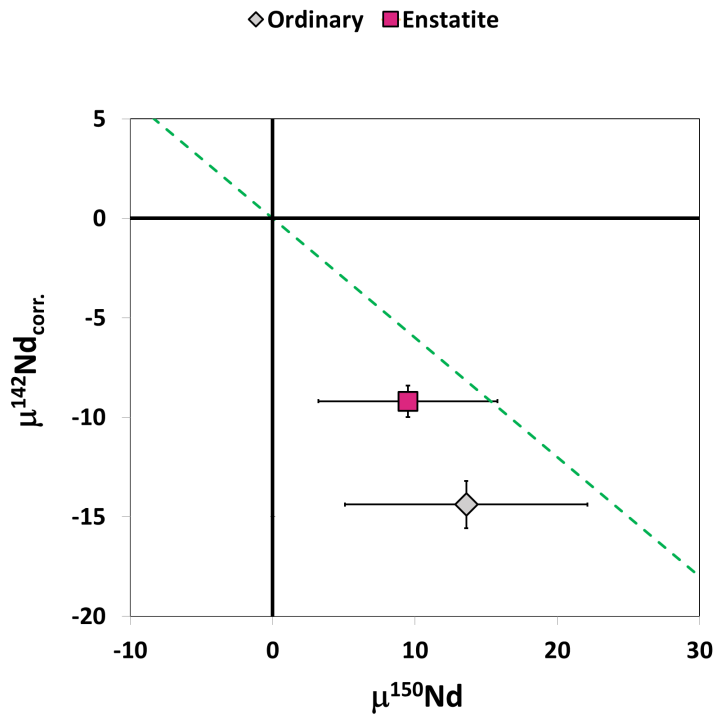


**Figure 2.7** Weighted average  $\mu^{150}\text{Nd}$  vs  $\mu^{142}\text{Nd}_{\text{corr.}}$  values for the weighted averages of enstatite and ordinary chondrite classes after anomalously fractionated samples have been removed. Error bars show the 95% confidence interval. The s-deficit relationship predicted by the stellar model is shown as a dashed green line

## 2.8 Discussion

### 2.8.1 Laboratory Averages

Three enstatite chondrites were analyzed at both the UH and Berlin laboratories (Table 2.10). The UH sample measurements have lower  $\mu^{145}\text{Nd}$  values than the Berlin sample measurements, but the differences are not resolvable within the  $\pm 2\text{SE}$  uncertainties. The UH sample measurements also have higher  $\mu^{150}\text{Nd}$  values. Only ALH 81021 has a resolvable  $\mu^{150}\text{Nd}$  difference between the two labs, with the UH sample measuring  $110.67 \pm 12.69$  (2SE) and the Berlin sample measuring  $-21.02 \pm 7.87$  (2SE).

**Table 2.10** Comparison of Nd isotope compositions of samples analyzed in both the UH laboratory and the Berlin laboratory. Errors for each sample are given as 2SE.

	$\mu^{142}\text{Nd}$	$\mu^{142}\text{Nd}_{\text{corr}}$	$\pm 2\text{SE}$	$\varepsilon^{143}\text{Nd}$	$\mu^{145}\text{Nd}$	$\pm 2\text{SE}$	$\mu^{150}\text{Nd}$	$\pm 2\text{SE}$
<b>EET 96341 EH4/5</b>								
<i>Berlin</i>	-7.26	-7.21	2.71	-0.53	2.06	2.00	28.63	8.46
<i>UH</i>	-12.63	-11.23	4.64	-0.70	-3.08	3.73	37.97	17.34
<i>Difference</i>	5.37	4.02		0.16	5.14		9.34	
<b>MAC 02747 EL4</b>								
<i>Berlin</i>	-7.76	-7.86	2.41	-0.48	2.49	1.61	4.06	7.15
<i>UH</i>	-9.60	-9.58	5.25	-0.16	0.68	3.16	17.46	17.34
<i>Difference</i>	1.83	1.73		0.32	1.81		13.40	
<b>ALH 81021 EL6</b>								
<i>Berlin</i>	-6.11	-12.10	2.46	1.80	1.03	1.79	-21.02	7.87
<i>UH</i>	-11.13	-9.22	3.98	-0.90	-2.30	3.16	110.67	12.69
<i>Difference</i>	5.02	2.88		2.70	3.33		131.69	

There are numerous variations in the chemical procedures used in purifying Nd from enstatite chondrites for isotope analyses. Samples have been digested under pressure and on hot plates using different combinations of acids. While many studies use some combination of Biorad AG50W-X8 and LN-Spec resins in their ion-exchange chromatography (Gannoun et al., 2011b; Bouvier and Boyet, 2016; Fukai and Yokoyama, 2017; Saji et al., 2020; Render and Brennecka, 2021), other studies use the MLA method and forego LN-Spec altogether (Boyet and Carlson, 2005; Carlson et al., 2007; Burkhardt et al., 2016). The acids used, their purity and their strength also differ between laboratories. Variations in static vs. multistatic/ multidynamic TIMS configurations may also play a role in contributing to the heterogeneity of data in enstatite chondrite Nd data. With no consistent method for how Nd is purified and measured, it is difficult to evaluate

if the heterogeneities in Nd isotope data for enstatite chondrites are real or simply an artifact due to lower Nd concentrations, or inhomogeneous distribution of nucleosynthetic components, in these samples.

The weighted average Nd isotope for laboratories that have contributed the most substantial number of analyses for enstatite chondrites (UH – This Study; Berlin – This Study; Burkhardt et al., 2016; Gannoun et al., 2011b) are shown in Table 2.11. Analyses from additional labs are shown in Figures 2.8-2.10. The variability in measured values, although typically not resolvable, again points to a need for consistency in sample purification and measurement procedure to determine if these discrepancies in bulk enstatite chondrite values per laboratory are an artifact of procedure. This is particularly important for  $^{150}\text{Nd}$  which shows resolvable differences in the bulk enstatite average between laboratories, but also shows anomalous fractionation patterns in individual samples across all laboratories.

**Table 2.11** Weighted average Nd isotope compositions for enstatite chondrites from four laboratories: UH – This Study; Berlin – This Study; Burkhardt et al. (2016); Gannoun et al. (2011b). Errors are given the 95% confidence interval.

Lab	n	$\mu^{142}\text{Nd}_{\text{corr}}$	$\pm\text{CI}$	$\mu^{145}\text{Nd}$	$\pm\text{CI}$	$\mu^{148}\text{Nd}$	$\pm\text{CI}$	$\mu^{150}\text{Nd}$	$\pm\text{CI}$
UH	17	-8.10	1.39	0.21	0.7	8.68	5.2	40.08	12.2
Berlin	9	-9.37	0.68	1.79	0.2			13.12	8.2
Burkhardt et al. 2016	8	-10.41	3.03	2.59	2.9	2.94	1.1	6.19	8.2
Gannoun et al. 2011	11	-9.22	2.55	2.82	2.9	3.29	8.9	20.93	18.8



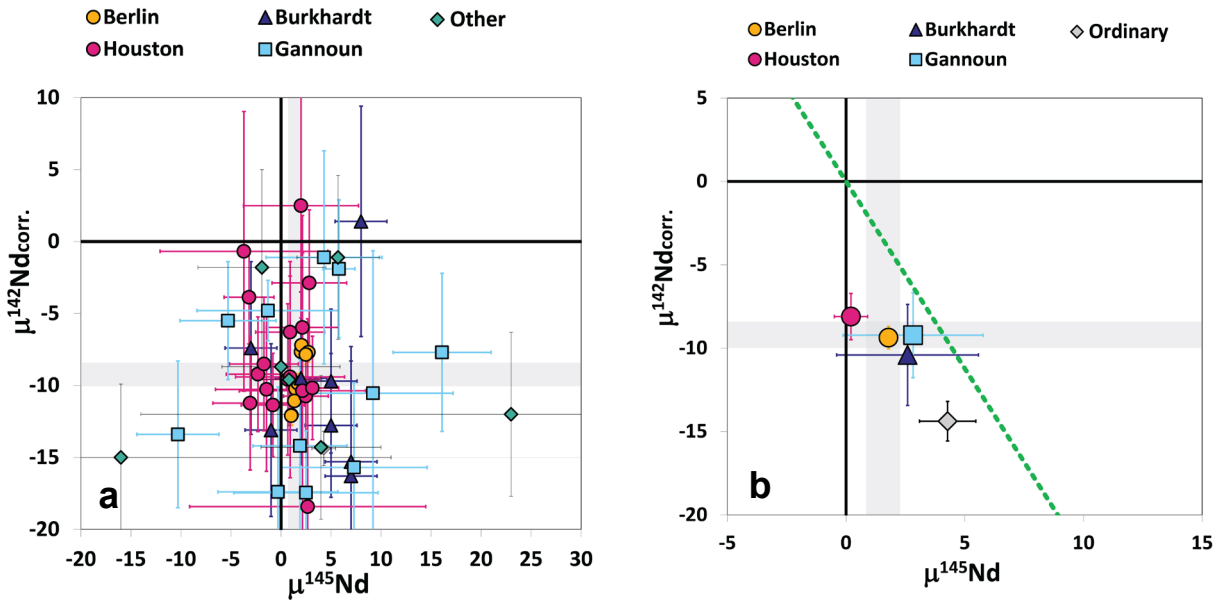


**Figure 2.8 (a)**  $\mu^{145}\text{Nd}$  vs  $\mu^{142}\text{Nd}_{\text{corr.}}$  values for enstatite chondrites analyzed at various laboratories. Other data from Carlson et al. (2007); Fukai and Yokoyama (2019); Saji et al. (2020). Error bars for each sample are given as 2SE **(b)** The weighted average  $\mu^{145}\text{Nd}$  vs  $\mu^{142}\text{Nd}_{\text{corr.}}$  values for enstatite chondrites from each laboratory and for all measured ordinary chondrites. Error bars show the 95% confidence interval. The weighted average of the enstatite chondrite class is shown as gray shading and the s-deficit relationship predicted by the stellar model is shown as a dashed green line.

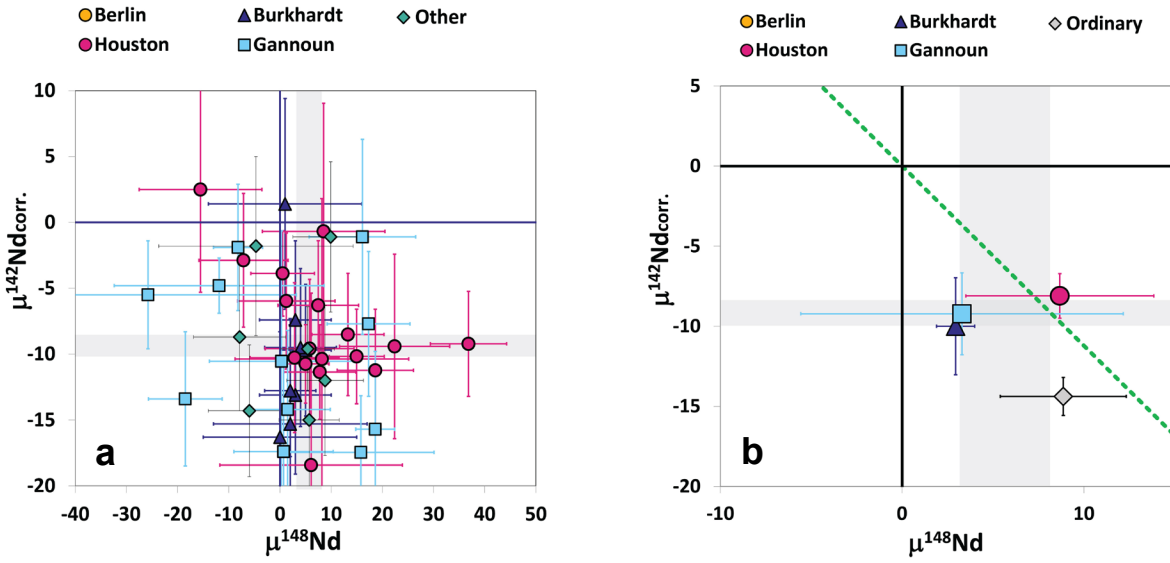


**Figure 2.9 (a)**  $\mu^{148}\text{Nd}$  vs  $\mu^{142}\text{Nd}_{\text{corr.}}$  values for enstatite chondrites analyzed at various laboratories. Other data from Carlson et al. (2007); Fukai and Yokoyama (2019); Saji et al. (2020). Error bars for each sample are given as 2SE **(b)** The weighted average  $\mu^{148}\text{Nd}$  vs  $\mu^{142}\text{Nd}_{\text{corr.}}$  values for enstatite chondrites from each laboratory and for all measured ordinary chondrites. Error bars show the 95% confidence interval. The weighted average of the enstatite chondrite class is shown as gray shading and the s-deficit relationship predicted by the stellar model is shown as a dashed green line.

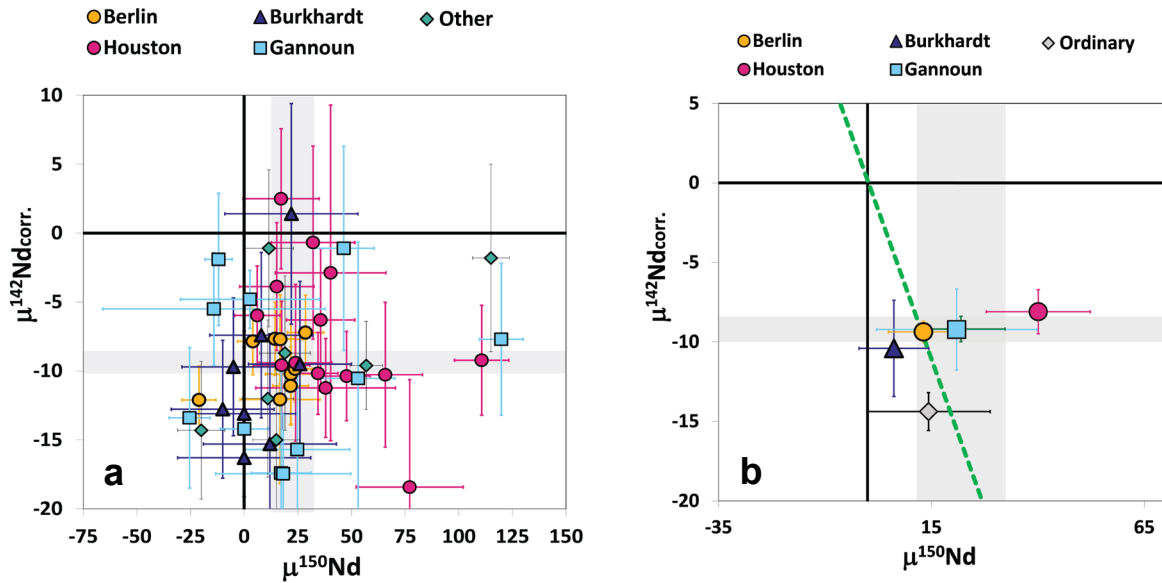


**Figure 2.10 (a)**  $\mu^{150}\text{Nd}$  vs  $\mu^{142}\text{Nd}_{\text{corr.}}$  values for enstatite chondrites analyzed at various laboratories. Other data from Carlson et al. (2007); Fukai and Yokoyama (2019); Saji et al. (2020). Error bars for each sample are given as 2SE **(b)** The weighted average  $\mu^{150}\text{Nd}$  vs  $\mu^{142}\text{Nd}_{\text{corr.}}$  values for enstatite chondrites from each laboratory and for all measured ordinary chondrites. Error bars show the 95% confidence interval. The weighted average of the enstatite chondrite class is shown as gray shading and the s-deficit relationship predicted by the stellar model is shown as a dashed green line. These averages include samples that show anomalous  $^{150}\text{Nd}$  fractionation.

## 2.8.2 Weathering of Sm/Nd – Host Phases

Unlike other chondrite groups, enstatite chondrites can typically host approximately half of their Sm and Nd in the mineral Oldhamite ( $\text{CaS}$ ) instead of silicates (Boyet et al., 2018). Oldhamite is particularly susceptible to terrestrial weathering. Because 66% of enstatite chondrites measured for high-precision Nd isotope compositions have been found as opposed to falls, one concern is the effect that terrestrial weathering could have on  $\mu^i\text{Nd}$  values. However, the weighted averages of  $\mu^{142}\text{Nd}$ ,  $\mu^{145}\text{Nd}$ ,  $\mu^{148}\text{Nd}$ , and  $\mu^{150}\text{Nd}$  for enstatite chondrite falls, which would not be subjected to

extensive terrestrial weathering, are not resolvable from the bulk weighted means of the total fall + find enstatite chondrite group (Table 2.12).

**Table 2.12** Weighted average Nd isotope composition for enstatite chondrite falls versus the entire enstatite chondrite group (falls + finds). Errors are given as the 95% confidence interval.

	$\mu^{142}\text{Nd}$	$\mu^{142}\text{Nd}_{\text{corr}}$	$\pm\text{CI}$	$\mu^{145}\text{Nd}$	$\pm\text{CI}$	$\mu^{148}\text{Nd}$	$\pm\text{CI}$	$\mu^{150}\text{Nd}$	$\pm\text{CI}$
All ECs	-9.80	-9.19	0.79	1.56	0.71	5.67	2.46	21.93	10.36
Falls Only	-11.23	-11.85	1.91	2.53	3.19	3.68	4.61	14.23	37.97

### 2.8.3 Variability in the $^{142}\text{Nd}$ Compositions of Earth and Enstatite Chondrites

The differences between the enstatite chondrite group weighted average and Earth for  $\mu^{145}\text{Nd}$ ,  $\mu^{148}\text{Nd}$ , and  $\mu^{150}\text{Nd}$  are not resolvable at the current level of analytical precision and number of samples. This is consistent with previous studies (Boyet et al., 2018). However, plots of  $\mu^{148}\text{Nd}$  versus  $\mu^{145}\text{Nd}$  and  $\mu^{148}\text{Nd}$  versus  $\mu^{150}\text{Nd}$  show that enstatite chondrites plot at an intermediate isotope composition between Earth and ordinary chondrites for these isotopes (Figure 2.4) indicating small nucleosynthetic differences between the chondrite parent bodies and Earth. The  $\mu^{142}\text{Nd}_{\text{corr}}$  average for enstatite chondrites maintains a  $-9.2 \pm 0.8$  (CI) deviation from Earth, even after correcting for radiogenic  $^{142}\text{Nd}$ . This highlights a key dichotomy. Neodymium isotopes that are produced solely by nucleosynthesis are not fully resolvable between enstatite chondrites and Earth but are consistent with small s-deficit anomalies. However,  $\mu^{142}\text{Nd}$  is neither consistent between enstatite chondrites and Earth, nor is it consistent with predicted s-deficit relationships with the Nd isotopes produced solely through nucleosynthesis. This inconsistency in  $\mu^{142}\text{Nd}$  could record deviations in the Earth's initial Sm/Nd ratio.

Using the difference between the amount of  $^{142}\text{Nd}$  needed to move the correlation of EC and OC with that of bulk Earth on a single s-deficit mixing line, is more sensitive to small differences in the Sm/Nd ratios in these materials than using differences between the measured  $^{143}\text{Nd}/^{144}\text{Nd}$  ratios. This is because the short-lived parent isotope of  $^{146}\text{Sm}$  means that no late process that fractionates Sm from Nd affects the resultant  $^{142}\text{Nd}/^{144}\text{Nd}$  ratio. Hence this small difference needed can be used to calculate the difference between Sm/Nd of the materials that accreted to form Earth and the EC parent body.

Taking the averaged excess in  $\mu^{142}\text{Nd}$  from Figure 2.11a and b of +5.9 for Earth relative to EC and OC chondrites, one can estimate the difference between the material that accreted to form Earth and the EC parent material for  $^{143}\text{Nd}/^{144}\text{Nd}$  and  $^{147}\text{Sm}/^{144}\text{Nd}$ . To do this calculation, the Sm and Nd isotope parameters of Bouvier et al. (2008) are used with CHUR values for  $^{143}\text{Nd}/^{144}\text{Nd}$  today of 0.512630,  $^{143}\text{Nd}/^{144}\text{Nd}$  at 4.568 Ga of 0.5066862,  $^{147}\text{Sm}/^{144}\text{Nd}$  of 0.1960, and  $^{146}\text{Sm}/^{144}\text{Sm}$  of 0.0085. For an excess of 5.9 ppm for Earth relative to chondrites produced by radiogenic ingrowth of  $^{142}\text{Nd}$  since 4.568 Ga, the resultant  $^{147}\text{Sm}/^{144}\text{Nd}$  of bulk Earth is 0.19939 and present-day  $^{143}\text{Nd}/^{144}\text{Nd}$  is 0.512733 ( $\epsilon\text{Nd} = 1.85$ ). This is a 1.7% difference in the Sm/Nd ratio for Earth and bulk chondrites.

Hence, a small deviation in the initial Sm/Nd ratio coupled with s-deficit nucleosynthetic anomalies for bulk Earth relative to chondrites, could produce the relationship observed in Figure 2.11. Multiple explanations have been proposed to explain how the early Earth could achieve a slightly higher Sm/Nd ratio than enstatite chondrites.

The next sections highlight key problems with some of these proposed models and additional work that is needed to test the validity of others.

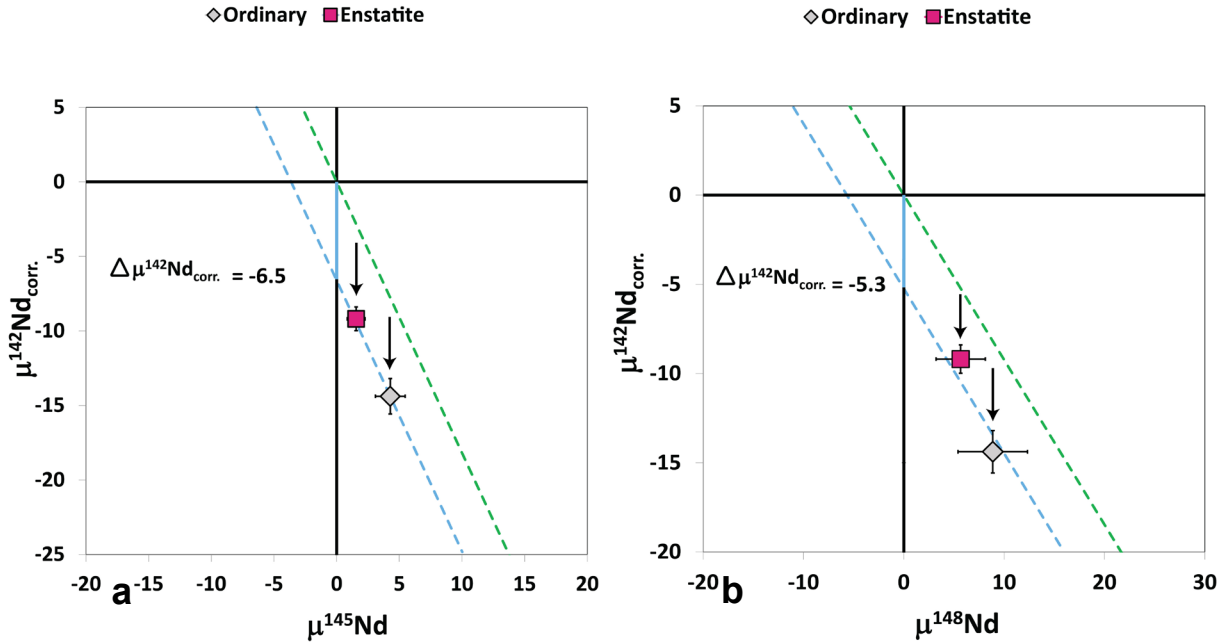


**Figure 2.11** (a)  $\mu^{145}\text{Nd}$  vs  $\mu^{142}\text{Nd}_{\text{corr.}}$  and (b)  $\mu^{148}\text{Nd}$  vs  $\mu^{142}\text{Nd}_{\text{corr.}}$  weighted averages of enstatite and ordinary chondrite classes. The enstatite chondrite weighted average is shown as a pink square and the ordinary chondrite weighted average is shown as a gray diamond. The s-deficit relationship predicted by the stellar model is shown as a dashed green line. Both classes show deviations in  $\mu^{142}\text{Nd}_{\text{corr.}}$  from predicted s-deficit relationships.

### 2.8.3.1 Hidden Reservoir

Boyet and Carlson (2005) proposed the formation of an enriched, hidden reservoir in the early Earth, before the giant impact that formed the Moon to explain the variability between  $\mu^{142}\text{Nd}$  values for Earth and chondrites. This early enriched reservoir, isolated near the core-mantle boundary, would leave the residual mantle with a superchondritic Sm/Nd ratio that would lead to more radiogenic  $^{142}\text{Nd}/^{144}\text{Nd}$  ratios for Earth, in comparison

to chondrites (Boyet and Carlson, 2006; Andreasen et al., 2008) However, Lunar samples and Earth have indistinguishable isotope compositions for K, Ti, Cr, and W (Humayun and Clayton, 1995; Lugmair and Shukolyukov, 1998; Touboul et al., 2007; Zhang et al., 2012; Wang and Jacobson, 2016), suggesting these two bodies formed from a homogenized mixture of proto-Earth and a Mars-sized impactor (Pahlevan and Stevenson, 2007). Lunar  $^{142}\text{Nd}$ - $^{143}\text{Nd}$ - $^{176}\text{Hf}$  systematics support homogenization during this impact (Brandon et al., 2009), meaning this reservoir would have had to have formed in the first 10-30 Myrs after solar system formation, before the giant impact that formed the moon (Touboul et al., 2007; Bourdon et al., 2008; Halliday, 2008; Caro and Bourdon, 2010). This reservoir would have had to have remained isolated from a completely molten mantle that would have homogenized on a week-long timescale following re-accretion of Earth after the giant impact event. (Canup, 2004; Pahlevan and Stevenson, 2007). Even if a giant impact could result in a hidden reservoir and explain a different Sm/Nd ratio, this cannot alone explain the nucleosynthetic Nd isotope differences between bulk Earth and the EC parent body material.

#### **2.8.3.2 Collisional Erosion**

Several studies have suggested that the composition of Earth may have been modified during the planet-building process by loss of an incompatible-element-enriched silicate crust during collisional erosion (Palme et al., 2003; Caro et al., 2008; O'Neill and Palme, 2008; Boujibar et al., 2015). The loss of this silicate crust to space would increase the Earth's Sm/Nd ratio compared to chondrites. Collisional-erosion models have been used to resolve other major-element abundance mismatches between Earth and enstatite

chondrites (Boujibar et al., 2015). Models in Allibert et al. (2021) and Carter et al. (2018) found that ~2-5% Sm/Nd fractionation of early Earth could be achieved when they applied varying partial melting rates and starting crustal compositions. The calculated 1.7% differences comparing Earth with EC and OC in Figure 2.11 is consistent with this. However, O'Neill et al. (2008) found that collisional erosion models lowered the Earth's concentration of heat-producing elements, U, Th, and K, by as much as 50%. This would require unrealistic cooling rates of Earth through geologic time (Campbell and O'Neill, 2012). Additionally, no meteorite sample has ever represented the incompatible-element-enriched material that would have been lost to space. This model also suffers the same issue as a hidden reservoir model in that it cannot explain the resolvable differences between nucleosynthetic Nd isotope compositions of bulk Earth and the EC parent body material.

### **2.8.3.3 Mineral Sorting**

A model that can incorporate both Sm/Nd and nucleosynthetic differences in the Nd isotope compositions between Earth and the EC parent body material would be the most straightforward explanation for the observations in Figure 2.11. The idea of Earth accreting from a reservoir of material with a different starting Sm/Nd ratio than enstatite chondrites hasn't been considered a viable scenario for two reasons. First, Sm and Nd are both refractory lithophile elements with similar condensation temperatures (Lodders, 2003). Second, bulk chondrites have an average Sm/Nd ratio of  $0.32 \pm 0.02$  and show only a small 4% variation in Sm/Nd, regardless of chondrite type (Patchett et al., 2004; Bouvier et al., 2008). Bulk aubrites, thought to be the product of early differentiation of an enstatite



chondrite parent body, also have an average Sm/Nd ratio of  $0.31 \pm 0.04$  (2SD), indistinguishable from the bulk chondrite average (Barrat et al., 2016).

However, recent studies of individual mineral phases in chondrites have shown more variability in their Sm/Nd ratios. For example, olivine phases, which can have higher Sm/Nd ratios with an average of  $0.67 \pm 0.56$  (2SD) (Jacquet et al., 2012; 2015a; 2015b; Jacquet and Marrocchi, 2017). Olivine also has higher Sm/Nd ratios than other measured mineral phases and chondrite components, including oldhamite, enstatite, plagioclase, and CAIs that have a combined average Sm/Nd ratio of  $0.43 \pm 0.05$  (2SD) (Gannoun et al., 2011a; Jacquet et al., 2012; 2015a; 2015b; Jacquet and Marrocchi, 2017).

Miyazaki and Korenaga (2021) have proposed a new thermochemical evolution model of the protoplanetary disk in which planetesimals from adjacent Earth – EC source reservoirs could have distinct major-element abundances. In this model, the Earth's higher Mg/Si ratio and heavier  $\delta^{30}\text{Si}$ , relative to enstatite chondrites, are explained by the inward flow of refractory minerals, such as Mg-rich olivine (forsterite), past an “evaporation front” of enstatite that separates the EC reservoir from an inner region where Earth forms. As enstatite evaporates, forsterite and other refractory minerals are incorporated into pebbles and are transported past the enstatite evaporation front. Oldhamite (CaS), one of the main host phases of Sm and Nd in enstatite chondrites, has a condensation temperature of 1379 K (Lodders and Fegley, 1993). This is similar to the condensation temperature of enstatite, 1400 K (Lodders, 2003; Miyazaki and Korenaga, 2021). Oldhamite would not have been transported into the inner disk, due to its low condensation temperature. Oldhamite's lower average Sm/Nd ratio of  $0.43 \pm 0.04$

(Gannoun et al., 2011a) in comparison to olivines that can have higher Sm/Nd ratios ( $0.67 \pm 0.56$ ), could leave the materials that formed Earth comparatively enriched in Sm.

As discussed above, olivine is the only measured mineral component in chondrites, other than niningerite (MgS), to show substantially higher average Sm/Nd ratios compared to bulk chondrites. Niningerite has a Sm/Nd ratio of  $0.81 \pm 0.42$  (Gannoun et al., 2011a). This mineral phase is produced from a reaction between forsterite and gaseous  $H_2S$ , at a much lower condensation temperature of about 1030 K (Lodders and Fegley, 1993) making it an unsuitable candidate for increasing the Sm/Nd ratio of early Earth. Although the preferential incorporation of forsterite into the early Earth reservoir by way of the inward flow of forsterite pebbles could potentially increase the starting Sm/Nd ratio of Earth, the Sm/Nd ratios of chondritic olivines have not been well characterized. Only 9 chondritic olivines have been analyzed to date (Weinbruch, 2000; Jacquet et al., 2012; 2015a; 2015b; Jacquet and Marrocchi, 2017) and have a range of Sm/Nd ratio from 0.31 – 1.00. Additional studies to more robustly characterize the Sm/Nd ratio of chondritic olivines are necessary to evaluate the plausibility of this scenario.

## 2.9 Conclusion

With the addition of 26 new measurements to the average enstatite chondrite Nd isotope composition, enstatite chondrites have a resolvable  $\mu^{142}Nd_{corr.}$  value of  $-9.2 \pm 0.8$  (CI) relative to Earth standards at 0. Enstatite chondrites do not exhibit resolvable anomalies from Earth for  $\mu^{145}Nd$ ,  $\mu^{148}Nd$ , and  $\mu^{150}Nd$  at the current level of analytical precision. However, comparisons of these Nd isotopes show that enstatite chondrites as a group plot at an intermediate isotope composition between Earth and ordinary

chondrites indicating that they have small resolvable nucleosynthetic anomalies compared to bulk Earth.

This average value for  $\mu^{142}\text{Nd}$ , when taking into consideration the average  $\mu^{145}\text{Nd}$ ,  $\mu^{148}\text{Nd}$ , and  $\mu^{150}\text{Nd}$  values for enstatite chondrites, is inconsistent with predicted s-deficit relationships for the  $^{142}\text{Nd}$  produced solely through nucleosynthesis. This inconsistency in  $\mu^{142}\text{Nd}$  may record deviations in the Earth's initial Sm/Nd ratio, coupled with s-deficit nucleosynthetic anomalies. Multiple explanations have been proposed to explain how the early Earth could achieve a different Sm/Nd ratio than enstatite chondrites. A missing reservoir stable in the deepest part of Earth, or collisional erosion during a giant impact that formed the Moon may explain the differences observed between the Sm/Nd ratio of bulk Earth and the EC parent body, but would not resolve the Nd isotope nucleosynthetic and Mg/Si differences between these bodies. A potentially more appealing model that can explain all of these differences would be mineral sorting in the solar nebula, via mineral evaporation fronts in the protoplanetary disk that could preferentially enrich Earth with material that has a higher Sm/Nd ratio as well as explain small differences in the isotope nucleosynthetic compositions and Mg/Si ratio between Earth and the EC parent body.

## Chapter III: Nd isotope analyses of CV-CK chondrites

### 3.1 Introduction

Carbonaceous chondrites (CCs) preserve a record of the earliest stages of solar system evolution (Greenwood et al., 2010; Dunn et al., 2016; Nanne et al., 2019). They have bulk chemical compositions that are mostly unfractionated relative to the Sun (Dunn et al., 2016; Braukmüller et al., 2018). However, CCs host large nucleosynthetic anomalies for numerous isotopic systems. Isotope compositions of Sr, Mo, Cr, Ti, Ni, and Zr have shown variations within the different groups of CCs (Trinquier et al., 2009; Warren, 2011; Burkhardt et al., 2011; Akram et al., 2015; Yokoyama et al., 2015; Burkhardt et al., 2016; Fukai and Yokoyama, 2019). The observed isotopic variations for CC parent bodies are likely due to both heterogeneous distributions of pre-solar grains within the larger CC reservoir, but also the variable incorporation of CAIs (Burkhardt et al., 2016).

The Nd isotope compositions of CC parent bodies are poorly understood. This is due to the limited high-precision Nd isotope analyses on CC samples. In addition, no such measurements have been made on equilibrated CC samples. The CK (Karoonda-like) chondrites are the only group of CC with equilibrated representatives at petrologic grades 5 and 6 and thus provide the opportunity to obtain Nd isotope compositions with assured, full access to nucleosynthetic components via traditional acid digestion techniques. While CV (Vigarano-like) chondrites have been the most extensively measured CC for Nd isotope compositions, these measurements have been almost exclusively on the sample Allende, with only two measurements made on non-Allende samples. Because CV

chondrites are a petrologically diverse group (McSween, 1977; Weisberg et al., 2006; Bonal et al., 2020), these Nd isotope analyses may not be representative of the entire CV group.

Open questions remain on the nucleosynthetic Nd isotope makeup of the CV and CK groups. First, do the nucleosynthetic Nd isotope compositions of these groups overlap with those for the other CC groups as well as enstatite and ordinary chondrite groups? If so this would indicate that their feeding zones were composed of the same nebular components as the other groups and any differences were a result of variable mixtures of nucleosynthetic components. At present, the CV Nd isotope data are interpreted to be consistent with this (Boyett and Carlson, 2005; Andreasen and Sharma, 2006; Rankenburg et al., 2006; Carlson et al., 2007; Gannoun et al., 2011b; Burkhardt et al., 2016; Fukai and Yokoyama, 2019) but more analyses need to be performed to further examine this issue. Second, in the CCs as a group, only the CK chondrites have equilibrated samples from petrologic groups 4, 5, and 6, where thermal metamorphism has homogenized samples and no presolar grains remain (Huss and Lewis, 1995; Huss et al., 2006). For these equilibrated CK chondrites, are their nucleosynthetic Nd isotope compositions distinctly different from the unequilibrated CV, CK, and other chondrite groups from petrologic groups 1, 2, and 3? If so, this would imply that these homogenized and equilibrated samples better represent the bulk Nd isotope makeup of their nebular feeding zones than for the unequilibrated samples. In this case, it may be possible that presolar grains in the unequilibrated samples remain poorly accessed for the Nd isotope compositions whereas these have been accessed because of thermal metamorphism in the higher petrological groups. Third, when comparing these CK Nd isotope compositions

to enstatite and ordinary chondrites in all thermal metamorphic grades, do they reveal heterogeneity or homogeneity in the nebular feeding zones for these different parent bodies? These issues have implications for how presolar grains were distributed within the solar nebula before accretion into rocky parent bodies. Finally, taking the Nd isotope compositions of all chondrites, how many nucleosynthetic components can be identified, what are their potential origins, and are there nuances in their compositions that will require additional examination?

In order to address these issues, here, CV and CK chondrites from petrologic grades 3 to 6, the total range of petrologic grades exhibited by these groups, are analyzed for their Nd isotope compositions. In the sections to follow, the mineralogic and isotopic variabilities of these two groups are discussed in the following sections, along with how their Nd isotope compositions compare with other CC groups.

### **3.2 CK and CV Chondrites**

The CK chondrites are highly oxidized meteorites that are dominated by equilibrated (petrologic grade 4-6) samples although some CK3 samples have been identified (Zipfel et al., 2000; Smith and Russell, 2003; Ivanova et al., 2000; 2003; Brandstatter et al., 2003;). The CK chondrites were first defined in Kallemeyn et al. (1991) as having high refractory-lithophile abundances and very low refractory-inclusion abundances. Later studies established that refractory inclusions are susceptible to thermal metamorphism (Greenwood et al., 1992; Russell et al., 1998; Chaumard et al., 2014), and numerous refractory inclusions have since been identified in CK chondrites (Zipfel et al., 2000; Ivanova et al., 2000; Greenwood et al., 2000; Bukovanská et al., 2003;

Smith and Russell, 2003; Brandstätter et al., 2003; Chaumard et al., 2014). Analyses by Greenwood et al. (2010) and Wasson et al. (2013) have also shown a significant overlap between the CV and CK groups in refractory-lithophile abundances.

The CV chondrites are a diverse group of unequilibrated (petrologic grade 3) samples. The CV group contains both reduced and oxidized samples, and the mineralogical variations between these samples may reflect late-stage alteration of the CV parent body (Krot et al., 2004). Typically, CV chondrites contain large ~1 mm chondrules, and abundant refractory inclusions (CAIs and Amoeboid Olivine Aggregates; Weisberg et al., 2006; Scott and Krot, 2014).

Because CK3-4 chondrites share many geochemical and mineralogical similarities with CV3 chondrites (Weisberg et al., 2006), recent studies have argued that the CV-CK clan should be merged into a single group (Greenwood et al. 2010; Wasson et al., 2013; Chaumard et al., 2014; Chaumard and Devouard, 2016). However, one major difference between the CV and CK chondrite groups is the degree of thermal metamorphism that each group has experienced. Greenwood et al. (2010) suggested that CK and CV chondrites may be derived from a single, thermally stratified parent asteroid with CK chondrites representing a progressively thermally altered core and CV chondrites representing the surface of the parent asteroid. However, later work found inconsistencies between the timing of peak metamorphism of CK chondrites and the thermally stratified parent asteroid model (Chaumard and Devouard, 2016). Wasson et al. (2013) suggested that CK chondrites may have formed due to fragmentation and heating during impacts of the CV parent asteroid.

The proposed model of CV and CK chondrites originating from a single parent body was later challenged by varying magnetite and chromium compositions between the two groups. In a study that looked at both equilibrated and non-equilibrated CK chondrites, Dunn et al. (2016) found that magnetites in CK chondrites were compositionally distinct from CV chondrites with respect to  $\text{Cr}_2\text{O}_3$ ,  $\text{NiO}$ , and  $\text{TiO}_2$  abundances. They posited that these compositional differences could not be explained by metamorphism. In later studies, Yin and Sanborn (2019) and Zhu et al. (2020) found that CK and CV chondrites had varying  $^{54}\text{Cr}$  compositions, suggesting these two chondrite groups did not originate from the same parent body. The open question of whether CK and CV chondrites shared a common parent-body source region, coupled with the lack of Nd isotope analyses on CK chondrites leads to the question: do CK and CV chondrites have similar Nd isotope compositions?

### **3.3 Samples**

To answer this question, five CV3 samples, two CK4 samples, two CK5 samples, and two CK6 samples were analyzed for their Nd isotope compositions using Thermal Ionization Mass Spectrometry (Table 3.1). The Nd concentration in CVs is  $0.967 \mu\text{g/g}$  (Burkhardt et al., 2016). To yield sufficient Nd through isotope dilution column chemistry for an effective TIMS measurement,  $\sim 2 \text{ g}$  of each sample was dissolved. LEW 87009 did not have sufficient sample to dissolve  $2 \text{ g}$ . These samples were processed through dissolution and column chemistry and analyzed via Thermal Ionization Mass Spectrometry as detailed in Section 2.6.



**Table 3.1 Sample List**

Sample Name	Class.	Weight	
Allende	CV3	1.86008	g
ALH 84028	CV3	1.89065	g
EET 96026	CV3	1.80838	g
GRA 06101	CV3	1.82549	g
LAR 12002	CV3	1.92218	g
ALH 85002	CK4	1.99415	g
SZA 12420	CK4	1.8572	g
EET 90015	CK5	2.00137	g
EET 92002	CK5	1.99973	g
LAR 06872	CK6	1.86495	g
LEW 87009	CK6	1.64659	g

### 3.4 Results

The Nd isotope compositions for the CV and CK chondrites analyzed in this study are given in Table 3.2. The  $\pm 2\text{SE}$  errors are listed in parentheses after each ratio for each measured run are for the last 2 decimal places in the listed ratios. Sample  $\mu^{\text{i}}\text{Nd}$  values are given in Table 3.3. All  $\mu^{142}\text{Nd}$  values have been corrected for ingrowth of radiogenic  $^{142}\text{Nd}$  as detailed in section 2.6.3. Measured CV3  $\mu^{142}\text{Nd}$  and  $\mu^{145}\text{Nd}$  values are similar to those found in previous studies (Boyet and Carlson, 2005; Andreasen and Sharma, 2006; Rankenburg et al., 2006; Carlson et al., 2007; Gannoun et al., 2011b; Burkhardt et al., 2016; Fukai and Yokoyama, 2019). ALH 84028 (CV3) and LAR 12002 (CV3) have

significantly higher  $\mu^{150}\text{Nd}$  values than other measured CV3 samples, with values of  $169.83 \pm 13.4$  and  $146.95 \pm 13.7$ , respectively. GRA 06101 (CV3) has an anomalously high  $\mu^{148}\text{Nd}$  value of  $53.48 \pm 8.0$ , without a proportional increase in  $\mu^{150}\text{Nd}$ . CK samples show less variation in  $\mu^i\text{Nd}$  values, particularly in r-process  $\mu^{148}\text{Nd}$  and  $\mu^{150}\text{Nd}$ . CK  $\mu^{148}\text{Nd}$  values vary from  $0.49 \pm 17.9$  to  $31.2 \pm 7.7$  and  $\mu^{150}\text{Nd}$  values vary from  $10.39 \pm 10.3$  to  $42.53 \pm 10.6$ . These values are similar to non-anomalous CV3 samples.

**Table 3.2** Measured Nd Ratios for CV and CK Chondrites. The  $\pm 2\text{SE}$  errors are listed in parentheses as the last two decimal places for each ratio.

Sample	Cycles	$^{142}\text{Nd}/^{144}\text{Nd}$	$^{143}\text{Nd}/^{144}\text{Nd}$	$^{145}\text{Nd}/^{144}\text{Nd}$	$^{148}\text{Nd}/^{144}\text{Nd}$	$^{150}\text{Nd}/^{144}\text{Nd}$
Allende	110	1.141793 (7)	0.512592 (4)	0.348403 (2)	0.241583 (2)	0.236472 (4)
ALH 84028	90	1.141808 (7)	0.512664 (3)	0.348406 (2)	0.241586 (2)	0.236493 (3)
EET 96026	70	1.141804 (6)	0.512625 (4)	0.348404 (2)	0.241584 (3)	0.236460 (4)
LAR 12002	90	1.141793 (7)	0.512624 (4)	0.348409 (2)	0.241589 (2)	0.236488 (3)
GRA 06101	110	1.141787 (8)	0.512547 (3)	0.348403 (2)	0.241594 (2)	0.236466 (3)
SZA 12420	110	1.141801 (7)	0.512697 (4)	0.348403 (2)	0.241582 (2)	0.236462 (3)
ALH 85002	90	1.141797 (7)	0.512594 (3)	0.348404 (2)	0.241582 (2)	0.236456 (2)
EET 92002	60	1.141779 (5)	0.512470 (3)	0.348404 (1)	0.241587 (1)	0.236463 (3)
EET 90015	40	1.141813 (16)	0.512768 (6)	0.348407 (3)	0.241581 (4)	0.236456 (6)
LAR 06872	140	1.141794 (6)	0.512533 (3)	0.348405 (2)	0.241589 (2)	0.236460 (3)
LEW 87009	40	1.141813 (10)	0.512600 (4)	0.348402 (3)	0.241586 (4)	0.236462 (6)

**Table 3.3** The Nd Isotope Compositions of CK and CV chondrites. Errors for each sample are given as  $\pm 2\text{SE}$ . Errors for group averages are given as the 95% confidence intervals.

Sample	$\mu^{142}\text{Nd}_{\text{corr.}}$	$\pm 2\text{SE}$	$\epsilon^{143}\text{Nd}$	$\pm 2\text{SE}$	$\mu^{145}\text{Nd}$	$\pm 2\text{SE}$	$\mu^{148}\text{Nd}$	$\pm 2\text{SE}$	$\mu^{150}\text{Nd}$	$\pm 2\text{SE}$
Allende	-32.38	6.4	-0.90	0.07	0.89	5.9	5.71	7.9	79.79	16.4
ALH 84028	-23.10	6.1	0.51	0.07	10.39	5.7	20.77	9.6	169.83	13.4
EET96026	-24.19	5.3	-0.25	0.08	2.21	5.6	10.34	10.3	27.60	19.6
LAR 12002	-34.23	6.6	-0.28	0.07	16.62	5.0	30.50	9.5	146.95	13.7
GRA 06101	-35.07	6.8	-1.78	0.07	-0.06	5.1	53.48	8.0	51.92	12.5
CV Average	-29.42	4.6 (CI)	-0.56	0.06 (CI)	6.18	5.3 (CI)	24.70	21.8 (CI)	99.60	129.4 (CI)
SZA 12420	-30.49	6.2	1.16	0.08	0.43	4.3	4.84	7.7	36.48	14.3
ALH 85002	-29.15	6.0	-0.85	0.06	4.05	5.0	2.81	8.0	10.39	10.3
EET 92002	-38.78	4.7	-3.28	0.05	4.51	3.9	22.72	4.6	42.53	10.6
EET 90015	-23.52	13.8	2.53	0.11	13.06	7.7	0.49	17.9	11.19	26.2
LAR 06872	-28.55	5.5	-2.05	0.06	5.83	4.3	31.62	7.7	27.30	14.0
LEW 87009	-15.65	8.8	-0.73	0.08	-3.44	8.0	17.88	15.9	38.77	25.3
CK Average	-29.36	5.6 (CI)	-0.97	0.12 (CI)	3.99	2.9 (CI)	15.50	11.1 (CI)	27.97	23.2 (CI)

**Table 3.4** Average Nd isotope compositions for CC groups. Errors are given as the 95% confidence intervals.

	$\mu^{142}\text{Nd}_{\text{corr.}}$	$\pm \text{CI}$	$\mu^{145}\text{Nd}$	$\pm \text{CI}$	$\mu^{148}\text{Nd}$	$\pm \text{CI}$	$\mu^{150}\text{Nd}$	$\pm \text{CI}$
<b>CI1</b>	-19.9	5.0	-0.1	6.7	0.5	1.6	-1.3	20.5
<b>CM</b>	-28.4	5.2	6.1	1.3	21.5	3.6	26.7	14.8
<b>CO</b>	-21.4	6.1	6.5	3.6	15.0	5.2	19.4	12.8
<b>CV</b>	<b>-29.1</b>	1.9	<b>3.9</b>	1.7	<b>10.6</b>	5.9	<b>34.4</b>	36.0
<b>CK</b>	<b>-29.4</b>	5.6	<b>4.0</b>	2.9	<b>15.5</b>	11.1	<b>28.0</b>	23.2

### 3.4.1 Group Averages

Carbonaceous chondrite  $\mu\text{Nd}$  weighted averages are given in Table 3.4. The CO3 sample NWA 2090 from Fukai and Yokoyama (2017) was excluded as it deviated away from the Sm/Nd isochron. The CR2 sample NWA 6043 from Saji et al. (2020) was also removed from the group average due to their assessment of possible column chemistry fractionation, although this is discussed in detail in section 3.5.5. The CK Nd

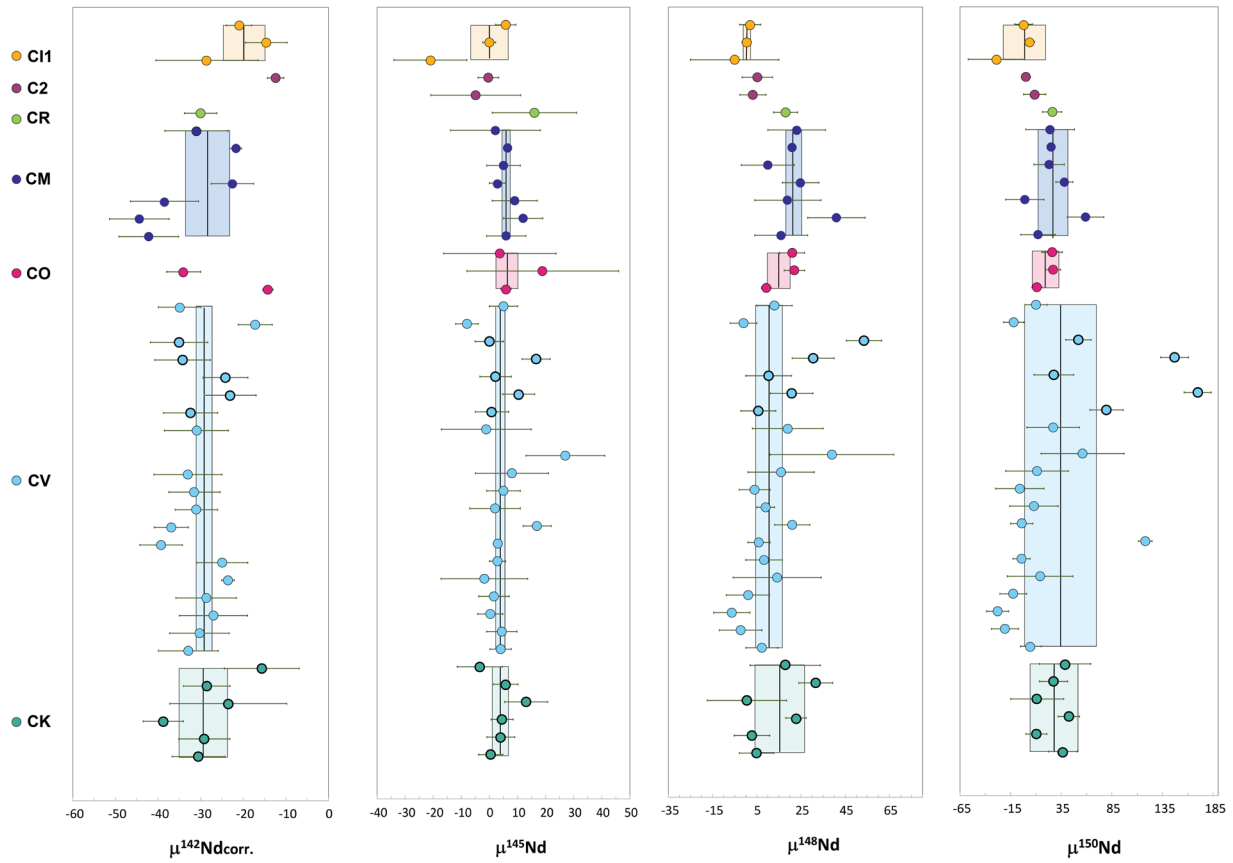


**Figure 3.1** The Nd Isotope compositions of CK, CV, CO, CM, CR, C2, and C11 chondrites (Table C.1). The CK and CV samples from this study are shown with a bolded outline. Error bars for each sample are given as 2SE (SE = standard error = standard deviation/ $\sqrt{n}$  in which n is the number of cycles per sample measurement. For chondrite groups with 3 or more samples, weighted averages of the group have been calculated and are shown as black lines. The 95% confidence interval of each weighted average measurement is shown as a gray box.

weighted averages are consistent with CV weighted averages, with differences of  $\Delta\mu^{142}\text{Nd}_{\text{corr.}} = 0.3$ ,  $\Delta\mu^{145}\text{Nd} = 0.1$ ,  $\Delta\mu^{148}\text{Nd} = 4.9$ , and  $\Delta\mu^{150}\text{Nd} = 6.4$ . CM group averages are within the CK average confidence intervals for  $\mu^{142}\text{Nd}_{\text{corr.}}$ ,  $\mu^{145}\text{Nd}$ ,  $\mu^{148}\text{Nd}$ , and  $\mu^{150}\text{Nd}$ . The CO group weighted average has an overlapping confidence interval with the CK group for  $\mu^{142}\text{Nd}_{\text{corr.}}$ , while CO  $\mu^{145}\text{Nd}$ ,  $\mu^{148}\text{Nd}$ , and  $\mu^{150}\text{Nd}$  weighted averages are within the CK confidence interval. and CR, CI1, and C2 group weighted averages are outside of the CK average confidence interval. This trend in similarity, CV being the most similar, then CM and CO, is consistent with previous studies on different isotopic systems (Warren et al., 2011; Fukai and Yokoyama, 2019). The CV3  $\mu^{148}\text{Nd}$  and  $\mu^{150}\text{Nd}$  data do not cluster near the average similar to other CC groups, as multiple CV3 samples have significant r-excess anomalies.

### 3.5 Discussion

#### 3.5.1 CK Nd Compositions Average Nd isotope compositions for CV and CK

chondrites are indistinguishable within error (Figure 3.1) indicating that Nd presolar carriers were homogeneously distributed amongst these two similar parent bodies. The CK chondrites show r-excess nucleosynthetic anomalies across all metamorphic grades (Figure 3.2). The Nd isotope compositions of these samples are generally consistent with unequilibrated CC samples, indicating that the carrier phases for Nd in unequilibrated samples are being fully accessed through traditional digestion techniques.

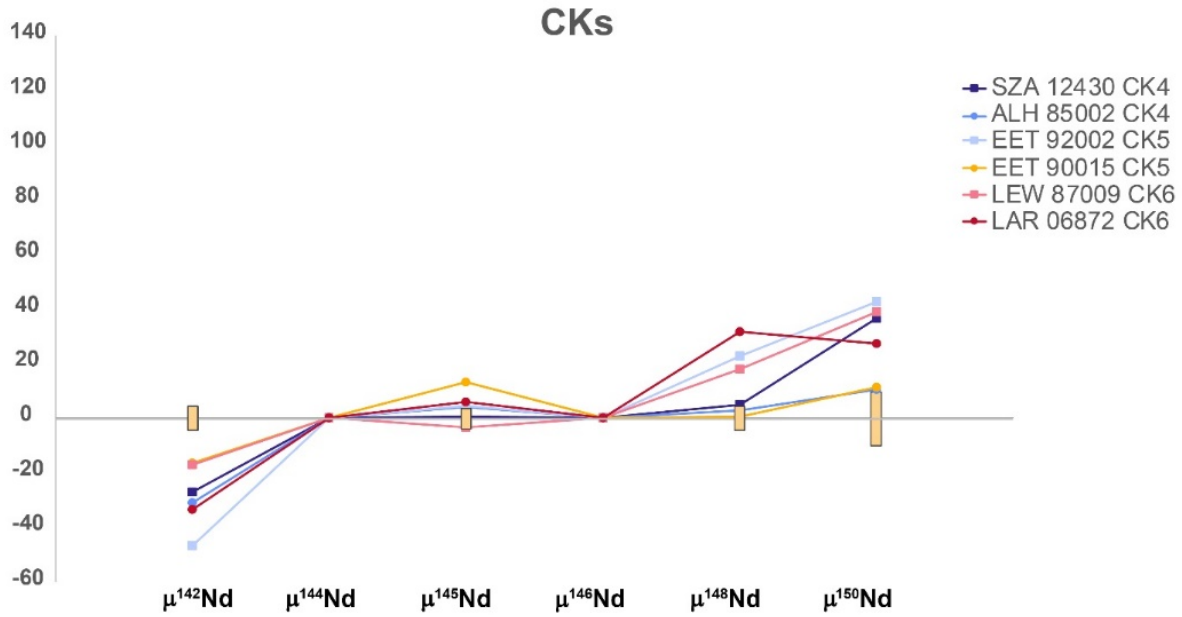


**Figure 3.2** The Nd isotope compositions of bulk CK samples relative to the JNdi standard with 2SD shown in yellow bars. All CK samples show deficits in  $\mu^{142}\text{Nd}$ , and excesses in  $\mu^{148}\text{Nd}$  and  $\mu^{150}\text{Nd}$ . There are no consistent isotopic trends in relation to petrologic grade.

### 3.5.2 CC Group Variations

The small ( $n < 7$ ) sample size for CC groups, other than the CV group, causes unresolvable differences in Nd isotopes. A plot of  $\mu^{145}\text{Nd}$  vs.  $\mu^{142}\text{Nd}_{\text{corr}}$  show that CK and CV chondrites plot in the same location for these isotopes (Figure 3.3). The deviation of CCs away from the stellar-predicted s-deficit line is influenced by the mixing of CAIs into the CC reservoir (Burkhardt et al., 2016). Plots of  $\mu^{150}\text{Nd}$  vs.  $\mu^{142}\text{Nd}_{\text{corr}}$  do not show as close of a correlation between CK and CV chondrites (Figure 3.4), although differences are not resolvable. Both CK and CV chondrites have variable  $\mu^{150}\text{Nd}$  anomalies, causing large error bars. On the  $\mu^{148}\text{Nd}$  vs.  $\mu^{145}\text{Nd}$  plot (Figure 3.5), the CK chondrite group is not resolvable from any CC group other than CI chondrites. The CV and CM chondrites are resolvable for this isotope pair.

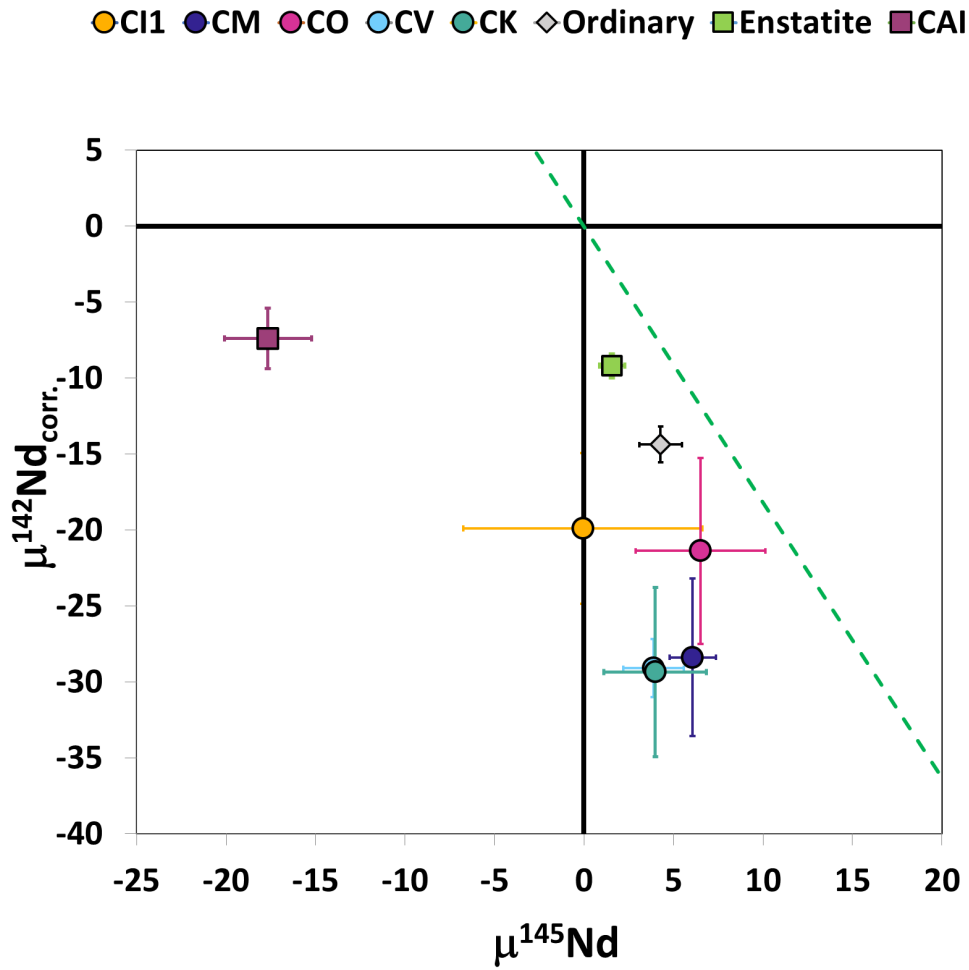


**Figure 3.3** Weighted average  $\mu^{145}\text{Nd}$  vs.  $\mu^{142}\text{Nd}_{\text{corr.}}$  values for carbonaceous chondrite groups and the enstatite and ordinary chondrite classes. Error bars show the 95% confidence interval for each group average. The s-deficit relationship predicted by the stellar model is shown as a dashed green line. Carbonaceous chondrite groups plot away from the stellar-model line toward the CAI group average.

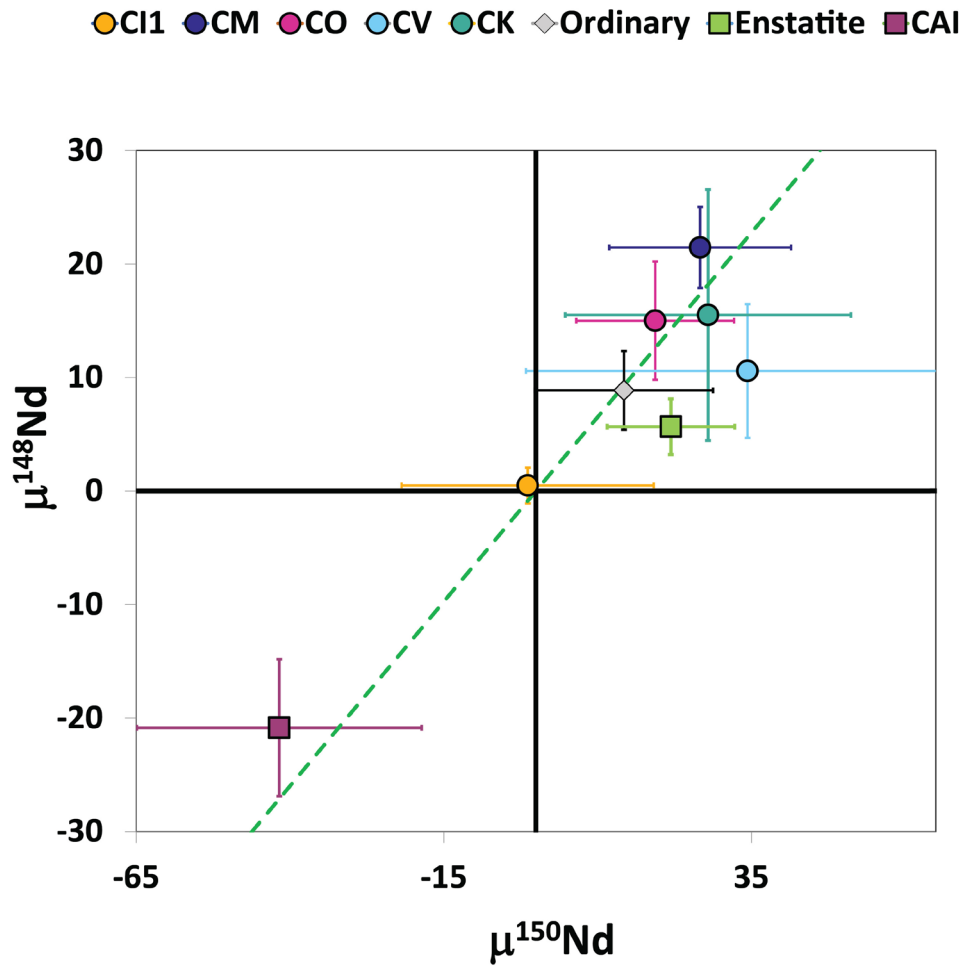


**Figure 3.4** Weighted average  $\mu^{150}\text{Nd}$  vs.  $\mu^{148}\text{Nd}$  values for carbonaceous chondrite groups and the enstatite and ordinary chondrite classes. Error bars show the 95% confidence interval for each group average. The s-deficit relationship predicted by the stellar model is shown as a dashed green line. CK group averages are not resolvable from any other carbonaceous chondrite group for this isotope pair. Despite large errors, CI1 chondrites plot closest to the terrestrial standard.



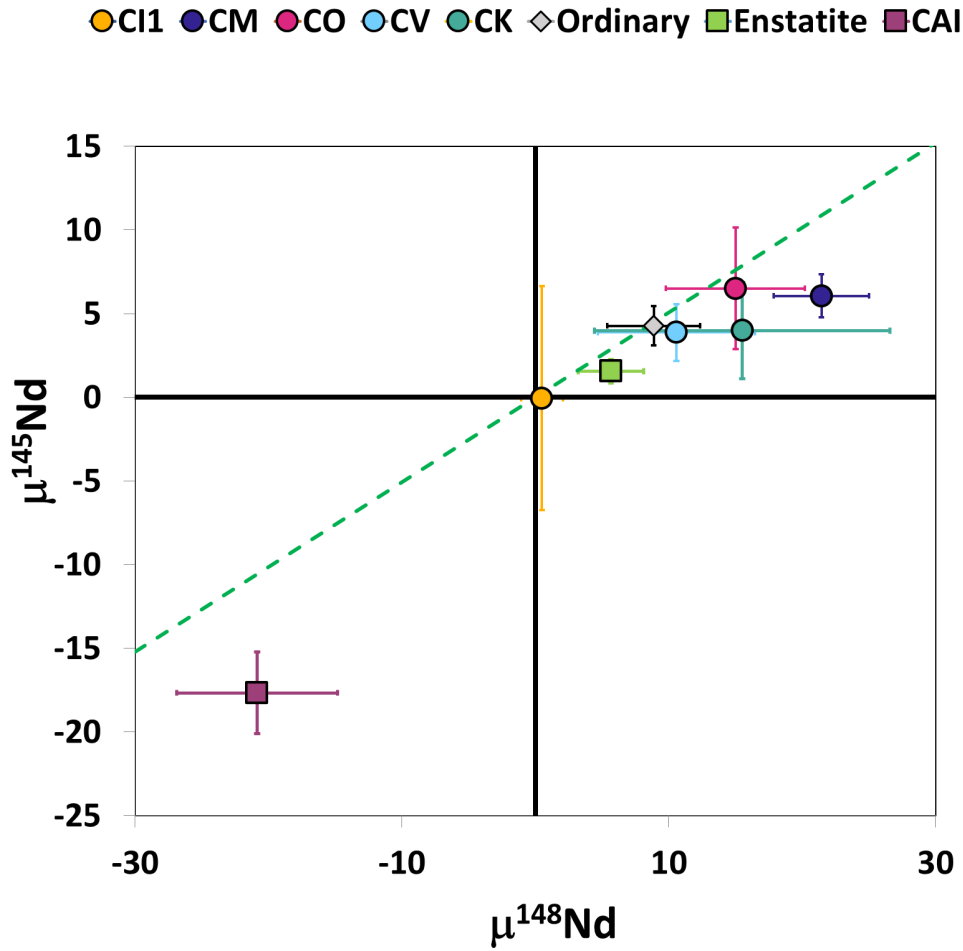


**Figure 3.5** Weighted average  $\mu^{148}\text{Nd}$  vs.  $\mu^{145}\text{Nd}$  values for carbonaceous chondrite groups and the enstatite and ordinary chondrite classes. The s-deficit relationship predicted by the stellar model is shown as a dashed green line. Error bars show the 95% confidence interval for each group average. The CK group averages are not resolvable from any other carbonaceous chondrite group for this isotope pair. The CV and CM chondrite groups are resolvable. Despite large errors, CI1 chondrites plot closest to the terrestrial standard.

When comparing two s-process dominated isotopes,  $^{142}\text{Nd}$  and  $^{54}\text{Cr}$ , carbonaceous and non-carbonaceous samples show the same bimodality (Figure 3.6) that influenced the original division of 'carbonaceous' and 'non-carbonaceous' chondrites

(Warren, 2011). In this case, CV and CM chondrites are the most similar, although none of the CC groups except for the CI group are truly resolvable from each other.

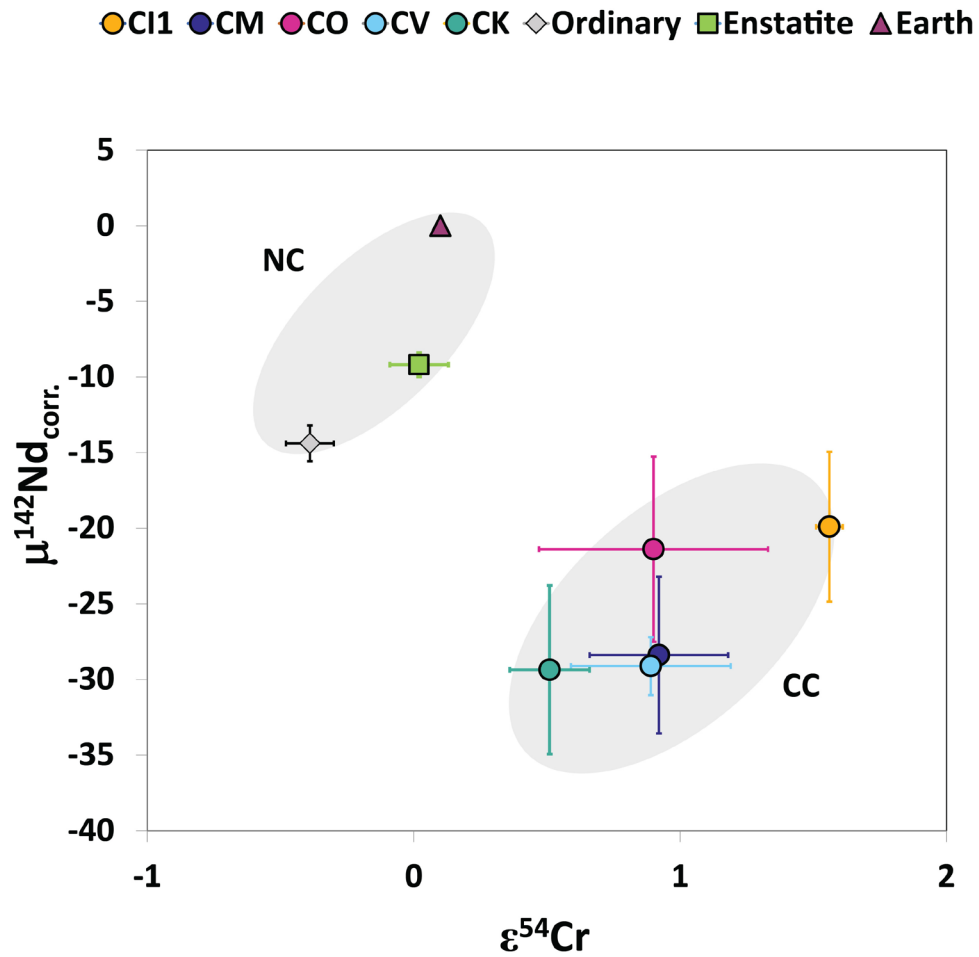


**Figure 3.6** Weighted average  $\epsilon^{54}\text{Cr}$  vs.  $\mu^{142}\text{Nd}_{\text{corr.}}$  values for carbonaceous chondrite (CC) vs. non-carbonaceous (NC) chondrites. The  $^{54}\text{Cr}$  data is referenced from Zhu et al. (2021). Error bars show the 95% confidence interval for each group average.

### 3.5.3 The Role of CAIs in CK and CV Chondrites

Calcium-aluminum-rich inclusions from Allende have large deficits in r-process  $\mu^{148}\text{Nd}$ , with values that range from -49.7 to 1.9, and even larger deficits in  $\mu^{150}\text{Nd}$ , with values that range from -118 to 41.9 (Figure 3.7). Eighty-eight percent of the CAIs measured have negative  $\mu^{150}\text{Nd}$  values. Although CAIs have uncorrected  $\mu^{142}\text{Nd}$  values that vary from -65.7 to 60.6, corrected  $\mu^{142}\text{Nd}$  values are less variable, ranging from -27.2 to 7.4. The abundances (area %) of CAIs in CKs range from 0% to 16.4%, with an average of 4%. There is a correlation between decreasing CAI modal abundance and increasing petrologic grade in CK chondrites (Chaumard, et al., 2014). Modal abundances in CV chondrites range from 0.65% to 13.1% with an average of 10% (May et al., 1999; Chaumard et al., 2014; Scott and Krot, 2014). The variations in CAI abundances between CV and CK chondrites are thought to be due to the CK metamorphic event leading to re-equilibration of CK-hosted CAIs with their host matrix (Chaumard et al., 2014). The CK5 and CK6 chondrites have the lowest abundances of CAIs, with one sample that has been analyzed for its Nd isotope composition, LEW 87009, having no recorded CAIs. Yet these low-CAI samples show no systematic shift towards higher  $\mu^{145}\text{Nd}$ ,  $\mu^{148}\text{Nd}$ , or  $\mu^{150}\text{Nd}$  values, indicating that their Nd isotope compositions are likely still controlled by the r-process deficits of now equilibrated CAIs. This supports the proposal that the lack of CAIs in these samples is due to their re-equilibration, rather than that the CK parent body didn't collect a similar abundance of CAIs during accretion.

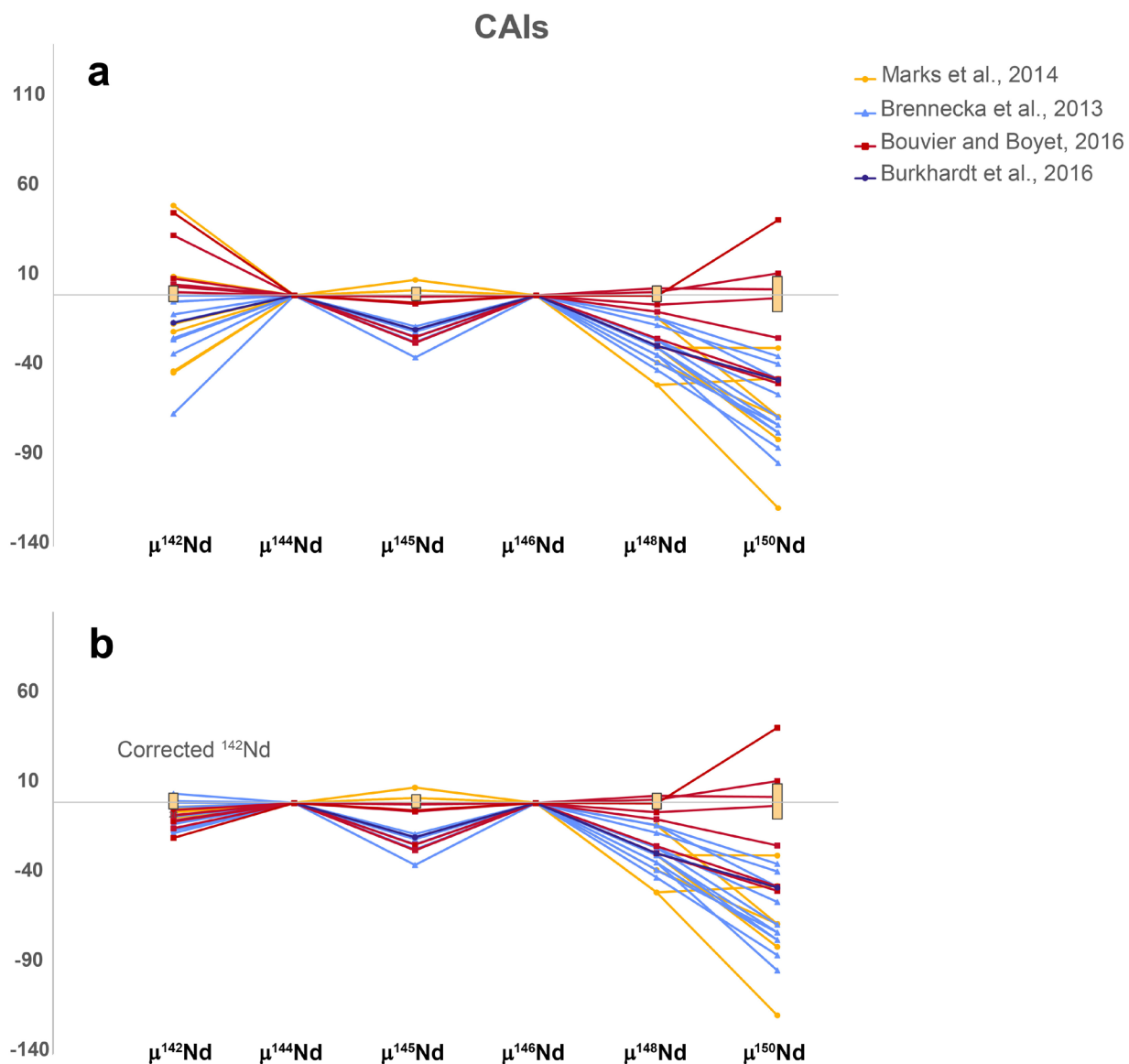


**Figure 3.7 (a)** Nd isotope compositions of bulk CAIs and CAI mineral components relative to the JNdi standard with 2SD shown in yellow bars. **(b)**  $\mu^{142}\text{Nd}$  has been corrected for ingrowth of radiogenic  $^{142}\text{Nd}$ . CAIs show large deficits in  $\mu^{148}\text{Nd}$  and  $\mu^{150}\text{Nd}$ . Although CAIs have a wide range of uncorrected  $\mu^{142}\text{Nd}$  values, corrected  $\mu^{142}\text{Nd}$  values have a much smaller range.

### 3.5.4 The Heterogeneity of Nd Isotopes in Allende

Heterogeneously mixed s- and r-process Nd carrier phases in nebular feeding zones may account for the isotopic variations seen in different chondrite groups. However, heterogeneously mixed r-process Nd carrier phases at a microscopic scale are required to explain the resolvable differences seen for  $^{148}\text{Nd}$  and  $^{150}\text{Nd}$  in different aliquots of single CV3 chondrites. For Allende, corrected values for  $\mu^{142}\text{Nd}$  range from -23.6 to -39.3 while values for  $\mu^{148}\text{Nd}$  range from -8.28 to 19 and  $\mu^{150}\text{Nd}$  range from -25.38 to 118. Allende  $\mu^{150}\text{Nd}$  values vary almost 10 times that of corrected  $\mu^{142}\text{Nd}$  values. CV3 samples ALH 84028 and LAR 12002, along with CK4 sample SZA 12420 have displayed the anomalous  $\mu^{150}\text{Nd}$  excess that some Allende aliquots show. Potential causes for these  $\mu^{150}\text{Nd}$  excesses are discussed in the following sections.

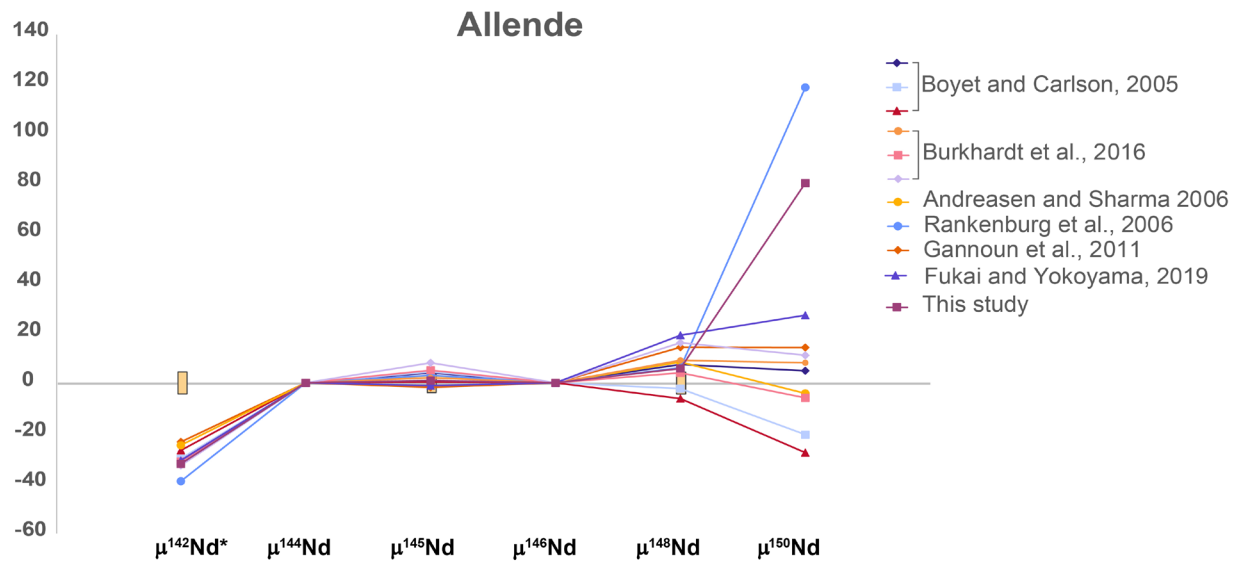


**Figure 3.8** Nd isotope compositions of bulk Allende samples relative to the JNdi standard with 2SD shown in yellow bars.  $^{142}\text{Nd}$  has been corrected for radiogenic ingrowth. Allende samples have deficits in  $\mu^{142}\text{Nd}_{\text{corr}}$ , while  $\mu^{148}\text{Nd}$  and  $\mu^{150}\text{Nd}$  exhibit a wide range of deficits and excesses.

### 3.5.5 Excess $^{150}\text{Nd}$ in Solar System Materials

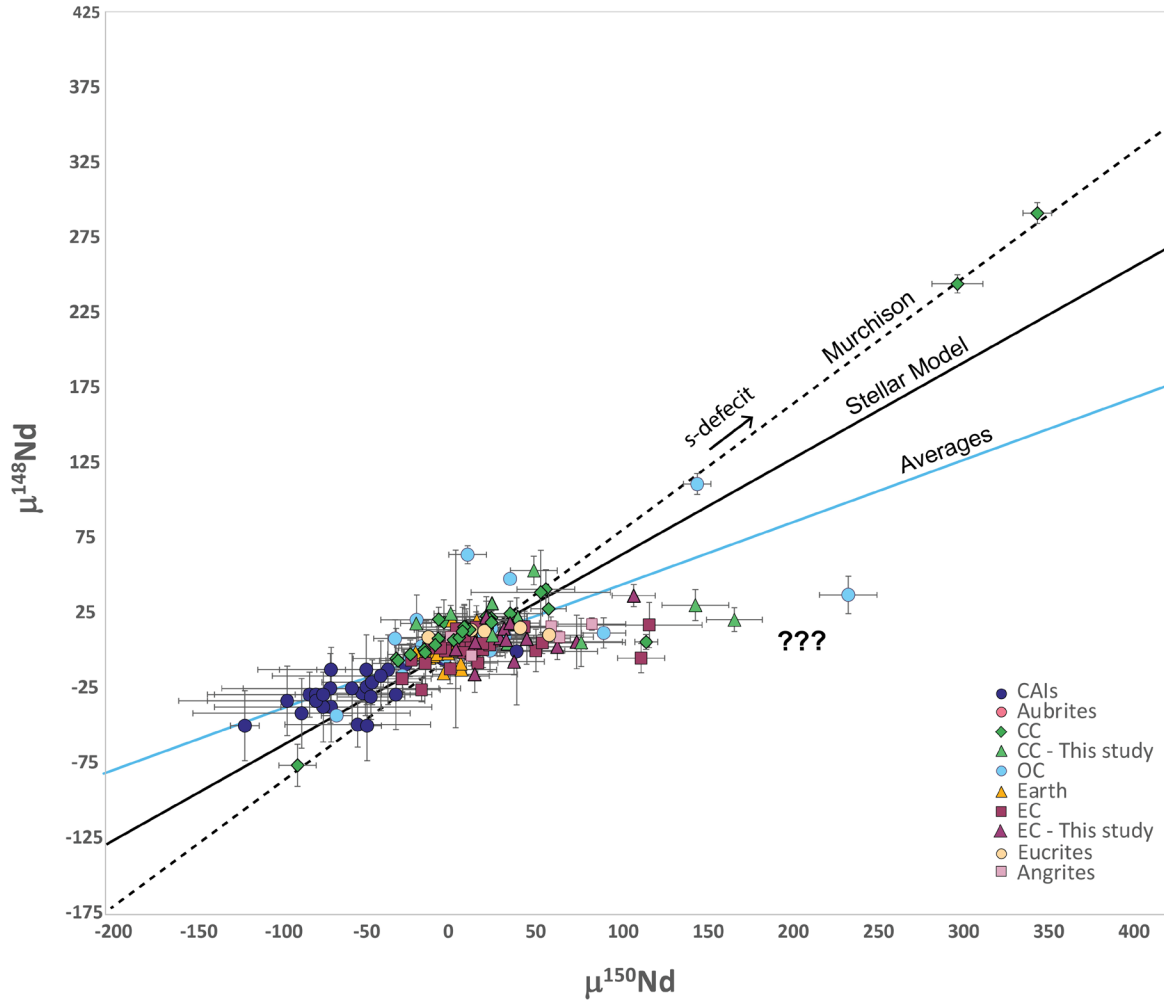


**Figure 3.9**  $\mu^{150}\text{Nd}$  vs.  $\mu^{148}\text{Nd}$  measured in CAIs, carbonaceous chondrites (CC), ordinary chondrites (OC), Earth, enstatite chondrites (EC), Eucrites, and Angrites. Error bars are given as 2SE. The s-deficit relationship predicted by the Murchison model is shown as a black dashed line. The stellar model is shown as a black solid line. The trendline for chondrite-class averages is shown as a light blue solid line. Numerous samples plot away from model-predicted s-deficit lines.

Three CV3, one CK4, one EH4, one EH4/5, and one EL3 sample evaluated in this study have an anomalous r-process signature with substantial excess  $\mu^{150}\text{Nd}$  without the expected increase in  $\mu^{145}\text{Nd}$  and  $\mu^{148}\text{Nd}$  based on stellar models (Figure 3.9). Some studies have noted individual samples with excess  $\mu^{150}\text{Nd}$  (Boyet and Gannoun, 2013;

Bouvier and Boyet, 2016). Other studies have suggested this excess as an analytical artifact (Carlson et al., 2007) likely due to contamination with the  $^{150}\text{Nd}$  spike used across various laboratories. Other studies have suggested that excess  $\mu^{150}\text{Nd}$  seen within their data is due to static TIMS collection of  $^{150}\text{Nd}$  (Render and Brennecka, 2021). To investigate potential causes of this excess, the Nd isotope compositions of chondrites, angrites, eucrites, and CAIs (Table C.2) that have been evaluated to date were compared, and significant trends in data were evaluated.

### 3.5.5.1 150-x Sample Summary

Samples with a substantial excess in  $\mu^{150}\text{Nd}$  are characterized by  $^{150}\text{Nd}:^{148}\text{Nd}$  ratios of  $\sim 6:1$  and  $^{150}\text{Nd}:^{145}\text{Nd}$  ratios of  $\sim 8:1$ . These samples form a continuous  $\mu^{150}\text{Nd}$  vs.  $\mu^{148}\text{Nd}$  line with samples that have deficits in  $\mu^{150}\text{Nd}$  but have the same  $^{150}\text{Nd}:^{148}\text{Nd}$  and  $^{150}\text{Nd}:^{145}\text{Nd}$  ratios. We have called the  $^{150}\text{Nd}$  vs.  $^{148}\text{Nd}$  line that these samples lie on the 150-x line (Figure 3.10), and have used these samples to evaluate potential causes of excess  $^{150}\text{Nd}$  in solar system materials that are more isotopically similar to stellar predictions. The samples on the 150-x line (Table 3.5) range across multiple chondrite groups, include multiple CAIs, and may include angrites and eucrites. Within the included chondrite groups, samples span a range of petrologic grades (3-6). Samples on this line span multiple, independent laboratories, using different generations of Triton TIMS.

As the least abundant isotope measured,  $^{150}\text{Nd}$  analyses have the largest errors. This issue is compounded by  $^{150}\text{Nd}$  being collected on the most peripheral cups, with two mass units between  $^{150}\text{Nd}$  and the next measured isotope,  $^{148}\text{Nd}$ . Many of the samples on the 150-x line were collected in traditional ‘static’ mode in which  $^{150}\text{Nd}$  was collected in one cup, creating potential biases. All Nd isotopes from this study were

**Table 3.5 List of Samples used to evaluate the anomalous 150 excess (150-x) line**

<b>Sample</b>	<b>Class.</b>	<b>Nd Isotope Study</b>	<b>Machine</b>	<b><sup>150</sup>Nd Mode</b>
Ucera	H5	Carlson et al., 2007	DTM Triton	Static
St. Severin	LL6	Andreasen & Sharma, 2006	Dartmouth Triton	Static
ALH 77295	EH3	Bouvier & Boyet, 2016	LMV Triton	Static
Sahara 97158	EH3	Gannoun et al., 2011b	LMV Triton	Static
EET 88746	EH4	This Study	UH Triton Plus	Multistatic
EET 96135	EH4/5	This Study	UH Triton Plus	Multistatic
MAC 02839	EL3	This Study	UH Triton Plus	Multistatic
MAC 02839	EL3	Bouvier & Boyet, 2016	LMV Triton	Static
MAC 02837	EL3	Bouvier & Boyet, 2016	LMV Triton	Static
PCA 91020	EL3	This Study	UH Triton Plus	Multistatic
Hvittis	EL6	Gannoun et al., 2011b	LMV Triton	Static
ALH 84028	CV3	This Study	UH Triton Plus	Multistatic
LAR 12002	CV3	This Study	UH Triton Plus	Multistatic
Allende	CV3	This Study	UH Triton Plus	Multistatic
Allende	CV3	Rankenburg et al., 2006	JSC Triton	Static
SZA 12420	CK4	This Study	UH Triton Plus	Multistatic
ADOR*	Angrite	Render & Brennecka, 2021	IPM Triton Plus	Static
NWA 4590*	Angrite	Render & Brennecka, 2021	IPM Triton Plus	Static
NWA 4801*	Angrite	Render & Brennecka, 2021	IPM Triton Plus	Static
Millbillillie*	Eucrite	Render & Brennecka, 2021	IPM Triton Plus	Static
CAI 164	CAI	Brennecka et al., 2013	LLNL Triton	Multidyn
CAI 168	CAI	Brennecka et al., 2013	LLNL Triton	Multidyn
CAI 171	CAI	Brennecka et al., 2013	LLNL Triton	Multidyn
CAI 172	CAI	Brennecka et al., 2013	LLNL Triton	Multidyn
pyx	CAI cut	Marks et al., 2014	LLNL Triton	Multidyn
d>3.26	CAI cut	Marks et al., 2014	LLNL Triton	Multidyn
d<3.26	CAI cut	Marks et al., 2014	LLNL Triton	Multidyn
Mel pyx	CAI cut	Marks et al., 2014	LLNL Triton	Multidyn
CAI NWA 6991 B4 fass-R	CAI cut	Bouvier & Boyet, 2016	LMV Triton	Static

collected in multistatic mode, such that <sup>150</sup>Nd was collected in two cups, and each amplifier was rotated between measurements to cancel out amplifier bias. Further, samples from this study had no reverse fractionation which could contribute additional



erroneous results (Andreasen and Sharma, 2006). Calcium-aluminum-rich inclusions from Brennecka et al. (2013) and Marks et al. (2014) were measured with a 2 line multidynamic technique. With multiple samples on the 150-x line having been run in multi-static and multi-dynamic mode cup and amplifier bias from running samples in static mode doesn't appear to be a primary contributing factor to the observed excess  $^{150}\text{Nd}$ .

### 3.5.5.2 Data Evaluation

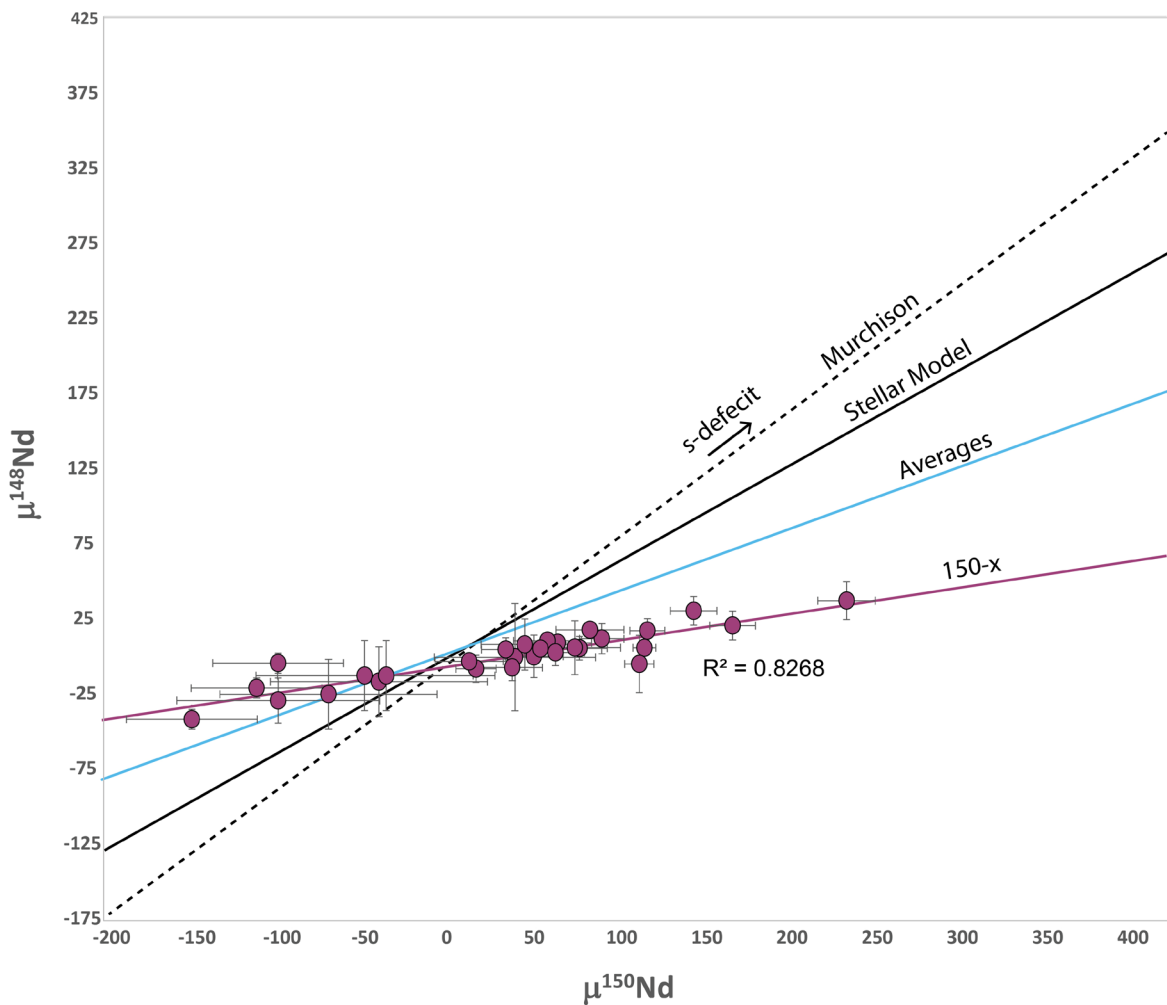
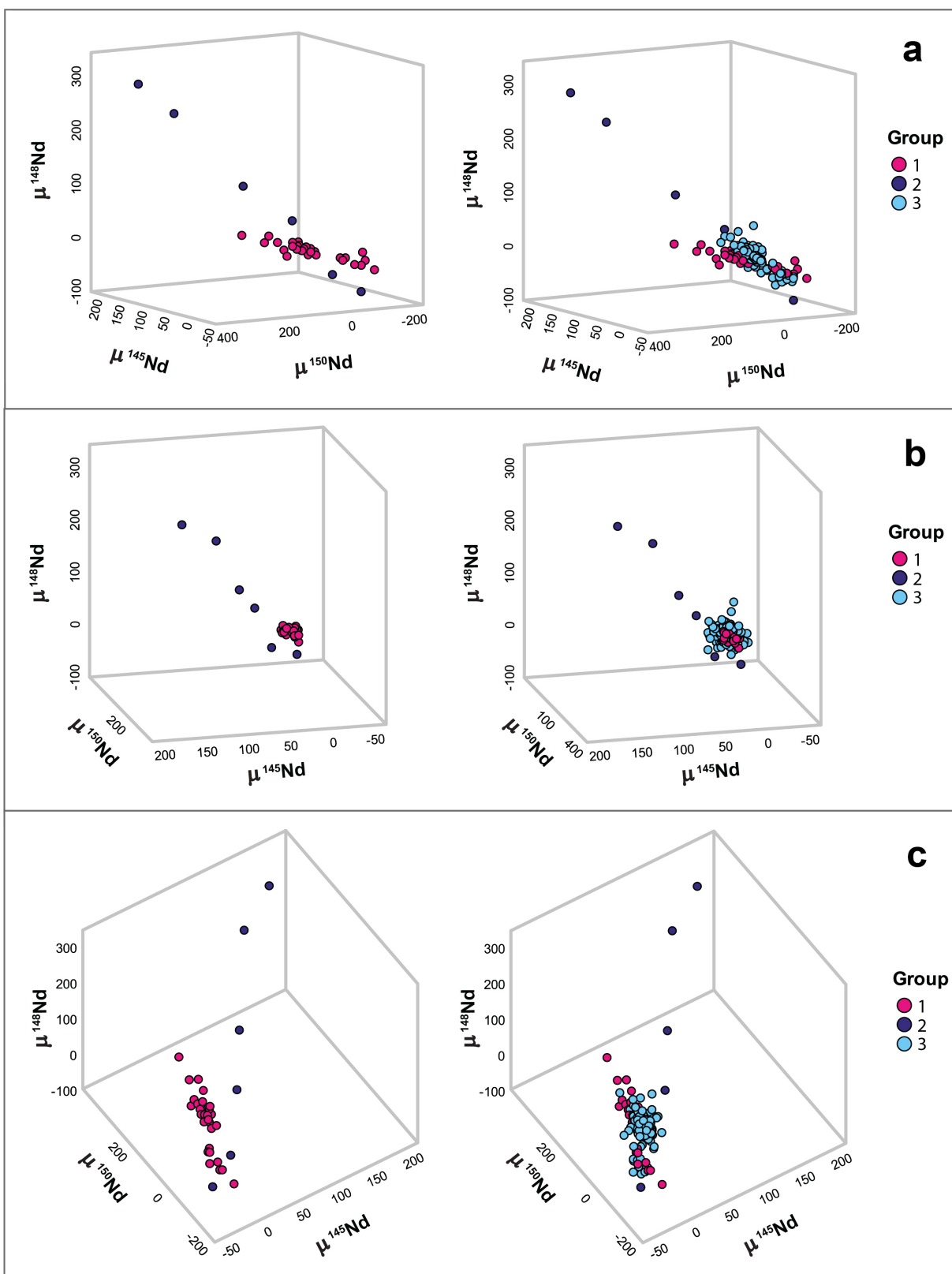


**Figure 3.10** Samples used to evaluate the 150-x line. Samples are shown as purple circles. Error bars are given as 2SE. The 150-x trendline ( $R^2 = 0.8262$ ) is shown as a purple solid line. The s-deficit relationship predicted by the Murchison model is shown as a black dashed line. The Stellar model is shown as a black solid line. The trendline for chondrite-class averages is shown as a light blue solid line.

Although seven samples on the 150-x line have errors that overlap with the Stellar and Murchison models for  $\mu^{148}\text{Nd}$  vs.  $\mu^{150}\text{Nd}$  in Figure 3.7, these samples follow a different  $\mu^{145}\text{Nd}$  vs.  $\mu^{150}\text{Nd}$  trend than the Stellar and Murchison models. Because r-process nucleosynthesis is the dominant production source in three Nd isotopes, not just two, 3D plots can offer additional insights into isotopic trends that traditional 2D plots are unable to achieve.

Samples that have been analyzed for high-precision Nd thus far, with reliable  $\mu^{145}\text{Nd}$ ,  $\mu^{148}\text{Nd}$ , and  $\mu^{150}\text{Nd}$  values, were plotted on 3D plots (Figure 3.11). Each plot has the same axes, viewed at different angles, with  $\mu^{150}\text{Nd}$  on the x-axis,  $\mu^{148}\text{Nd}$  on the y-axis, and  $\mu^{145}\text{Nd}$  on the z-axis. Samples were divided into 3 groups. Group 1 includes samples on the 150-x line. Group 2 includes the Murchison and QUE 97008 leachates from Qin et al. (2011). In this model, this group is representative of the typical s-deficit lines in 2D diagrams. Murchison- and Stellar-model lines are similar, although not identical, for all three isotopes. Group 3 includes the remaining cluster of samples.

**Figure 3.11 (on following page)**  $\mu^{150}\text{Nd}$  vs.  $\mu^{148}\text{Nd}$  vs.  $\mu^{145}\text{Nd}$  for solar system materials. Samples with anomalous  $\mu^{150}\text{Nd}$  values are shown in pink as Group 1. Leachate, residue, and whole-rock analyses of Murchison and QUE 97008 are shown in dark blue as Group 2. In this model these samples are representative of typical stellar model predicted relationships. All other samples are shown in light blue as Group 3. Group 1 data follows a substantially different slope in 3D space than Group 2 data.



Group 1 data follows a substantially shallower  $\mu^{150}\text{Nd}$  vs.  $\mu^{148}\text{Nd}$  slope than Group 2 data, while maintaining a more narrow range of  $\mu^{145}\text{Nd}$  vs.  $\mu^{148}\text{Nd}$  values than the remaining cluster of Group 3. Group 1 data is not widely scattered and follows a distinct, clustered line in 3D space. This 3D analysis also allowed for additional samples from the Group 3 cluster to be identified as Group 1 (Table 3.6). Because Group 1 data does not follow stellar-predicted relationships for  $\mu^{145}\text{Nd}$  and  $\mu^{148}\text{Nd}$  vs.  $\mu^{150}\text{Nd}$ , a non-nucleosynthetic origin is investigated for these relationships in the following sections.

### **3.5.5.3 Assessing Potential Nuclear Field Shift Effects**

When Nd isotope measurements of chondritic samples have been corrected for radiogenic ingrowth and mass-dependent fractionation from thermal ionization, and still do not correlate with predicted nucleosynthetic relationships, the next potential cause of isotopic anomalies to explore is mass-independent fractionation. Nuclear field shift effects induced by laboratory-scale chemical exchange reactions have become an increasing concern in the interpretation of high-precision isotope data (Fujii et al., 2009).

Nuclear field shift effects are caused predominately by differences in the nuclear size of isotopes. Nuclear shapes also have a small effect (Yang and Liu, 2016). There is a transition from more spherical to deformed nuclei that occurs between neutron numbers  $N = 88$  and  $N = 90$  (Saksena et al., 1969; King, 1984; Fuji et al., 2009). This transition, which occurs over  $^{148}\text{Nd}$ - $^{150}\text{Nd}$ , is strongly influenced by mass-independent fractionation during solvent extraction (Fujii et al., 1998; 1999; 2000; 2009). Nuclear field shift effects may also occur in the high-temperature environment of the early solar nebula (Fujii et al., 2006; Moynier et al., 2009; 2013). The interaction of condensing material with nebular

gas could fractionate the condensing material, which is then heterogeneously dispersed across the protoplanetary disk. This was previously suggested as the cause of Te isotope anomalies in CAIs (Moynier et al., 2009).

Recent studies have shown that the traditional column chemistry used in processing Nd in chondrites can induce nuclear field shift effects in progressive elutions of standards (Wakaki and Tanaka, 2012; Saji et al., 2016; Garçon et al., 2018). However, standards from Wakaki and Tanaka (2012) showed no resolvable differences in Nd isotope compositions between standards not run through column chemistry and bulk mass-balance corrected samples, despite the latter showing fractionation at different stages through the columns. Wakaki and Tanaka (2012) eluted their samples through single columns with Biorad AG50W-X8 resin, using HIBA solute.

Saji et al. (2016) also documented progressive fractionation through LN spec columns, consistent with nuclear field shift effects. Samples started with substantial  $\mu^{150}\text{Nd}$  excesses that became increasingly negative with progressive elutions. Saji et al. (2016) did not complete a mass-balance correction of their sample, due to incomplete recovery of the final sample fraction. Our study used both Biorad AG50W-X8 and LN-spec resin. Many of the studies that contributed samples to the 150-x line reported using some combination of these resins. Further analysis is needed of fractionation of Nd isotopes in bulk samples using the methods from this study to ensure that this is not a source of anomalies.

The predicted nuclear field shift effect in  $\mu_{iNd}$  for each Nd isotope can be predicted using the following equation (Moynier et al., 2013; Saji et al., 2016; Garçon et al., 2018) for data normalized to the  $^{146}\text{Nd}/^{144}\text{Nd}$  ratio:

$$\mu_{iNd} = \left[ (\langle r^2 \rangle_{iNd} - \langle r^2 \rangle_{^{144}\text{Nd}}) - \left( \frac{m_{^{146}\text{Nd}} \times (m_i - m_{^{144}\text{Nd}})}{m_i \times (m_{^{146}\text{Nd}} - m_{^{144}\text{Nd}})} \right) \times (\langle r^2 \rangle_{^{146}\text{Nd}} - \langle r^2 \rangle_{^{144}\text{Nd}}) \right] \times \alpha$$

In which  $\langle r^2 \rangle_i$  is the mean-square nuclear charge radius of Nd isotope  $i$  (Angeli and Marinova, 2013),  $m_i$  is its atomic mass, and  $\alpha$  is a scaling factor that changes the amplitude of the field shift effect. For each sample,  $\alpha$  was varied such that the  $\mu^{150}\text{Nd}$  predicted by the equation was the same as the sample's measured value (within error).

The  $\mu^{148}\text{Nd}$  values predicted by the nuclear field shift model are consistent with measured values for samples (Figure 3.12). However, predicted  $\mu^{145}\text{Nd}$  values are inconsistent with measured values for samples, although these differences are not always resolvable. Measured  $\mu^{145}\text{Nd}$  values show an excess if the model predicts a deficit, and a deficit if the model predicts an excess. Samples such as LAR 12002 maintain a 40 ppm  $\mu^{145}\text{Nd}$  excess compared to nuclear field shift predictions, even when the model's  $\mu^{150}\text{Nd}$  is brought to the lowest value within error of the sample. This is consistent with other samples on the 150-x line. The column fractionation observed in Saji et al., (2016) did not have this observed  $\mu^{145}\text{Nd}$  mismatch. The measured values from their study trended with nuclear field shift predictions.



**Figure 3.12** Nd isotope compositions of four bulk chondrites. Measured sample compositions are shown as pink lines. Each sample's nuclear field shift effects are modeled (NFS model) in dark blue. Stellar-model s-deficit composition predictions tied to each sample's  $\mu^{145}\text{Nd}$  value are shown as long dashed blue lines. Measured  $\mu^{150}\text{Nd}$  values correspond with predicted nuclear field shifts. Measured  $\mu^{142}\text{Nd}$ ,  $\mu^{145}\text{Nd}$ , and  $\mu^{148}\text{Nd}$  values correspond with stellar-model s-deficit predicted compositions.

The samples used to evaluate the 150-x line do not show deviations away from the stellar model that would be consistent with nuclear field shifts for  $\mu^{148}\text{Nd}$  vs.  $\mu^{145}\text{Nd}$  (Figure 3.13) when using the conditions of our model (nuclear field shift predicted  $\mu^{150}\text{Nd}$  = sample  $\mu^{150}\text{Nd}$ ). However, samples may show mixing between the stellar and nuclear

field shift models for  $\mu^{150}\text{Nd}$  vs.  $\mu^{145}\text{Nd}$  (Figure 3.14) Samples show scattered  $\mu^{145}\text{Nd}$  vs.  $\mu^{142}\text{Nd}$  (Figure 3.15a) but when  $\mu^{142}\text{Nd}$  is corrected for radiogenic ingrowth, two populations appear (Figure 3.15b). When corrected, CAIs move towards the nuclear field shift model while chondrites and achondrites remain scattered around the stellar model. This implies that nuclear field shift effects may have occurred before radiogenic ingrowth of  $^{142}\text{Nd}$  in these CAIs.

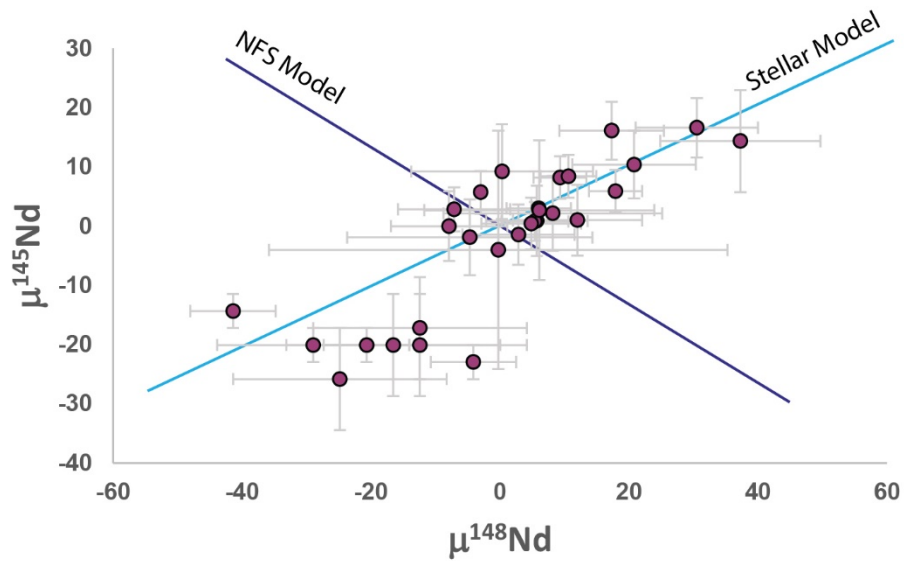


**Figure 3.13** Measured  $\mu^{148}\text{Nd}$  vs.  $\mu^{145}\text{Nd}$  for samples used to evaluate the 150-x line. Error bars are given in 2SD. Stellar model values are shown as a light blue line and Nuclear Field Shift (NFS) Model values are shown as a dark blue line. Sample are generally consistent with the stellar model for this isotope pair.



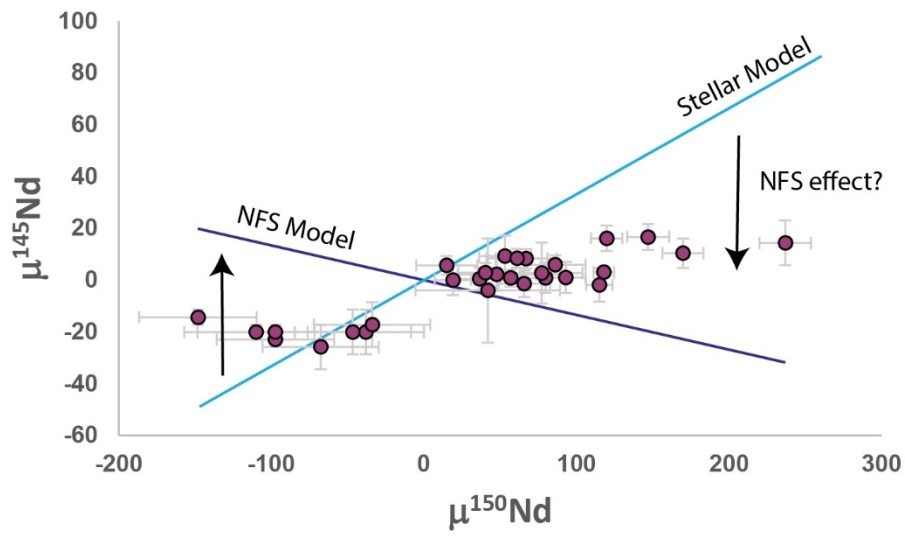


**Figure 3.14** Measured  $\mu^{150}\text{Nd}$  vs.  $\mu^{145}\text{Nd}$  for samples used to evaluate the 150-x line. Error bars are given in 2SE. Stellar model values are shown as a light blue line and Nuclear Field Shift (NFS) Model values are shown as a dark blue line. Samples show potential mixing between both models.

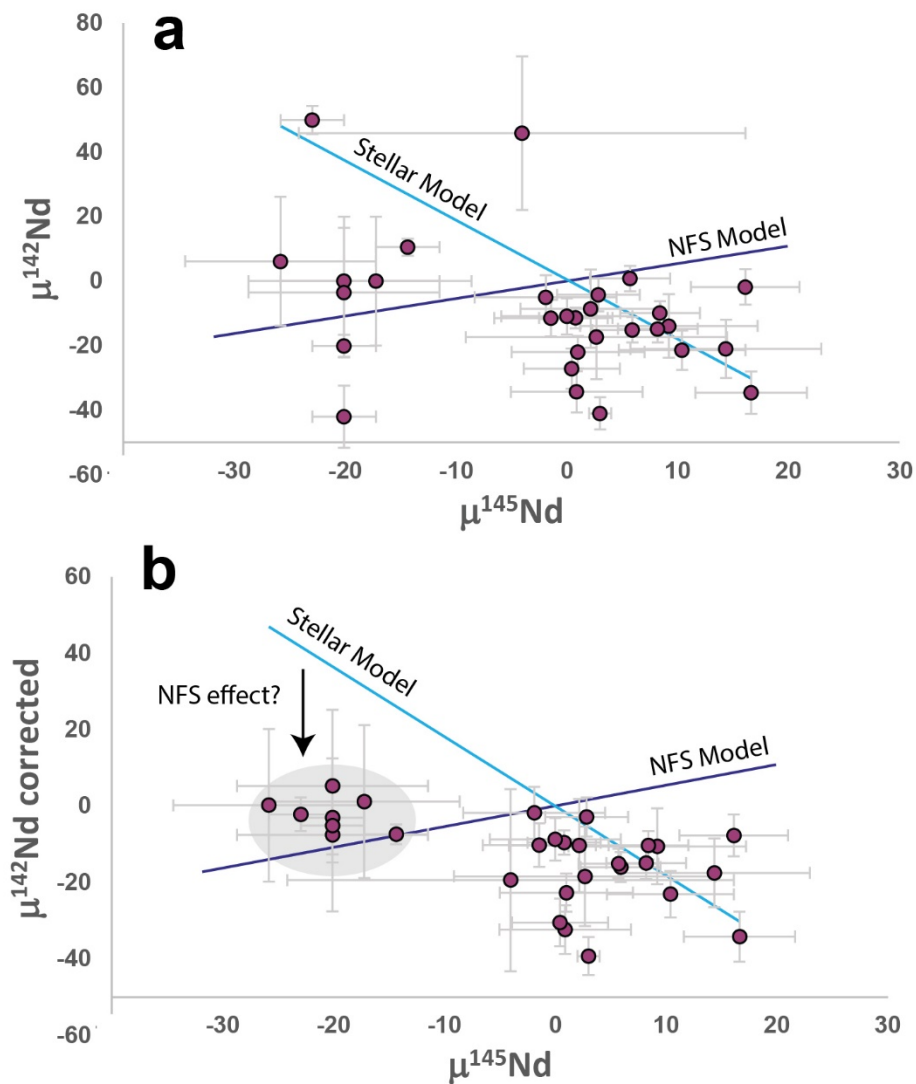


**Figure 3.15 (a)** Measured  $\mu^{145}\text{Nd}$  vs. measured  $\mu^{142}\text{Nd}$  and **(b)** corrected  $\mu^{142}\text{Nd}$  for samples used to evaluate the 150-x line. Error bars are given in 2SE. Stellar model values are shown as a light blue line and Nuclear Field Shift (NFS) Model values are shown as a dark blue line. Samples in the gray circle indicate CAIs. Chondrite samples are consistent with the stellar model for this isotope pair, but CAIs show a shift towards the NFS model after correcting for radiogenic  $^{142}\text{Nd}$ .

When the s-deficit stellar model assumes that  $\mu^{145}\text{Nd}$  has not been affected by laboratory procedure and reflects the sample's true value, sample compositions reflect stellar model values for  $\mu^{142}\text{Nd}$ ,  $\mu^{145}\text{Nd}$ , and  $\mu^{148}\text{Nd}$ . Chondrite and achondrite samples have deviations in  $\mu^{142}\text{Nd}$  from the stellar-predicted values of ~5-30 ppm. Due to the complexities of correcting for the extinct  $^{146}\text{Sm}$ - $^{142}\text{Nd}$  decay scheme and knowing that nuclear field shift effects have little impact on  $^{142}\text{Nd}$  (Garçon et al., 2018), these discrepancies may simply be due to the multiple assumptions made during radiogenic corrections. However, this model also assumes that the measured  $^{145}\text{Nd}/^{144}\text{Nd}$  ratios for each sample, from which the stellar-predicted  $\mu^{142}\text{Nd}$  is predicted, represents the true value for the sample, and does not take  $^{145}\text{Nd}/^{144}\text{Nd}$  measurement errors into account.

#### **3.5.5.4 Excess $^{150}\text{Nd}$ not from Spike Contamination**

The  $\mu^{150}\text{Nd}$  vs.  $\mu^{148}\text{Nd}$  relationships for samples with excess  $\mu^{150}\text{Nd}$  do not follow expected trends for addition of random concentrations of  $^{150}\text{Nd}$  spike (Figure 3.16). Because our beakers were cleaned in bulk, and our samples on the 150-x line were processed in different batches, it seems unlikely that no samples in between (using the same bulk cleaned beakers) would be affected. Spike contamination cannot explain the CAIs with  $\mu^{150}\text{Nd}$  deficits on the 150-x line. Further, if spike contamination is affecting up to 30% of all high-precision chondrite, angrite, and eucrite Nd data processed in clean labs across the world, then clean-lab procedures for Nd chemistry would need to be stringently reevaluated.

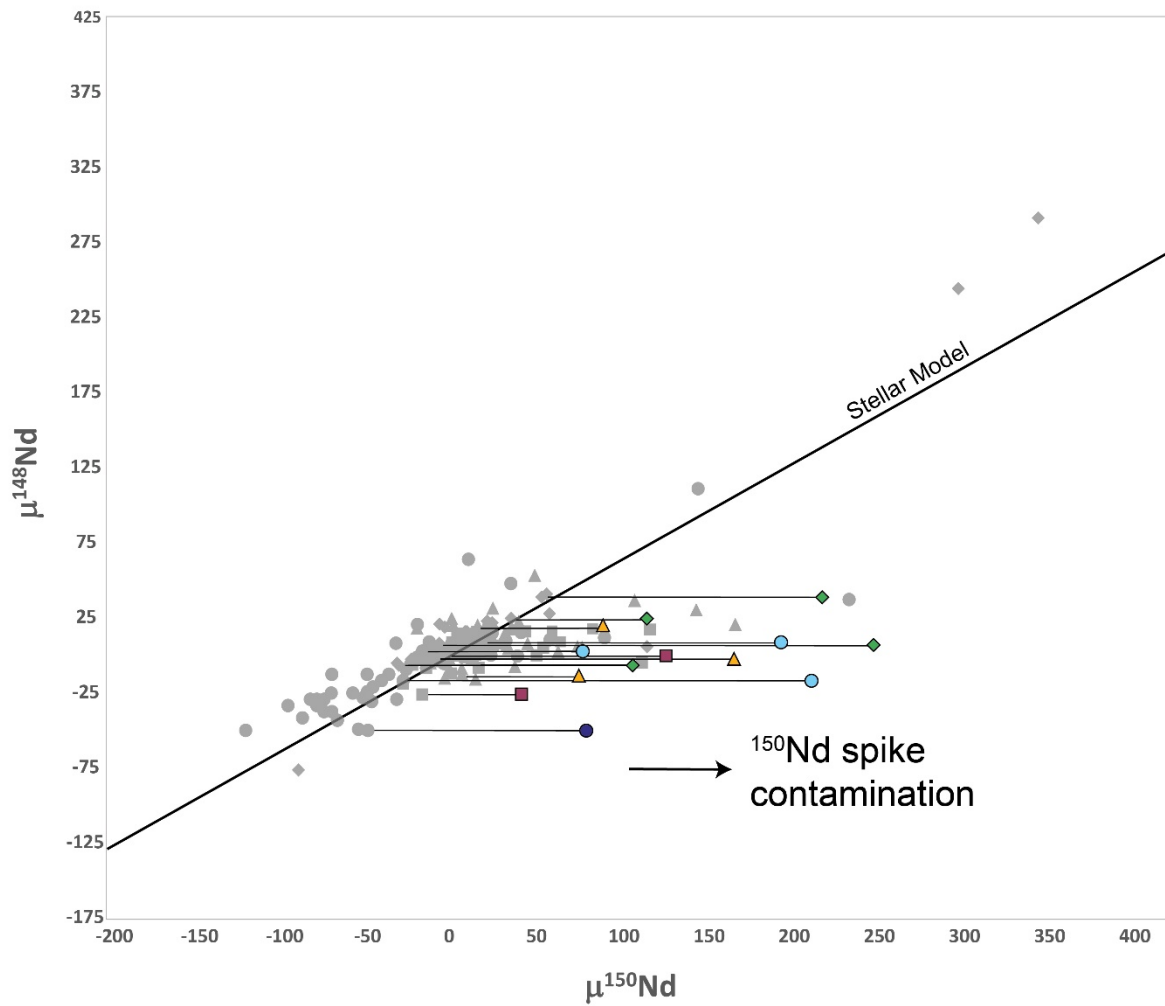


**Figure 3.16 Hypothetical effect of  $^{150}\text{Nd}$  spike contamination on  $\mu^{150}\text{Nd}$  vs.  $\mu^{148}\text{Nd}$  results of measured samples near the stellar model. The stellar model is shown as a black line. Measured samples are shown with a gray overlay. Hypothetically contaminated samples are shown in color.**

To account for the natural slope between  $\mu^{148}\text{Nd}$  -  $\mu^{150}\text{Nd}$  due to stellar processes, each sample on the 150-x line was stripped of the  $^{150}\text{Nd}$  that is predicted by the stellar model using the following equation:

$$\mu^{150}\text{Nd}_{\text{excess}} = \mu^{150}\text{Nd}_{\text{measured}} - \mu^{150}\text{Nd}_{\text{stellar-model}}$$

in which  $\mu^{150}\text{Nd}_{\text{stellar-model}}$  was calculated using both the predicted relationships between  $^{145}\text{Nd}$ - $^{150}\text{Nd}$  and  $^{148}\text{Nd}$ - $^{150}\text{Nd}$ , and also the average of these two predictions. The  $^{145}\text{Nd}$ - and  $^{148}\text{Nd}$ - predicted  $\mu^{150}\text{Nd}_{\text{stellar-model}}$  values had an average variation of 16 ppm. The  $\mu^{150}\text{Nd}_{\text{excess}}$  was compared with measured  $\mu^{145}\text{Nd}$  and  $\mu^{148}\text{Nd}$  for each sample. When compared to  $\mu^{145}\text{Nd}$ ,  $\mu^{150}\text{Nd}_{\text{excess}}$  was calculated using both the  $^{148}\text{Nd}$ - $^{150}\text{Nd}$  stellar relationship and the average of the  $^{145}\text{Nd}$ - $^{150}\text{Nd}$  and  $^{148}\text{Nd}$ - $^{150}\text{Nd}$  stellar relationships. When compared to  $\mu^{148}\text{Nd}$ ,  $\mu^{150}\text{Nd}_{\text{excess}}$  was calculated using both the  $^{145}\text{Nd}$ - $^{150}\text{Nd}$  stellar relationship and the average of the  $^{145}\text{Nd}$ - $^{150}\text{Nd}$  and  $^{148}\text{Nd}$ - $^{150}\text{Nd}$  stellar relationships. Calculated  $\mu^{150}\text{Nd}_{\text{excess}}$  positively trends with measured  $\mu^{148}\text{Nd}$  in agreeance with nuclear field shift effects (Figure 3.14). However,  $\mu^{150}\text{Nd}_{\text{excess}}$  shows no defined correlation with  $\mu^{145}\text{Nd}$  (Figure 3.15). While CAIs and bulk samples show distinct relationships between  $\mu^{150}\text{Nd}_{\text{excess}}$  and  $\mu^{145}\text{Nd}$ , neither are consistent with the trend for nuclear field shift effects.

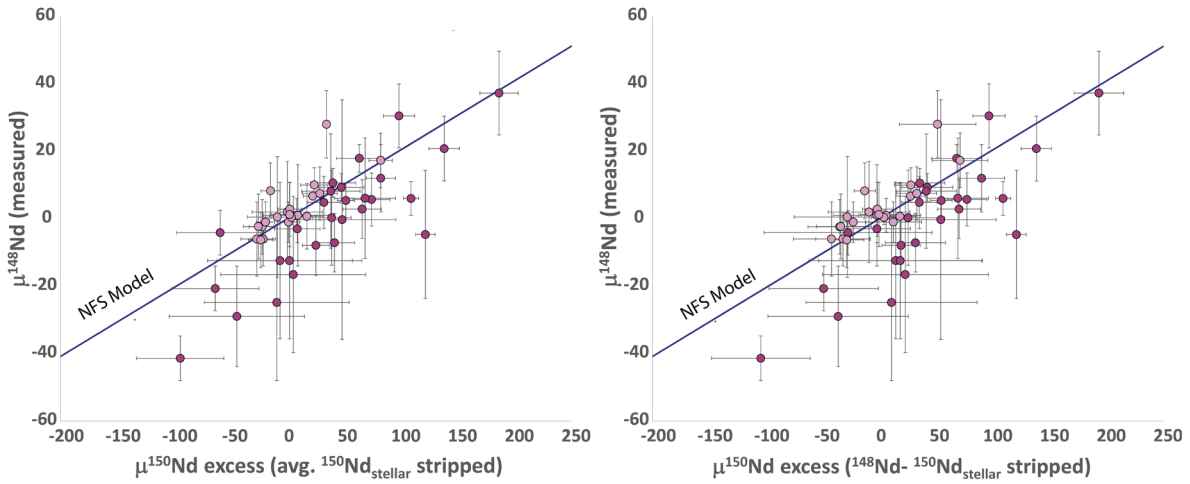


**Figure 3.17** (a) Calculated  $\mu^{150}\text{Nd}_{\text{excess}}$  vs. measured  $\mu^{148}\text{Nd}$  for all samples showing anomalous  $\mu^{150}\text{Nd}$ - $\mu^{148}\text{Nd}$  relationships, in which the  $\mu^{150}\text{Nd}_{\text{excess}}$  was calculated by stripping the average stellar-model  $\mu^{150}\text{Nd}$  predicted by  $\mu^{145}\text{Nd}$  and  $\mu^{148}\text{Nd}$  relationships (b)  $\mu^{150}\text{Nd}_{\text{excess}}$  vs. measured  $\mu^{148}\text{Nd}$  in which the  $\mu^{150}\text{Nd}_{\text{excess}}$  was calculated by stripping the average stellar-model  $\mu^{150}\text{Nd}$  predicted by  $\mu^{145}\text{Nd}$  only. Samples used to evaluate the 150-x line are shown in dark purple. Additional samples from Table 3.6 are shown in light purple. Error bars are given in 2SE. Nuclear Field Shift (NFS) Model values are shown as a dark blue line.

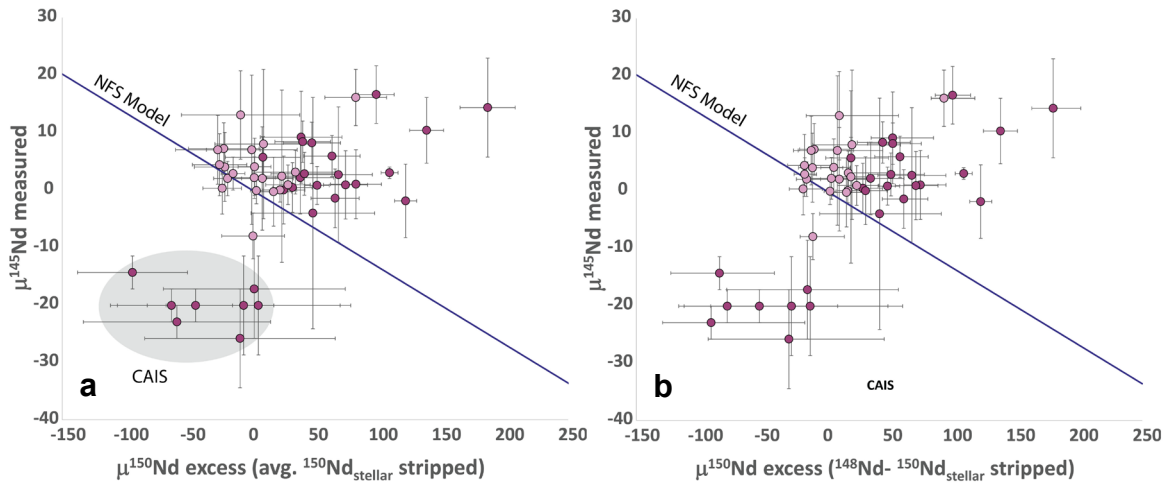


**Figure 3.18** (a) Calculated  $\mu^{150}\text{Nd}_{\text{excess}}$  vs. measured  $\mu^{145}\text{Nd}$  for all samples showing anomalous  $\mu^{150}\text{Nd}$ - $\mu^{148}\text{Nd}$  relationships, in which the  $\mu^{150}\text{Nd}_{\text{excess}}$  was calculated by stripping the average stellar-model  $\mu^{150}\text{Nd}$  predicted by  $\mu^{145}\text{Nd}$  and  $\mu^{148}\text{Nd}$  relationships (b)  $\mu^{150}\text{Nd}_{\text{excess}}$  vs. measured  $\mu^{145}\text{Nd}$  in which the  $\mu^{150}\text{Nd}_{\text{excess}}$  was calculated by stripping the average stellar-model  $\mu^{150}\text{Nd}$  predicted by  $\mu^{148}\text{Nd}$  only. Samples used to evaluate the 150-x line are shown in dark purple. Additional samples from Table 3.6 are shown in light purple. Error bars are given in 2SE. Nuclear Field Shift (NFS) Model values are shown as a dark blue line. Samples in the gray circle indicate CAIS.

### 3.5.5.5 Nuclear Field Shift Effects and Nucleosynthesis

Other isotope systems, such as Ba, Ti, Cr, Mo, and Sm have shown mismatches in nuclear field shift predicted data for single isotopes (Fuji et al., 2006; Burkhardt et al., 2011; Brennecka et al., 2013; Moynier et al., 2013), similar to the mismatch seen for  $\mu^{145}\text{Nd}$  in the data presented here. This suggests that a combination of nucleosynthetic anomalies and nuclear field shift effects produce the predictable isotopic patterns seen in these samples (Moynier et al., 2013).

**Table 3.6** Full list of fractionated samples with percent of meteorites per study impacted.

<b>Sample</b>	<b>Nd Isotope Study</b>
Sharp	Boyett and Carlson 2005
Sharp	Boyett and Carlson 2005
Allende	Boyett and Carlson 2005
Allende Bomb	Boyett and Carlson 2005
<b>4/17 = 24%</b>	
St. Severin	Andreassen and Sharma, 2006
<b>1/4 = 25%</b>	
Allende	Rankenburg et al., 2006
<b>2/7 = 29%</b>	
Gladstone	Carlson et al., 2007
Ucera	Carlson et al., 2007
Homestead	Carlson et al., 2007
Peace River	Carlson et al., 2007
Indarch	Carlson et al., 2007
Grosnaja	Carlson et al., 2007
<b>6/12 = 50%</b>	
Hvittis	Gannoun et al., 2011b
Sahara 97158	Gannoun et al., 2011b
Sahara 97072	Gannoun et al., 2011b
Indarch	Gannoun et al., 2011b
<b>4/15 = 27%</b>	
CAI 164	Brennecka et al., 2013
CAI 168	Brennecka et al., 2013

CAI 171	Brennecka et al., 2013
CAI 172	Brennecka et al., 2013
<b>4/12 = 33%</b>	
pyx	Marks et al., 2014
d>3.26	Marks et al., 2014
d<3.26	Marks et al., 2014
Mel pyx	Marks et al., 2014
<b>4/6 = 67%</b>	
CAI NWA 6991 B4 fass-R	Bouvier and Boyet, 2016
ALH 77295	Bouvier and Boyet, 2016
MAC 02839	Bouvier and Boyet, 2016
MAC 02837	Bouvier and Boyet, 2016
<b>4/13 = 31%</b>	
Bruderheim	Burkhardt et al., 2016
Abee	Burkhardt et al., 2016
Indarch	Burkhardt et al., 2016
Hvittis	Burkhardt et al., 2016
<b>4/29 = 14%</b>	
Hamlet	Fukai and Yokoyama, 2017
<b>1/15 = 7%</b>	
Ivuna	Saji et al., 2020
NWA 6043	Saji et al., 2020
<b>2/14 = 14%</b>	
ADOR*	Render and Brennecka, 2021
NWA 4590*	Render and Brennecka, 2021
NWA 4801*	Render and Brennecka, 2021
NWA 6291	Render and Brennecka, 2021
Millbillillie*	Render and Brennecka, 2021
<b>5/10 = 50%</b>	
EET 88746	This Study
EET 96135	This Study
MAC 02839	This Study
PCA 91020	This Study
ALH 84028	This Study
LAR 12002	This Study
Allende	This Study
EET 96299	This Study
LEW 88180	This Study
ALH 85002	This Study



EET 90015	This Study
SZA 12420	This Study
<b>12/26 = 46%</b>	

### 3.5.6 The Effect of Excess $^{150}\text{Nd}$ on CK and CV Chondrites

The data presented here are currently inconsistent with lab-induced mass-independent fractionation as the cause of excess  $\mu^{150}\text{Nd}$  in chondritic samples. However, additional studies are needed to understand the cause of this excess, and whether it is imparted in the solar system or through process of materials in the laboratory environment. When  $^{150}\text{Nd}$  analyses that show anomalous fractionation are removed from chondrite-group averages, a new, although unresolvable relationship between CV and CK chondrites appears for r-process isotopes (Figure 3.19). The CV-chondrite weighted average that is stripped of anomalous samples plots closer to ordinary and enstatite chondrites and further away from CK chondrites (Figure 3.19b). The CK-chondrite weighted average shifts away from the stellar-predicted values, although this could be the result of a small remaining sample size ( $n=3$ ). This divergence, rather than convergence, of average  $\mu^{150}\text{Nd}$  vs.  $\mu^{148}\text{Nd}$  when anomalously fractionated samples are removed highlights the need to understand whether this fractionation is laboratory or solar-system induced.

## 3.6 Conclusion

There are no resolvable differences in the average Nd compositions of CK and CV chondrites. CAIs contribute s-excess anomalies to both CV and CK chondrites. CK5 and CK6 chondrites do not show a trend toward r-excess anomalies that are different from CV3 and CK4 chondrites, indicating that their lower abundance of CAIs is likely due to

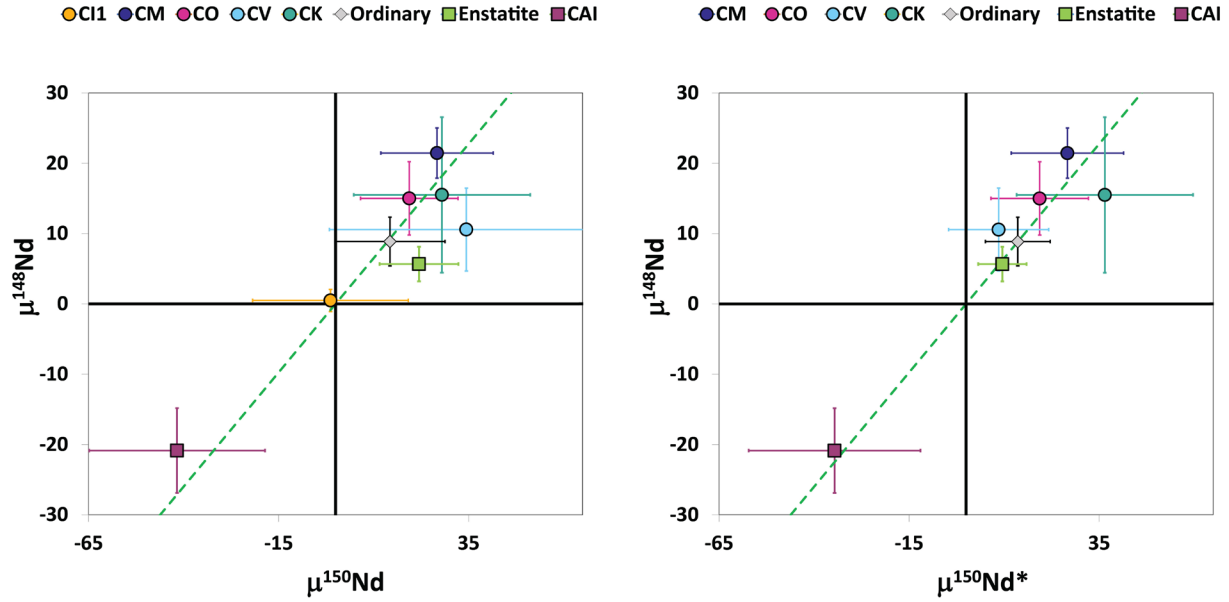


**Figure 3.19 (a)** Weighted average  $\mu^{150}\text{Nd}$  vs.  $\mu^{148}\text{Nd}$  values for carbonaceous chondrite groups and the enstatite and ordinary chondrite classes. **(b)** Weighted average  $\mu^{150}\text{Nd}$  for groups in which samples with anomalous  $\mu^{150}\text{Nd}$  have been removed. Error bars show the 95% confidence interval for each group average. The s-deficit relationship predicted by the stellar model is shown as a dashed green line. The CV chondrites plot closer to the stellar-model s-deficit line after removal of anomalous samples, while CK chondrites plot farther away from the line. Both CV and CK chondrites plot farther away from each other after removal of anomalous samples.

thermal re-equilibrium, rather than a lack of CAIs in their parent material. While multiple CV samples show extreme r-excess anomalies, the sample size for CV chondrites is much larger ( $n = 24$ ) than other CC groups ( $n = 2-7$ ) and these anomalies may exist in these other groups. Different aliquots of Allende, analyzed at different laboratories, show a tenfold variation in r-process  $\mu^{150}\text{Nd}$  compared to s-process  $\mu^{142}\text{Nd}$ .

Numerous samples from varying chondrite and achondrite groups show anomalous  $\mu^{150}\text{Nd}$  compositions that cannot be explained by the stellar model. Spike contamination is unable to explain the positively correlated, non-random ratios of

$\mu^{150}\text{Nd}_{\text{excess}}:\mu^{148}\text{Nd}$ . It is also unable to explain the same fractionation pattern found in samples with  $\mu^{150}\text{Nd}$  deficits. Samples that deviate from stellar-model  $\mu^{150}\text{Nd}$  predictions show  $\mu^{150}\text{Nd}_{\text{excess}}$  to  $\mu^{148}\text{Nd}$  deviations of 5:1, consistent with nuclear field shift effects. Measured  $\mu^{142}\text{Nd}_{\text{corr}}$ ,  $\mu^{145}\text{Nd}$ , and  $\mu^{148}\text{Nd}$  can be explained for most bulk samples using stellar model predicted relationships. However, when comparing  $\mu^{142}\text{Nd}$  vs.  $\mu^{145}\text{Nd}$ , anomalous CAIs that have been corrected for radiogenic ingrowth move towards the nuclear field shift model. This suggests that nuclear field shift effects may have occurred before radiogenic ingrowth of  $^{142}\text{Nd}$  in these CAIs.

This anomalous fractionation pattern is seen in up to 25-30% of all high precision Nd isotope data collected for all chondrites, angrites, eucrites, and CAIs. If this fractionation is induced by column chemistry, it highlights the necessity for more robust studies of nuclear field shift effects on Nd isotopes for bulk samples, and a need to evaluate every step of chemistry and TIMS procedure for fractionation. If this is found to be a laboratory-induced effect, affected samples cannot continue to be averaged into chondrite and achondrite group data and used in broad interpretations.

However, the Nd isotope compositions of the anomalous samples presented here are not consistent with the laboratory-induced fractionation patterns measured in previous studies (Wakaki and Tanaka, 2012; Saji et al., 2016). The mismatch seen for measured vs. nuclear-field-shift predicted  $\mu^{145}\text{Nd}$  in the data presented here suggests that a combination of nucleosynthetic anomalies and nuclear field shift effects produced the predictable isotopic patterns seen in these samples (Moynier et al., 2013). If this mass-independent fractionation is solar-system induced, it could provide an additional

fingerprint for nebular feeding zones. Due to the variability in Nd chemistry protocols, additional studies should be pursued to evaluate lab-induced mass-independent fractionation in high-precision Nd isotope analyses. The inclusion of these anomalous data has implications for CK and CV chondrite group Nd isotope compositions, thus understanding their cause is critical for understanding the Nd isotope compositions of these and other chondrite groups.

## **Chapter IV: Non-Arrhenius $^4\text{He}$ diffusion kinetics in treated zircons**

### **4.1 Introduction**

Zircon-helium dating is a commonly used thermochronologic method, providing information about time-temperature histories of samples at low temperatures ( $<180^\circ\text{C}$ ). Understanding helium diffusion kinetics in zircon is important for creating reliable interpretations for He closure-temperatures in zircons. Previous step-heating experiments have shown that early-heating steps on zircons produce non-Arrhenius behavior (Reiners et al., 2002, 2004; Guenthner et al., 2013). Multiple causes for this behavior have been suggested, including multiple intracrystalline diffusion domains of varying sizes and/or diffusivities, inhomogeneous distribution of He in the crystal, and interaction between radiation zones within the crystal with the outside surface of the crystal (Reiners, 2005; Reiners et al., 2002, 2004; Guenthner et al., 2013). We attempted to better understand this behavior by comparing  $^4\text{He}$  step-heating results from samples with radiation damage to those with no radiation damage. This required synthetic He saturation of zircon samples after annealing, as it is not possible in nature to have samples with no radiation damage, but with the resultant He.

### **4.2 Experimental Procedure**

#### **4.2.1 Sample Preparation**

A 1.5 cm piece of gem-quality Mud Tank zircon was cut into a 1.5 mm thick slab with a low-speed diamond saw. This slab was then crushed into ~3-5 mm pieces and these pieces were selected for the absence of inclusions and oxide staining. Approximately 200 fragments were handpicked. These fragments were 1-3 mm in length

and 0.2 to 0.5 mm wide. A handful of these samples were selected for analysis at this stage. These were labeled PC0-01, PC0-02, etc. The remainder of the fragments were annealed in air at 1250°C for one week to eliminate in-grown  $^4\text{He}$  and repair possible mechanical damage caused by crushing and damage due to radioactive decay. Next, these fragments were pressurized with 1.04 kbar of tank He in a cold-seal pressure vessel and heated under pressure at  $750\pm 1^\circ\text{C}$  for 21 days. The material was then quenched isobarically; cooling to room temperature took 20 minutes. Fragments were individually picked under the microscope to further avoid cracks, shards, or small inclusions. These samples were labeled PC1-000-01, PC1-000-02, etc.

#### **4.2.2 $^4\text{He}$ Step-heating Analyses**

Step-heating experiments were conducted on two treated samples and two untreated samples using a lightbulb furnace modified from the design of Farley et al., (1999). Lightbulbs were Eiko FX bulbs coated in aluminum using an ion sputterer. These bulbs were sometimes capable of reaching 500°C before structurally failing. One treated sample and one untreated sample were step-heated on an accelerated schedule, while the other two samples were step-heated on a longer schedule (Figure 4.1). The longer schedule was utilized to attempt to deplete potential smaller diffusion domains of all He. These two schedules can be seen in contrast to the previously utilized schedule of Guenthner et al., (2013). After step heating, all samples were analyzed by laser-heating in repeated steps until the  $^4\text{He}$  fraction of that step was less than 0.5% of the total  $^4\text{He}$  measured for the sample. Five additional samples were measured for total [ $^4\text{He}$ ] using only the laser.

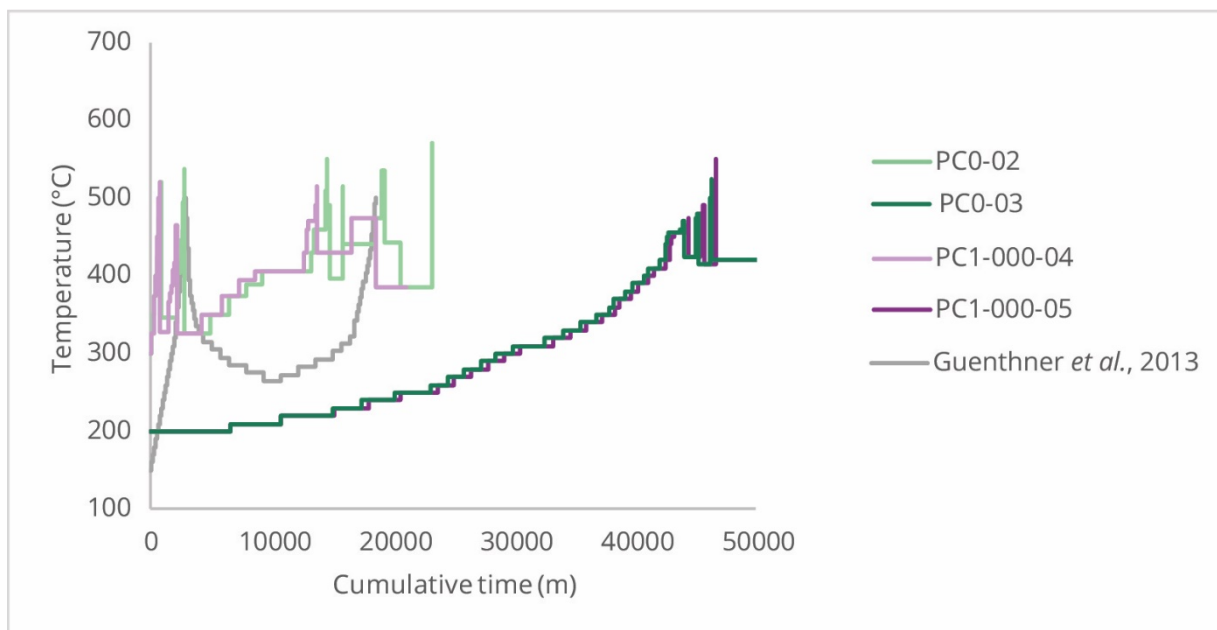


**Figure 4.1** Cumulative heating time vs. set temperature of heating step for four samples from this study and from the procedure of Guenther et al., 2013.

#### 4.2.3 Mass, Volume, and Surface Area

The masses of five He-saturated zircon fragments were measured on a microgram scale, five to eight times, and averaged. The length of each fragment side was determined using a microscope. Their volumes and surface areas were estimated by assuming each sample's closest shape (cube, wedge, etc.).

### 4.3 Results

#### 4.3.1 $^4\text{He}$ Step-heating

The results of the step-heating experiments on the two treated and two untreated zircon fragments are summarized in Table 4.1. The Arrhenius plot for each sample can be seen in Figure 4.2. Data collected for temperatures set at 400°C and higher were

summed into the  $^4\text{He}$  (ncc) total as the temperatures were highly unreliable due to complications with the thermocouple regulators.

**Table 4.1** Step-heating results for all samples.

Temperature (°C)	Time (s)	$^4\text{He}$ (ncc)	f	$\ln(D/a^2)$
<b>PC0-02</b>				
300	7200	0.04	0.0002	-28.72
325	7200	0.19	0.0011	-25.03
350	7020	0.41	0.0030	-23.04
375	7200	1.00	0.0078	-21.20
386	154320	0.65	0.4969	-19.64
total		210.18		
Temperature (°C)	Time (s)	$^4\text{He}$ (ncc)	f	$\ln(D/a^2)$
<b>PC0-03</b>				
200	399180	9.98	0.0127	-24.06
210	250560	3.36	0.0170	-23.83
220	256800	3.12	0.0210	-23.68
230	142920	1.79	0.0233	-23.49
240	162120	1.55	0.0252	-23.67
250	181140	1.69	0.0274	-23.61
260	83880	12.89	0.0438	-20.50
270	81360	2.01	0.0464	-22.08
280	82380	2.02	0.0489	-22.03
290	75780	1.24	0.0505	-22.40
300	82080	3.33	0.0548	-21.43
310	160680	4.49	0.0605	-21.70
320	90300	5.50	0.0675	-20.82
330	81960	4.84	0.0736	-20.74
340	81240	5.58	0.0808	-20.50
350	66180	4.68	0.0867	-20.38
360	22980	1.47	0.0886	-20.43
370	57120	9.81	0.1011	-19.36



380	33720	3.90	0.1061	-19.66
390	54000	23.78	0.1364	-18.15
total		784.96		

Temperature (°C)	Time (s)	<sup>4</sup> He (ncc)	f	ln(D/a <sup>2</sup> )
------------------	----------	-----------------------	---	-----------------------

**PC1-000-04**

300	7200	9.38	0.0144	-19.79
325	8040	4.39	0.0212	-19.75
350	5640	3.06	0.0259	-19.47
375	5400	3.02	0.0305	-19.26
total		650.18		

Temperature (°C)	Time (s)	<sup>4</sup> He (ncc)	f	ln(D/a <sup>2</sup> )
------------------	----------	-----------------------	---	-----------------------

**PC1-000-05**

200	399180	9.39	0.0501	-21.30
210	250560	1.42	0.0577	-21.94
220	258600	1.37	0.0650	-21.87
230	172620	1.85	0.0748	-21.03
240	162120	1.65	0.0836	-20.95
250	181140	0.68	0.0872	-21.87
260	83280	0.69	0.0909	-21.02
270	81000	0.45	0.0933	-21.38
280	90420	0.76	0.0974	-20.93
290	77340	0.85	0.1020	-20.62
300	80280	0.82	0.1063	-20.65
310	158880	1.30	0.1133	-20.81
320	87540	1.04	0.1188	-20.38
330	79260	1.17	0.1250	-20.10
340	79260	1.00	0.1304	-20.21
350	63720	1.22	0.1369	-19.75
360	24420	4.11	0.1588	-17.46
370	55560	2.81	0.1738	-18.52
380	33540	8.81	0.2208	-16.67
390	55080	3.16	0.2376	-18.01
total		118.33		

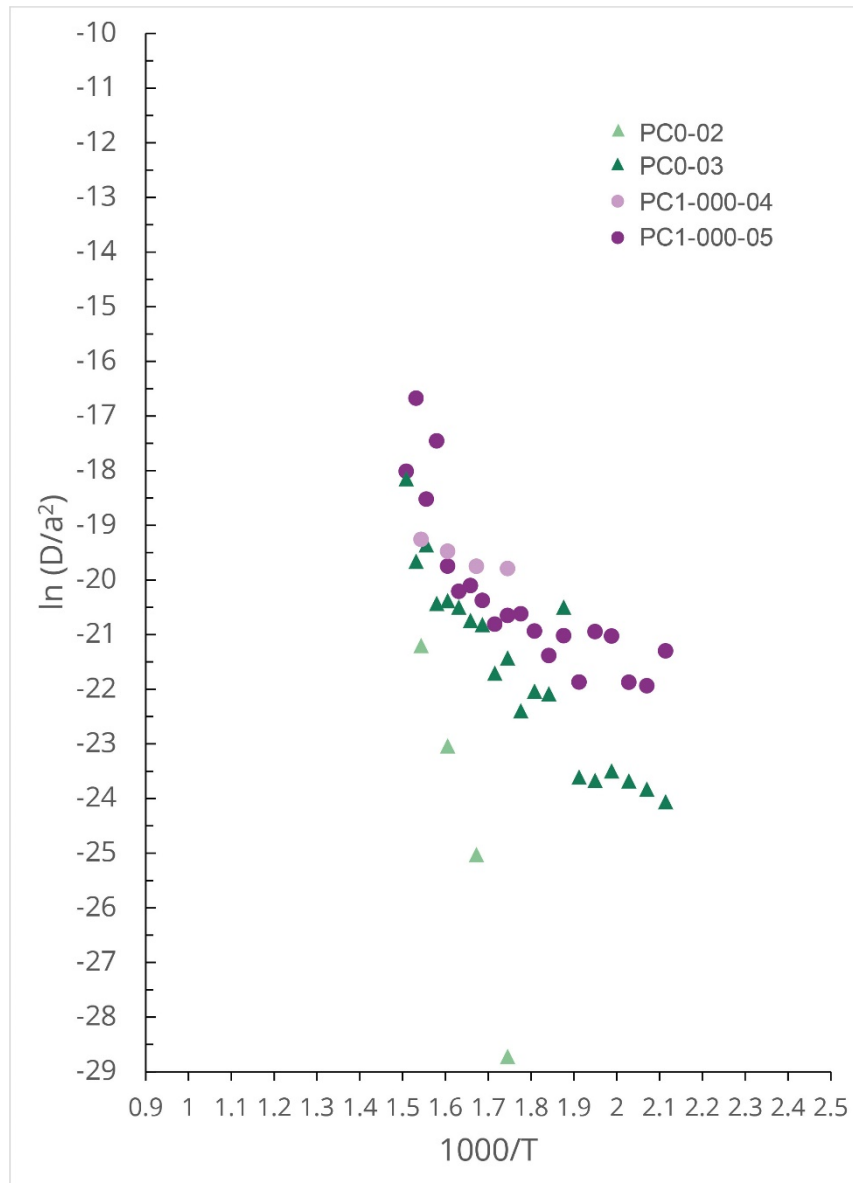


**Figure 4.2** Arrhenius plots for four zircon fragments. Samples PC0-02 and PC0-03 are untreated, while samples PC1-000-04 and PC1-000-05 have been annealed and artificially saturated with He.

#### 4.3.2 Mass, Volume, and Surface Area

The mass, volume, surface area, and bulk  $^4\text{He}$  (ncc) of five additional samples were measured. The  $^4\text{He}$  errors were less than 0.5 ncc while errors in mass were less than 6%. However, the error in volume and surface area could only be estimated, as we were assuming ideal shapes for non-ideal samples. We assumed errors for each measurement of 7.5%. The surface area/volume was calculated for each sample and estimated to have a 10% total error. The He/g were also calculated for each sample. Each of these measurements can be seen in Table 4.2.

**Table 4.2**  $^4\text{He}$  concentrations, volume, and surface area measurements for five zircon fragments.

	$^4\text{He}$ (ncc)	Mass (g)	Volume ( $\mu\text{m}^3$ )	Surface Area ( $\mu\text{m}^2$ )	surf. area/volume	$^4\text{He/g}$
PC1-000-06	3302.8	0.00278	61306956	985320	0.0161	1187507
PC1-000-07	1469.4	0.00214	269259926	3265646	0.0120	687942
PC1-000-09	1154.0	0.00229	492355885	4218387	0.0086	504831
PC1-000-11	664.8	0.00068	167612955	1957291	0.0117	975186
PC1-000-12	587.9	0.00069	218374957	2411000	0.0110	847166

## 4.4 Discussion

Our initial treatment of these samples had the goal of annealing damage  $\alpha$ -damage within the fragments to better understand the role that this damage plays on He diffusion kinetics. Annealing of  $\alpha$ -damage in zircons is dependent on the amount of accumulated damage in the sample. Less damaged samples will recover faster, and at lower temperatures (Capitani et al., 2017). A previous study of Mud Tank zircon fragments estimated that they had a neutron fluence of  $0.0122 \times 10^{18} \text{ a/g}$  (Guenther et al., 2013). Raman analyses in Zhang et al. (2004) showed full structural recovery in zircon samples with 15 times more damage than Mud Tank samples, at  $826^\circ\text{C}$  for one hour. Transmission electron microscopy analyses in Capitani et al. (2017) showed substantial recrystallization of partially metamict samples ( $8 \times 10^{18} \text{ a/g}$ ) at  $1126^\circ\text{C}$  for one hour. With our samples' low amounts of damage, and our procedure utilizing higher temperatures and longer hold times than previous studies, we are confident that the  $\alpha$ -damage in our samples was repaired and is no longer a factor in influencing He diffusion kinetics.

### 4.4.1 $^4\text{He}$ step-heating

The proximity of the diffusion-cell lightbulbs on our machine caused thermal disturbances amongst lightbulbs when one control temperature was changed. This would cause the thermocouple control of the adjacent lightbulbs to oscillate the control temperature along a  $200^\circ\text{C}$  temperature swing. The controls would also begin oscillating without a change in any of the control temperatures. The vibrations from the nearby vacuum pump may have initiated these oscillations. This behavior was more prevalent during the high-temperature steps that are used to calculate  $E_a$ ,  $D_0/a^2$ , and  $T_c$ . These temporary jumps in temperature likely had a significant effect on He diffusion, creating

unreliable scatter in the data. Figure 4.3 shows that while our data generally follows trends from previously measured Mud Tank fragments and zircons, it has substantial scatter. Inaccuracy in temperature measurements is the most likely cause of this scatter.

#### 4.4.2 $^4\text{He}$ Concentration vs. Surface Area and Volume

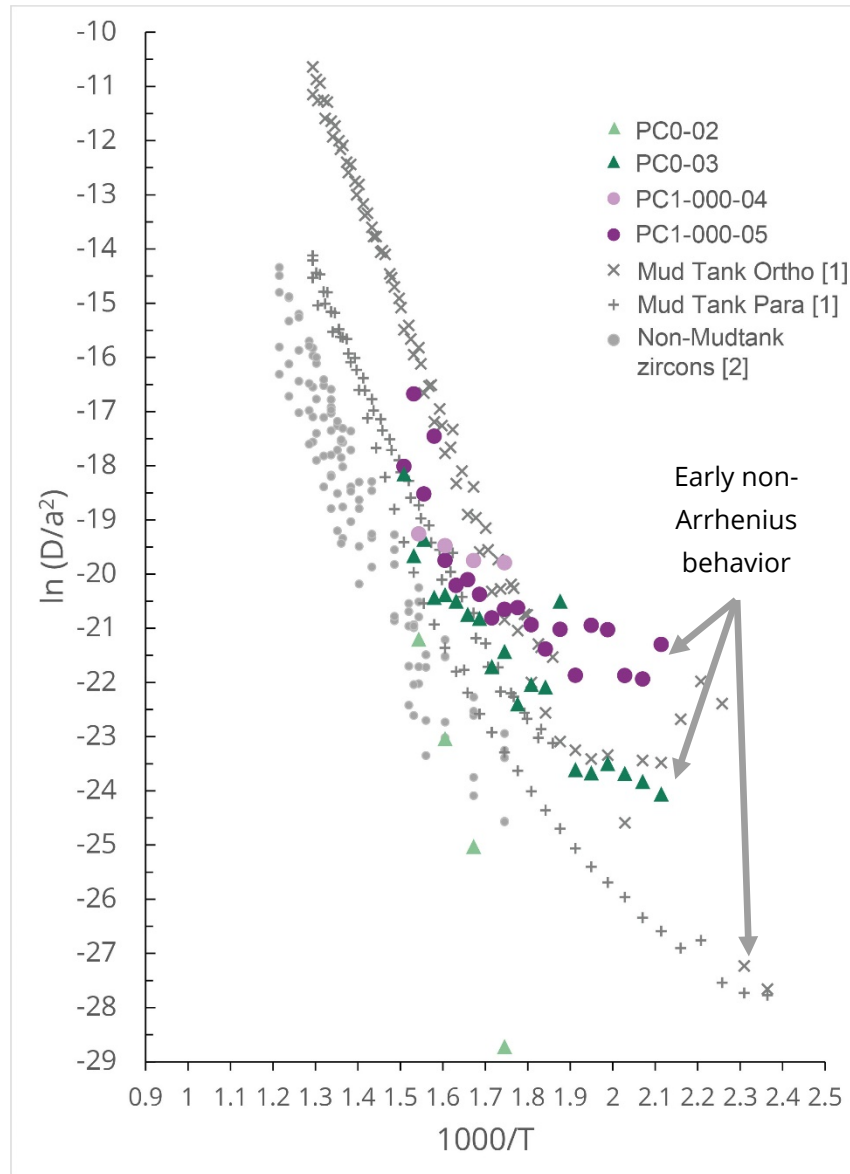


**Figure 4.3** Arrhenius plots for four zircon fragments from this study two zircon fragments from [1] Guenthner et al. (2013) and zircons from [2] Reiners et al. (2004). Mud Tank samples analyzed in this study and Guenthner et al. (2013) show non-Arrhenius behavior in the initial heating steps. However, samples analyzed in this study show substantial scatter.

The samples analyzed in this study show an increase in  $^4\text{He}$  ncc/g with larger surface area to volume ratios (Figure 4.4). If He was evenly saturated throughout these samples, we would expect this line to be flat. This implies that our method to saturate these samples with He may not have been successful in saturating the cores. While this method was successfully employed in calcite (Copeland et al., 2015), zircon has a higher  $^4\text{He}$  closure temperature than zircon, which may have made it difficult to saturate.

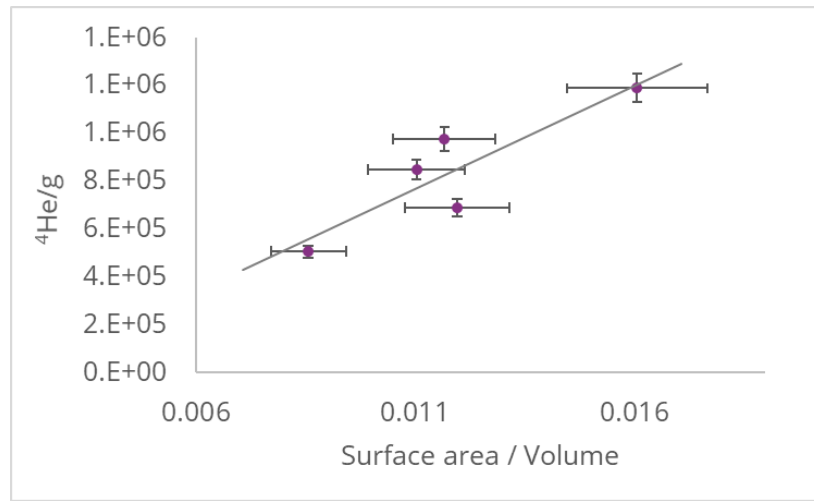


**Figure 4.4** Surface area over volume of sample vs.  $^4\text{He}$  (ncc) per gram of sample. Samples with a higher surface area to volume ratio have higher concentrations of  $^4\text{He}$ .

#### 4.5 Conclusions

Pressurizing zircon fragments with 1.04 kbar of tank He in a cold-seal pressure vessel at  $750 \pm 1^\circ\text{C}$  for 21 days was likely insufficient to fully saturate the fragments with He. While radiation damage annealing is not the cause of early non-Arrhenius behavior in these samples, this concentration gradient makes it impossible to evaluate potential multiple-diffusion domains inherent to the structure of zircon. The unreliable temperature data makes this data unsuitable to be used to calculate  $E_a$ ,  $D_0/a^2$ , and  $T_c$ .

## Appendix A: Muscovite $^{40}\text{Ar}/^{39}\text{Ar}$ Ages and Enrichment-Factor Calculations in the Narayani Catchment

**Table A.1** The age, location, and literature reference for all muscovite  $^{40}\text{Ar}/^{39}\text{Ar}$  data used to create age contours of the Narayani catchment.

Reference	Latitude	Longitude	Musc $^{40}\text{Ar}/^{39}\text{Ar}$ age (Ma)	+/-
Martin et al., 2015	28.41742	83.82075	9.6	1.5
	28.42823	83.8261	9.9	0.1
	28.43072	83.83379	16	0.5
	28.44343	83.84626	15	3.8
	28.36896	83.96693	4.3	0.1
	28.38749	83.98079	7	0.2
	28.34251	84.00661	4.8	0.4
	28.30601	84.09038	5.8	1.6
	28.32365	84.09097	11	1.3
	28.39211	84.11944	6	0.7
	28.32031	84.28823	4.7	0.1
	28.30042	84.30199	3.2	0.1
	28.39588	83.79992	7.2	1.3
Godin et al., 2001	28.65797	83.59148	12.7	0.4
	28.63802	83.63480	11.8	0.4
	28.60740	83.64308	15.5	0.3
	28.65549	83.57095	13.4	0.2
	28.64536	83.57023	14.3	0.2
	28.71791	83.64211	18.1	0.7
Vannay and Hodges, 1996	28.52292	83.67418	13.9	0.6
	28.56902	83.64631	14.7	0.8
	28.67138	83.58675	13.1	0.5
	28.64957	83.59091	14.5	0.2
	28.62709	83.66457	13	0.3
Bollinger et al., 2004	28.23600	84.38500	10.9	0.3
	28.24000	84.33900	7.2	0.3
	28.24100	84.37500	6	0.2
	28.24300	84.35900	6.1	0.2
	28.24400	84.37400	8.7	0.2
	28.24500	84.33800	6.6	0.2
	28.24800	84.33300	5.5	0.2
	28.25000	84.33400	4.1	0.2
	28.26100	84.35500	6.1	0.4

	28.26300	84.36000	4.4	0.2
	28.32900	84.33600	2.4	0.1
	27.90000	84.26900	22	0.5
	27.91700	84.24700	21.4	0.2
	27.91100	84.24200	26.9	0.5
	27.91400	84.27400	67.3	1.4
	27.90100	84.25500	26.3	0.3
Arita et al., 1997	27.82501	85.00254	15.1	0.1
	27.86360	85.17913	13.6	0.1
	27.73254	85.14902	31	0.1
	27.61828	85.12742	44	0.1
	27.56391	85.09671	19.6	0.1
Huntington and Hodges, 2006	28.38213	84.46456	5.3	0.24
	28.36446	84.45968	2.46	0.22
	28.35548	84.46038	3.32	0.22
	28.34860	84.44497	3.84	0.08
	28.34379	84.44149	4.13	0.54
	28.34022	84.43994	4.98	0.11
	28.33720	84.43658	3.49	0.09
	28.32935	84.41907	5.1	0.23
Catlos et al., 2001	28.57333	84.27632	15.5	1.1
	28.44000	84.36184	8.6	0.2
	28.39333	84.37500	9.4	0.2
	28.34667	84.36842	3.1	0.1
	28.35333	84.38158	6.2	0.1
	28.31333	84.35526	2.8	0.1
	28.27333	84.74342	4.4	0.1
	28.26000	84.72368	5.7	0.1
	28.24667	84.72368	7.9	0.6
	28.24667	84.73026	2.8	0.1
	28.24000	84.72368	3.3	0.1
	28.22667	84.72368	2.64	0.03
	28.20667	84.70395	2.8	0.3
	28.19333	84.69079	3.4	0.3
	28.14000	84.65132	6.28	0.03
	28.12667	84.65789	9.2	0.1
	28.12000	84.66447	4.85	0.04
	28.01333	84.60526	125	1
	28.00667	84.55921	257	1
Copeland et al., 1991	28.14000	84.59211	9	0.2



	28.08667	85.00000	32.9	0.4
	28.09333	84.77632	7	0
	27.93333	84.58553	397.5	0.8
	28.39333	84.82895	9.4	0.2
	28.34000	84.84211	5.4	0.1
	28.25333	84.86184	3.8	0.3
	28.23333	84.86184	3.1	0.2
Copeland et al., 1990	28.70199	84.34868	16.5	0.1
	28.67550	85.13208	14.7	0.2
	28.74834	84.95000	17.9	0.6
	28.70861	85.07018	16.6	0.1
	28.72848	85.00000	17.6	0.1
	28.74834	85.21311	17.1	0.1
	28.72185	85.08108	16.7	0.2
	28.70199	84.98750	18.4	0.1
	28.58940	85.64557	13.3	0.1
Herman et al., 2010	27.58100	85.12400	<20	
	27.55600	85.11700	<40	
	27.47200	85.04900	20.8	0.1
	27.90700	85.47200	9.6	0.1
	28.05000	85.45200	7	0.1
	28.07100	85.41200	7.8	0.1
	28.00000	85.44500	5.1	0.4
	27.84600	85.35300	12.1	0.2
	27.80100	85.31300	12.1	0.1
	28.03900	85.31800	12.1	0.1
	27.94000	85.36800	7.5	0.1
	27.93600	85.40700	8.3	0.1
	27.84900	85.53600	9.8	0.1
	27.49600	85.26600	22	0.2
	27.74700	84.81800	19.5	0.2
	27.78100	84.99900	16.6	0.1
	27.75800	85.01500	15.1	0.2
	27.79100	85.22800	12	0.2
	27.76700	85.21800	13.5	0.3
	27.71800	85.54900	14.2	0.2
	27.71200	85.53400	18.9	0.3
	27.72900	85.55900	13.5	0.3
	27.76000	85.56400	17.1	0.3
	27.76400	85.56800	13.7	0.4

27.77900	85.55900	38.8	0.5
27.78200	85.53700	17.2	0.3
27.77500	85.37900	12	0.3
27.77900	85.35700	12	0.2
27.78800	85.36300	12.9	0.2
27.79500	85.50600	13.2	0.2
27.87400	85.62500	7.3	0.2
27.94400	85.64100	5.6	0.4
27.97200	85.67900	7.1	0.4
27.87100	85.53500	8.8	0.1
27.89600	85.54700	8.3	0.1
27.93900	85.54800	7.7	0.2
28.00000	85.52500	7.1	0.2
28.00800	85.51200	7.9	0.1
27.95900	85.46700	9.1	0.3
27.87400	85.41100	9.4	0.3
28.09700	85.34700	6.8	0.1
28.10700	85.32400	9.8	0.2
27.79300	85.37900	12.5	0.1
27.69800	85.47300	14.1	0.1
27.70100	85.48800	14.6	0.1
27.70500	85.50800	15.5	0.2
27.63100	85.61800	15.3	0.2
27.49500	85.07100	22.5	0.5
27.50600	85.09000	17.6	0.2
27.55400	84.89300	20.2	0.2
27.56600	84.90400	<25	
27.57700	84.90700	19.9	0.2
27.73500	84.85400	15.2	0.1
27.73500	84.85400	16.4	0.4
27.73900	84.89900	16.9	0.1
27.69000	84.89500	19.6	0.4
27.63700	84.84800	18.9	0.3
27.62100	84.84000	17.6	0.1
27.58100	84.92400	<22	
27.59700	84.92500	<22	
27.61100	84.94100	17	0.4
27.62000	84.97000	19.9	0.3
27.57900	85.15500	18.4	0.1
27.51700	85.24000	<18	
27.59900	85.12100	19.1	0.3

27.60500	85.07200	<29	
27.48400	85.51000	19.8	0.4
27.47600	85.55500	<18	
28.13600	85.34600	7.5	0.2
28.13500	85.36600	6.4	0.2
28.14500	85.40100	7.4	0.3
28.16200	85.41600	6.9	0.1
28.16900	85.42400	6.8	0.1
28.20300	85.59200	12.3	0.1
28.20900	85.54200	12.1	0.2
28.21100	85.52600	8.8	0.1
28.21400	85.49100	7.3	0.1
28.19100	85.43600	7.8	0.2
28.15800	85.38500	6.8	0.2
27.66600	85.03200	<16	
27.69700	85.00400	<19	
27.69800	84.84300	18.1	0.2
27.96500	85.29400	11.6	0.1
27.87800	85.53300	8.9	0.1
27.89600	85.53900	10.1	0.3
27.94500	85.54500	7.9	0.3
27.95100	85.54000	8.6	0.5
27.96100	85.53400	8.8	0.2
27.97400	85.52900	8.2	0.1
27.98700	85.52700	8.2	0.2
27.91000	85.48200	11.6	0.2
27.88500	85.47300	9.6	0.2
27.88000	85.46700	10.8	0.2
27.86900	85.45400	10.3	0.2
27.86500	85.44900	10.2	0.2
27.86500	85.43800	9	0.1
27.87000	85.39600	9.9	0.1
27.87400	85.39000	10.3	0.1
27.86600	85.38000	11	0.2
27.87300	85.36900	11.7	0.1
27.86700	85.32900	11.4	0.2
27.87400	85.24100	17.1	0.2
27.86800	85.23900	64.7	0.5
27.87900	85.15400	<225	
28.06800	85.42700	10.9	0.1
28.08100	85.40800	10.1	0.1

	28.08700	85.37200	7.5	0.3
	28.09100	85.35900	11.2	0.1
	28.10100	85.33000	8.5	0.1
	28.10000	85.31400	4.9	0.2
	28.09300	85.30700	5.8	0.4
	28.09300	85.30700	13.4	0.2
	28.09300	85.30700	9.3	0.1
	27.75800	85.41700	14.1	0.1
	27.79300	85.34000	13.6	0.1
	28.23200	84.84100	3.1	0.2
	27.91400	84.60900	397.5	0.8
Soucy La Roche et al. 2018	28.98667	81.77632	17.4	0.1
	29.12000	81.88816	21.2	0.1
	29.11333	81.94079	16	2
	29.23333	81.98026	17.3	0.2
	29.24667	82.05921	15.3	0.1
	29.26000	82.09868	14.2	0.1
Coleman and Hodges 1995	28.55452	84.28071	18	0.3
Edwards 1995	28.39669	84.40897	2.6	0.1
	28.34647	84.41424	6	0.1

**Table A.2** The calculated EF and log(EF) for upstream catchments and subcatchments for four detrital samples.

#### MO-217

Age Fraction (Ma)	% of PDP	% Area of Basin	EF	log(EF)
0-4	9.7	3.4	2.8	0.45
4-8	23.3	10.7	2.2	0.34
8-12	28.2	14.7	1.9	0.28
12-16	19.0	21.4	0.9	-0.05
16-20	11.2	23.4	0.5	-0.32
20-24	4.8	16.6	0.3	-0.54
24-28	2.8	4.5	0.6	-0.20
>28	0.9	5.3	0.2	-0.75

#### MO-139

Age Fraction (Ma)	% of PDP	% Area of Basin	EF	log(EF)
0-4	1.0	0.7	1.3	0.13
4-8	20.6	8.9	2.3	0.36
8-12	53.8	11.6	4.6	0.67
12-16	17.5	24.9	0.7	-0.15
16-20	4.8	21.7	0.2	-0.65
20-24	1.1	19.2	0.1	-1.24
24-28	1.1	2.1	0.5	-0.29
>28	0.0	10.8	0.0	

### Guy-2

Age Fraction (Ma)	% of PDP	% Area of Basin	EF	log(EF)
0-4	3.7	0.8	4.5	0.65
4-8	46.0	10.7	4.3	0.63
8-12	34.2	9.7	3.5	0.55
12-16	11.0	25.0	0.4	-0.36
16-20	4.4	24.6	0.2	-0.75
20-24	0.8	21.1	0.0	-1.40
24-28	0.0	0.6	0.0	
>28	0.0	7.5	0.0	

### S24

Age Fraction (Ma)	% of PDP	% Area of Basin	EF	log(EF)
0-4	41.6	8.0	5.2	0.72
4-8	35.0	11.0	3.2	0.51
8-12	15.0	13.8	1.1	0.04
12-16	5.6	16.2	0.3	-0.46
16-20	1.9	33.7	0.1	-1.26
20-24	0.9	11.4	0.1	-1.09
24-28	0.0	1.6	0.0	
>28	0.0	4.4	0.0	

## Appendix B: The Nd Ratios and $\mu$ Nd Values for Enstatite and Ordinary Chondrites and Mantle-derived Melts

**Table B.1** Nd ratios for enstatite chondrites analyzed in this study

Sample	$^{142}\text{Nd}/^{144}\text{Nd}$	$\pm 2\text{SE}$	$^{143}\text{Nd}/^{144}\text{Nd}$	$\pm 2\text{SE}$	$^{145}\text{Nd}/^{144}\text{Nd}$	$\pm 2\text{SE}$	$^{148}\text{Nd}/^{144}\text{Nd}$	$\pm 2\text{SE}$	$^{150}\text{Nd}/^{144}\text{Nd}$	$\pm 2\text{SE}$
<b>UH</b>										
GRO 95517	1.14183377	0.00000410	0.5127001	0.00000170	0.3484049	0.0000011	0.2415839	0.0000017	0.2366377	0.0000077
GRO 95517	1.14182959	0.00000340	0.5126151	0.00000140	0.3484061	0.00000078	0.2415832	0.0000011	0.236535	0.0000022
LAR 06252	1.14183164	0.00000530	0.5126064	0.00000190	0.3484046	0.0000012	0.2415852	0.0000017	0.2365405	0.0000031
MET 01018	1.1418286	0.00000410	0.5125867	0.00000149	0.3484063	0.00000091	0.2415856	0.0000013	0.2364605	0.0000025
MIL 07028	1.14183386	0.00000370	0.512553	0.00000140	0.3484041	0.00000087	0.2415821	0.0000015	0.2364559	0.0000026
PCA 91238	1.14183141	0.0000111	0.5126307	5.36E-06	0.3484015	0.00000292	0.2415833	2.89E-06	0.2364608	5.06E-06
EET 88746	1.14182961	0.00000650	0.5126062	0.00000240	0.3484047	0.00000178	0.2415827	0.0000021	0.2364679	0.0000004
EET 96341	1.14182829	0.00000530	0.5126022	0.00000230	0.3484041	0.0000013	0.2415865	0.0000018	0.2364613	0.0000041
EET 96135	1.14183785	0.00000580	0.5126027	0.00000230	0.3484062	0.0000013	0.2415803	0.0000021	0.2364619	0.0000042
EET 96299	1.14183434	0.00000590	0.512603	0.00000210	0.348406	0.00000126	0.2415823	0.0000023	0.2364538	3.76E-06
LEW 8818C	1.14183383	0.00000560	0.5126006	0.00000220	0.3484055	0.0000012	0.2415838	0.0000019	0.2364608	0.0000036
LEW 87223	1.14183968	0.00000890	0.5125277	0.00000320	0.3484059	0.0000002	0.2415782	0.0000029	0.2364564	0.0000059
MAC 02831	1.14183293	0.00001390	0.5126659	0.00000488	0.348406	0.0000022	0.241584	0.0000041	0.2364636	0.0000061
PCA 91020	1.14181238	0.0000149	0.512652	8.74E-06	0.3484037	0.00000411	0.2415827	4.31E-06	0.2364715	6.35E-06
MAC 02741	1.14183175	0.00000600	0.5126297	0.00000260	0.3484054	0.0000011	0.2415834	0.0000021	0.2364565	0.0000041
ALHA 8102	1.1418300	0.00000455	0.512592	0.00000160	0.3484044	0.0000011	0.2415909	0.0000018	0.2364785	0.0000003
GRO 95628	1.14183212	0.00000800	0.5126327	0.00000300	0.3484055	0.0000019	0.2415874	0.0000026	0.236458	0.0000046
QUE 94204	1.14188605	0.00000502	0.513709	2.22E-06	0.3484049	0.00000127	0.2415798	1.25E-06	0.2364555	2.15E-06
<b>Berlin</b>										
PCA 91461	1.1418277	0.00000414	0.512597	1.68E-06	0.348407	9.44E-07	0.241586	1.37E-06	0.236459	2.82E-06
KLE 98300	1.14183062	0.00000303	0.5125394	1.31E-06	0.3484072	0.00000085	0.2415864	0.0000011	0.2364572	2.27E-06
ALH 84170	1.14182559	0.00000697	0.5126106	1.87E-06	0.3484069	0.00000128	0.2415851	1.98E-06	0.2364578	4.41E-06
EET 96341	1.14183114	0.00000309	0.5126106	1.16E-06	0.3484072	6.97E-07	0.241595	0.0000011	0.2364606	0.0000002
MAC 88131	1.14183058	0.00000368	0.5126338	1.39E-06	0.3484075	0.00000095	0.2415901	1.26E-06	0.2364578	2.48E-06
MAC 88131	1.14182672	0.00000324	0.5126328	1.17E-06	0.348407	7.11E-07	0.2415906	0.0000011	0.236459	1.97E-06

MAC 0274: 1.1418304 0.00000275 0.5126133 0.000001 0.3484074 0.00000056 0.2415886 8.96E-07 0.2364548 1.69E-06

**Table B.1** Continued

Sample	$^{142}\text{Nd}/^{144}\text{Nd}$	$\pm 2\text{SE}$	$^{143}\text{Nd}/^{144}\text{Nd}$	$\pm 2\text{SE}$	$^{145}\text{Nd}/^{144}\text{Nd}$	$\pm 2\text{SE}$	$^{148}\text{Nd}/^{144}\text{Nd}$	$\pm 2\text{SE}$	$^{150}\text{Nd}/^{144}\text{Nd}$	$\pm 2\text{SE}$
Blithfield	1.14175038	0.0000045	0.514062	1.54E-06	0.3484074	0.00000108	0.2415847	1.76E-06	0.2364546	2.92E-06
Blithfield	1.14175015	0.00000317	0.5140612	6.25E-06	0.3484061	6.25E-07	0.2415973	1.24E-06	0.2364707	0.0000021
Blithfield	1.14175277	0.00000289	0.5140623	0.0000011	0.3484071	6.88E-07	0.241583	9.23E-07	0.2364533	1.89E-06
LON 94100	1.14182812	0.00000275	0.512674	0.0000011	0.3484071	0.0000006	0.2415836	8.43E-07	0.2364595	1.87E-06
ALH 81021	1.14182555	0.00000281	0.5127305	9.7E-07	0.3484069	6.23E-07	0.2415892	9.4E-07	0.2364489	1.86E-06

**Table B.2** Nd ratios for mantle-derived melt samples analyzed in this study

Sample	$^{142}\text{Nd}/^{144}\text{Nd}$	$\pm 2\text{SE}$	$^{143}\text{Nd}/^{144}\text{Nd}$	$\pm 2\text{SE}$	$^{145}\text{Nd}/^{144}\text{Nd}$	$\pm 2\text{SE}$	$^{148}\text{Nd}/^{144}\text{Nd}$	$\pm 2\text{SE}$	$^{150}\text{Nd}/^{144}\text{Nd}$	$\pm 2\text{SE}$
UH										
ICE9a-3245	1.14183547	0.00000475	0.5130293	2.11E-06	0.3484008	0.00000109	0.2415827	1.35E-06	0.2364532	2.07E-06
ICE9a-3296	1.14183723	0.0000015	0.5130324	9.4E-07	0.3484021	0.00000043	0.2415803	3.9E-07	0.2364532	8.5E-07
ICE9a-3497	1.14183602	0.0000026	0.5130345	1.24E-06	0.3484043	6.03E-07	0.2415783	6.9E-07	0.2364554	1.17E-06
ICE9a-3502	1.14184429	0.00000288	0.5130368	1.49E-06	0.3484032	7.11E-07	0.2415791	0.0000008	0.2364554	0.0000015
ICE9a-3503	1.14184397	0.00000497	0.5130319	2.59E-06	0.3484022	0.00000125	0.2415775	1.39E-06	0.236453	2.41E-06
ICE9a-3504	1.14184751	0.0000028	0.51303389	0.0000012	0.3484031	5.97E-07	0.2415797	7.5E-07	0.2364539	1.33E-06
Berlin										
Biu8 Basalt	1.14183273	0.00000249	0.5129108	0.0000010	0.3484066	6.18E-07	0.2415804	#####	0.2364539	1.68E-06
Komatit	1.14183851	0.00000349	0.513003	0.0000015	0.3484062	8.46E-07	0.2416088	1.35E-06	0.2364564	2.43E-06
Miringa Basalt	1.14183914	0.00000441	0.5129498	1.58E-06	0.3484059	9.97E-07	0.241582	1.58E-06	0.2364487	2.46E-06

**Table B.3** Enstatite chondrite Nd isotope compositions from this study and literature used in weighted group averages. References for all tables are at the end of Appendix.

Reference	Sample	$\mu^{142}\text{Nd}$	$\mu^{142}\text{Nd}_{\text{corr.}}$	$\pm 2\text{SE}$	$\mu^{145}\text{Nd}$	$\pm 2\text{SE}$	$\mu^{148}\text{Nd}$	$\pm 2\text{SE}$	$\mu^{150}\text{Nd}$	$\pm 2\text{SE}$	
Enstatite Chondrites											
EH											
[5]	Sahara 97072	EH3	-16.10	-10.60	4.3	13.50	8.4	14.70	8.4	6.40	3.1
[5]	Sahara 97072	EH3	-11.20	-6.48	8.0	0.00	2.1	6.70	1.1	27.40	8.2
[5]	Sahara 97096	EH3	-19.90	-17.46	4.3	2.50	7.2	15.80	14.3	18.20	31.5
[5]	Sahara 97158	EH3	-13.90	-10.54	9.9	9.20	8.0	0.30	14.1	53.10	17.1
[5]	ALHA 77295	EH3	-2.30	-1.10	7.4	4.30	5.8	16.10	10.4	46.40	14.1
[15]	ALHA 77295	EH3	-10.90	-8.70	5.6	0.00	5.9	-7.90	9.0	19.00	11.8
[8]	Y 691	EH3	-14.00	-12.00	5.7	23.00	37.0	8.80	7.5	11.00	12.0
[10]	PCA91238	EH3	-0.68	-0.68	9.7	-3.70	8.4	8.52	12.0	32.08	21.4
[10]	MET 01018	EH3	-12.36	-10.18	3.6	3.15	2.6	14.97	5.4	34.42	10.6
[10]	GRO 95517	EH3	-7.83	-11.36	3.6	-0.81	3.2	7.77	7.0	783.87	32.5
[10]	LAR 06252	EH3	-9.69	-8.51	4.6	-1.70	3.4	13.28	7.0	372.92	13.1
[10]	MIL 07028	EH3	-7.75	-3.87	3.2	-3.19	2.5	0.53	6.2	15.22	11.0
[10]	GRO 95517	EH3	-11.49	-10.74	3.0	2.49	2.2	5.00	4.6	349.75	9.3
[9]	SAH97159	EH3	-17.10	-12.60	4.1	3.90	5.3	7.20	9.9	10.80	8.3
[4]	Indarch	EH4	-14.60	-14.30	5.0	4.00	6.0	-6.00	8.0	-20.00	11.0
[5]	Indarch	EH4	-17.70	-17.40	7.3	-0.30	6.0	0.70	9.7	17.20	13.9
[6]	Abee	EH4	-18.90	-7.40	6.0	-3.00	6.0	3.00	7.0	8.00	24.0
[6]	Abee	EH4	-5.50	1.40	8.0	8.00	13.0	1.00	15.0	22.00	31.0
[6]	Indarch	EH4	-13.50	-13.10	6.0	-1.00	6.0	3.00	7.0	0.00	24.0
[6]	Indarch	EH4	-16.30	-15.30	8.0	7.00	13.0	2.00	15.0	12.00	31.0
[10]	EET 88746	EH4	-11.47	-10.27	5.7	-1.44	5.1	2.84	8.7	65.76	16.9
[10]	EET 96135	EH4/5	-4.26	-2.88	5.1	2.83	3.7	-7.13	8.7	40.30	17.8
[10]	EET 96299	EH4/5	-7.33	-5.97	5.2	2.14	3.6	1.23	9.5	6.08	15.9
[10]	EET 96341	EH4/5	-12.63	-11.23	4.6	-3.08	3.7	18.62	7.5	37.97	17.3
[5]	St. Mark's	EH5	-17.00	-15.70	5.9	7.30	7.3	18.60	3.8	24.80	24.4
[10]	LEW 88180	EH5	-7.78	-6.30	4.9	0.91	3.4	7.48	7.9	35.65	15.2



[6]	Saint Sauvier	EH6	-10.00	-9.70	5.0	5.00	9.0	5.00	5.0	-5.00	24.0
[8]	Y 980223	EH6	-24.00	-15.00	5.1	-16.00	27.0	5.70	5.9	15.00	11.0
<b>EL</b>											
[5]	MAC 02839	EL3	-4.20	-4.80	2.1	-1.30	7.1	-11.90	20.5	2.70	32.4
[5]	MAC 02837	EL3	-4.40	-5.50	4.1	-5.30	4.8	-25.80	29.0	-14.10	51.8
[15]	MAC 02839	EL3	-5.00	-1.80	6.8	-1.90	6.4	-4.70	19.0	115.00	8.6
[15]	MAC 02837	EL3	-11.40	-9.60	3.2	0.80	3.3	5.40	5.2	56.90	7.6
[5]	MAC 88180	EL3	3.10	-1.90	4.8	5.80	1.6	-8.20	4.8	-11.90	6.3
[15]	MS-177	EL3	-10.90	-1.10	5.7	5.70	4.1	9.90	7.4	11.50	11.5
[10]	PCA 91020	EL3	-17.35	-18.42	13.0	2.67	11.8	6.08	17.8	77.12	26.9
[10]	MAC 02839	EL3	-8.57	-10.37	12.2	2.14	6.3	8.18	17.0	47.74	25.8
[10]	LEW 87223	EL3	-2.65	2.49	7.8	2.00	5.7	-15.53	12.0	17.21	25.0
[10]	MAC 02747	EL4	-9.60	-9.58	5.3	0.68	3.2	5.78	8.7	17.46	17.3
[5]	Hvittis	EL6	-1.80	-7.70	5.5	16.10	4.9	17.30	8.1	119.80	10.2
[5]	Khairpur	EL6	-13.20	-13.40	5.1	-10.30	4.1	-18.50	7.2	-25.40	9.5
[5]	Eagle 4725	EL6	-10.90	-14.20	6.0	1.90	4.7	1.50	8.3	0.10	11.2
[6]	Hvittis	EL6	-6.30	-12.78	5.0	5.00	9.0	2.00	5.0	-10.00	24.0
[6]	Hvittis	EL6	-3.50	-9.50	6.0	2.00	6.0	4.00	7.0	26.00	24.0
[6]	Hvittis	EL6	-9.60	-16.30	8.0	7.00	13.0	0.00	15.0	0.00	31.0
[6]	Atlanta	EL6	-4.60	-12.40	6.0	2.00	6.0	2.00	7.0	-3.00	24.0
[6]	Atlanta	EL6	-8.40	-16.30	8.0	2.00	13.0	-2.00	15.0	15.00	31.0
[6]	Blithfield	EL6	22.00	-18.80	6.0	4.00	6.0	-1.00	7.0	11.00	24.0
[6]	Blithfield	EL6	-8.50	-10.00	8.0	4.00	13.0	5.00	15.0	22.00	31.0
[9]	NWA 8552	EL6	14.20	-7.00	9.5	1.20	7.1	0.00	15.0	15.00	18.0
[10]	ALHA 81021	EL6	-11.13	-9.22	4.0	-2.30	3.2	36.83	7.5	110.67	12.7
[10]	GRO 95626	EL6	-9.27	-9.41	7.0	0.91	5.5	22.38	10.8	23.93	19.5
<b>Aubrite</b>											
[10]	QUE 94204		47.17	-7.10	4.4	6.08	3.6	-5.80	5.2	9.29	9.1

**Table B.4** Mantle-derived melt Nd isotope compositions from this study and literature used in weighted group averages of the Bulk Silicate Earth. References for all tables are at the end of Appendix.

Reference	Sample	$\mu^{142}\text{Nd}$	$\mu^{142}\text{Nd}_{\text{corr.}}$	$\pm 2\text{SE}$	$\mu^{145}\text{Nd}$	$\pm 2\text{SE}$	$\mu^{148}\text{Nd}$	$\pm 2\text{SE}$	$\mu^{150}\text{Nd}$	$\pm 2\text{SE}$
<b>Earth</b>										
[10]	ICE9a-3249	2.87		4.2	-5.80	3.1	6.16	5.6	-0.10	8.8
[10]	ICE9a-3296	4.41		1.3	-2.01	1.2	-3.73	1.6	-0.19	3.6
[10]	ICE9a-3497	3.35		2.3	4.25	1.7	-12.26	2.9	9.20	4.9
[10]	ICE9a-3502	10.36		2.5	0.82	2.0	-8.44	3.3	9.01	6.3
[10]	ICE9a-3503	10.08		4.4	-2.19	3.6	-14.90	5.8	-1.09	10.2
[11]	<i>H-5</i>	3.22		2.9	-4.31	2.3	4.61	4.6	9.93	9.7
[11]	<i>H-11</i>	1.73		3.3	-4.59	3.4	20.34	6.6	4.01	12.3
[11]	<i>H-23</i>	-1.43		3.4	-4.31	2.6	7.51	6.6	17.96	14.4
[11]	<i>KOOCF.f1</i>	3.65		2.1	-3.44	1.7	0.89	2.9	-4.87	6.8
[11]	<i>KOOCF.f2</i>	2.60		2.1	-2.01	1.7	1.30	3.3	-1.49	6.3
[11]	<i>KOOCF.f2.rpt</i>	3.92		2.1	-1.44	1.7	2.13	3.3	6.97	6.8
[11]	<i>LO-0201.f1</i>	2.25		2.5	-0.86	2.0	2.54	4.6	-1.91	8.5
[11]	<i>LO-0201.f2</i>	0.76		2.2	-2.87	1.4	-2.01	3.7	-13.76	5.9
[11]	<i>MK-1-6</i>	1.46		2.6	-2.30	3.2	-0.77	4.1	-17.56	8.9
[11]	<i>83</i>	2.25		1.9	-0.29	1.4	0.47	2.9	-5.72	5.5
[11]	<i>83.rpt</i>	3.83		1.7	-0.57	1.4	-4.08	2.9	-12.06	5.5
[11]	<i>83A</i>	-2.48		1.9	2.30	1.4	-4.49	3.3	-9.53	6.3
[11]	<i>83A.rpt</i>	-1.34		1.6	0.86	1.4	-3.25	2.5	-6.99	5.1
[11]	<i>173-2</i>	0.24		1.8	2.58	1.4	-3.67	2.9	-11.64	5.5
[11]	<i>ICE 3</i>	3.30		2.9	2.30	1.7	8.34	2.9	25.58	5.9
[11]	<i>ICE 8a</i>	-0.11		2.1	2.01	1.7	8.75	3.7	17.12	6.3
[11]	<i>ICE10(1)</i>	-0.29		2.6	-0.29	2.0	-2.01	4.6	-4.87	8.0
[11]	<i>ICE10(2)</i>	0.41		3.2	-1.15	2.3	4.61	5.4	4.01	8.9

[11] ICE10(3) 1.03 3.0 -2.87 2.0 20.34 5.0 18.39 10.1

**Table B.5** Ordinary chondrite Nd isotopic compositions from literature used in weighted group averages. References for all tables are at the end of Appendix.

Reference	Sample	$\mu^{142}\text{Nd}$	$\mu^{142}\text{Nd}_{\text{corr.}}$	$\pm 2\text{SE}$	$\mu^{145}\text{Nd}$	$\pm 2\text{SE}$	$\mu^{148}\text{Nd}$	$\pm 2\text{SE}$	$\mu^{150}\text{Nd}$	$\pm 2\text{SE}$	
Ordinary Chondrites											
H											
[1]	Sharps	H3.4	-16.20	-15.90	4.1	8.50	3.1	1.60	5.0	-13.30	7.7
[1]	Sharps	H3.4	-13.90	-13.90	6.1	7.20	4.5	-2.40	8.1	-13.20	11.5
[1]	Dhajala	H3.8	-19.27	-18.90	7.0	5.74	5.7	-4.14	8.3	0.00	12.7
[4]	Gladstone	H4	-19.00	-19.20	5.0	7.00	6.0	-6.00	11.0	-21.00	14.0
[7]	Kesen	H4	-12.00	-12.00	4.9	-4.40	14.0	15.00	4.9	27.00	12.0
[6]	Sainte Marguerite	H4	-16.00	-16.60	6.0	10.00	6.0	11.00	7.0	21.00	24.0
[6]	Sainte Marguerite	H4	-24.40	-24.70	8.0	10.00	13.0	6.00	15.0	18.00	31.0
[1]	Richardton	H5	-24.52	-23.70	11.4	2.87	8.6	20.70	16.6	-16.92	21.1
[1]	Richardton Bomb	H5	-19.27	-19.20	7.9	2.87	5.7	8.28	12.4	-29.60	12.7
[4]	Ucera	H5	-22.00	-22.70	5.0	1.00	6.0	12.00	10.0	93.00	13.0
[5]	Jilin	H5	-22.40	-19.43	5.0	2.90	2.6	4.50	15.5	-11.30	18.5
[6]	Allegan	H5	-16.10	-15.38	5.0	5.00	9.0	11.00	6.0	25.00	24.0
[6]	Forest City	H5	-18.60	-16.99	5.0	5.00	9.0	4.00	6.0	7.00	24.0
[7]	Forest City	H5	-12.00	-12.00	7.4	17.00	27.0	11.00	7.6	17.00	19.0
[6]	Pultusk	H5	-16.00	-19.00	8.0	13.00	13.0	11.00	15.0	18.00	31.0
[8]	Forest City	H5	-12.00	-12.00	7.4	17.00	27.0	11.00	7.6	17.00	19.0
[6]	Queens Mercy	H6	-19.80	-18.17	5.0	2.00	9.0	6.00	5.0	16.00	24.0
L											
[9]	NWA5697 (1)	L3	-16.00	-13.40	1.7	4.64	0.9	7.70	5.3	9.40	3.7
[9]	NWA5697 (2)	L3	-14.90	-12.00	2.3	5.20	2.9	9.70	3.6	16.10	4.9
[9]	NWA5697 (3)	L3	-12.00	-7.80	3.2	-0.10	4.2	7.80	4.0	12.50	3.6
[12]	QUE 97008 leach 1	L3.05	-201.00		1.0	73.00	5.0	111.00	7.0	148.00	8.0
[12]	QUE 97008 leach 2	L3.05	-139.00		8.0	40.00	6.0	48.00	2.0	38.00	2.0

[12]	QUE 97008 leach 3	L3.05	-35.00		1.0	8.00	2.0	4.00	2.0	-1.00	15.0
[12]	QUE 97008 residue	L3.05	60.00		2.0	-17.00	2.0	-43.00	2.0	-64.00	9.0
[12]	QUE 97008 WR	L3.05	-18.00		4.0	7.00	2.0	3.00	2.0	-14.00	6.0
[8]	Saratov	L4	-14.00	-13.00	5.1	6.80	16.0	13.00	5.9	20.00	11.0
[7]	Etter	L5	-16.00	-15.00	4.0	-12.00	27.0	8.90	4.6	19.00	7.4
[6]	Farmington	L5	-15.90	-14.00	6.0	10.00	6.0	10.00	7.0	24.00	24.0
[4]	Homestead	L5	-20.00	-19.60	3.0	2.00	3.0	-1.00	6.0	-17.00	8.0
[9]	SAH97172	L5	-6.70	-3.70	1.8	0.50	1.4	4.60	3.5	9.30	8.8
[6]	Bruderheim	L6	-19.40	-16.10	5.0	2.00	9.0	1.00	5.0	12.00	24.0
[1]	Bruderheim	L6	-8.76	-8.10	7.9	2.87	5.7	-16.56	12.4	-25.38	12.7
[8]	Modoc	L6	-19.00	-13.00	5.1	-6.10	16.0	8.10	59.0	6.00	11.0
[4]	Peace River	L6	-17.30	-17.80	8.0	22.10	9.0	0.40	14.0	26.20	19.0

## LL

[7]	Hamlet	LL4	-7.50	-7.20	4.9	2.40	15.0	10.00	5.1	35.00	12.0
[6]	Chelyabinsk	LL5	-18.30	-19.19	5.0	2.00	9.0	3.00	4.0	8.00	24.0
[8]	Tuxtuac	LL5	-11.00	-12.00	5.1	-7.30	16.0	64.00	5.9	13.00	11.0
[8]	Saint-Severin	LL6	-12.00	-8.90	7.8	-5.70	14.0	10.00	12.0	23.00	12.0
[2]	St. Severin	LL6	-21.00	-17.50	9.0	14.35	8.6	37.26	12.4	236.84	16.9
[6]	Dhurmsala	LL6	-14.30	-14.65	5.0	0.00	9.0	9.00	5.0	22.00	24.0

## References for all Tables

- [1] Boyet and Carlson, 2005
- [2] Andreasen and Sharma, 2006
- [3] Rankenburg et al., 2006
- [4] Carlson et al., 2007
- [5] Gannoun et al., 2011
- [6] Burkhardt et al., 2016
- [7] Fukai and Yokoyama, 2017

- [8] Fukai and Yokoyama, 2019
- [9] Saji et al., 2020
- [10] This Study - UH
- [11] Murphy et al., 2010
- [12] Qin et al., 2011
- [13] Brennecka et al., 2013
- [14] Marks et al., 2014
- [15] Bouvier and Boyet, 2016
- [16] Boyet et al., 2018
- [17] Render and Brennecka, 2021

## Appendix C: All $\mu$ Nd Values for Solar System Materials

**Table C.1**

Carbonaceous chondrite Nd isotope compositions from this study and literature used in weighted group averages. References for all tables are at the end of the Appendix.

Ref.	Sample	$\mu^{142}\text{Nd}$	$\mu^{142}\text{Nd}_{\text{corr.}}$	$\pm 2\text{SE}$	$\mu^{145}\text{Nd}$	$\pm 2\text{SE}$	$\mu^{148}\text{Nd}$	$\pm 2\text{SE}$	$\mu^{150}\text{Nd}$	$\pm 2\text{SE}$
<b>CV</b>										
[1]	Allende	-36.60	-32.90	7.0	4.00	3.8	7.30	7.2	4.80	10.3
[1]	Allende	-33.90	-30.30	7.0	4.40	5.4	-2.30	9.6	-20.70	13.3
[1]	Allende Bomb	-29.70	-27.00	8.0	0.30	4.5	-6.30	8.2	-27.90	10.9
[1]	Allende	-32.00	-28.70	7.1	1.60	5.4	1.00	9.8	-12.50	13.2
[5]	Allende	-21.80	-23.60	1.5	-1.80	15.4	14.20	19.9	14.10	32.5
[2]	Allende	-30.00	-24.95	6.0	2.87	2.9	8.28	8.3	-4.23	8.5
[3]	Allende	-41.00	-39.30	5.0	3.00	1.0	6.00	5.0	118.00	6.7
[4]	Allende	-40.00	-36.90	4.0	17.00	5.0	21.00	8.0	-4.00	11.0
[6]	Allende	-30.00	-31.00	5.0	2.00	9.0	9.00	4.0	8.00	24.0
[6]	Allende	-30.00	-31.44	6.0	5.00	6.0	4.00	7.0	-6.00	24.0
[6]	Allende	-33.00	-33.00	8.0	8.00	13.0	16.00	15.0	11.00	31.0
[8]	Allende	-32.00	-31.00	7.5	-1.10	16.0	19.00	16.0	27.00	26.0
[10]	Allende	-34.33	-32.38	6.4	0.89	5.9	5.71	7.9	79.79	16.4
[10]	ALH 84028	-21.40	-23.10	6.1	10.39	5.7	20.77	9.6	169.83	13.4
[10]	EET 96026	-24.46	-24.19	5.3	2.21	5.6	10.34	10.3	27.60	19.6
[10]	LAR 12002	-34.58	-34.23	6.6	16.62	5.0	30.50	9.5	146.95	13.7
[10]	GRA 06101	-39.29	-35.07	6.8	-0.06	5.1	53.48	8.0	51.92	12.5
[4]	Grosnaja	-7.00	-17.20	4.0	-8.00	4.0	-1.00	6.0	-12.00	10.0
[4]	Mokoia	-34.00	-34.90	5.0	5.00	5.0	13.00	8.0	10.00	11.0
<b>CM</b>										
[4]	Cold Bokkveid	-42.00	-42.20	7.0	6.00	7.0	16.00	12.0	12.00	17.0
[4]	Mighei	-45.00	-44.40	7.0	12.00	7.0	41.00	13.0	59.00	18.0
[4]	Murray	-38.00	-38.50	8.0	9.00	8.0	19.00	15.0	-1.00	19.0

[2]	Murchison	CM2	-26.00	-22.55	5.0	2.87	2.9	24.84	8.3	38.06	8.5
[9]	Jbilet	CM2	-26.80	-21.80	1.4	6.50	1.3	20.90	1.2	24.90	3.8
[8]	Murchison	CM2	-31.00	-31.00	7.4	2.10	16.0	23.00	13.0	24.00	24.0
<b>CK</b>											
[10]	SZA 12420	CK4	-27.14	-30.49	6.2	0.43	4.3	4.84	7.7	36.48	14.3
[10]	ALH 85002	CK4	-30.98	-29.15	6.0	4.05	5.0	2.81	8.0	10.39	10.3
[10]	EET 92002	CK5	-46.87	-38.78	4.7	4.51	3.9	22.72	4.6	42.53	10.6
[10]	EET 90015	CK5	-16.63	-23.52	13.8	13.06	7.7	0.49	17.9	11.19	26.2
[10]	LAR 06872	CK6	-33.47	-28.55	5.5	5.83	4.3	31.62	7.7	27.30	14.0
[10]	LEW 87009	CK6	-17.17	-15.65	8.8	-3.44	8.0	17.88	15.9	38.77	25.3
<b>CO</b>											
[9]	SAH 99544	CO3	-15.20	-14.20	1.2	5.90	1.9	9.30	2.2	10.90	5.0
[7]	DaG 190	CO3	-34.00	-34.00	4.0	19.00	27.0	22.00	4.6	27.00	7.4
[7]	NWA 2090*	CO3	-5.60		5.1	-6.70	48.0	0.80	5.9	4.30	11.0
[8]	Kainsaz	CO3.2	-35.00		4.8	3.70	20.0	21.00	5.6	26.00	10.0
<b>CR</b>											
[9]	NWA 6043*	CR2	-37.00	-36.40	11.0	3.10	3.8	28.00	10.0	60.60	2.2
[7]	Dho 1432	CR2	-28.00	-30.00	3.8	16.00	15.0	18.00	5.4	26.00	9.5
<b>CI</b>											
[4]	Orgueil	CI1	-28.00	-28.50	12.0	-21.00	13.0	-5.00	20.0	-29.00	28.0
[9]	Ivuna	CI1	-14.60	-14.60	4.9	-0.10	2.3	0.40	2.1	3.70	4.7
[8]	Orgueil	CI1	-21.00	-21.00	3.0	5.80	3.6	2.00	4.8	-2.10	8.9

\* These samples were not used in the group averages.

**Table C.2** Nd isotope compositions of chondrites, achondrites, and earth samples used to evaluate excess  $^{150}\text{Nd}$  in solar system materials. References for all tables are at the end of the Appendix.

Reference	Sample		$\mu^{142}\text{Nd}$	$\mu^{142}\text{Nd}_{\text{corr.}}$	$\pm 2\text{SE}$	$\mu^{145}\text{Nd}$	$\pm 2\text{SE}$	$\mu^{148}\text{Nd}$	$\pm 2\text{SE}$	$\mu^{150}\text{Nd}$	$\pm 2\text{SE}$
Ordinary Chondrites											
H											
[1]	Sharps	H3.4	-16.20	-15.90	4.1	8.50	3.1	1.60	5.0	-13.30	7.7
[1]	Sharps	H3.4	-13.90	-13.90	6.1	7.20	4.5	-2.40	8.1	-13.20	11.5
[1]	Dhajala	H3.8	-19.27	-18.90	7.0	5.74	5.7	-4.14	8.3	0.00	12.7
[4]	Gladstone	H4	-19.00	-19.20	5.0	7.00	6.0	-6.00	11.0	-21.00	14.0
[7]	Kesen	H4	-12.00	-12.00	4.9	-4.40	14.0	15.00	4.9	27.00	12.0
[6]	Sainte Marguerite	H4	-16.00	-16.60	6.0	10.00	6.0	11.00	7.0	21.00	24.0
[6]	Sainte Marguerite	H4	-24.40	-24.70	8.0	10.00	13.0	6.00	15.0	18.00	31.0
[1]	Richardton	H5	-24.52	-23.70	11.4	2.87	8.6	20.70	16.6	-16.92	21.1
[1]	Richardton Bomb	H5	-19.27	-19.20	7.9	2.87	5.7	8.28	12.4	-29.60	12.7
[4]	Ucera	H5	-22.00	-22.70	5.0	1.00	6.0	12.00	10.0	93.00	13.0
[5]	Jilin	H5	-22.40	-19.43	5.0	2.90	2.6	4.50	15.5	-11.30	18.5
[6]	Allegan	H5	-16.10	-15.38	5.0	5.00	9.0	11.00	6.0	25.00	24.0
[6]	Forest City	H5	-18.60	-16.99	5.0	5.00	9.0	4.00	6.0	7.00	24.0
[7]	Forest City	H5	-12.00	-12.00	7.4	17.00	27.0	11.00	7.6	17.00	19.0
[6]	Pultusk	H5	-16.00	-19.00	8.0	13.00	13.0	11.00	15.0	18.00	31.0
[8]	Forest City	H5	-12.00	-12.00	7.4	17.00	27.0	11.00	7.6	17.00	19.0
[6]	Queens Mercy	H6	-19.80	-18.17	5.0	2.00	9.0	6.00	5.0	16.00	24.0
L											
[9]	NWA5697 (1)	L3	-16.00	-13.40	1.7	4.64	0.9	7.70	5.3	9.40	3.7



[9]	NWA5697 (2)	L3	-14.90	-12.00	2.3	5.20	2.9	9.70	3.6	16.10	4.9
[9]	NWA5697 (3)	L3	-12.00	-7.80	3.2	-0.10	4.2	7.80	4.0	12.50	3.6
[12]	QUE 97008 leach 1	L3.05	-201.00		1.0	73.00	5.0	111.00	7.0	148.00	8.0
[12]	QUE 97008 leach 2	L3.05	-139.00		8.0	40.00	6.0	48.00	2.0	38.00	2.0
[12]	QUE 97008 leach 3	L3.05	-35.00		1.0	8.00	2.0	4.00	2.0	-1.00	15.0
[12]	QUE 97008 residue	L3.05	60.00		2.0	-17.00	2.0	-43.00	2.0	-64.00	9.0
[12]	QUE 97008 WR	L3.05	-18.00		4.0	7.00	2.0	3.00	2.0	-14.00	6.0
[8]	Saratov	L4	-14.00	-13.00	5.1	6.80	16.0	13.00	5.9	20.00	11.0
[7]	Etter	L5	-16.00	-15.00	4.0	-12.00	27.0	8.90	4.6	19.00	7.4
[6]	Farmington	L5	-15.90	-14.00	6.0	10.00	6.0	10.00	7.0	24.00	24.0
[4]	Homestead	L5	-20.00	-19.60	3.0	2.00	3.0	-1.00	6.0	-17.00	8.0
[9]	SAH97172	L5	-6.70	-3.70	1.8	0.50	1.4	4.60	3.5	9.30	8.8
[6]	Bruderheim	L6	-19.40	-16.10	5.0	2.00	9.0	1.00	5.0	12.00	24.0
[1]	Bruderheim	L6	-8.76	-8.10	7.9	2.87	5.7	-16.56	12.4	-25.38	12.7
[8]	Modoc	L6	-19.00	-13.00	5.1	-6.10	16.0	8.10	59.0	6.00	11.0
[4]	Peace River	L6	-17.30	-17.80	8.0	22.10	9.0	0.40	14.0	26.20	19.0

## LL

[7]	Hamlet	LL4	-7.50	-7.20	4.9	2.40	15.0	10.00	5.1	35.00	12.0
[6]	Chelyabinsk	LL5	-18.30	-19.19	5.0	2.00	9.0	3.00	4.0	8.00	24.0
[8]	Tuxtuac	LL5	-11.00	-12.00	5.1	-7.30	16.0	64.00	5.9	13.00	11.0
[8]	Saint-Severin	LL6	-12.00	-8.90	7.8	-5.70	14.0	10.00	12.0	23.00	12.0
[2]	St. Severin	LL6	-21.00	-17.50	9.0	14.35	8.6	37.26	12.4	236.84	16.9
[6]	Dhurmsala	LL6	-14.30	-14.65	5.0	0.00	9.0	9.00	5.0	22.00	24.0

Reference	Sample	$\mu^{142}\text{Nd}$	$\mu^{142}\text{Nd}_{\text{corr.}}$	$\pm 2\text{SE}$	$\mu^{143}\text{Nd}$	$\pm 2\text{SE}$	$\mu^{140}\text{Nd}$	$\pm 2\text{SE}$	$\mu^{150}\text{Nd}$	$\pm 2\text{SE}$	
Enstatite Chondrites											
EH											
[5]	Sahara 97072	EH3	-16.10	-10.60	4.3	13.50	8.4	14.70	8.4	6.40	3.1
[5]	Sahara 97072	EH3	-11.20	-6.48	8.0	0.00	2.1	6.70	1.1	27.40	8.2

[5]	Sahara 97096	EH3	-19.90	-17.46	4.3	2.50	7.2	15.80	14.3	18.20	31.5
[5]	Sahara 97158	EH3	-13.90	-10.54	9.9	9.20	8.0	0.30	14.1	53.10	17.1
[5]	ALHA 77295	EH3	-2.30	-1.10	7.4	4.30	5.8	16.10	10.4	46.40	14.1
[15]	ALHA77295	EH3	-10.90	-8.70	5.6	0.00	5.9	-7.90	9.0	19.00	11.8
[8]	Y 691	EH3	-14.00	-12.00	5.7	23.00	37.0	8.80	7.5	11.00	12.0
[10]	PCA91238	EH3	-0.68	-0.68	9.7	-3.70	8.4	8.52	12.0	32.08	21.4
[10]	MET 01018	EH3	-12.36	-10.18	3.6	3.15	2.6	14.97	5.4	34.42	10.6
[10]	GRO 95517	EH3	-7.83	-11.36	3.6	-0.81	3.2	7.77	7.0	783.87	32.5
[10]	LAR 06252	EH3	-9.69	-8.51	4.6	-1.70	3.4	13.28	7.0	372.92	13.1
[10]	MIL 07028	EH3	-7.75	-3.87	3.2	-3.19	2.5	0.53	6.2	15.22	11.0
[10]	GRO 95517	EH3	-11.49	-10.74	3.0	2.49	2.2	5.00	4.6	349.75	9.3
[9]	SAH97159	EH3	-17.10	-12.60	4.1	3.90	5.3	7.20	9.9	10.80	8.3
[4]	Indarch	EH4	-14.60	-14.30	5.0	4.00	6.0	-6.00	8.0	-20.00	11.0
[5]	Indarch	EH4	-17.70	-17.40	7.3	-0.30	6.0	0.70	9.7	17.20	13.9
[6]	Abee	EH4	-18.90	-7.40	6.0	-3.00	6.0	3.00	7.0	8.00	24.0
[6]	Abee	EH4	-5.50	1.40	8.0	8.00	13.0	1.00	15.0	22.00	31.0
[6]	Indarch	EH4	-13.50	-13.10	6.0	-1.00	6.0	3.00	7.0	0.00	24.0
[6]	Indarch	EH4	-16.30	-15.30	8.0	7.00	13.0	2.00	15.0	12.00	31.0
[10]	EET 88746	EH4	-11.47	-10.27	5.7	-1.44	5.1	2.84	8.7	65.76	16.9
[10]	EET 96135	EH4/5	-4.26	-2.88	5.1	2.83	3.7	-7.13	8.7	40.30	17.8
[10]	EET 96299	EH4/5	-7.33	-5.97	5.2	2.14	3.6	1.23	9.5	6.08	15.9
[10]	EET 96341	EH4/5	-12.63	-11.23	4.6	-3.08	3.7	18.62	7.5	37.97	17.3
[5]	St. Mark's	EH5	-17.00	-15.70	5.9	7.30	7.3	18.60	3.8	24.80	24.4
[10]	LEW 88180	EH5	-7.78	-6.30	4.9	0.91	3.4	7.48	7.9	35.65	15.2
[6]	Saint Sauvier	EH6	-10.00	-9.70	5.0	5.00	9.0	5.00	5.0	-5.00	24.0
[8]	Y 980223	EH6	-24.00	-15.00	5.1	-16.00	27.0	5.70	5.9	15.00	11.0

# EL

[5]	MAC 02839	EL3	-4.20	-4.80	2.1	-1.30	7.1	-11.90	20.5	2.70	32.4
[5]	MAC 02837	EL3	-4.40	-5.50	4.1	-5.30	4.8	-25.80	29.0	-14.10	51.8
[15]	MAC 02839	EL3	-5.00	-1.80	6.8	-1.90	6.4	-4.70	19.0	115.00	8.6

[15]	MAC 02837	EL3	-11.40	-9.60	3.2	0.80	3.3	5.40	5.2	56.90	7.6
[5]	MAC 88180	EL3	3.10	-1.90	4.8	5.80	1.6	-8.20	4.8	-11.90	6.3
[15]	MS-177	EL3	-10.90	-1.10	5.7	5.70	4.1	9.90	7.4	11.50	11.5
[10]	PCA 91020	EL3	-17.35	-18.42	13.0	2.67	11.8	6.08	17.8	77.12	26.9
[10]	MAC 02839	EL3	-8.57	-10.37	12.2	2.14	6.3	8.18	17.0	47.74	25.8
[10]	LEW 87223	EL3	-2.65	2.49	7.8	2.00	5.7	-15.53	12.0	17.21	25.0
[10]	MAC 02747	EL4	-9.60	-9.58	5.3	0.68	3.2	5.78	8.7	17.46	17.3
[5]	Hvittis	EL6	-1.80	-7.70	5.5	16.10	4.9	17.30	8.1	119.80	10.2
[5]	Khairpur	EL6	-13.20	-13.40	5.1	-10.30	4.1	-18.50	7.2	-25.40	9.5
[5]	Eagle 4725	EL6	-10.90	-14.20	6.0	1.90	4.7	1.50	8.3	0.10	11.2
[6]	Hvittis	EL6	-6.30	-12.78	5.0	5.00	9.0	2.00	5.0	-10.00	24.0
[6]	Hvittis	EL6	-3.50	-9.50	6.0	2.00	6.0	4.00	7.0	26.00	24.0
[6]	Hvittis	EL6	-9.60	-16.30	8.0	7.00	13.0	0.00	15.0	0.00	31.0
[6]	Atlanta	EL6	-4.60	-12.40	6.0	2.00	6.0	2.00	7.0	-3.00	24.0
[6]	Atlanta	EL6	-8.40	-16.30	8.0	2.00	13.0	-2.00	15.0	15.00	31.0
[6]	Blithfield	EL6	22.00	-18.80	6.0	4.00	6.0	-1.00	7.0	11.00	24.0
[6]	Blithfield	EL6	-8.50	-10.00	8.0	4.00	13.0	5.00	15.0	22.00	31.0
[9]	NWA 8552	EL6	14.20	-7.00	9.5	1.20	7.1	0.00	15.0	15.00	18.0
[10]	ALHA 81021	EL6	-11.13	-9.22	4.0	-2.30	3.2	36.83	7.5	110.67	12.7
[10]	GRO 95626	EL6	-9.27	-9.41	7.0	0.91	5.5	22.38	10.8	23.93	19.5

#### Aubrite

[10]	QUE 94204		47.17	-7.10	4.4	6.08	3.6	-5.80	5.2	9.29	9.1
------	-----------	--	-------	-------	-----	------	-----	-------	-----	------	-----

Reference	Sample	$\mu^{142}\text{Nd}$	$\mu^{142}\text{Nd}_{\text{corr.}}$	$\pm 2\text{SE}$	$\mu^{143}\text{Nd}$	$\pm 2\text{SE}$	$\mu^{149}\text{Nd}$	$\pm 2\text{SE}$	$\mu^{150}\text{Nd}$	$\pm 2\text{SE}$
-----------	--------	----------------------	-------------------------------------	------------------	----------------------	------------------	----------------------	------------------	----------------------	------------------

#### CV

[1]	Allende	CV3	-36.60	-32.90	7.0	4.00	3.8	7.30	7.2	4.80	10.3
[1]	Allende	CV3	-33.90	-30.30	7.0	4.40	5.4	-2.30	9.6	-20.70	13.3
[1]	Allende Bomb	CV3	-29.70	-27.00	8.0	0.30	4.5	-6.30	8.2	-27.90	10.9
[1]	Allende	CV3	-32.00	-28.70	7.1	1.60	5.4	1.00	9.8	-12.50	13.2
[5]	Allende	CV3	-21.80	-23.60	1.5	-1.80	15.4	14.20	19.9	14.10	32.5

[2]	Allende	CV3	-30.00	-24.95	6.0	2.87	2.9	8.28	8.3	-4.23	8.5
[3]	Allende	CV3	-41.00	-39.30	5.0	3.00	1.0	6.00	5.0	118.00	6.7
[4]	Allende	CV3	-40.00	-36.90	4.0	17.00	5.0	21.00	8.0	-4.00	11.0
[6]	Allende	CV3	-30.00	-31.00	5.0	2.00	9.0	9.00	4.0	8.00	24.0
[6]	Allende	CV3	-30.00	-31.44	6.0	5.00	6.0	4.00	7.0	-6.00	24.0
[6]	Allende	CV3	-33.00	-33.00	8.0	8.00	13.0	16.00	15.0	11.00	31.0
[8]	Allende	CV3	-32.00	-31.00	7.5	-1.10	16.0	19.00	16.0	27.00	26.0
[10]	Allende	CV3	-34.33	-32.38	6.4	0.89	5.9	5.71	7.9	79.79	16.4
[10]	ALH 84028	CV3	-21.40	-23.10	6.1	10.39	5.7	20.77	9.6	169.83	13.4
[10]	EET 96026	CV3	-24.46	-24.19	5.3	2.21	5.6	10.34	10.3	27.60	19.6
[10]	LAR 12002	CV3	-34.58	-34.23	6.6	16.62	5.0	30.50	9.5	146.95	13.7
[10]	GRA 06101	CV3	-39.29	-35.07	6.8	-0.06	5.1	53.48	8.0	51.92	12.5
[4]	Grosnaja	CV3.3	-7.00	-17.20	4.0	-8.00	4.0	-1.00	6.0	-12.00	10.0
[4]	Mokoia	CV3.2	-34.00	-34.90	5.0	5.00	5.0	13.00	8.0	10.00	11.0

#### CM

[4]	Cold Bokkveld	CM2	-42.00	-42.20	7.0	6.00	7.0	16.00	12.0	12.00	17.0
[4]	Mighei	CM2	-45.00	-44.40	7.0	12.00	7.0	41.00	13.0	59.00	18.0
[4]	Murray	CM2	-38.00	-38.50	8.0	9.00	8.0	19.00	15.0	-1.00	19.0
[2]	Murchison	CM2	-26.00	-22.55	5.0	2.87	2.9	24.84	8.3	38.06	8.5
[9]	Jbilet	CM2	-26.80	-21.80	1.4	6.50	1.3	20.90	1.2	24.90	3.8
[8]	Murchison	CM2	-31.00	-31.00	7.4	2.10	16.0	23.00	13.0	24.00	24.0

#### CK

[10]	SZA 12420	CK4	-27.14	-30.49	6.2	0.43	4.3	4.84	7.7	36.48	14.3
[10]	ALH 85002	CK4	-30.98	-29.15	6.0	4.05	5.0	2.81	8.0	10.39	10.3
[10]	EET 92002	CK5	-46.87	-38.78	4.7	4.51	3.9	22.72	4.6	42.53	10.6
[10]	EET 90015	CK5	-16.63	-23.52	13.8	13.06	7.7	0.49	17.9	11.19	26.2
[10]	LAR 06872	CK6	-33.47	-28.55	5.5	5.83	4.3	31.62	7.7	27.30	14.0
[10]	LEW 87009	CK6	-17.17	-15.65	8.8	-3.44	8.0	17.88	15.9	38.77	25.3

#### CO

[9]	SAH 99544	CO3	-15.20	-14.20	1.2	5.90	1.9	9.30	2.2	10.90	5.0
[7]	DaG 190	CO3	-34.00	-34.00	4.0	19.00	27.0	22.00	4.6	27.00	7.4
[7]	NWA 2090	CO3	-5.60		5.1	-6.70	48.0	0.80	5.9	4.30	11.0
[8]	Kainsaz	CO3.2	-35.00		4.8	3.70	20.0	21.00	5.6	26.00	10.0
<b>CR</b>											
[9]	NWA 6043	CR2	-37.00	-36.40	11.0	3.10	3.8	28.00	10.0	60.60	2.2
[7]	Dho 1432	CR2	-28.00	-30.00	3.8	16.00	15.0	18.00	5.4	26.00	9.5
<b>CI</b>											
[4]	Orgueil	CI1	-28.00	-28.50	12.0	-21.00	13.0	-5.00	20.0	-29.00	28.0
[9]	Ivuna	CI1	-14.60	-14.60	4.9	-0.10	2.3	0.40	2.1	3.70	4.7
[8]	Orgueil	CI1	-21.00	-21.00	3.0	5.80	3.6	2.00	4.8	-2.10	8.9
<b>Reference</b>	<b>Sample</b>		$\mu^{142}\text{Nd}$	$\mu^{142}\text{Nd}_{\text{corr.}}$	$\pm 2\text{SE}$	$\mu^{145}\text{Nd}$	$\pm 2\text{SE}$	$\mu^{148}\text{Nd}$	$\pm 2\text{SE}$	$\mu^{150}\text{Nd}$	$\pm 2\text{SE}$
<b>CAIs</b>											
[6]	CAI A-ZH-5		-15.20		7.8	-19.00	13.0	-28.00	15.0	-47.00	31.0
[15]	CAI Allende 322		1.76	-6.91	5.3	-0.76	4.2	4.00	7.0	3.34	9.4
[15]	CAI Allende 323		6.14	-14.01	4.5	-0.55	3.4	-9.06	5.9	-23.62	8.1
[15]	CAI NWA 6991 B4		9.37	-9.73	3.9	-4.70	2.9	-5.12	5.1	-1.52	6.6
[15]	CAI NWA 6991 B4 bulk-R		33.33	-10.29	12.5	-23.16	10.0	1.87	17.8	12.26	26.5
[15]	CAI NWA 6991 B4 fass-R		45.89	-19.40	23.8	-4.03	20.1	-0.27	35.5	41.87	47.4
[15]	CAI NWA 2364 bulk		4.88	-3.94	3.3	-26.26	3.5	-27.90	6.1	-48.85	8.2
	CAI NWA 2364										
	bulk (duplicate - rerun)		1.88	-6.78	3.9	-26.28	3.7	-23.91	6.7	-46.33	9.8
[15]	NWA 2364 CAIs bulk-R		60.58	-9.13	8.5	-25.33	7.2	-30.46	14.6	-43.85	19.8
[15]	NWA 2364 CAIs mel-R		23.61	7.35	18.1	-11.45	19.4	-48.90	35.1	-51.60	42.8
[15]	NWA 2364 CAIs fass-R		26.68	-27.17	12.8	3.05	11.9	-20.79	21.9	-43.09	29.6
[14]	Mel pyx Allende		-20.14	-5.15	1.1	-20.09	2.9	-20.70	6.6	-109.96	38.5

[14]	melilite Allende	-42.91	-2.40	32.6	-20.09	2.9	-20.70	6.6	-59.21	38.5
[14]	pyx Allende	49.92	-2.17	41.3	-22.96	2.9	-4.14	6.6	-97.27	38.5
[14]	d>3.26 Allende	10.51	-7.41	23.8	-14.35	2.9	-41.39	6.6	-148.02	38.5
[14]	d<3.26 Allende	-42.04	-3.03	93.9	-20.09	2.9	-28.98	14.9	-97.27	59.6
[14]	fines Allende	-15.76	-8.16	32.6	-14.35	2.9	-41.39	6.6	-76.12	38.5
[13]	CAI 164	6.13	0.19	20.0	-25.83	8.6	-24.84	23.2	-67.67	38.1
[13]	CAI 165	-32.40	-14.74	20.0	-25.83	8.6	-41.39	23.2	-84.58	38.1
[13]	CAI 166	-24.52	-16.72	20.0	-22.96	8.6	-33.12	23.2	-93.04	38.1
[13]	CAI 167	-23.65	-15.24	20.0	-22.96	8.6	-37.25	23.2	-71.90	38.1
[13]	CAI 168	0.00	1.16	20.0	-17.22	8.6	-12.42	23.2	-33.83	38.1
[13]	CAI 170	-3.50	-2.30	20.0	-22.96	8.6	-24.84	23.2	-54.98	38.1
[13]	CAI 171	0.00	5.23	20.0	-20.09	8.6	-12.42	23.2	-46.52	38.1
[13]	CAI 172	-3.50	-7.58	20.0	-20.09	8.6	-16.56	23.2	-38.06	38.1
[13]	CAI 173	-14.89	-9.70	20.0	-22.96	8.6	-28.98	23.2	-76.12	38.1
[13]	CAI 174	-10.51	-9.70	20.0	-34.44	8.6	-33.12	23.2	-76.12	38.1
[13]	CAI 175	-65.68	-11.68	20.0	-25.83	8.6	-28.98	23.2	-71.90	38.1

Reference	Sample	$\mu^{142}\text{Nd}$	$\mu^{142}\text{Nd}_{\text{corr.}}$	$\pm 2\text{SE}$	$\mu^{143}\text{Nd}$	$\pm 2\text{SE}$	$\mu^{146}\text{Nd}$	$\pm 2\text{SE}$	$\mu^{150}\text{Nd}$	$\pm 2\text{SE}$
Earth										
[10]	ICE9a-3249	2.87		4.16	-5.80	3.1	6.16	5.6	-0.10	8.8
[10]	ICE9a-3296	4.41		1.31	-2.01	1.2	-3.73	1.6	-0.19	3.6
[10]	ICE9a-3497	3.35		2.28	4.25	1.7	-12.26	2.9	9.20	4.9
[10]	ICE9a-3502	10.36		2.52	0.82	2.0	-8.44	3.3	9.01	6.3
[10]	ICE9a-3503	10.08		4.35	-2.19	3.6	-14.90	5.8	-1.09	10.2
[11]	<i>H-5</i>	3.22		2.89	-4.31	2.3	4.61	4.6	9.93	9.7
[11]	<i>H-11</i>	1.73		3.33	-4.59	3.4	20.34	6.6	4.01	12.3
[11]	<i>H-23</i>	-1.43		3.42	-4.31	2.6	7.51	6.6	17.96	14.4
[11]	<i>KOOCF.f1</i>	3.65		2.1	-3.44	1.7	0.89	2.9	-4.87	6.8
[11]	<i>KOOCF.f2</i>	2.60		2.1	-2.01	1.7	1.30	3.3	-1.49	6.3
[11]	<i>KOOCF.f2.rpt</i>	3.92		2.1	-1.44	1.7	2.13	3.3	6.97	6.8

[11]	LO-0201.f1	2.25		2.45	-0.86	2.0	2.54	4.6	-1.91	8.5
[11]	LO-0201.f2	0.76		2.19	-2.87	1.4	-2.01	3.7	-13.76	5.9
[11]	MK-1-6	1.46		2.63	-2.30	3.2	-0.77	4.1	-17.56	8.9
[11]	83	2.25		1.93	-0.29	1.4	0.47	2.9	-5.72	5.5
[11]	83.rpt	3.83		1.66	-0.57	1.4	-4.08	2.9	-12.06	5.5
[11]	83A	-2.48		1.93	2.30	1.4	-4.49	3.3	-9.53	6.3
[11]	83A.rpt	-1.34		1.58	0.86	1.4	-3.25	2.5	-6.99	5.1
[11]	173-2	0.24		1.84	2.58	1.4	-3.67	2.9	-11.64	5.5
[11]	ICE 3	3.30		2.89	2.30	1.7	8.34	2.9	25.58	5.9
[11]	ICE 8a	-0.11		2.1	2.01	1.7	8.75	3.7	17.12	6.3
[11]	ICE10(1)	-0.29		2.63	-0.29	2.0	-2.01	4.6	-4.87	8.0
[11]	ICE10(2)	0.41		3.15	-1.15	2.3	4.61	5.4	4.01	8.9
[11]	ICE10(3)	1.03		2.98	-2.87	2.0	20.34	5.0	18.39	10.1
Reference	Sample	$\mu^{142}\text{Nd}$	$\mu^{142}\text{Nd}_{\text{corr.}}$	$\pm 2\text{SE}$	$\mu^{143}\text{Nd}$	$\pm 2\text{SE}$	$\mu^{146}\text{Nd}$	$\pm 2\text{SE}$	$\mu^{150}\text{Nd}$	$\pm 2\text{SE}$
<b>Angrites</b>										
[17]	ADOR	-1.60		-16.00	3.9	5.90	3.6	17.90	4.1	86.00
[17]	D'Orbigny	-25.00		-17.30	3.8	7.70	3.6	9.40	4.1	3.00
[17]	NWA 4590	19.70		-14.90	4.2	8.20	3.6	9.30	4.1	67.00
[17]	NWA 4801	0.80		-15.10	3.9	5.70	3.6	-3.00	4.1	15.00
[17]	NWA 6291	32.00		-15.60	5.5	9.60	3.6	16.50	6.1	62.00
[9]	Sahara 99555	-7.70			4.5	5.20	4.8	16.60	8.1	26.00
<b>Eucrites</b>										
[17]	Bouvante	-16.00		-17.70	3.7	8.30	3.6	13.20	4.1	23.00
[17]	Juvinas	-1.40		-18.10	3.9	8.40	3.6	15.40	4.1	44.00
[17]	Millbillillie	-13.20		-10.30	3.7	8.40	3.6	10.60	4.3	61.00
[17]	Petersburg	-17.60		-14.30	3.7	6.30	3.6	9.10	4.1	-10.00
[17]	Stannern	-22.50		-18.40	3.7	6.40	3.6	14.00	4.1	15.00

## References

- [1] Boyet and Carlson, 2005
- [2] Andreassen and Sharma, 2006
- [3] Rankenburg et al., 2006
- [4] Carlson et al., 2007
- [5] Gannoun et al., 2011
- [6] Burkhardt et al., 2016
- [7] Fukai and Yokoyama, 2017
- [8] Fukai and Yokoyama, 2019
- [9] Saji et al., 2020
- [10] This Study - UH
- [11] Murphy et al., 2010
- [12] Qin et al., 2011
- [13] Brennecka et al., 2013
- [14] Marks et al., 2014
- [15] Bouvier and Boyet, 2016
- [16] Boyet et al., 2018
- [17] Render and Brennecka, 2021



## Bibliography

- Ader, T., Avouac, J.P., Liu-Zeng, J., Lyon-Caen, H., Bollinger, L., Galetzka, J., Genrich, J., Thomas, M., Chanard, K., Sapkota, S. N., and Rajaure, S. (2012), Convergence rate across the Nepal Himalaya and interseismic coupling on the Main Himalayan Thrust: Implications for seismic hazard. *Journal of Geophysical Research: Solid Earth*, 117(B4)
- Akram, W., Schönbächler, M., Bisterzo, S., and Gallino, R. (2015) Zirconium isotope evidence for the heterogeneous distribution of s-process materials in the solar system. *Geochimica et Cosmochimica Acta*, 165, 484-500.
- Allibert, L., Charnoz, S., Siebert, J., Jacobson, S. A., and Raymond, S. N. (2021) Quantitative estimates of impact induced crustal erosion during accretion and its influence on the Sm/Nd ratio of the Earth. *Icarus*, 114412.
- Amari, S., and Zinner, E. (1997) Supernova grains from meteorites. In *AIP Conference Proceedings*, 402(#1), 287-305.
- Amari, S., Zinner, E., and Lewis, R. S. (1999) A singular presolar SiC grain with extreme <sup>29</sup>Si and <sup>30</sup>Si excesses. *The Astrophysical Journal Letters*, 517(1), L59.
- Ambrose, T.K., Larson, K.P., Guilmette, C., Cottle, J.M., Buckingham, H., and Rai S. (2015) Lateral extrusion, underplating, and out-of-sequence thrusting within the Himalayan metamorphic core, Kanchenjunga, Nepal. *Lithosphere*, 7(4), 441-464.
- Andermann, C., Bonnet, S., and Gloaguen, R. (2011), Evaluation of precipitation data sets along the Himalayan front. *Geochemistry, Geophysics, Geosystems*, 12(7), 1-16.
- Anders, E., and Ebihara, M. (1982) Solar-system abundances of the elements. *Geochimica et Cosmochimica Acta*, 46(11), 2363-2380.
- Andreasen, R., and Sharma, M. (2006) Solar nebula heterogeneity in p-process samarium and neodymium isotopes. *Science*, 314(5800), 806-809.
- Andreasen, R., Sharma, M., Subbarao, K. V., and Viladkar, S. G. (2008) Where on Earth is the enriched Hadean reservoir?. *Earth and Planetary Science Letters*, 266(1-2), 14-28.
- Andreasen, R., and Sharma, M. (2009) Fractionation and mixing in a thermal ionization mass spectrometer source: implications and limitations for high-precision Nd isotope analyses. *International Journal of Mass Spectrometry*, 285(1-2), 49-57.

- Angeli, I., and Marinova, K. P. (2013) Table of experimental nuclear ground state charge radii: An update. *Atomic Data and Nuclear Data Tables*, 99(1), 69-95.
- Arita, K., Dallmeyer, R.D., and Takasu, A. (1997), Tectonothermal evolution of the Lesser Himalaya, Nepal: Constraints from  $^{40}\text{Ar}/^{39}\text{Ar}$  ages from the Kathmandu Nappe. *Island Arc*, 6(4), 372-385.
- Arlandini, C., Käppeler, F., Wisshak, K., Gallino, R., Lugaro, M., Busso, M., and Straniero, O. (1999) Neutron capture in low-mass asymptotic giant branch stars: cross sections and abundance signatures. *The Astrophysical Journal*, 525(2), 886.
- Barrat, J. A., Greenwood, R. C., Keil, K., Rouget, M. L., Boesenberg, J. S., Zanda, B., and Franchi, I. A. (2016) The origin of aubrites: Evidence from lithophile trace element abundances and oxygen isotope compositions. *Geochimica et Cosmochimica Acta*, 192, 29-48.
- Bilham, R. (2019) Himalayan earthquakes: a review of historical seismicity and early 21<sup>st</sup> century slip potential. *Geological Society, London, Special Publications*, 383(1), 423-482.
- Bilham, R., Guar, V.K., and Molnar, P. (2001) Himalayan seismic hazard. *Science*, 293, 1442-1444.
- Bilham, R. and Ambraseys, N. (2005), Apparent Himalayan slip deficit from the summation of seismic moments for Himalayan earthquakes, 1500-2000. *Current Science*, 88, 1658-1663.
- Bizzarro, M., Baker, J. A., and Haack, H. (2004) Mg isotope evidence for contemporaneous formation of chondrules and refractory inclusions. *Nature*, 431(7006), 275-278.
- Blythe, A.E., Burbank, D.W., Carter, A., Schmidt, K., and Putkonen, J. (2007), Plio-Quaternary exhumation history of the central Nepalese Himalaya: 1. Apatite and zircon fission track and apatite [U/Th]/He analyses. *Tectonics*, 26(3)
- Bollinger, L., Avouac, J.P., Beyssac, O., Catlos, E.J., Harrison, T.M., Grove, M., Goffé, B., and Sapkota, S. (2004), Thermal structure and exhumation history of the Lesser Himalaya in central Nepal. *Tectonics*, 23(5) 1-19.
- Bonal, L., Gattacceca, J., Garenne, A., Eschrig, J., Rochette, P., and Ruggiu, L. K. (2020) Water and heat: New constraints on the evolution of the CV chondrite parent body. *Geochimica et Cosmochimica Acta*, 276, 363-383.

- Bonetti, M., Perego, A., Dotti, M., and Cescutti, G. (2019) Neutron star binary orbits in their host potential: effect on early r-process enrichment. *Monthly Notices of the Royal Astronomical Society*, 490(1), 296-311.
- Bookhagen, B. and Burbank, D.W. (2006), Topography, relief, and TRMM-derived rainfall variations along the Himalaya. *Geophysical Research Letters*, 33(8)
- Boujibar, A., Andraut, D., Bolfan-Casanova, N., Bouhifd, M. A., and Monteux, J. (2015) Cosmochemical fractionation by collisional erosion during the Earth's accretion. *Nature communications*, 6(1), 1-7.
- Bourdon, B., Touboul, M., Caro, G., and Kleine, T. (2008) Early differentiation of the Earth and the Moon. *Philosophical Transactions of the Royal Society A: Mathematical, Physical and Engineering Sciences*, 366(1883), 4105-4128.
- Bouvier, A., and Boyet, M. (2016) Primitive Solar System materials and Earth share a common initial 142 Nd abundance. *Nature*, 537(7620), 399-402.
- Bouvier, A., Vervoort, J. D., and Patchett, P. J. (2008) The Lu–Hf and Sm–Nd isotopic composition of CHUR: constraints from unequilibrated chondrites and implications for the bulk composition of terrestrial planets. *Earth and Planetary Science Letters*, 273(1-2), 48-57.
- Boyer, S. E., and Elliott, D. (1982) Thrust systems. *American Association of Petroleum Geologists Bulletin*, 66, 1196–1230.
- Boyet, M., and Carlson, R. W. (2005) 142Nd evidence for early (> 4.53 Ga) global differentiation of the silicate Earth. *Science*, 309(5734), 576-581.
- Boyet, M., and Carlson, R. W. (2006) A new geochemical model for the Earth's mantle inferred from 146Sm–142Nd systematics. *Earth and Planetary Science Letters*, 250(1-2), 254-268.
- Boyet, M., and Gannoun, A. (2013) Nucleosynthetic Nd isotope anomalies in primitive enstatite chondrites. *Geochimica et Cosmochimica Acta*, 121, 652-666.
- Boyet, M., Bouvier, A., Frossard, P., Hammouda, T., Garçon, M., and Gannoun, A. (2018) Enstatite chondrites EL3 as building blocks for the Earth: The debate over the 146Sm–142Nd systematics. *Earth and Planetary Science Letters*, 488, 68-78.
- Brandon, A. D., Lapen, T. J., Debaille, V., Beard, B. L., Rankenburg, K., and Neal, C. (2009) Re-evaluating 142Nd/144Nd in lunar mare basalts with implications for the early evolution and bulk Sm/Nd of the Moon. *Geochimica et Cosmochimica Acta*, 73(20), 6421-6445.

- Brandstätter, F., Bukovanská, M., and Kurat, G. (2003) NWA 1559: another anomalous CK3 chondrite. *Meteoritic and Planetary Science*, 38(A63)
- Braukmüller, N., Wombacher, F., Hezel, D. C., Escoube, R., and Münker, C. (2018) The chemical composition of carbonaceous chondrites: Implications for volatile element depletion, complementarity and alteration. *Geochimica et Cosmochimica Acta*, 239, 17-48.
- Brennecka, G. A., Borg, L. E., and Wadhwa, M. (2013) Evidence for supernova injection into the solar nebula and the decoupling of r-process nucleosynthesis. *Proceedings of the National Academy of Sciences*, 110(43), 17241-17246.
- Brewer, I. D., Burbank, D. W., and Hodges, K. V. (2003) Modeling detrital cooling-age populations: Insights from two Himalayan catchments. *Basin Research*, 15(3), 305–320.
- Brewer, I. D., Burbank, D. W., and Hodges, K. V. (2006) Downstream development of a detrital cooling-age signal: Insights from  $^{40}\text{Ar}/^{39}\text{Ar}$  muscovite thermochronology in the Nepalese Himalaya. *Special Papers-Geological Society of America*, 398, 321–338.
- Bukovanská, M., Brandstätter, F., and Kurat, G. (2003) NWA 1560 (CK4/5) and NWA 1563 (CK5) – a comparison with HaH 280 (CK4) chondrite. *Meteoritic and Planetary Science*, 38(A84)
- Burbank, D. W., Blythe, A. E., Putkonen, J., Pratt-Sitaula, B., Gabet, E., Oskin, M., Barros, A., and Ojha, T. P. (2003) Decoupling of erosion and precipitation in the Himalayas. *Nature*, 426(6967), 652–655.
- Burkhardt, C., Kleine, T., Oberli, F., Pack, A., Bourdon, B., and Wieler, R. (2011) Molybdenum isotope anomalies in meteorites: constraints on solar nebula evolution and origin of the Earth. *Earth and Planetary Science Letters*, 312(3-4), 390-400.
- Burkhardt, C., Borg, L. E., Brennecka, G. A., Shollenberger, Q. R., Dauphas, N., and Kleine, T. (2016) A nucleosynthetic origin for the Earth's anomalous  $^{142}\text{Nd}$  composition. *Nature*, 537(7620), 394-398.
- Campbell, I. H., and O'Neill, H. S. C. (2012) Evidence against a chondritic Earth. *Nature*, 483(7391), 553-558.
- Cannon, J. M., Murphy, M. A., and Taylor, M. (2018) Segmented strain accumulation in the high Himalaya expressed in river channel steepness. *Geosphere*, 14, 1131–1149.
- Canup, R. M. (2004) Origin of the terrestrial planets and the Earth-Moon system. *Physics Today*, 57(4), 56-62.

- Capitani, G. C., Leroux, H., Doukhan, J. C., Rios, S., Zhang, M., and Salje, E. K. H., (2000) A TEM investigation of natural metamict zircons: structure and recovery of amorphous domains. *Physics and Chemistry of Minerals*, 27, 545-556.
- Caro, G., and Bourdon, B. (2010) Non-chondritic Sm/Nd ratio in the terrestrial planets: consequences for the geochemical evolution of the mantle–crust system. *Geochimica et Cosmochimica Acta*, 74(11), 3333-3349.
- Caro, G., Bourdon, B., Halliday, A. N., and Quitté, G. (2008) Super-chondritic Sm/Nd ratios in Mars, the Earth and the Moon. *Nature*, 452(7185), 336-339.
- Carosi, R., Montomoli, C., Rubatto, D., and Visona, D. (2010) Late Oligocene high-temperature shear zones in the core of the higher Himalayan crystallines (lower Dolpo, western Nepal) *Tectonics*, 29, TC4029.
- Carlson, R. W., Boyet, M., and Horan, M. (2007) Chondrite barium, neodymium, and samarium isotopic heterogeneity and early earth differentiation. *Science*, 316(5828), 1175-1178.
- Carter, P. J., Leinhardt, Z. M., Elliott, T., Stewart, S. T., and Walter, M. J. (2018) Collisional stripping of planetary crusts. *Earth and Planetary Science Letters*, 484, 276-286.
- Catlos, E. J., Harrison, T. M., Kohn, M. J., Grove, M., Ryerson, F. J., Manning, C. E., and Upreti, B. N. (2001) Geochronologic and thermobarometric constraints on the evolution of the Main Central Thrust, Central Nepal Himalaya. *Journal of Geophysical Research*, 106(B8), 16,177–16,204.
- Catlos, E. J., Lovera, O. M., Kelly, E. D., Ashley, K. T., Harrison, T. M., and Etzel, T. (2018) Modeling high-resolution pressure-temperature paths across the Himalayan Main Central Thrust (Central Nepal): Implications for the dynamics of collision. *Tectonics*, 37, 2363–2388.
- Cattin, R., and Avouac, J. P. (2000) Modeling mountain building and the seismic cycle in the Himalaya of Nepal. *Journal of Geophysical Research*, 105(B6), 13,389–13,407.
- Célérier, J., Harrison, T. M., Beyssac, O., Herman, F., Dunlap, W. J., and Webb, A. A. G. (2009) The Kumaun and Garwhal lesser Himalaya, India: Part 2. Thermal and deformation histories. *GSA Bulletin*, 121(9–10), 1281–1297.
- Chaumard, N., Devouard, B., Bouvier, A., and Wadhwa, M. (2014) Metamorphosed calcium-aluminum-rich inclusions in CK carbonaceous chondrites. *Meteoritics and Planetary Science*, 49(3), 419-452.

- Chaumard, N., and Devouard, B. (2016) Chondrules in CK carbonaceous chondrites and thermal history of the CV–CK parent body. *Meteoritics and Planetary Science*, 51(3), 547–573.
- Clift, P. D., Giosan, L., Blusztajn, J., Campbell, I. H., Allen, C., Pringle, M., Tabrez, A. R., Danish, M., Rabbani, M. M., Alizai, A., and Carter, A. (2008) Holocene erosion of the lesser Himalaya triggered by intensified summer monsoon. *Geology*, 36(1), 79–82.
- Copeland, P., Harrison, T. M., and Le Fort, P. (1990) Age and cooling history of the Manaslu granite: Implications for Himalayan tectonics. *Journal of Volcanology and Geothermal Research*, 44(1–2), 33–50.
- Copeland, P., Harrison, T. M., Hodges, K. V., Maruéjol, P., Le Fort, P., and Pecher, A. (1991) An early Pliocene thermal disturbance of the Main Central Thrust, central Nepal: Implications for Himalayan tectonics. *Journal of Geophysical Research*, 96(B5), 8475–8500.
- Copeland, P., Bertrand, G., France-Lanord, C., and Sundell, K. (2015a)  $^{40}\text{Ar}/^{39}\text{Ar}$  ages of muscovites from modern Himalayan rivers: Himalayan evolution and the relative contribution of tectonics and climate. *Geosphere*, 11, 1837–1859.
- Copeland, P., Cox, K., and Watson, E. B. (2015b) The potential of crinoids as (U+ Th+ Sm)/He thermochronometers. *Earth and Planetary Science Letters*, 422, 1–10.
- Corrie, S. L., and Kohn, M. J. (2011) Metamorphic history of the central Himalaya, Annapurna region, Nepal, and implications for tectonic models. *Bulletin*, 123(9–10), 1863–1879.
- Côté, B., Fryer, C. L., Belczynski, K., Korobkin, O., Chruślińska, M., Vassh, N., Mumpower, M. R., Lippuner, J., Sprouse, T. M., Surman, R., and Wollaeger, R. (2018) The Origin of r-process Elements in the Milky Way. *The Astrophysical Journal*, 855(2), 99.
- Cottle, J. M., Larson, K. P., and Kellett, D. A. (2015) How does the mid-crust accommodate deformation in large, hot collisional orogens? A review of recent research in the Himalayan orogen. *Journal of Structural Geology*, 78, 119–133.
- Coutand, I., Whipp, D. M., Grujic, D., Bernet, M., Fellin, M. G., Bookhagen, B., Landry, K. R., Ghalley, S. K., and Duncan, C. (2014) Geometry and kinematics of the Main Himalayan thrust and Neogene crustal exhumation in the Bhutanese Himalaya derived from the inversion of multithermochronologic data. *Journal of Geophysical Research: Solid Earth*, 119, 1446–1481.

- DeCelles, P. G., Gehrels, G. E., Quade, J., and Ojha, T. P. (1998) Eocene-early Miocene foreland basin development and the history of Himalayan thrusting, western and Central Nepal. *Tectonics*, 17(5), 741–765.
- DeCelles, P. G., Robinson, D. M., Quade, J., Ojha, T. P., Garzzone, C. N., Copeland, P., and Upreti, B. N. (2001) Stratigraphy, structure, and tectonic evolution of the Himalayan fold-thrust belt in western Nepal. *Tectonics*, 17(5), 741–765.
- Dodson, M. H. (1973) Closure temperature in cooling geochronological and petrological systems. *Contributions to Mineralogy and Petrology*, 40(3), 259-274.
- Dunn, T. L., Gross, J., Ivanova, M. A., Runyon, S. E., and Bruck, A. M. (2016) Magnetite in the unequilibrated CK chondrites: Implications for metamorphism and new insights into the relationship between the CV and CK chondrites. *Meteoritics and Planetary Science*, 51(9), 1701-1720.
- Elliott, J. R., Jolivet, R., González, P. J., Avouac, J. P., Hollingsworth, J., Searle, M. P., and Stevens, V. L. (2016) Himalayan megathrust geometry and relation to topography revealed by the Gorkha earthquake. *Nature Geoscience*, 9, 174–180.
- Feldl, N., and Bilham, R. (2006) Great Himalayan earthquakes and the Tibetan plateau. *Nature*, 444(7116), 165–170.
- Floss, C., and Haenecour, P. (2016) Presolar silicate grains: Abundances, isotopic and elemental compositions, and the effects of secondary processing. *Geochemical Journal*, 50(1), 3-25.
- Frank, D., M. Zolensky, J. Martinez, T. Mikouchi, K. Ohsumi, K. Hagiya, W. Satake, L. Le, D. Ross, and Peslier, A. (2011) A CAI in the Ivuna C11 chondrite. *Lunar and Planetary Science Conference*, 42(#2785)
- Fujii, T., Yamamoto, T., Nishizawa, K., Inagawa, J., Gunji, K., and Watanabe, K. (1998) Separation of samarium isotopes by a crown ether. *Solvent extraction and ion exchange*, 16(4), 985-999.
- Fujii, T., Yamamoto, T., Watanabe, K., Nishizawa, K., Inagawa, J., and Gunji, K. (1999) Field shift effects in chemical isotope enrichment of neodymium using dicyclohexano-18-crown-6. *Technology reports of the Osaka University*, 49(2348-2365), 229-235.
- Fujii, T., Yamamoto, T., Inagawaa, J., Gunji, K., Watanabe, K., and Nishizawa, K. (2000) Nuclear size and shape effects in chemical isotope enrichment of neodymium using a crown ether. *Solvent Extraction and Ion Exchange*, 18(6), 1155-1166.

- Fujii, T., Moynier, F., and Albarède, F. (2006) Nuclear field vs. nucleosynthetic effects as cause of isotopic anomalies in the early Solar System. *Earth and Planetary Science Letters*, 247(1-2), 1-9.
- Fujii, T., Moynier, F., and Albarède, F. (2009) The nuclear field shift effect in chemical exchange reactions. *Chemical Geology*, 267(3-4), 139-156.
- Fukai, R., and Yokoyama, T. (2017) Neodymium isotope heterogeneity of ordinary and carbonaceous chondrites and the origin of non-chondritic  $^{142}\text{Nd}$  compositions in the Earth. *Earth and Planetary Science Letters*, 474, 206-214.
- Fukai, R., and Yokoyama, T. (2019) Nucleosynthetic Sr–Nd isotope correlations in chondrites: Evidence for nebular thermal processing and dust transportation in the early Solar System. *The Astrophysical Journal*, 879(2), 79.
- Gabet, E. J., Burbank, D. W., Pratt-Sitaula, B., Putkonen, J., and Bookhagen, B. (2008) Modern erosion rates in the high Himalayas of Nepal. *Earth and Planetary Science Letters*, 267(3–4), 482–494.
- Gannoun, A., Boyet, M., El Goresy, A., and Devouard, B. (2011a) REE and actinide microdistribution in Sahara 97072 and ALHA77295 EH3 chondrites: A combined cosmochemical and petrologic investigation. *Geochimica et Cosmochimica Acta*, 75(11), 3269-3289.
- Gannoun, A., Boyet, M., Rizo, H., and El Goresy, A. (2011b)  $^{146}\text{Sm}$ – $^{142}\text{Nd}$  systematics measured in enstatite chondrites reveals a heterogeneous distribution of  $^{142}\text{Nd}$  in the solar nebula. *Proceedings of the National Academy of Sciences*, 108(19), 7693-7697.
- Garzanti, E., Vezzoli, G., Ando, S., Lavé, J., Attal, M., France-Lanord, C., and DeCelles, P. (2007) Quantifying sand provenance and erosion (Marsyandi River, Nepal Himalaya) *Earth and Planetary Science Letters*, 258(3–4), 500–515.
- Gautam, I., Ray, J. S., Bhutani, R., Balakrishnan, S., and Dash, J. K. (2017) Role of fractionation correction in accurate determination of  $^{142}\text{Nd}/^{144}\text{Nd}$  by TIMS: a case study of 1.48 Ga alkaline rocks from Khariar, India. *Chemical Geology*, 466, 479-490.
- Garçon, M., Boyet, M., Carlson, R. W., Horan, M. F., Auclair, D., and Mock, T. D. (2018) Factors influencing the precision and accuracy of Nd isotope measurements by thermal ionization mass spectrometry. *Chemical Geology*, 476, 493-514.
- Godard, V., Cattin, R., and Lavé, J. (2004) Numerical modeling of mountain building: Interplay between erosion law and crustal rheology. *Geophysical Research Letters*, 31, L23607.



- Godard, V., Bourlès, D. L., Spinabella, F., Burbank, D. W., Bookhagen, B., Fisher, G. B., Moulin, A., and Léanni, L. (2014) Dominance of tectonics over climate in Himalayan denudation. *Geology*, 42, 243–246.
- Godin, L., Parrish, R. R., Brown, R. L., and Hodges, K. V. (2001) Crustal thickening leading to exhumation of the Himalayan metamorphic core of Central Nepal: Insight from U-Pb geochronology and  $^{40}\text{Ar}/^{39}\text{Ar}$  thermochronology. *Tectonics*, 20(5), 729–747.
- Grandin, R., Doin, M. P., Bollinger, L., Pinel-Puysségur, B., Ducret, G., Jolivet, R., and Sapkota, S. N. (2012) Long-term growth of the Himalaya inferred from interseismic InSAR measurement. *Geology*, 40(12), 1059–1062.
- Greenwood, R. C., Hutchison, R., Huss, G. R., and Hutcheon I. D. (1992) CAIs in CO<sub>3</sub> meteorites: parent body or nebular alteration? *Meteoritics*, 27. (abstr.)
- Greenwood, J. P., McKeegan, K. D., and Wasson, J. T., (2000) A Karoonda conundrum: primordial oxygen in magnetite, olivine and iron-rich spinel in a metamorphosed calcium-aluminum-rich inclusion. *Meteoritics and Planetary Science*, 35(A63)
- Greenwood, R. C., Franchi, I. A., Kearsley, A. T., and Alard, O. (2010) The relationship between CK and CV chondrites. *Geochimica et Cosmochimica Acta*, 74(5), 1684–1705.
- Guenther, W. R., Reiners, P. W., Ketcham, R. A., Nasdala, L., and Giester, G. (2013) Helium diffusion in natural zircon: Radiation damage, anisotropy, and the interpretation of zircon (U-Th)/He thermochronology. *American Journal of Science*, 313(3), 145–198.
- Halliday, A. N. (2008) A young Moon-forming giant impact at 70–110 million years accompanied by late-stage mixing, core formation and degassing of the Earth. *Philosophical Transactions of the Royal Society A: Mathematical, Physical and Engineering Sciences*, 366(1883), 4163–4181.
- Harrison, T. M., Célérier, J., Aikman, A. B., Hermann, J., and Heizler, M. T. (2009) Diffusion of  $^{40}\text{Ar}$  in muscovite. *Geochimica et Cosmochimica Acta*, 73(4), 1039–1051.
- Harrison, T. M., Ryerson, F. J., Le Fort, P., Yin, A., Lovera, O. A., and Catlos, E. J. (1997) A late Miocene-Pliocene origin for the central Himalayan inverted metamorphism. *Earth and Planetary Science Letters*, 146(1–2), E1–E7.
- Hart, S. R., and Zindler, A. (1989) Isotope fractionation laws: a test using calcium. *International Journal of Mass Spectrometry and Ion Processes*, 89(2–3), 287–301.

- Harvey, J. E., Burbank, D. W., and Bookhagen, B. (2015) Along strike changes in Himalayan thrust geometry: Topographic and tectonic discontinuities in western Nepal. *Lithosphere*, 7, 511–518.
- He, D., Webb, A. A. G., Larson, K. P., Martin, A. J., and Schmitt, A. K. (2015) Extrusion vs. duplexing models of Himalayan mountain building 3: Duplexing dominates from the Oligocene to present. *International Geology Review*, 57, 1–27.
- Herman, F., Copeland, P., Avouac, J. P., Bollinger, L., Mahéo, G., Le Fort, P., Rai, S., Foster, D., Pêcher, A., Stüwe, K. and Henry, P. (2010) Exhumation, crustal deformation, and thermal structure of the Nepal Himalaya derived from the inversion of thermochronological and thermobarometric data and modeling of the topography. *Journal of Geophysical Research*, 115, B06407.
- Hertogen, J., Janssens, M. J., Takahashi, H., Morgan, J. W., and Anders, E. (1983) Enstatite chondrites: Trace element clues to their origin. *Geochimica et Cosmochimica Acta*, 47(12), 2241–2255.
- Hetényi, G., Le Roux-Mallouf, R., Berthet, T., Cattin, R., Cauzzi, C., Phuntsho, K., and Grolimund, R. (2016) Joint approach combining damage and paleoseismology observations constrains the 1714 AD Bhutan earthquake at magnitude  $8 \pm 0.5$ . *Geophysical Research Letters*, 43, 10,695–10,702.
- Hodges, K. V., Hurtado, J. M., and Whipple, K. X. (2001) Southward extrusion of Tibetan crust and its effect on Himalayan tectonics. *Tectonics*, 20(6), 799–809.
- Hodges, K. V., Parrish, R. R., and Searle, M. P. (1996) Tectonic evolution of the Central Annapurna range, Nepalese Himalayas. *Tectonics*, 15(6), 1264–1291.
- Hodges, K. V., Wobus, C., Ruhl, K., Schildgen, T., and Whipple, K. (2004) Quaternary deformation, river steepening, and heavy precipitation at the front of the higher Himalayan ranges. *Earth and Planetary Science Letters*, 220(3–4), 379–389.
- Hopp, J., Trierloff, M., and Ott, U. (2016) I–Xe ages of enstatite chondrites. *Geochimica et Cosmochimica Acta*, 174, 196–210.
- Hoppe, P., and Zinner, E. (2000) Presolar dust grains from meteorites and their stellar sources. *Journal of Geophysical Research: Space Physics*, 105(A5), 10371–10385.
- Hotokezaka, K., Piran, T., and Paul, M. (2015) Short-lived  $^{244}\text{Pu}$  points to compact binary mergers as sites for heavy r-process nucleosynthesis. *Nature Physics*, 11(12), 1042–1042.
- Hoyle, F., and Fowler, W. A. (1960) Nucleosynthesis in Supernovae. *The Astrophysical Journal*, 132, 565.

- Hubbard, J., Almeida, R., Foster, S. N., Burgi, P., and Tapponnier, P. (2016) Structural segmentation controlled the 2015 Mw 7.8 Gorkha earthquake rupture in Nepal. *Geology*, 44, 639–642.
- Humayun, M., and Clayton, R. N. (1995) Precise determination of the isotopic composition of potassium: Application to terrestrial rocks and lunar soils. *Geochimica et Cosmochimica Acta*, 59(10), 2115-2130.
- Huntington, K. W., Blythe, A. E., and Hodges, K. V. (2006) Climate change and late Pliocene acceleration of erosion in the Himalaya. *Earth and Planetary Science Letters*, 252(1–2), 107–118.
- Huntington, K. W., and Hodges, K. V. (2006) A comparative study of detrital mineral and bedrock age elevation methods for estimating erosion rates. *Journal of Geophysical Research*, 111, F03011.
- Huss, G. R., Rubin, A. E., and Grossman, J. N. (2006) Thermal metamorphism in chondrites. *Meteorites and the early solar system II*, 943, 567-586.
- Ivanova, M. A., Nazarov, A., Kononkova, N. N., Taylor, L. A., Patchen, A., Clayton, R. N., and Mayeda T. K. (2000) Dhofar 015, a new CK3 chondrite: a record of nebular processes. *Meteoritics and Planetary Science*, 35(A83).
- Ivanova, M. A., Nazarov, M. A., Clayton, R. N., Mayeda, T. K., and Taylor, L. A. (2003) Sayh Al Uhaymir 085, CV3 chondrite: Mineralogical links with CK chondrites. *Lunar and Planetary Science Conference*, 24(#1226).
- Jacobsen, S. B., and Wasserburg, G. J. (1980) Sm-Nd isotopic evolution of chondrites. *Earth and Planetary Science Letters*, 50(1), 139-155.
- Jacquet, E., and Marrocchi, Y. (2017) Chondrule heritage and thermal histories from trace element and oxygen isotope analyses of chondrules and amoeboid olivine aggregates. *Meteoritics and Planetary Science*, 52(12), 2672-2694.
- Jacquet, E., Alard, O., and Gounelle, M. (2012) Chondrule trace element geochemistry at the mineral scale. *Meteoritics and Planetary Science*, 47(11), 1695-1714.
- Jacquet, E., Alard, O., and Gounelle, M. (2015a) Trace element geochemistry of ordinary chondrite chondrules: The type I/type II chondrule dichotomy. *Geochimica et Cosmochimica Acta*, 155, 47-67.
- Jacquet, E., Alard, O., and Gounelle, M. (2015b) The formation conditions of enstatite chondrites: Insights from trace element geochemistry of olivine-bearing chondrules in Sahara 97096 (EH 3) *Meteoritics and Planetary Science*, 50(9), 1624-1642.

- Jacquet, E., Piani, L., and Weisberg, M.K. (2018) Chondrules in enstatite chondrites. In S.A. Russell, H.C. Connolly Jr., and A.N. Krot, Eds., *Chondrules: Records of protoplanetary disk processes*, pp. 175–195. Cambridge University Press.
- Jouanne, F., Mugnier, J. L., Gamond, J. F., Le Fort, P., Pandey, M. R., Bollinger, L., Flouzat, M., and Avouac, J. P. (2004) Current shortening across the Himalayas of Nepal. *Geophysical Journal International*, 157(1), 1–14.
- Kallemeyn, G. W., and Wasson, J. T. (1986) Compositions of enstatite (EH3, EH4, 5 and EL6) chondrites: Implications regarding their formation. *Geochimica et Cosmochimica Acta*, 50(10), 2153-2164.
- Kallemeyn, G. W., Rubin, A. E., and Wasson, J. T. (1991) The compositional classification of chondrites: V. The Karoonda (CK) group of carbonaceous chondrites. *Geochimica et Cosmochimica Acta*, 55(3), 881-892.
- Kallemeyn, G. W., Rubin, A. E., and Wasson, J. T. (1996) The compositional classification of chondrites: VII. The R chondrite group. *Geochimica et Cosmochimica Acta*, 60(12), 2243-2256.
- Karakas, A. I., and Lattanzio, J. C. (2014) The Dawes review 2: nucleosynthesis and stellar yields of low-and intermediate-mass single stars. *Publications of the Astronomical Society of Australia*, 31.
- Keil, K. (1989) Enstatite meteorites and their parent bodies. *Meteoritics*, 24(4), 195-208.
- Khanal, S., and Robinson, D. M. (2013) Upper crustal shortening and forward modeling of the Himalayan thrust belt along the Budhi-Gandaki River, Central Nepal. *International Journal of Earth Sciences*, 102, 1871–1891.
- King, W.H., (1984) *Isotope shifts in atomic spectra*. Plenum Press, New York.
- Kirby, E., and Whipple, K. X. (2001) Quantifying differential rock-uplift rates via stream profile analysis. *Geology*, 29(5), 415–418.
- Kirby, E., and Whipple, K. X. (2012) Expression of active tectonics in erosional landscapes. *Journal of Structural Geology*, 44, 54–75.
- Kleine, T., Budde, G., Burkhardt, C., Kruijer, T. S., Worsham, E. A., Morbidelli, A., and Nimmo, F. (2020) The Non-carbonaceous–Carbonaceous Meteorite Dichotomy. *Space Science Reviews*, 216, 1-27.
- Krot, A. N., Petaev, M. I., and Bland, P. A. (2004) Multiple formation mechanisms of ferrous olivine in CV carbonaceous chondrites during fluid-assisted metamorphism. *Antarctic Meteorite Research*, 17, 153.

- Krot, A. N., Keil, K., Scott, E. R. D., Goodrich, C. A., and Weisberg, M. K. (2014) Classification of meteorites and their genetic relationships. *Meteorites and cosmochemical processes*, 1, 1-63.
- Kumar, S., Wesnousky, S. G., Jayangondaperumal, R., Nakata, T., Kumahara, Y., and Singh, V. (2010) Paleoseismological evidence of surface faulting along the northeastern Himalayan front, India: Timing, size, and spatial extent of great earthquakes. *Journal of Geophysical Research*, 51, 105–112.
- Kumar, S., Wesnousky, S. G., Rockwell, T. K., Briggs, R. W., Thakur, V. C., and Jayangondaperumal, R. (2006) Paleoseismic evidence of great surface rupture earthquakes along the Indian Himalaya. *Journal of Geophysical Research*, 111, B03304.
- Landry, K. R., Coutand, I., Whipp, D. M., Grujic, D., and Hourigan, J. K. (2016) Late Neogene tectonically driven crustal exhumation of the Sikkim Himalaya: Insights from inversion of multithermochronologic data. *Tectonics*, 35, 833–859.
- Larsen, K. K., Wielandt, D., Schiller, M., Krot, A. N., and Bizzarro, M. (2020) Episodic formation of refractory inclusions in the Solar System and their presolar heritage. *Earth and Planetary Science Letters*, 535, 116088.
- Larson, K. P., Ambrose, T. K., Webb, A. A. G., Cottle, J. M., and Shrestha, S. (2015) Reconciling Himalayan midcrustal discontinuities: The Main Central Thrust system. *Earth and Planetary Science Letters*, 429, 139–146.
- Larson, K. P., Gervais, F., and Kellett, D. A. (2013) AP-T-t-D discontinuity in east-Central Nepal: Implications for the evolution of the Himalayan mid-crust. *Lithos*, 179, 275–292.
- Lavé, J., and Avouac, J. P. (2001) Fluvial incision and tectonic uplift across the Himalayas of central Nepal. *Journal of Geophysical Research*, 106(B11), 26,561–26,591.
- Leshin, L. A., Rubin, A. E., and McKeegan, K. D. (1997) The oxygen isotopic composition of olivine and pyroxene from CI chondrites. *Geochimica et Cosmochimica Acta*, 61(4), 835-845.
- Liu, N. (2014) *Isotopic compositions of s-process elements in acid-cleaned mainstream presolar silicon carbide*. (Ph.D. thesis) Location: The University of Chicago.
- Lodders, K. (2003) Solar system abundances and condensation temperatures of the elements. *The Astrophysical Journal*, 591(2), 1220.

- Lodders, K., and Fegley Jr, B. (1993) Lanthanide and actinide chemistry at high CO/ratios in the solar nebula. *Earth and Planetary Science Letters*, 117(1-2), 125-145.
- Lodders, K., and Amari, S. (2005) Presolar grains from meteorites: Remnants from the early times of the solar system. *Geochemistry*, 65(2), 93-166.
- Lugmair, G. W., and Shukolyukov, A. (1998) Early solar system timescales according to <sup>53</sup>Mn-<sup>53</sup>Cr systematics. *Geochimica et Cosmochimica Acta*, 62(16), 2863-2886.
- MacPherson, G. J., Simon, S. B., Davis, A. M., Grossman, L., and Krot, A. N. (2005) Calcium-aluminum-rich inclusions: Major unanswered questions. In *Chondrites and the protoplanetary disk*, 341, p.225.
- Marks, N. E., Borg, L. E., Hutcheon, I. D., Jacobsen, B., and Clayton, R. N. (2014) Samarium-neodymium chronology and rubidium-strontium systematics of an Allende calcium-aluminum-rich inclusion with implications for <sup>146</sup>Sm half-life. *Earth and Planetary Science Letters*, 405, 15-24.
- Martin, A. J., Gehrels, G. E., & DeCelles, P. G. (2007) The tectonic significance of (U, Th)/Pb ages of monazite inclusions in garnet from the Himalaya of central Nepal. *Chemical Geology*, 244(1-2), 1-24.
- Martin, A. J., Copeland, P., and Benowitz, J. A. (2015) Muscovite <sup>40</sup>Ar/<sup>39</sup>Ar ages help reveal the Neogene tectonic evolution of the southern Annapurna range, Central Nepal. *Geological Society, London, Special Publications*, 412, 199–220.
- Mathews, G. J., and Cowan, J. J. (1990) New insights into the astrophysical r-process. *Nature*, 345(6275), 491-494.
- May, C., Russell, S. S., and Grady, M. M. (1999) Analysis of chondrule and CAI size and abundance in CO3 and CV3 chondrites: A preliminary study. *Lunar and Planetary Science Conference*, 30(#1688)
- McQuarrie, N., and Ehlers, T. (2015) Influence of thrust belt geometry and shortening rate on thermochronometer cooling ages: Insights from thermokinematic and erosion modeling of the Bhutan Himalaya. *Tectonics*, 34, 1055–1079.
- McSween Jr, H. Y. (1977) Carbonaceous chondrites of the Ornans type: A metamorphic sequence. *Geochimica et Cosmochimica Acta*, 41(4), 477-491.
- Meade, B. J. (2010) The signature of an unbalanced earthquake cycle in Himalayan topography. *Geology*, 38(11), 987–990.

- Mendoza, M. M., Ghosh, A., Karplus, M. S., Klemperer, S. L., Sapkota, S. N., Adhikari, L. B., and Velasco, A. (2019) Duplex in the Main Himalayan Thrust illuminated by aftershocks of the 2015 Mw 7.8 Gorkha earthquake. *Nature Geoscience*, 12, 1018–1022.
- Mezger, K., Schönbächler, M., and Bouvier, A. (2020) Accretion of the Earth—Missing Components?. *Space science reviews*, 216(2), 1-24.
- Miyazaki, Y., and Korenaga, J. (2021) Dynamic evolution of major element chemistry in protoplanetary disks and its implications for Earth-enstatite chondrite connection. *Icarus*, 361, 114368.
- Montomoli, C., Iaccarino, S., Carosi, R., Langone, A., and Visonà, D. (2013) Tectonometamorphic discontinuities within the greater Himalayan sequence in Western Nepal (central Himalaya): Insights on the exhumation of crystalline rocks. *Tectonophysics*, 608, 1349–1370.
- Moynier, F., Fujii, T., and Albarède, F. (2009) Nuclear field shift effect as a possible cause of Te isotopic anomalies in the early solar system—An alternative explanation of Fehr et al.(2006 and 2009) *Meteoritics and planetary science*, 44(11), 1735-1742.
- Moynier, F., Fujii, T., Brennecka, G. A., and Nielsen, S. G. (2013) Nuclear field shift in natural environments. *Comptes Rendus Geoscience*, 345(3), 150-159.
- Mukhopadhyay, B. (2011) Clusters of moderate size earthquakes along Main central thrust (MCT) in Himalaya. *International Journal of Geosciences*, 02(03), 318–325.
- Mukul, M. (2000) The geometry and kinematics of the main boundary thrust and related neotectonics in the Darjiling Himalayan fold-and-thrust belt, West Bengal, India. *Journal of Structural Geology*, 22(9), 1261–1283.
- Murphy, M. A., and Yin, A. (2003) Structural evolution and sequence of thrusting in the Tethyan fold-thrust belt and Indus-Yalu suture zone, Southwest Tibet. *GSA Bulletin*, 115(1), 21–34.
- Nanne, J. A., Nimmo, F., Cuzzi, J. N., and Kleine, T. (2019) Origin of the non-carbonaceous–carbonaceous meteorite dichotomy. *Earth and Planetary Science Letters*, 511, 44-54.
- Nennewitz, M., Thiede, R. C., and Bookhagen, B. (2018) Fault activity, tectonic segmentation, and deformation pattern of the western Himalaya on Ma timescales inferred from landscape morphology. *Lithosphere*, 10, 632–640.

- Nishimura, S., Kotake, K., Hashimoto, M. A., Yamada, S., Nishimura, N., Fujimoto, S., and Sato, K. (2006) r-Process nucleosynthesis in magnetohydrodynamic jet explosions of core-collapse supernovae. *The Astrophysical Journal*, 642(1), 410.
- Nittler, L. R. (2003) Presolar stardust in meteorites: recent advances and scientific frontiers. *Earth and Planetary Science Letters*, 209(3-4), 259-273.
- Olen, S. M., Bookhagen, B., and Strecker, M. R. (2016) Role of climate and vegetation density in modulating denudation rates in the Himalaya. *Earth and Planetary Science Letters*, 445, 57–67.
- O'Neill, H. S. C., and Palme, H. (2008) Collisional erosion and the non-chondritic composition of the terrestrial planets. *Philosophical Transactions of the Royal Society A: Mathematical, Physical and Engineering Sciences*, 366(1883), 4205-4238.
- Pahlevan, K., and Stevenson, D. J. (2007) Equilibration in the aftermath of the lunar-forming giant impact. *Earth and Planetary Science Letters*, 262(3-4), 438-449.
- Palme, H., O'Neill, H. S. C., and Benz, W. (2003, March) Evidence for collisional erosion of the Earth. In *Lunar and Planetary Science Conference*, 34(#1741)
- Pape, J., Mezger, K., Bouvier, A. S., and Baumgartner, L. P. (2019) Time and duration of chondrule formation: Constraints from <sup>26</sup>Al-<sup>26</sup>Mg ages of individual chondrules. *Geochimica et cosmochimica acta*, 244, 416-436.
- Parsons, A. J., Law, R. D., Searle, M. P., Phillips, R. J., and Lloyd, G. E. (2016) Geology of the Dhaulagiri-Annapurna-Manaslu Himalaya, Western region, Nepal. 1:200,000. *Journal of Maps*, 12, 100–110.
- Patchett, P. J., Vervoort, J. D., Söderlund, U., and Salters, V. J. (2004) Lu–Hf and Sm–Nd isotopic systematics in chondrites and their constraints on the Lu–Hf properties of the Earth. *Earth and Planetary Science Letters*, 222(1), 29-41.
- Pearson, O. (2002) Structural evolution of the central Nepal fold-thrust belt and regional tectonic and structural significance of the Ramgarh thrust (Ph.D. thesis) Location: University of Arizona.
- Rankenburg, K., Brandon, A. D., and Neal, C. R. (2006) Neodymium isotope evidence for a chondritic composition of the Moon. *Science*, 312(5778), 1369-1372.
- Reiners, P. W. (2005) Zircon (U-Th)/He thermochronometry. *Reviews in Mineralogy and Geochemistry*, 58(1), 151-179.
- Reiners, P. W., Farley, K. A., and Hickes, H. J. (2002) He diffusion and (U–Th)/He thermochronometry of zircon: initial results from Fish Canyon Tuff and Gold



- Butte. *Tectonophysics*, 349(1-4), 297-308.
- Reiners, P. W., Spell, T. L., Nicolescu, S., and Zanetti, K. A. (2004) Zircon (U-Th)/He thermochronometry: He diffusion and comparisons with  $^{40}\text{Ar}/^{39}\text{Ar}$  dating. *Geochimica et cosmochimica acta*, 68(8), 1857-1887.
- Render, J., and Brennecka, G. A. (2021) Isotopic signatures as tools to reconstruct the primordial architecture of the Solar System. *Earth and Planetary Science Letters*, 555, 116705.
- Robert, X., van der Beek, P., Braun, J., Perry, C., Dubille, M., and Mugnier, J. L. (2009) Assessing quaternary reactivation of the Main Central Thrust zone (central Nepal Himalaya): New thermochronologic data and numerical modeling. *Geology*, 37(8), 731–734.
- Robert, X., Van Der Beek, P., Braun, J., Perry, C., and Mugnier, J. L. (2011) Control of detachment geometry on lateral variations in exhumation rates in the Himalaya: Insights from low-temperature thermochronology and numerical modeling. *Journal of Geophysical Research*, 116, B05202.
- Robinson, D. M., and Martin, A. J. (2014) Reconstructing the greater Indian margin: A balanced cross section in central Nepal focusing on the lesser Himalayan duplex. *Tectonics*, 33, 2143–2168.
- Ruhl, K. W., and Hodges, K. V. (2005) The use of detrital mineral cooling ages to evaluate steady state assumptions in active orogens: An example from the central Nepalese Himalaya. *Tectonics*, 24, TC4015
- Russell, W. A., Papanastassiou, D. A., and Tombrello, T. A. (1978) Ca isotope fractionation on the Earth and other solar system materials. *Geochimica et Cosmochimica Acta*, 42(8), 1075-1090.
- Russell, S. S., Huss, G. R., Fahey, A. J., Greenwood, R. C., Hutchison, R., and Wasserburg, G. J. (1998) An isotopic and petrologic study of calcium-aluminum-rich inclusions from CO3 meteorites. *Geochimica et Cosmochimica Acta*, 62(4), 689-714.
- Russell, S. S., A. N. Krot, G. R. Huss, K. Keil, S. Itoh, H. Yurimoto, and MacPherson, G. J. (2005) The genetic relationship between refractory inclusions and chondrules. *Chondrites and the protoplanetary disk*, 341, 317-350.
- Saji, N. S., Wielandt, D., Paton, C., and Bizzarro, M. (2016) Ultra-high-precision Nd-isotope measurements of geological materials by MC-ICPMS. *Journal of analytical atomic spectrometry*, 31(7), 1490-1504.

- Saji, N. S., Wielandt, D., Holst, J. C., and Bizzarro, M. (2020) Solar system Nd isotope heterogeneity: Insights into nucleosynthetic components and protoplanetary disk evolution. *Geochimica et Cosmochimica Acta*, 281, 135-148.
- Saksena, G. D., Ahmad, S. A., and Meenakshi, K. (1969) Isotope shift in 5525-A line of Neodymium. *Indian Journal of Pure Applied Physics*, 7(11), 743-745.
- Sapkota, S. N., Bollinger, L., Klinger, Y., Tapponnier, P., Gaudemer, Y., and Tiwari, D. (2013) Primary surface ruptures of the great Himalayan earthquakes in 1934 and 1255. *Nature Geoscience*, 6, 152–176.
- Scherler, D., Bookhagen, B., and Strecker, M. R. (2014) Tectonic control on <sup>10</sup>Be-derived erosion rates in the Garhwal Himalaya, India. *Journal of Geophysical Research: Earth Surface*, 119, 83–105.
- Scott, E. R. D., and Krot, A. N. (2014) Chondrites and their components. *Meteorites and cosmochemical processes*, 1, 65-137.
- Sears, D. W., Kallemeyn, G. W., and Wasson, J. T. (1982) The compositional classification of chondrites: II The enstatite chondrite groups. *Geochimica et Cosmochimica Acta*, 46(4), 597-608.
- Seeber, L., and Gornitz, V. (1983) River profiles along the Himalayan arc as indicators of active tectonics. *Tectonophysics*, 92(4), 335–367.
- Siegel, D. M., and Metzger, B. D. (2017) Three-dimensional general-relativistic magnetohydrodynamic simulations of remnant accretion disks from neutron star mergers: outflows and r-process nucleosynthesis. *Physical Review Letters*, 119(23), 231102.
- Siegel, D. M., Barnes, J., and Metzger, B. D. (2019) Collapsars as a major source of r-process elements. *Nature*, 569(7755), 241-244.
- Smith, C. L., and Russell, S. S. (2003) Dar al Gani 431: unravelling nebular and parent body processes. *Meteoritic and Planetary Science*, 38(A5222)
- Soucy La Roche, R., Godin, L., Cottle, J. M., and Kellett, D. A. (2018) Preservation of the early evolution of the Himalayan middle crust in foreland klippen: Insights from the Karnali klippe, West Nepal. *Tectonics*, 37, 1161–1193.
- Stephan, T., Trappitsch, R., Davis, A. M., Pellin, M. J., Rost, D., Savina, M. R., Jadhav, M., Kelly, C. H., Gyngard, F., Hoppe, P., and Dauphas, N. (2018) Strontium and barium isotopes in presolar silicon carbide grains measured with CHILI—two types of X grains. *Geochimica et Cosmochimica Acta*, 221, 109-126.

- Stevens, V. L., and Avouac, J. P. (2015) Interseismic coupling on the main Himalayan thrust. *Geophysical Research Letters*, 42, 5828–5837.
- Stevens, V. L., and Avouac, J. P. (2016) Millenary  $M_w > 9.0$  earthquakes required by geodetic strain in the Himalaya. *Geophysical Research Letters*, 43, 1118–1123.
- Stübner, K., Grujic, D., Dunkl, I., Thiede, R., and Eugster, P. (2018) Pliocene episodic exhumation and the significance of the Munsiri thrust in the northwestern Himalaya. *Earth and Planetary Science Letters*, 481, 273–283.
- Thiede, R. C., Bookhagen, B., Arrowsmith, J. R., Sobel, E. R., and Strecker, M. R. (2004) Climatic control on rapid exhumation along the Southern Himalayan front. *Earth and Planetary Science Letters*, 222(3–4), 791–806.
- Thiede, R. C., and Ehlers, T. A. (2013) Large spatial and temporal variations in Himalayan denudation. *Earth and Planetary Sciences Letters*, 371, 278–293.
- Thiede, R. C., Ehlers, T. A., Bookhagen, B., and Strecker, M. R. (2009) Erosional variability along the northwest Himalaya. *Journal of Geophysical Research*, 114, F01015.
- Thielemann, F. K., Eichler, M., Panov, I. V., and Wehmeyer, B. (2017) Neutron star mergers and nucleosynthesis of heavy elements. *Annual Review of Nuclear and Particle Science*, 67, 253–274.
- Touboul, M., Kleine, T., Bourdon, B., Palme, H., and Wieler, R. (2007) Late formation and prolonged differentiation of the Moon inferred from W isotopes in lunar metals. *Nature*, 450(7173), 1206–1209.
- Trinquier, A., Elliott, T., Ulfbeck, D., Coath, C., Krot, AN, and Bizzarro, M. (2009) Origin of nucleosynthetic isotope heterogeneity in the solar protoplanetary disk. *Science*, 324 (5925), 374–376.
- Qin, L., Carlson, R. W., and Alexander, C. M. D. (2011) Correlated nucleosynthetic isotopic variability in Cr, Sr, Ba, Sm, Nd and Hf in Murchison and QUE 97008. *Geochimica et Cosmochimica Acta*, 75(24), 7806–7828.
- Upadhyay, D., Scherer, E. E., and Mezger, K. (2008) Fractionation and mixing of Nd isotopes during thermal ionization mass spectrometry: implications for high precision  $^{142}\text{Nd}/^{144}\text{Nd}$  analyses. *Journal of Analytical Atomic Spectrometry*, 23(4), 561–568.
- van der Beek, P., Litty, C., Bauding, M., Mercier, J., Robert, X., and Hardwick, E. (2016) Contrasting tectonically driven exhumation patterns, western versus Central Nepal Himalaya. *Geology*, 44, 327–330.

- Vannay, J. C., and Hodges, K. V. (1996) Tectonometamorphic evolution of the Himalayan metamorphic core between the Anapurna and Dhaulagiri, Central Nepal. *Journal of Metamorphic Geology*, 14(5), 635–656.
- Wakaki, S., and Tanaka, T. (2012) Stable isotope analysis of Nd by double spike thermal ionization mass spectrometry. *International Journal of Mass Spectrometry*, 323, 45-54.
- Walters, J. B., and Kohn, M. J. (2017) Protracted thrusting followed by late rapid cooling of the Greater Himalayan sequence, Annapurna Himalaya, Central Nepal: Insights from titanite petrochronology. *Journal of Metamorphic Geology*, 35, 897–917.
- Wang, K., and Jacobsen, S. B. (2016) Potassium isotopic evidence for a high-energy giant impact origin of the Moon. *Nature*, 538(7626), 487-490.
- Warren, P. H. (2011) Stable-isotopic anomalies and the accretionary assemblage of the Earth and Mars: A subordinate role for carbonaceous chondrites. *Earth and Planetary Science Letters*, 311(1-2), 93-100.
- Wasson, J. T., Isa, J., and Rubin, A. E. (2013) Compositional and petrographic similarities of CV and CK chondrites: A single group with variations in textures and volatile concentrations attributable to impact heating, crushing and oxidation. *Geochimica et Cosmochimica Acta*, 108, 45-62.
- Weeks, K. S., and Sears, D. W. (1985) Chemical and physical studies of type 3 chondrites - V: The enstatite chondrites. *Geochimica et Cosmochimica Acta*, 49(7), 1525-1536.
- Weinbruch, S., Palme, H., and Spettel, B. (2000) Refractory forsterite in primitive meteorites: Condensates from the solar nebula?. *Meteoritics and Planetary Science*, 35(1), 161-171.
- Weisberg, M. K., McCoy, T. J., and Krot, A. N. (2006) Systematics and evaluation of meteorite classification. *Meteorites and the early solar system II*, 19.
- Wesnousky, S. G., Kumar, S., Mohindra, R., and Thakur, V. C. (1999) Uplift and convergence along the Himalayan frontal thrust of India. *Tectonics*, 18(6), 967–976.
- Weyrauch, M., Horstmann, M., and Bischoff, A. (2018) Chemical variations of sulfides and metal in enstatite chondrites—introduction of a new classification scheme. *Meteoritics and Planetary Science*, 53(3), 394-415.

- Whipp, D. M., Ehlers, T. A., Blythe, A., Huntington, K. W., Hodges, K. V., and Burbank, D. W. (2007) Plio-Quaternary exhumation history of the central Nepalese Himalaya: 2. Thermokinematic and thermochronometer age prediction model. *Tectonics*, 26, TC3003.
- Whipple, K. X. (2001) Fluvial landscape response time: How plausible is steady-state denudation? *American Journal of Science*, 301(4–5), 313–325.
- Whipple, K. X. (2009) The influence of climate on the tectonic evolution of mountain belts. *Nature Geoscience*, 2(2), 97–104.
- Whipple, K. X., Shirzaei, M., Hodges, K. V., and Arrowsmith, J. R. (2016) Active shortening within the Himalayan orogenic wedge implied by the 2015 Gorkha earthquake. *Nature*, 9, 711–716.
- Whipple, K. X., and Tucker, G. E. (1999) Dynamics of the stream-power river incision model: Implications for the height limits of mountain ranges, landscape response timescales, and research needs. *Journal of Geophysical Research*, 104(B8), 17,661–17,674.
- Wobus, C., Heimsath, A., Whipple, K., and Hodges, K. (2005) Active out-of-sequence thrust faulting in the central Nepalese Himalaya. *Nature*, 434(7036), 1008–1011.
- Wobus, C. W., Hodges, K. V., and Whipple, K. X. (2003) Has focused denudation sustained active thrusting at the Himalayan topographic front? *Geology*, 31(10), 861–864.
- Wobus, C. W., Whipple, K. X., and Hodges, K. V. (2006) Neotectonics of the central Nepalese Himalaya: Constraints from geomorphology, detrital  $^{40}\text{Ar}/^{39}\text{Ar}$  thermochronology, and thermal modeling. *Tectonics*, 25, TC4011.
- Yang, S., and Liu, Y. (2016) Nuclear field shift effects on stable isotope fractionation: a review. *Acta Geochimica*, 35(3), 227–239.
- Yin, Q. Z., and Sanborn, M. E. (2019) An update on disconnecting CV and CK Chondrites parent bodies and more. *Lunar and Planetary Science Conference*, 50(# 2132).
- Yokoyama, T., Fukami, Y., Okui, W., Ito, N., and Yamazaki, H. (2015) Nucleosynthetic strontium isotope anomalies in carbonaceous chondrites. *Earth and Planetary Science Letters*, 416, 46–55.
- Zhang, M., Salje, E. K. H., Ewing, R. C., Daniel, P., and Geisler, T. (2004) Applications of near-infrared FT-Raman spectroscopy in metamict and annealed zircon: oxidation state of U ions. *Physics and chemistry of minerals*, 31(7), 405–414.

- Zhang, J., Dauphas, N., Davis, A. M., Leya, I., and Fedkin, A. (2012) The proto-Earth as a significant source of lunar material. *Nature Geoscience*, 5(4), 251-255.
- Zinner, E. (2014) Presolar grains. *Meteorites and cosmochemical processes*, 1, 181-213.
- Zipfel, J., Palme, H., Clayton, R. N., Mayeda, T. K., Spettel, B., and Wolf, D. (2000) Dar al Gani 431: a new anomalous CK3 chondrite? *Lunar and Planetary Science Conference*, 31(#1668).
- Zhu, K., Moynier, F., Schiller, M., Alexander, C. M. D., Davidson, J., Schrader, D. L., van Kooten, E., and Bizzarro, M. (2021) Chromium isotopic insights into the origin of chondrite parent bodies and the early terrestrial volatile depletion. *Geochimica et Cosmochimica Acta*. (In Press).